2013-10

Sequential Structural and Fluid Dynamics Analysis of Balloon-Expandable Coronary Stents.

David Martin
Technological University Dublin, david.martin@tudublin.ie

Sequential Structural and Fluid Dynamics Analysis of Balloon-Expandable Coronary Stents

by

David M. Martin, B.Eng. (Hons)

A thesis submitted to Dublin Institute of Technology in partial fulfilment of the requirements for the degree of

Doctor of Philosophy

Supervisor: Dr. Fergal J. Boyle

Department of Mechanical Engineering
Dublin Institute of Technology

October 2013

ABSTRACT

As in-stent restenosis following coronary stent deployment has been strongly linked with stent-induced arterial injury and altered vessel hemodynamics, the sequential numerical analysis of the mechanical and hemodynamic impact of stent deployment within a coronary artery is likely to provide an excellent indication of coronary stent performance. Despite this observation, very few numerical studies have considered both the mechanical and hemodynamic impact of stent deployment. In light of this observation, the aim of this research is to develop a robust numerical methodology for investigating the performance of balloon-expandable coronary stents in terms of their mechanical and hemodynamic impact within a coronary artery. The proposed methodology is divided into two stages. In the first stage, a numerical model of the stent is generated and a computational structural analysis is carried out to simulate its deployment within a coronary artery. In the second stage, the results of the structural analysis are used to generate a realistic model of the stented coronary lumen and a computational fluid dynamics analysis is carried out to simulate pulsatile blood flow within a coronary artery. Following the completion of the analyses, the mechanical impact of the stent is evaluated in terms of the stress distribution predicted within the artery whilst the hemodynamic impact of the stent is evaluated in terms of the wall shear stress distribution predicted upon the luminal surface of the artery. In order to demonstrate its application, the proposed numerical methodology was applied to six generic stents. Comparing the predicted performance of the generic stents revealed that strut thickness is likely to have a significant influence upon both the mechanical and hemodynamic impact of coronary stent deployment. Additionally, comparing the predicted performance of three of the investigated stents to the clinical performance of three comparable commercial stents, as reported in two large-scale clinical trials, revealed that that the proposed numerical methodology successfully identified the stents that resulted in higher rates of angiographic in-stent restenosis, late lumen loss and target-vessel revascularisation at short-term follow-up. In light of the conflicting requirements of coronary stent design, the proposed numerical methodology should prove useful in the design and optimisation of future coronary stents.

DECLARATION

I certify that this thesis, which I now submit for examination for the award of Doctor of Philosophy, is entirely my own work and has not been taken from the work of others, save and to the extent that such work has been cited and acknowledged within the text of my work.

This thesis was prepared according to the regulations for post-graduate study by research of the Dublin Institute of Technology and has not been submitted in whole or in part for another award in any institute.

The work reported in this thesis conforms to the principles and requirements of the Institute's guidelines for ethics in research.

The Institute has permission to keep, lend or copy this thesis in whole or in part, on condition that any such use of the material of the thesis is duly acknowledged.

Signature _____ Date _____

ACKNOWLEDGEMENTS

First and foremost I would like to thank Dublin Institute of Technology for providing me with the opportunity to carry out this research. I would also like to express my sincere thanks and gratitude to my supervisor, Dr. Fergal Boyle, for the endless time and effort that he has invested in guiding this research over the years.

I would also like to thank the following people for their various contributions to this research over the years: Prof. David Kennedy for always making time for me and for his excellent advice and assistance, Prof. Steve Jerrams and the Centre for Elastomer Research for their generous financial assistance during the acquirement of software licences, Dr. Barry Duignan and Dr. Graham Gavin for introducing me to numerical modelling and for their advice when things inevitably went wrong, Alan Brereton, Ian Campbell, Simon Farrell and Michael Faherty for their technical assistance, Bill Murphy and the rest of the Bolton Street librarians for their continuous support and Derek Sweeney (IDAC, Ireland), Dr. Bryan MacDonald and Emmet Galvin (Dublin City University) and James Grogan (National University of Ireland, Galway) for the kind responses to my requests for advice and assistance over the years. I would also like to thank the Irish Centre of High-End Computing (ICHEC) for the provision of computational expertise and resources. In particular, I would like to extend a special thanks to Peter Nash for his excellent technical support and assistance.

I would also like to thank the many post-graduate students in Bolton Street for their support and friendship. In particular, I would like to thank Jonathan Murphy, Eileen Mageean, Marissa Llorens-Salvador, Fergal O'Rourke, Zhe Li, Eoin Murphy and Mingzhu Chen. It was a pleasure to get to know all of you. I would also like to thank Danny, Neil, Glen and the rest of the lads for their friendship and advice. Finally, and most importantly, I would like to express my deepest thanks and gratitude to my parents, Brian and Maria, my sisters, Jenny and Aoife, and my girlfriend, Amanda, for their relentless support, encouragement and patience. I'm sorry that it took me so long to put this together, but thanks to you I got there in the end.

NOMENCLATURE

Abbreviations

3D	Three-dimensional
2D	Two-dimensional
EC	Endothelial cell
VSMC	Vascular smooth muscle cell
vWF	von Willebrand factor
ADP	Adenosine diphosphate
PAF	Platelet-activating factor
VCAM-1	Vascular-cell adhesion molecule-1
ICAM-1	Intracellular adhesion molecule-1
FGF	Fibroblast growth factor
PDGF	Platelet-derived growth factor
TNF	Tumour necrosis factor
VEGF	Vascular-endothelial growth factor
EPC	Endothelial progenitor cell
TVR	Target-vessel revascularisation
LL	Late lumen loss
CS	Computational structural
CFD	Computational fluid dynamics
RR	Radial recoil
LF	Longitudinal foreshortening
ES	Equivalent von Mises stress
WSS	Wall shear stress
TAWSS	Time-averaged wall shear stress
OSI	Oscillatory shear index
RRT	Relative residence time
SC	Spearman rank correlation coefficient
PC	Pearson product-moment correlation coefficient

Scalars

t	Time
T	Period
J	Jacobian determinant
dv	Infinitesimal spatial volume element
dV	Infinitesimal material volume element
Δv	Spatial volume element
ΔV	Material volume element
ds	Infinitesimal spatial surface element
dS	Infinitesimal material surface element
Δs	Spatial surface element
ΔS	Material surface element
$\lambda_1, \lambda_2, \lambda_3$	First, second and third principal values
I, II, III	First, second and third principal invariants
ρ	Spatial density
ρ_0	Material density
m	Spatial mass of a volume element
Δm_0	Material mass of a volume element
W	Strain energy function
λ, μ	Lamé constants, first and second viscosity coefficients
E	Young's modulus
ν	Poisson's ratio
μ	Dynamic viscosity
$\dot{\gamma}$	Shear strain rate
μ_∞, μ_0	High and low shear viscosities
λ_t, q	Bird-Carreau coefficients
υ	Kinematic viscosity
κ	Bulk viscosity
p_0	Hydrostatic pressure
p	Thermodynamic pressure, Lagrange multiplier

C_1, C_2	Mooney-Rivlin hyperelastic material constants
μ_i, α_i, D_i	Ogden hyperelastic material constants
Φ	Yield criterion
σ_e	Equivalent stress
σ_y	Yield stress
α	Isotropic hardening parameter
$d\lambda$	Plastic multiplier
g	Plastic potential
N_a	Nodal shape function, Element shape function
Δt	Time step
ω_{max}	Maximum element eigenvalue
ϕ	Transport variable
Γ	Diffusion coefficient
S	Source term
$\bar{S}$	Cell-averaged source term
$\bar{b}$	Solution-independent, cell-averaged source term
$\bar{S}(\phi)$	Solution-dependent, cell-averaged source term
$\dot{m}$	Mass flow rate
β	Blend factor
v_{cl}	Centreline velocity
a, b_n, ω_n, ϕ_n	Fourier coefficients
D_{load}	Stent diameter at maximum loading
D_{unload}	Stent diameter following unloading
$L_{initial}$	Initial stent length prior to loading
L_{load}	Stent length following unloading
r	Radial distance from the centreline of the artery
R	Radius of the unstented artery
L	Length of a flat plate
U_∞	Free-stream velocity
δ	Boundary layer thickness

Re_x	Local Reynolds number over a flat plate
x, y, z	Cartesian coordinates
x^*, y^*, z^*	Non-dimensional Cartesian coordinates
u, v, w	Cartesian components of the velocity vector
u^*, v^*, w^*	Non-dimensional Cartesian components of the velocity vector
p^*	Non-dimensional thermodynamic pressure
η	Similarity variable
$f(\eta)$	Similarity function
ψ	Stream function
C_f	Skin friction coefficient
$\tau_{w,x}, \tau_{w,y}, \tau_{w,z}$	Cartesian components of the wall shear stress vector

Vectors

$\mathbf{x}$	Spatial points/coordinates
$\mathbf{X}$	Material points/coordinates
$\boldsymbol{\varphi}$	Motion (vector mapping)
$\boldsymbol{\varphi}^{-1}$	Inverse motion (vector mapping)
$\mathbf{u}$	Spatial displacement vector
$\mathbf{U}$	Material displacement vector
$\mathbf{n}$	Spatial surface normal vector
$\mathbf{N}$	Material surface normal vector
$\widehat{\mathbf{N}}_1, \widehat{\mathbf{N}}_2, \widehat{\mathbf{N}}_3$	First, second and third principal directions
$\mathbf{v}$	Spatial velocity vector
$\mathbf{V}$	Material velocity vector
$\mathbf{a}$	Spatial acceleration vector
$\mathbf{A}$	Material acceleration vector
$\mathbf{t}^{(\mathbf{n})}$	Spatial traction vector for the spatial surface normal vector $\mathbf{n}$
$\mathbf{t}^{(\mathbf{N})}$	Spatial traction vector for the material surface normal vector $\mathbf{N}$
$\mathbf{T}^{(\mathbf{N})}$	Material traction vector for the material surface normal vector $\mathbf{N}$
$\Delta\mathbf{f}$	Spatial force vector

$\Delta\mathbf{f}$	Material force vector
$d\mathbf{f}$	Infinitesimal spatial force vector
$d\mathbf{F}$	Infinitesimal material force vector
$\boldsymbol{\tau}_w$	Wall shear stress vector
$\mathbf{b}$	Spatial body force vector
$\mathbf{B}$	Material body force vector
$\boldsymbol{\eta}$	Weighting function
$\delta\mathbf{u}$	Virtual displacement vector
$\mathbf{R}$	Global vector of internal forces
$\mathbf{P}$	Global vector of external forces
$\mathbf{ds}$	Spatial outward surface vector
$\mathbf{dS}$	Material outward surface vector
$\Delta\mathbf{r}$	Upwind node vector
$\boldsymbol{\phi}$	Solution vector
$\mathbf{r}$	Residual vector

Second-Order Tensors

$\mathbf{I}$	Identity tensor
$\mathbf{F}$	Deformation gradient tensor
$\mathbf{F}^{-1}$	Inverse deformation gradient tensor
$\mathbf{h}$	Spatial displacement gradient tensor
$\mathbf{H}$	Material displacement gradient tensor
$\mathbf{R}$	Rotation tensor
$\mathbf{v}$	Left stretch tensor
$\mathbf{U}$	Right stretch tensor
$\mathbf{b}$	Left Cauchy-Green deformation tensor
$\mathbf{C}$	Right Cauchy-Green deformation tensor
$\mathbf{e}$	Euler-Almansi strain tensor
$\mathbf{E}$	Green-Lagrange strain tensor
$\boldsymbol{\varepsilon}$	Infinitesimal strain tensor

$\mathbf{l}$	Spatial velocity gradient tensor
$\mathbf{d}$	Spatial rate of deformation tensor
$\mathbf{w}$	Spatial spin tensor
$\boldsymbol{\sigma}$	Cauchy stress tensor
$\mathbf{P}$	First Piola-Kirchoff stress tensor
$\mathbf{S}$	Second Piola-Kirchoff stress tensor
$d\boldsymbol{\varepsilon}$	Total strain increment tensor
$d\boldsymbol{\varepsilon}^e$	Elastic strain increment tensor
$d\boldsymbol{\varepsilon}^p$	Plastic strain increment tensor
$\mathbf{s}$	Deviatoric stress tensor
$\bar{\boldsymbol{\alpha}}$	Kinematic hardening back stress tensor
$\boldsymbol{\tau}$	Viscous stress tensor

Fourth-Order Tensors

$\mathcal{C}$	Elasticity tensor
$\mathcal{K}$	Viscosity tensor

Matrices

$\mathbf{B}$	Strain-displacement matrix
$\mathbf{M}$	Mass matrix
$\mathbf{A}$	Coefficient matrix
$\mathbf{b}$	Right-hand side matrix

Operators

$\boldsymbol{\nabla}$	Gradient (spatial coordinates)
$\boldsymbol{\nabla}_0$	Gradient (material coordinates)
$\boldsymbol{\nabla} \cdot (\cdot)$	Divergence (spatial coordinates)
$\boldsymbol{\nabla}_0 \cdot (\cdot)$	Divergence (material coordinates)
$\mathrm{tr}(\cdot)$	Trace operator

Statistical Variables

μ_{vw}	Volume-weighted mean
μ_{aw}	Area-weighted mean
σ_{vw}	Volume-weighted standard deviation
σ_{aw}	Area-weighted standard deviation
S_{vw}	Volume-weighted skewness
S_{aw}	Area-weighted skewness
x_i	Ranked values of the variable X
y_i	Ranked values of the variable Y
$\bar{x}_i$	Mean values of the variable X
$\bar{y}_i$	Mean values of the variable Y
t_s	Student's t-statistic
n	Number of degrees of freedom

Subscripts

a	Node
ip	Integration point

TABLE OF CONTENTS

LIST OF FIGURES

LIST OF TABLES

CHAPTER 1
INTRODUCTION

1.1 Introduction

In this chapter, both the anatomy and physiology of the heart are first introduced and the burden of coronary heart disease is then discussed. Coronary stent deployment, which is the currently preferred treatment for symptomatic coronary heart disease, is then introduced and the major limitation of this procedure, called in-stent restenosis, is described. The relationship between in-stent restenosis and both arterial injury and altered vessel hemodynamics is then investigated and the computational numerical analysis of coronary stents is introduced. The aims of the research are then presented and the structure of the thesis is described. The original contributions of the research are then discussed and the publications derived from the research are noted.

1.2 The Heart

The heart is a remarkable muscular organ that contracts approximately 100,000 times per day in order to pump almost 8,000 litres of blood to the various tissues within the body. The mammalian heart is conical in shape, similar in size to a clenched fist and weighs approximately 0.25 kg. Blood is pumped from the heart through a network of vessels that extend between the heart and the different tissues within the body. These vessels are organised into two primary circulatory routes which are referred to as the systemic and pulmonary circulations. The systemic circulation supplies oxygenated blood to the tissues throughout the body and returns deoxygenated blood to the heart. The deoxygenated blood then enters the pulmonary circulation and is pumped to the lungs where carbon dioxide is exchanged for oxygen. The freshly oxygenated blood then returns to the heart and re-enters the systemic circulation. The vessels that carry blood away from the heart are called arteries whilst the vessels that carry blood to

the heart are called veins. Thin-walled vessels called capillaries connect the smallest arteries and the smallest veins. Capillaries are also called exchange vessels as their thin walls permit the exchange of nutrients between the blood and the neighbouring tissues. The heart, the lungs and the vessels of both the systemic and the pulmonary circulations are collectively referred to as the cardiovascular system.

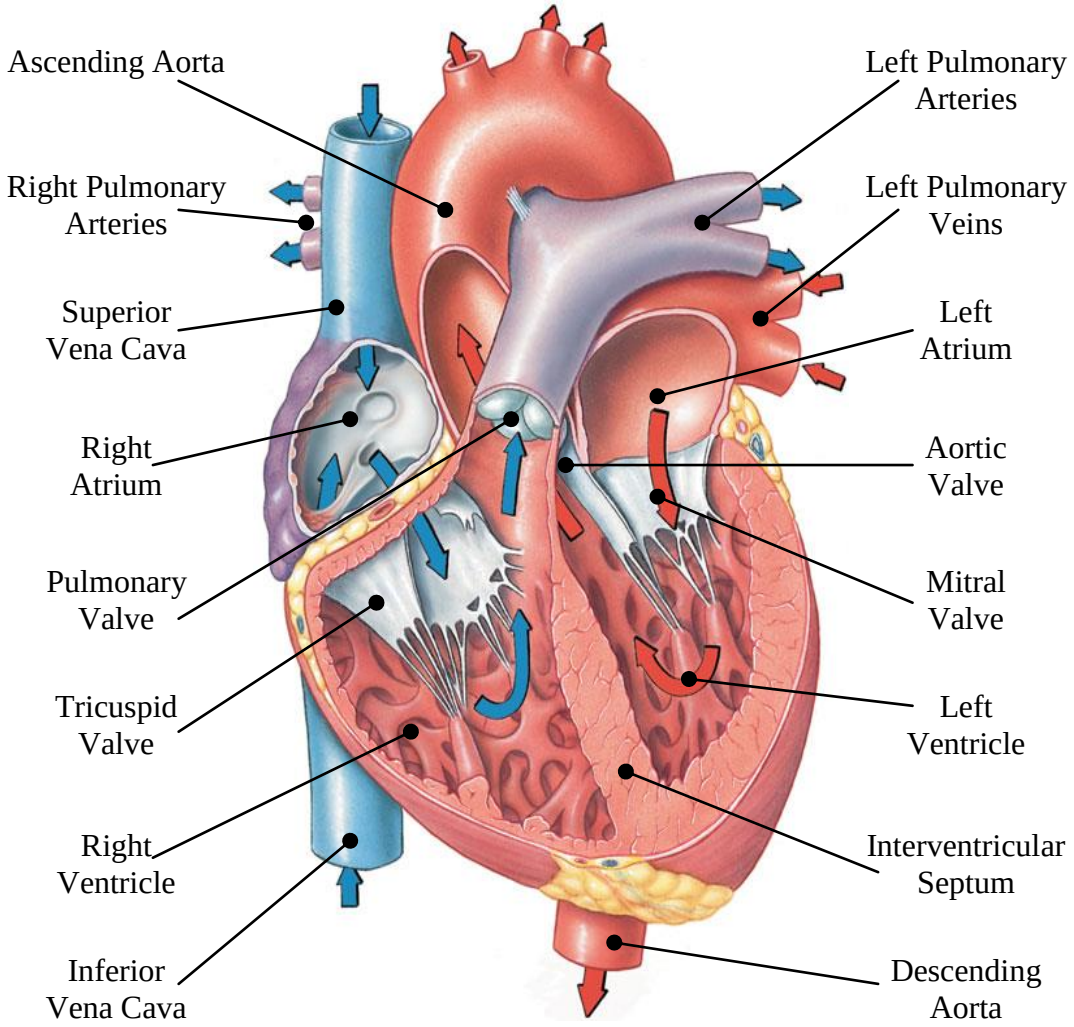

Figure 1.1: Cross-sectional view of the human heart [1]**.**

The heart is located in the centre of the chest within an anatomical region called the mediastinum. As shown in Figure 1.1, the interior of the heart is divided into two receiving chambers, called atria, and two pumping chambers, called ventricles. The atria are separated by a thin muscular wall, called the interatrial septum, whilst the ventricles are separated by a much thicker muscular wall, called the interventricular septum. The right atrium receives blood from the superior vena cava, the inferior vena cava and the coronary sinus whilst the left atrium receives blood from both the right and left pulmonary veins. Blood flow from the right and left atria to the right

and left ventricles is regulated by the tricuspid and mitral valves, respectively, and these valves are referred to as the atrioventricular valves. The atrioventricular valves are anchored to the walls of the right and left ventricles by chordae tendineae, which prevent the valves from inverting. Blood flow from the right and left ventricles to the pulmonary and systemic circulations is then regulated by the pulmonary and aortic valves, respectively, and these valves are referred to as the semilunar valves. These valves do not have chordae tendineae, and are more similar to valves that are located within veins than the atrioventricular valves. The cardiac valves are each composed of dense connective tissue and prevent blood from flowing backwards during the contraction of the heart. Finally, the atria are separated from the ventricles by four dense bands of collagen called the fibrous skeleton of the heart. The fibrous skeleton of the heart surrounds and supports each of the four cardiac valves and establishes an electrically impermeable boundary between the atria and the ventricles.

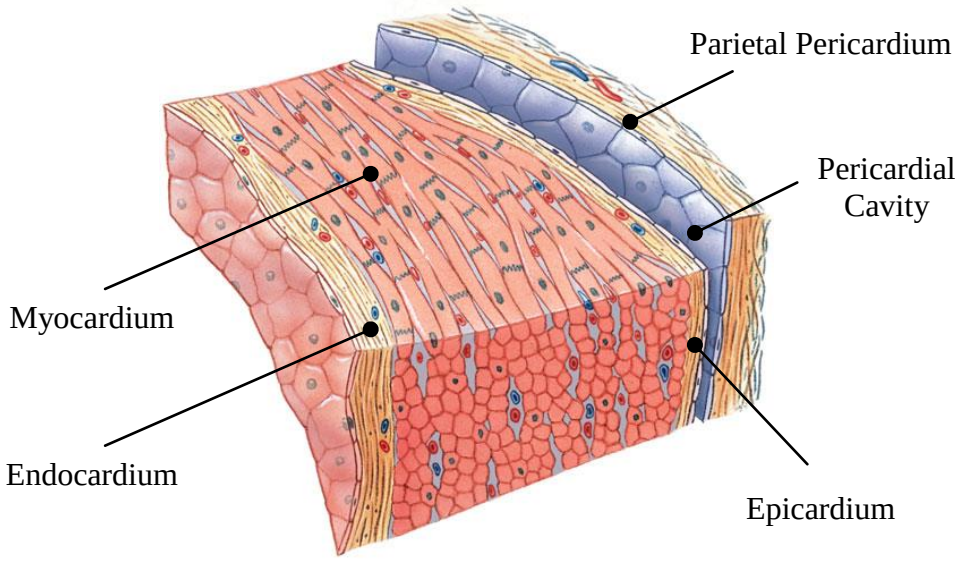

Figure 1.2: Cross-sectional view of the wall of the human heart [1]**.**

As shown in Figure 1.2, the wall of the heart is divided into an inner layer, called the endocardium, an intermediate layer, called the myocardium, and an outer layer that is called the epicardium. The endocardium lines the inner surface of both the cardiac chambers and the cardiac valves and is composed of a monolayer of endothelial cells (ECs) which are supported by a membrane of collagen and elastin. The myocardium makes up about 95% of the wall of the heart and is the functional tissue that endows the cardiac chambers with the ability to pump blood. The myocardium is composed of specialised cardiac muscle cells, called cardio-myocytes, which are arranged into

striated muscle fibres. These cardiac muscle fibres surround each of the individual chambers of the heart and are embedded within an extracellular network of collagen. The epicardium surrounds the myocardium and is composed of both fibroelastic and adipose tissue. Both the heart and the trunks of the great vessels are surrounded by a dual-layered fibrous sac called the pericardium. The outer layer of the pericardium is referred to as the fibrous pericardium whereas the inner layer of the pericardium is referred to as the serous pericardium. The serous pericardium, in turn, is divided into two layers called the parietal pericardium and the visceral pericardium. The parietal pericardium is fused to the fibrous pericardium whilst the visceral pericardium forms part of the epicardium. The cavity between the parietal and visceral pericardium is called the pericardial cavity and is lubricated by a thin fluid, called pericardial fluid. The pericardium maintains the heart within the mediastinum and prevents excessive dilation of the cardiac chambers during cases of acute volume overload.

The continuous contraction and relaxation of the heart is called the cardiac cycle and is divided into four distinct phases called atrial systole, atrial diastole, ventricular systole and ventricular diastole. At the beginning of the cycle, the atria and ventricles are relaxed and the atrioventricular valves are fully open. During this initial stage of the cycle, blood flows from the atria to the ventricles until the ventricles fill to about 75% of their total capacity. During atrial systole, which lasts for approximately 100 ms, the atria start to contract and the subsequent increase in atrial pressure forces blood through the atrioventricular valves and into the ventricles. Once the ventricles have been filled to capacity, atrial diastole begins and the atria start to relax. Atrial diastole begins at the same time as ventricular systole and lasts until the start of the following cycle. During ventricular systole, which lasts for approximately 270 ms, the ventricles start to contract and the subsequent increase in ventricular pressure forces the atrioventricular valves to close. As the ventricular pressure continues to increase, the semilunar valves are forced open and the blood contained within the ventricles is ejected into the systemic and pulmonary circulations. During ventricular diastole, which lasts for approximately 530 ms, the ventricles start to relax and the subsequent reduction in ventricular pressure allows the atrioventricular valves to reopen. For the remainder of the current cycle, the atria and ventricles then fill with blood in a relaxed manner. Once the ventricles have filled to about 75% of their total capacity, atrial systole begins and the entire cardiac cycle is repeated.

In order to operate efficiently, the heart must contract and relax in a precise rhythmic sequence. The precise rhythmic contraction of the heart is coordinated by a series of electrical impulses that are both generated and transmitted by the cardiac conduction system. As shown in Figure 1.3, the cardiac conduction system is composed of two impulse-generating nodes, called the sinoatrial node and the atrioventricular node, and two sets of impulse-transmitting fibres, called the bundle of His and the Perkinje fibres. The sinoatrial node is a small mass of auto-rhythmic cells that is located near the entrance of the superior vena cava within the upper wall of the right atrium. The atrioventricular node is a slightly larger mass of auto-rhythmic cells that is located in the base of the right atrium near the entrance of the coronary sinus. The bundle of His is a band of nerve fibres that originate at the atrioventricular node and split into right and left branches that then pass along the interventricular septum to the right and left ventricles. Finally, the Perkinje fibres are the branchings of the bundle of His that extend between muscle fibres within the ventricular myocardium.

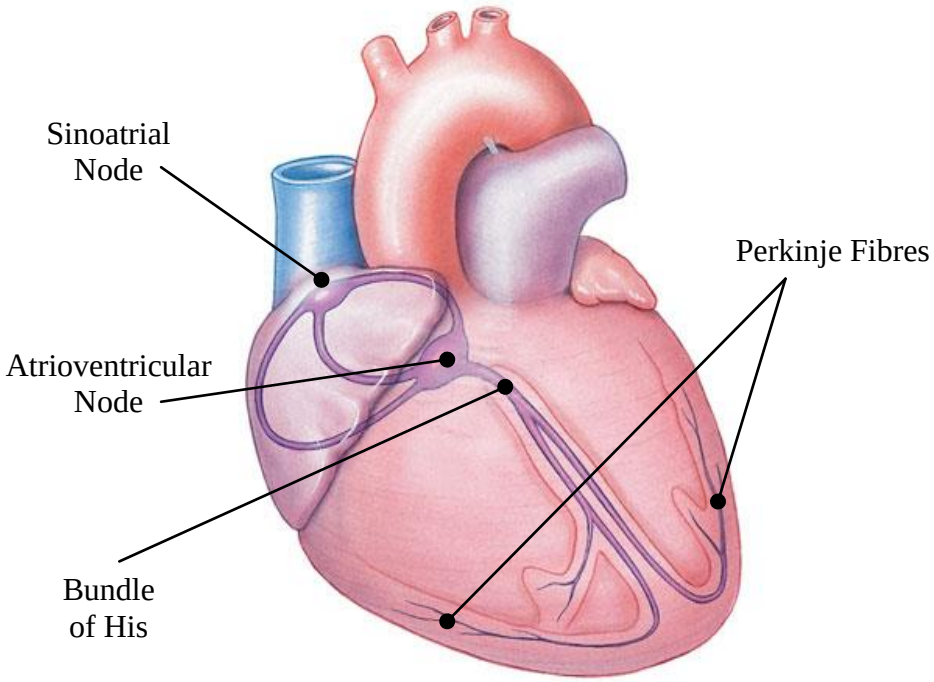

Figure 1.3: The cardiac conduction system of the human heart [1].

The cardiac cycle is initiated by the auto-rhythmic cells within the sinoatrial node. These auto-rhythmic cells do not have a stable resting potential and generate regular electrical impulses as their membranes depolarise. Cardiac muscle cells contain actin and myosin filaments that slide across each other in response to an electrical impulse

and stimulate the contraction of the cardiac muscle fibre. The cardiac muscle cells also contain intercellular junctions, called gap junctions, which transmit the electrical impulse from one muscle fibre to another. In this manner, the electrical impulse that is generated by the sinoatrial node propagates throughout the atrial myocardium and induces atrial systole. As the atria and the ventricles are insulated from one another by the fibrous skeleton, the electrical impulse must reach the atrioventricular node before it is transmitted to the ventricular myocardium. When the electrical impulse reaches the atrioventricular node, it is delayed by approximately 100 ms due to slight differences in the size of the auto-rhythmic cells located within the atrioventricular node. This brief delay provides just enough time for the atria to contract and for the ventricles to fill with blood. The electrical impulse is then transmitted along the right and left branches of the bundle of His to the Perkinje fibres such that it propagates throughout the ventricular myocardium and induces ventricular systole.

1.3 The Coronary Circulation

For the average human, the cardiac cycle is repeated between 60 and 90 times per minute and the myocardium requires a constant supply of oxygenated blood in order to meet this demand. This supply is met by an essential sub-network of the systemic circulation called the coronary circulation. The two main coronary arteries, called the right and left coronary arteries, originate at the base of the ascending aorta near the aortic sinus where the blood pressure within the systemic circulation is at its highest. During ventricular systole, oxygenated blood contained within the left ventricle is ejected into the ascending aorta which causes the walls of the vessel to dilate. During ventricular diastole, the left ventricle starts to relax and the subsequent reduction in aortic pressure causes the walls of the vessel to recoil. The elastic recoil of the aorta forces blood either forward, into the systemic circulation, or backwards, through the right and left aortic sinuses and into the right and left coronary arteries, respectively. As such, the elastic recoil of the ascending aorta propels oxygenated blood through the coronary arteries, capillaries and veins during ventricular diastole.

As shown in Figure 1.4, the right coronary artery follows the right coronary sulcus around the heart and supplies blood to the right atrium and to portions of both the right and left ventricles. Below the right atrium, the right coronary artery divides into the posterior interventricular (or the right posterior descending) artery and one

or more marginal arteries. The posterior interventricular artery follows the posterior interventricular sulcus and supplies the ventricular myocardium with blood. Beyond the coronary sulcus, the marginal arteries run along the right margin of the heart and supply blood to the right ventricular myocardium. The left coronary artery supplies blood to the left atrium, the left ventricle and the interventricular septum. As shown in Figure 1.4, the left coronary artery divides into the anterior interventricular (or the left anterior descending) artery and the circumflex artery upon reaching the anterior surface of the heart. The circumflex artery curves around the coronary sulcus and then fuses with the branches of the right coronary artery whereas the larger anterior interventricular artery swings around the pulmonary trunk and runs along the surface of the left ventricle within the anterior interventricular sulcus.

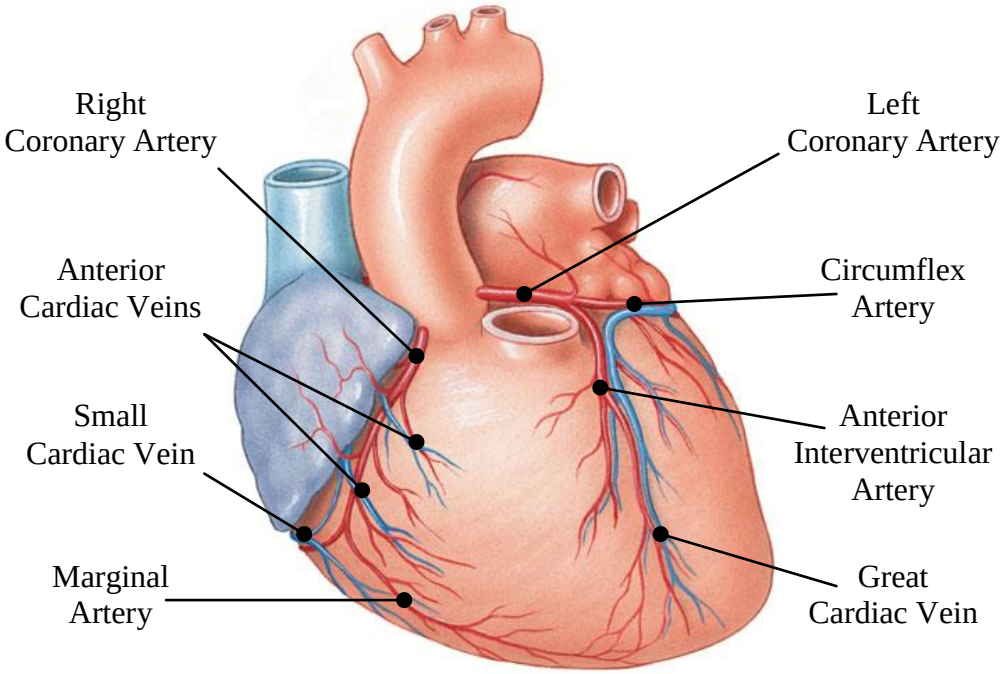

Figure 1.4: Anterior surface of the human heart [1].

After blood has passed through the coronary arteries it flows into the coronary capillaries where it delivers oxygen and nutrients to the myocardium and collects carbon dioxide and other waste products. As shown in Figure 1.4, the great cardiac vein is located upon the anterior surface of the ventricles, along the interventricular sulcus. The great cardiac vein drains the region of the heart that is supplied by the anterior interventricular artery. The great cardiac vein curves around the left side of the heart and empties into the coronary sinus, which lies within the posterior portion of the coronary sulcus. The coronary sinus then empties into the right atrium near the

base of the inferior vena cava. As shown in Figure 1.5, a number of smaller cardiac veins, such as the posterior, middle and small cardiac veins empty directly into the great cardiac vein. The posterior cardiac vein drains the region of the heart which is supplied by the circumflex artery, the middle cardiac vein drains the region supplied by the posterior interventricular artery and the small cardiac vein drains the posterior surface of the right atrium. Finally, the anterior cardiac veins then drain the anterior surface of the right ventricle and empty into the right atrium.

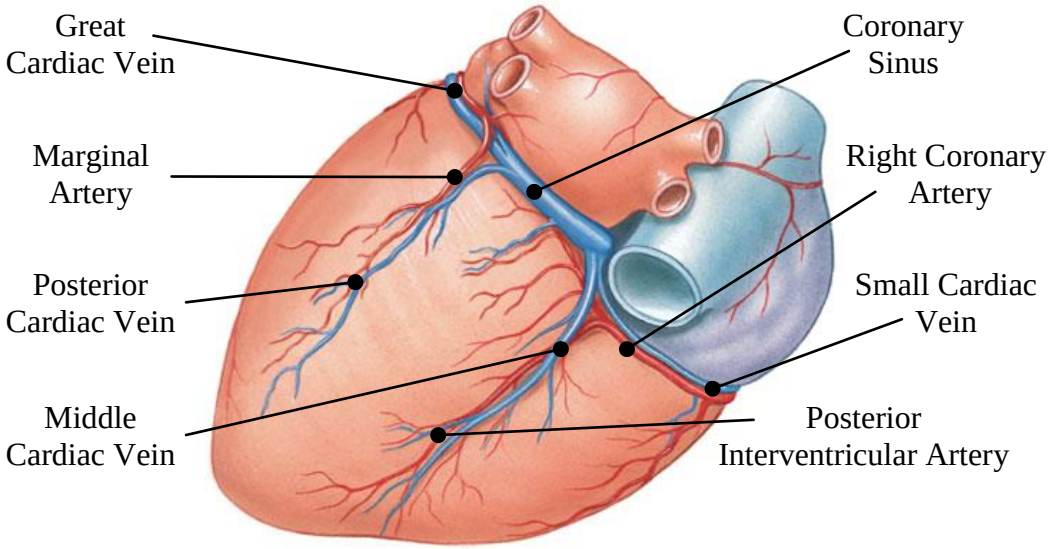

Figure 1.5: Posterior surface of the human heart [1]**.**

As shown in Figure 1.6, the wall of the coronary arteries is divided into an inner layer, called the tunica intima, an intermediate layer, called the tunica media, and an outer layer, called the tunica adventitia. The intima lines the inner surface of the coronary arteries and is composed of a monolayer of ECs which are supported by a thin basal lamina that is referred to as the basement membrane. This monolayer of ECs, called the vascular endothelium, is an important component of the artery wall that regulates the release of chemical mediators in response to both mechanical and hemodynamic stimuli. The media makes up the bulk of the artery and is composed of concentric layers of vascular smooth muscle cells (VSMCs) which are embedded within an extracellular network of collagen and elastin fibres. The primary role of the media is to regulate the diameter of the lumen. Specifically, the VSMCs located within the media contract and relax in response to local stimulating factors in order to narrow or dilate the lumen. Finally, the adventitia forms a protective layer around the media and is composed of collagen fibres, elastin fibres, nerves, fibroblasts and

small blood vessels. The intima is separated from the media by a thin layer of elastic fibres called the internal elastic lamina and the media is separated from the adventitia by a similar layer of elastic fibres called the external elastic lamina.

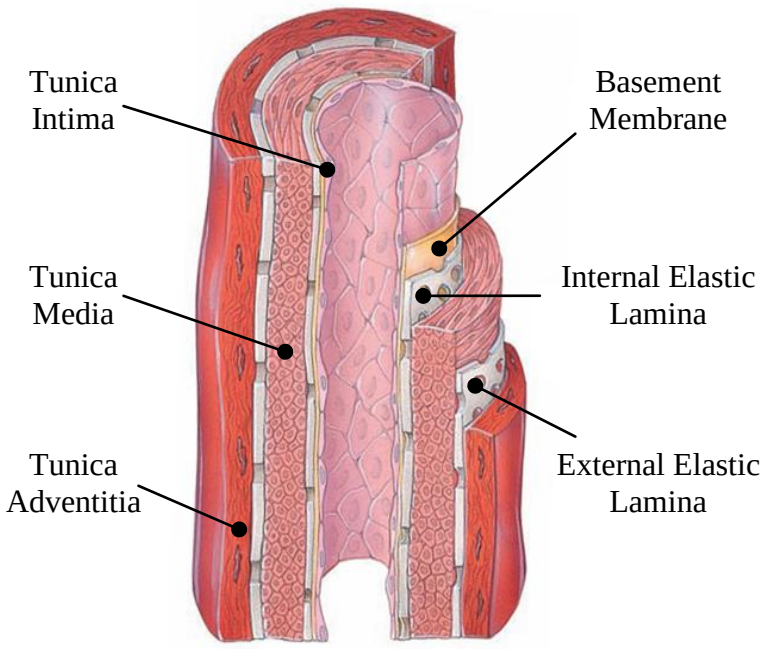

Figure 1.6: Cross-sectional view of a human coronary artery [1]**.**

1.4 Cardiovascular and Coronary Heart Disease

The term cardiovascular disease refers to any disease that affects the cardiovascular system and the most common forms of cardiovascular disease are cardiac diseases, peripheral arterial diseases and vascular diseases of the brain and kidneys. According to recent mortality data published by the European Heart Network, cardiovascular disease accounts for 1.9 million deaths (47% of the total annual mortality) per year within the European Union [2]. To convey the economic impact of this figure, the European Heart Network estimates that the treatment of cardiovascular disease costs the European Union €196 billion per year. Of the different forms of cardiovascular disease, coronary heart disease is by far the most prevalent. Coronary heart disease, which refers to the failure of the coronary circulation to provide an adequate supply of oxygenated blood to the myocardium, is caused by the narrowing and stiffening of the coronary arteries. This narrowing and stiffening of the coronary arteries is caused by a common vascular disorder, called atherosclerosis, which develops over many years and results in the growth of raised lesions, called plaques, within the intimal layer of the coronary arteries. As these plaques increase in size, they can protrude

into the lumen and restrict the flow of oxygenated blood to the myocardium. If left untreated, this can cause arrhythmia (abnormal heart rate or rhythm), angina pectoris (severe chest pain) and acute myocardial infarction (heart attack).

1.5 Coronary Stent Deployment

The preferred treatment for symptomatic coronary heart disease is currently coronary stent deployment. A stent is a small cylindrical device that is used to restore the flow of blood within a narrowed blood vessel. Today, the majority of coronary stents are balloon-expandable and are manufactured in a crimped configuration and positioned upon a balloon-tipped catheter [3]. During the deployment of a balloon-expandable coronary stent, a thin guide wire is inserted into the lumen of the femoral, brachial or radial artery and then directed to the narrowed artery using x-ray fluoroscopy. The balloon-tipped catheter is then threaded over the guide wire and advanced toward to the narrowed artery as before. Once the stent has been positioned across the plaque, the angioplasty balloon is inflated to a nominal pressure. As shown in Figure 1.7, the inflation of the angioplasty balloon, forces the deployment of the stent, compresses the plaque against the artery wall and restores the flow of blood within the narrowed artery. Following the deployment of the stent, both the catheter and guide wire are retracted and the stent remains within the artery where it minimises elastic recoil and negative remodelling. The first coronary stent deployment procedure in a human was carried out by Jacques Puel and Ulrich Sigwart in France in 1986 [4].

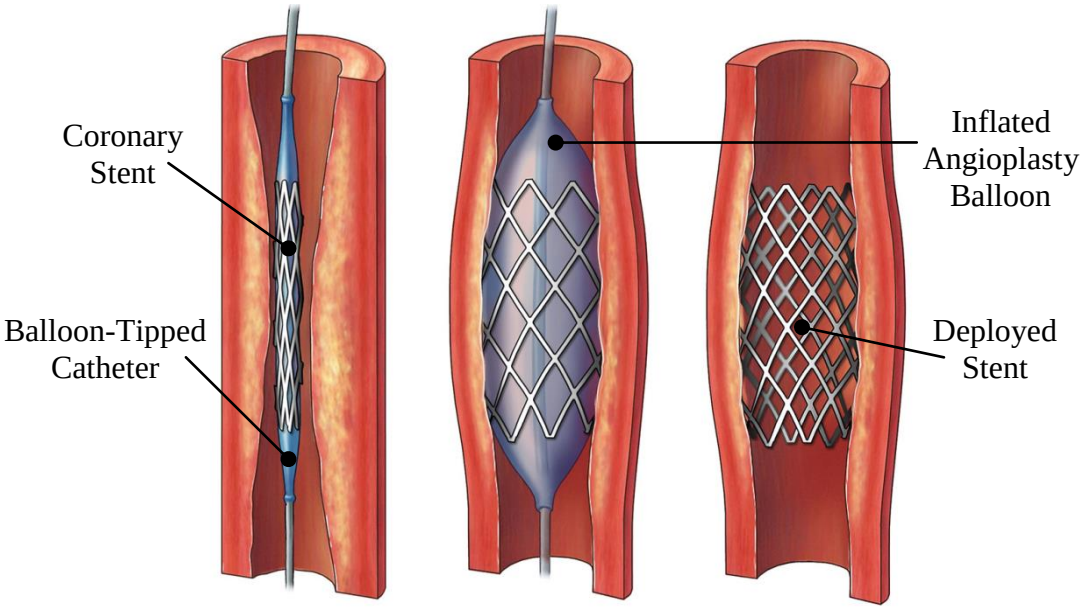

Figure 1.7: Stent deployment within an atherosclerotic coronary artery.

1.6 In-Stent Restenosis

The majority of balloon-expandable coronary stents that were introduced in the mid- to late-1990s are manufactured from biologically inert metallic materials, such as medical grade 316L stainless steel and are referred to as bare-metal stents. For many patients who suffer from coronary heart disease, treatment with a bare-metal balloon-expandable coronary stent provides symptomatic relief and provides good prospects for event-free survival. For between 20 and 30% of patients, however, re-narrowing of the stented artery is observed at short-term follow-up [5–7]. This re-narrowing of the stented artery, called in-stent restenosis, is the major limitation of coronary stent deployment. In an attempt to reduce rates of in-stent restenosis, drug-eluting stents were introduced in 2003. A drug-eluting stent is simply a bare-metal stent that has been coated with an anti-restenotic drug and a suitable carrier material. Over the past decade, clinical evaluation of drug-eluting stents has demonstrated reduced rates of in-stent restenosis compared to bare-metal stents across a wide range of both patient and lesion subsets [8–14]. Despite this success, however, in-stent restenosis remains the major limitation of coronary stent deployment. Although the pathogenesis of in-stent restenosis is not fully understood, its pathology includes thrombus formation, inflammation, neointimal hyperplasia and re-endothelialisation. These four different biological processes are discussed in detail in the following sections.

1.6.1 Thrombus Formation

Following coronary stent deployment, the exposure of sub-endothelial components, such as collagen and elastin, and the secretion of glycoproteins, such as fibronectin and von Willebrand factor (vWF), from damaged ECs stimulate the activation and recruitment of platelets. Activated platelets adhere to the injury site and secrete pro-thrombotic agents, such as thromboxane, adenosine diphosphate (ADP) and platelet-activating factor (PAF), which promote further platelet activation and recruitment. The activated platelets also promote the synthesis of thrombin, which stimulates the conversion of blood-borne fibrinogen molecules into fibrin monomers. These fibrin monomers form long fibrin strands that bind the aggregated platelets together at the injury site in order to form a mural thrombus (blood clot). Thrombus formation is the dominant physiological response in the hours following coronary stent deployment and typically persists for a week [15]. The cellular components involved in thrombus formation following coronary stent deployment are shown in Figure 1.8.

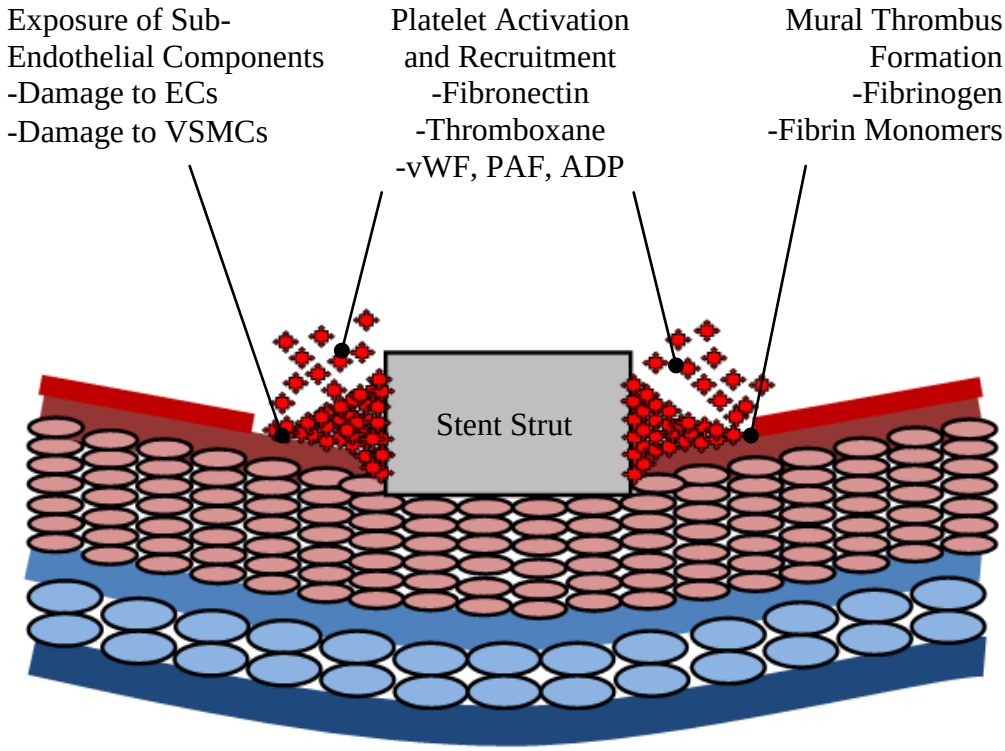

Figure 1.8: Thrombus formation following coronary stent deployment.

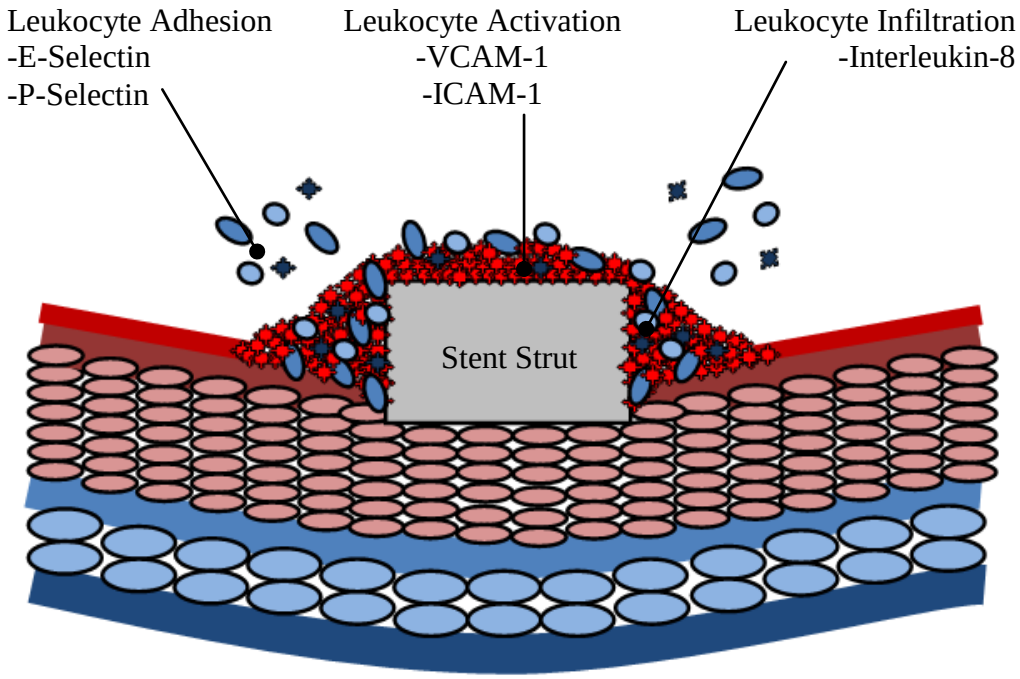

Figure 1.9: Inflammation following coronary stent deployment.

1.6.2 Inflammation

Following coronary stent deployment, both damaged ECs and VSMCs secrete cell-adhesion molecules, such as E-selectin and P-selectin, and form loose bonds with leukocytes (white blood cells), such as neutrophils, lymphocytes and monocytes, which are present within the lumen. These leukocytes roll along the surface of the mural thrombus until they are either returned to the lumen or they are activated by cell-adhesion molecules, such as vascular cell adhesion molecule-1 (VCAM-1) and intercellular adhesion molecule-1 (ICAM-1). During the following weeks, activated leukocytes migrate through the mural thrombus towards the injury site where they differentiate into macrophages, consume damaged ECs and VSMCs and secrete cell-signalling molecules, such as interleukin-8, to promote further leukocyte activation and recruitment. Inflammation is typically observed within a week of coronary stent deployment and may persist for six months [15]. The acute inflammatory response is characterised by the infiltration of neutrophils at the injury site whilst the chronic inflammatory response is characterised by the infiltration of both lymphocytes and monocytes at the injury site. The cellular components involved in the inflammatory response following coronary stent deployment are shown in Figure 1.9.

1.6.3 Neointimal Hyperplasia

Following coronary stent deployment, a number of cell-signalling molecules, such as fibroblast growth factor (FGF), platelet-derived growth factor (PDGF) and tumour necrosis factor (TNF), are secreted by activated leukocytes and both damaged ECs and VSMCs. The secretion of these cell-signalling molecules prompts the normally quiescent VSMCs which are located within the media to shift from a contractile to a synthetic phenotype. This change in phenotype causes VSMCs to migrate toward the injury site where they then begin to proliferate and synthesise extracellular matrix components such as collagen and elastin. The uncontrolled proliferation of VSMCs and the subsequent synthesis of extracellular matrix components is called neointimal hyperplasia. Neointimal hyperplasia is generally responsible for approximately 80% of the intimal thickening observed following coronary stent deployment and, as such, in-stent restenosis is mainly attributed to neointimal hyperplasia [15–17]. Neointimal hyperplasia is observed within a week of coronary stent deployment and may persist for up to eighteen months [15]. The cellular components involved in neointimal hyperplasia following coronary stent deployment are shown in Figure 1.10.

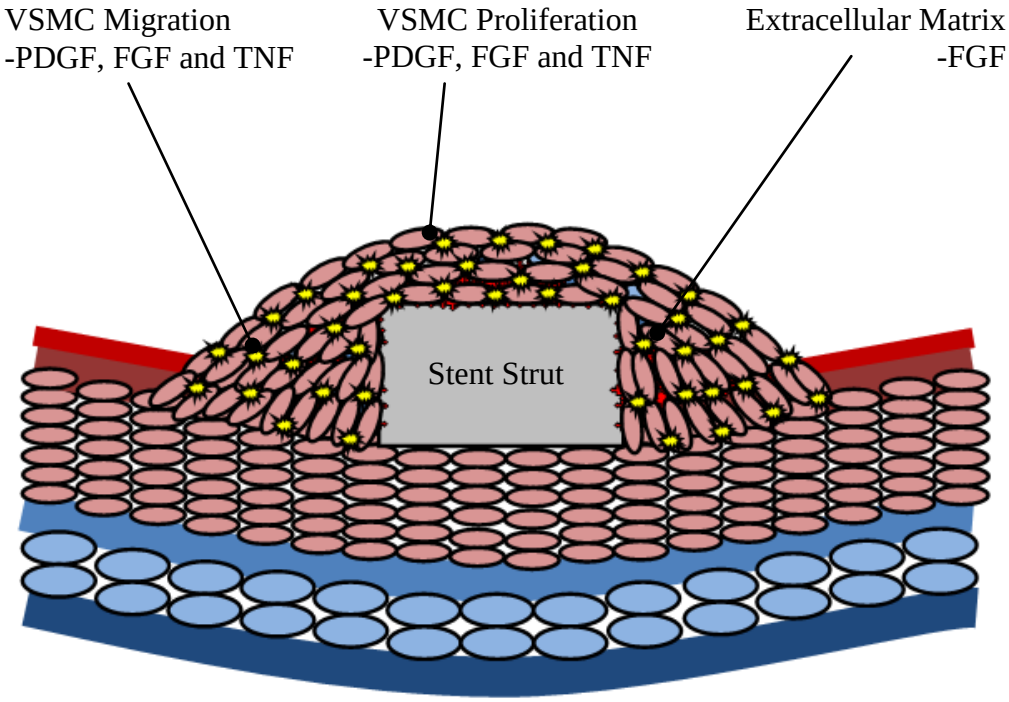

Figure 1.10: Neointimal hyperplasia following coronary stent deployment.

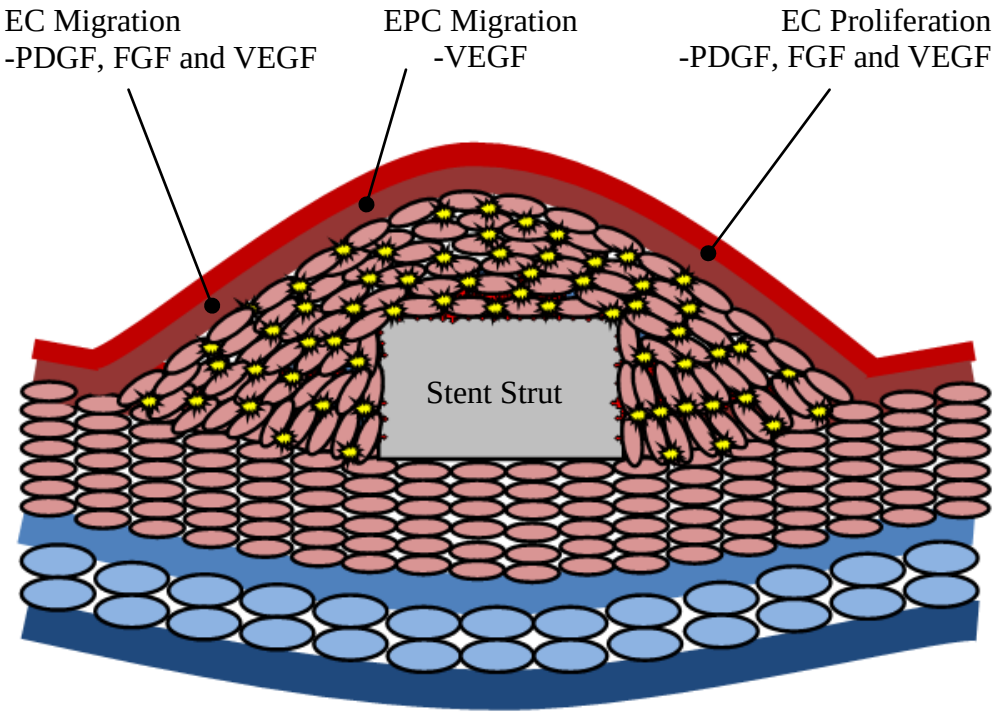

Figure 1.11: Re-endothelialisation following coronary stent deployment.

1.6.4 Re-Endothelialisation

Following coronary stent deployment, cell-signalling molecules, such as PDGF, FGF and vascular-endothelial growth factor (VEGF), are secreted by activated leukocytes and both damaged ECs and VSMCs. The secretion of these cell-signalling molecules causes ECs to migrate from healthy regions of the vascular endothelium towards the injury site. The healthy ECs then adhere to the proteins and cell-signalling molecules at the injury site and begin to proliferate. The secretion of cell-signalling molecules also causes stem-cell derived endothelial progenitor cells (EPCs) to mobilise, enter the bloodstream and migrate towards the injury site. These stem-cell derived EPCs adhere to the proteins and cell-signalling molecules at the injury site and differentiate into mature ECs. The time course of re-endothelialisation varies quite significantly for bare-metal and drug-eluting coronary stents. In a recent morphological study, near-complete re-endothelialisation was observed within four months of bare-metal coronary stent deployment whereas delayed re-endothelialisation was observed over three years after drug-eluting coronary stent deployment [18]. In order to accelerate re-endothelialisation following drug-eluting coronary stent deployment, second- and third-generation drug-eluting coronary stents are typically coated with biocompatible carrier materials. The various cellular components involved in re-endothelialisation following coronary stent deployment are shown in Figure 1.11.

1.7 In-Stent Restenosis and Injury

During coronary stent deployment, a significant portion of the vascular endothelium is either damaged or completely denuded from the artery wall and over-expansion of the stent can result in the perforation of the internal elastic lamina, the media and the external elastic lamina. One of the earliest clinical studies to evaluate the relationship between arterial injury and in-stent restenosis was carried out by Schwartz et al. in 1992 [19]. In this study, 26 porcine coronary arteries were subjected to injury using over-expanded tantalum coil stents. At four week follow-up, the arteries were then harvested and divided into a number of histological sections. For each individual artery, the histological section that featured the most severe lumen stenosis was then identified and used to make all subsequent measurements. Within each histological section, the neointimal thickness was first measured at each stent strut and an injury score was then assigned to each strut based upon the arterial components which it

had perforated during the deployment of the stent. This injury score ranged from zero, which indicated an intact internal elastic lamina, to three, which indicated a perforated external elastic lamina. A mean neointimal thickness and a mean injury score was then assigned to each histological section and, as shown in Figure 1.12, a statistically-significant strong positive linear correlation was observed between the mean injury scores and mean neointimal thicknesses. Based upon these results, the authors concluded that arterial injury is likely to have a significant influence on the severity of the neointimal response observed following coronary stent deployment. This finding was later corroborated in a number of clinical studies [20–26].

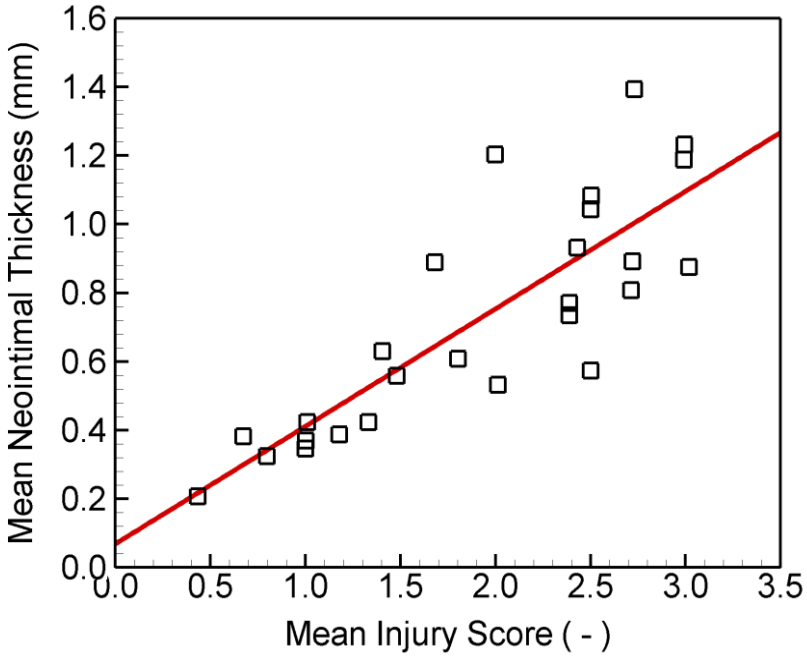

Figure 1.12: Strong positive linear correlation observed between mean injury score and mean neointimal thickness, as described by Schwartz et al. [19]**.**

As discussed in Section 1.6.2, inflammation following coronary stent deployment is one of the key biological processes that are involved in the development of in-stent restenosis. One of the earliest clinical studies to investigate the relationship between arterial injury and inflammation was carried out by Kornowski et al. in 1998 [27]. In this study, 21 porcine coronary arteries were subjected to arterial injury using over-expanded stainless-steel stents. At four week follow-up, the arteries were harvested and divided into a number of histological sections. For each artery, the histological section that featured the most severe lumen stenosis was identified and employed to make all subsequent measurements. Within each histological section, the neointimal

thickness was first measured at each stent strut and an injury score was then assigned to each strut as previously described. An inflammation score was also assigned to each strut based upon the severity of the inflammatory response observed within the surrounding tissue. This score ranged from zero, which indicated no inflammation, to three, which indicated significant inflammation. A mean neointimal thickness, mean injury score and mean inflammation score was then assigned to each histological section and, as shown in Figure 1.13, a statistically-significant strong positive linear correlation was observed between the mean injury scores and mean inflammation scores. As strong linear correlations were also observed between mean neointimal thicknesses and both mean injury and inflammation scores, it was concluded that arterial injury is likely to have a major influence upon the severity of the neointimal and inflammatory response observed following coronary stent deployment. These findings were later corroborated in a number of clinical studies [22,25].

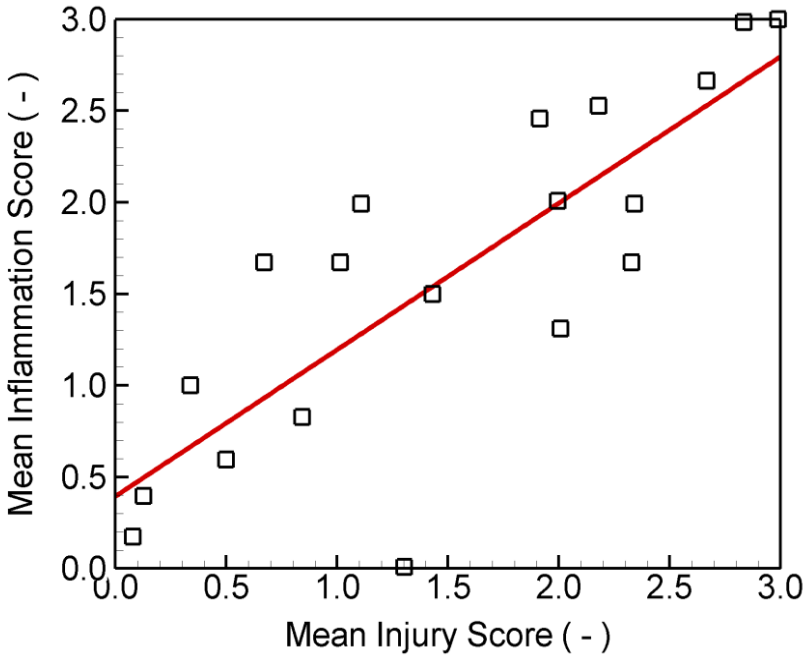

Figure 1.13: Strong positive linear correlation observed between mean injury and inflammation score, as described by Kornowski et al. [27]**.**

1.8 In-Stent Restenosis and Hemodynamics

During coronary stent deployment, the geometry of the artery may be straightened quite significantly and this can have a major influence upon the local hemodynamics within the vessel. The protrusion of stent struts into the lumen is also likely to result in the development of disturbed flow regions, such as flow separation, recirculation

and reattachment zones, upon the luminal surface of the artery. One of the earliest clinical studies to investigate the relationship between altered vessel hemodynamics and in-stent restenosis was conducted by Wentzel et al. in 2001 [28]. In this study, 14 patients were treated using self-expanding elgiloy stents and both intravascular ultrasound and biplane coronary angiography were performed at six month follow-up. Realistic geometrical models of the stented arteries were then generated from the imaging data and used to evaluate the neointimal thickness at a number of positions within the investigated arteries. To evaluate the relationship between altered vessel hemodynamics and in-stent restenosis, computational analyses were then carried out to simulate mean flow conditions within each of the realistic geometrical models of the stented coronary arteries. Following the completion of the analyses, regions of disturbed flow were identified by evaluating the wall shear stress (WSS) distribution predicted upon the luminal surface of the arteries. The term WSS is used to describe the flow-induced viscous stress that is exerted upon the luminal surface. As shown in Figure 1.14, a negative linear correlation was observed between WSS and neointimal thickness in nine of the investigated arteries. Based on these results, it was concluded that altered vessel hemodynamics are likely to have a significant influence upon the severity of the neointimal response observed following coronary stent deployment. This finding was later corroborated in a number of clinical studies [29–31].

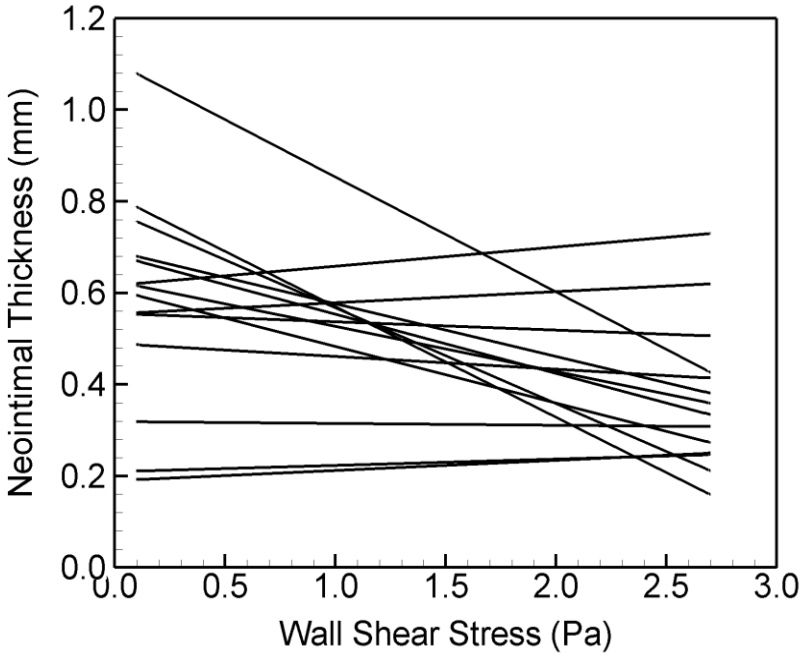

Figure 1.14: Linear correlations observed between WSS and neointimal thickness for 14 stented arteries, as described by Wentzel et al. [28]**.**

In 2003, Carlier et al. conducted a similar study to evaluate the relationship between altered vessel hemodynamics and in-stent restenosis [32]. In this study, 18 stainless-steel stents were deployed within the right and left external iliac arteries of 9 rabbits (1 stent per vessel). For each of the rabbits, a flow divider was then deployed within one of the stented iliac arteries. A flow divider is a medical device that is designed to reduce rates of in-stent restenosis by increasing the overall magnitude of the WSS distribution in the stented segment of the artery. At four week follow-up, the arteries were then harvested and divided into a number of histological sections. For each of the stented arteries, seven histological sections were considered. Two sections were located outside of the stented segment of the artery whilst five sections were located inside the stented segment of the artery. Within each of the histological sections, the neointimal thickness was first measured at the individual stent struts and both injury and inflammation scores were then assigned to each strut as previously described. A mean neointimal thickness, mean injury score and mean inflammation score was then assigned to each of the histological sections. An idealised geometrical model of an artery was then generated and computational analyses were carried out to evaluate the influence of the flow divider on the hemodynamic environment predicted within the artery. Following the completion of the computational analyses, the flow divider was found to significantly increase the magnitude of the WSS distribution upon the luminal surface within the stented segment of the coronary artery. The analysis of the histological sections then revealed that this increase in the magnitude of the WSS distribution was accompanied by reduced mean neointimal thicknesses, mean injury scores and mean inflammation scores. Based on these results, it was concluded that altered vessel hemodynamics are likely to have a significant influence on the severity of the neointimal response observed following coronary stent deployment.

1.9 Computational Analysis of Coronary Stents

In light of the clinical results discussed in Sections 1.7 and 1.8, a significant body of research has been carried out to investigate the relationship between stent design and both arterial injury and altered vessel hemodynamics. Due to the difficulty involved in the experimental evaluation of these phenomena, however, a substantial portion of this research has been carried out using computational methods of analysis. These computational methods of analysis employ sophisticated numerical techniques, such as the finite element and the finite volume methods, to obtain approximate numerical

solutions to complex physical problems. In recent years, a large number of studies have employed either computational structural (CS) or computational fluid dynamics (CFD) analyses to evaluate the mechanical or hemodynamic impact of coronary stent deployment. In many of these studies, the results of the computational analyses are used to identify potential geometrical modifications that may improve the clinical performance of the investigated stents. In the vast majority of these studies, however, the fact that in-stent restenosis has been strongly correlated with both arterial injury and altered vessel hemodynamics is overlooked and, as such, it is possible that the proposed geometrical modifications may actually hinder the clinical performance of the investigated stents. In CS analyses of coronary stent deployment, for example, geometrical modifications which are likely to reduce the mechanical impact of the investigated stents are generally recommended. As these studies focus exclusively upon the mechanical impact of the investigated stents, however, the corresponding hemodynamic impact of the recommended geometrical modifications is neglected. Similarly, in CFD analyses of coronary stent deployment, geometrical modifications which are likely to reduce the hemodynamic impact of the investigated stents are generally recommended. As these studies focus exclusively upon the hemodynamic impact of the investigated stents, however, the corresponding mechanical impact of the recommended geometrical modifications is neglected. As in-stent restenosis has been strongly correlated with both arterial injury and altered vessel hemodynamics, the sequential numerical analysis of the mechanical and hemodynamic impact of stent deployment is likely to provide an improved indication of stent performance. Despite this observation, however, very few numerical studies have considered both the mechanical and hemodynamic impact of coronary stent deployment.

1.10 Aim of the Research

The aim of this research is to develop a robust numerical methodology for evaluating the performance of balloon-expandable coronary stents in terms of their mechanical and hemodynamic impact within the coronary artery. The proposed methodology is divided into two stages. In the first stage, a CS model of the investigated stent is first generated and a nonlinear CS analysis is then carried out to simulate its deployment within a coronary artery. In the second stage, the results of the CS analysis are first used to generate a realistically-deformed CFD model of the stented coronary lumen and a transient CFD analysis is then carried out to simulate pulsatile flow conditions

within a coronary artery. Following the completion of the analyses, the performance of the investigated stent is evaluated in terms of its mechanical and hemodynamic impact within the coronary artery. The mechanical impact of the investigated stent is evaluated in terms of the stress distribution predicted within the artery wall and the hemodynamic impact of the investigated stent is then evaluated in terms of the WSS distribution predicted upon the luminal surface of the artery. In order to ensure that the mechanical and hemodynamic impact of the investigated stent is fully elucidated, various mechanical and hemodynamic variables of interest are calculated and the distribution of these variables is evaluated using a comprehensive statistical method of analysis. In order to demonstrate its application, the proposed methodology is then applied to six generic stents that each resembles a current commercially-available coronary stent. The predicted performance of each of the investigated stents is then compared and contrasted in order to investigate the relationship between stent design and performance. Finally, in order to determine whether the proposed methodology is capable of predicting coronary stent performance, the predicted performance of three of the investigated stents is then compared to the clinical performance of three comparable stents, as reported in two large-scale clinical trials.

1.11 Structure of the Thesis

The thesis is divided into six chapters and two additional appendices. In Chapter 2, the fundamental concepts of continuum mechanics are introduced and the governing equations of structural and fluid mechanics are described. In Chapter 3, the literature is reviewed and the limitations associated with the evaluation of stent performance solely in terms of either the mechanical or hemodynamic impact predicted within the artery are noted. In Chapter 4, the details of the proposed methodology are presented and the calculation of both the mechanical and hemodynamic variables of interest is described. In Chapter 5, the performance of the investigated stents is first evaluated and then compared and contrasted in order to investigate the relationship between stent design and performance. In Chapter 6, the conclusions drawn from the results are presented and the limitations of the proposed methodology are then discussed. In Appendix A, the details of the mesh, cycle and time step convergence studies that were carried out to determine appropriate spatial discretisation, transient loading and temporal discretisation schemes, respectively, in both the CS and CFD analyses are presented. Finally, in Appendix B, the details of the CFD analyses that were carried

out to validate the accuracy of the custom-written Python script which was employed to calculate the hemodynamic variables of interest are described.

1.12 Novelty and Contribution

The work presented in this thesis contributes to the body of knowledge in this area as it represents one of the first attempts to evaluate coronary stent performance in terms of both the mechanical and hemodynamic impact predicted within a coronary artery. The novelty of this work arises from the fact that it is the first time that:

1. Several different variables of interest and a comprehensive statistical method of analysis have been employed in order to fully elucidate the mechanical and hemodynamic impact of the investigated stent.

2. A number of different coronary stents have been compared and contrasted in terms of their mechanical and hemodynamic impact within a coronary artery to evaluate the relationship between stent design and performance.

3. The relationship between common geometrical properties of the investigated stents and the magnitude of both the mechanical and hemodynamic variables of interest has been evaluated using statistical measures of correlation.

To date, the work presented in this thesis has led to the publication of three peer-reviewed journal papers in international biomedical engineering journals and four conference papers in the annual proceedings of the Conference of the Bioengineering Section of the Royal Academy of Medicine in Ireland [33–39].

CHAPTER 2
FUNDAMENTAL THEORY

2.1 Introduction

The fundamental laws of continuum mechanics describe the conservation of various physical quantities, such as mass, momentum and energy, and provide the basis from which the governing equations of structural and fluid mechanics are derived. In this chapter, the concepts of motion, deformation and strain are first introduced and the notion of stress is discussed. The conservation laws of mass and linear momentum are then presented and a number of constitutive equations are described. Finally, the governing equations of structural and fluid mechanics are derived and the procedures involved in both their discretisation and solution are then discussed. Due to its scope, this chapter provides merely an overview of the fundamental theory. The interested reader is referred to the many excellent resources available within the literature for a more extensive treatment of the topics discussed in this chapter [40–47].

2.2 Kinematics

2.2.1 Motion

Matter is comprised of discrete numbers of both atomic and sub-atomic particles and is inherently discontinuous. When the dimensions of a body are much greater than its atomic length scale, however, it is reasonable to assume that matter is continuously distributed and that the body completely fills the space it occupies. This assumption is called the continuum assumption and the evaluation of the mechanical behaviour of continuously distributed (or continuum) bodies is known as continuum mechanics. Consider the motion of a deformable continuum body, which may be imagined as a set of continuously distributed material particles which are located within the three-dimensional (3D) Euclidean space. As shown in Figure 2.1, the body transforms

from a reference configuration B_0 at time $t = 0$ to a current configuration B_t at time $t = t$. Throughout this chapter, upper-case and lower-case letters and subscripts are employed to describe scalars, vectors and tensors that are derived with respect to the reference and current configurations, respectively. The position of a material particle within the reference configuration of the body may be described by the vector $\mathbf{X}$ with respect to the coordinate axes $\mathbf{E}_\mathrm{A}$. The corresponding position of the material particle within the current configuration may be described by the vector $\mathbf{x}$ with respect to the coordinate axes $\mathbf{e}_\mathrm{i}$. The components of the vector $\mathbf{X}$ are written with respect to the reference configuration and are called material coordinates whilst the components of the vector $\mathbf{x}$ are written with respect to the current configuration and are referred to as spatial coordinates. The motion of the body is defined as follows:

$$\mathbf{x} = \boldsymbol{\varphi}(\mathbf{X}, t) \tag{2.1}$$

The mapping $\boldsymbol{\varphi}$ carries the material particles from their position within the reference configuration to their corresponding position within the current configuration for all fixed values of time and is referred to as the motion of the body. The motion of the body is assumed to be continuously differentiable with respect to space and time and uniquely invertible such that its inverse may be defined as follows:

$$\mathbf{X} = \boldsymbol{\varphi}^{-1}(\mathbf{x}, t) \tag{2.2}$$

The mapping $\boldsymbol{\varphi}^{-1}$ carries material particles from their position within the current configuration to their corresponding position within the reference configuration for all fixed values of time and is called the inverse motion of the body. The motion of a body may include a rigid-body and/or a distortional component. A rigid-body motion involves a change in position and/or orientation whilst a distortional motion involves a change in size and/or shape and is often referred to as a deformation. As it has no impact on the derivations that follow, the coordinate axes $\mathbf{E}_\mathrm{A}$ and $\mathbf{e}_\mathrm{i}$ are assumed to be coincident throughout this chapter. The notational distinction between the axes is maintained, however, to identify quantities with either the reference or the current configuration of the body. Although a significant effort has been made to avoid any ambiguity, there are instances throughout this chapter where the same symbol is used to describe multiple variables. In the few situations where this occurs, the context of the discussion preceding the symbol should dictate its interpretation.

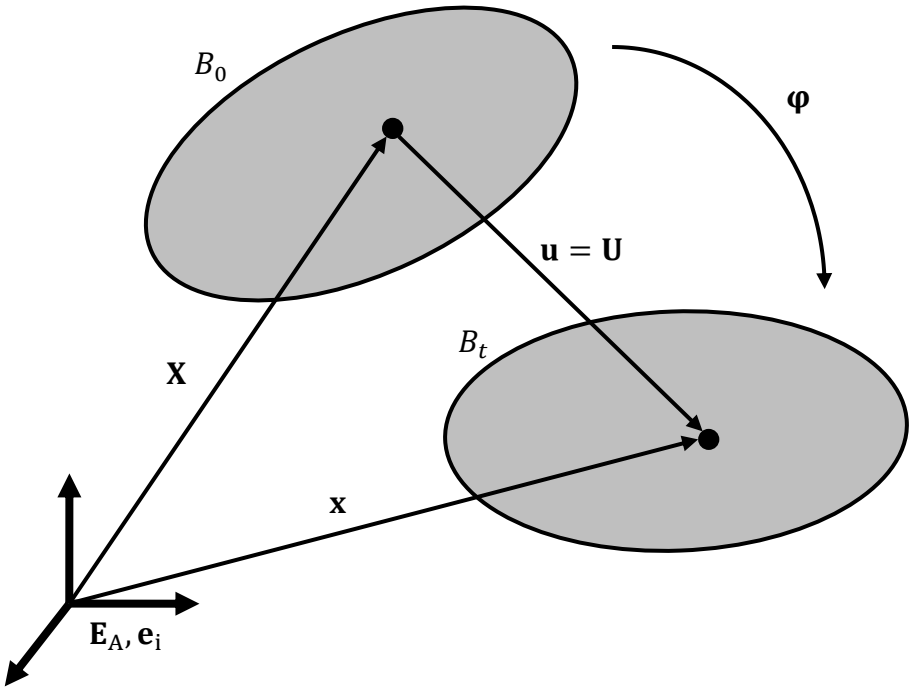

Figure 2.1: General motion of a deformable continuum body.

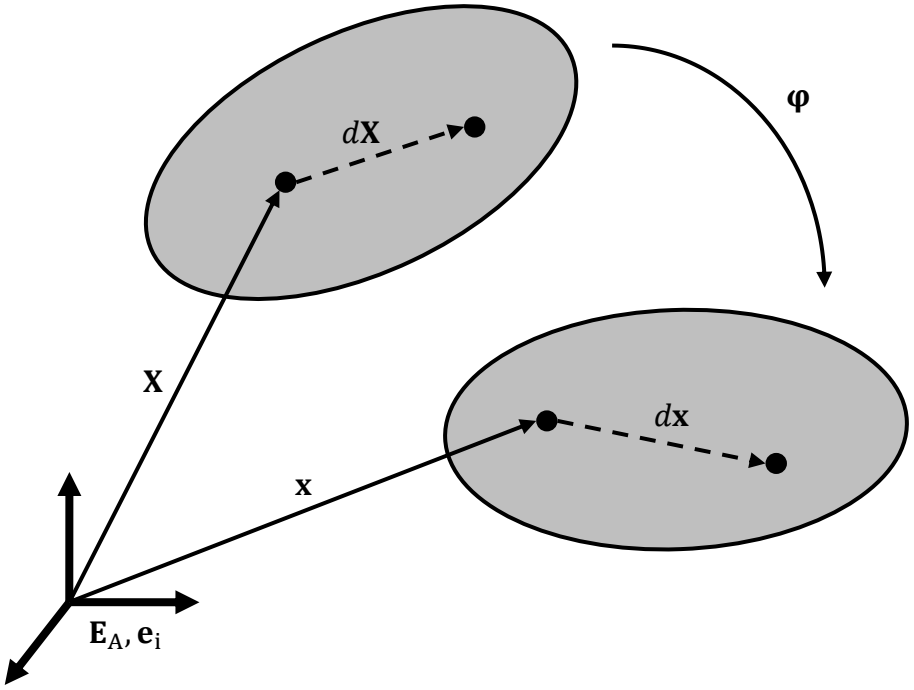

Figure 2.2: General motion in the neighbourhood of a material particle.

2.2.2 Material and Spatial Descriptions

In continuum mechanics, physical quantities may be described with respect to either the material or spatial coordinates. The former approach is called the material (or Lagrangian) description whilst the latter approach is called the spatial (or Eulerian description). The material description focuses on the variation of quantities at a fixed material particle whilst the spatial description focuses on the variation of quantities at a fixed spatial position. The displacement of a material particle, for example, is defined as the difference between its current position and its reference position and may be derived with respect to either material or spatial coordinates as follows:

$$\mathbf{U}(\mathbf{X}, t) = \mathbf{x}(\mathbf{X}, t) - \mathbf{X} \tag{2.3}$$

$$\mathbf{u}(\mathbf{x}, t) = \mathbf{x} - \mathbf{X}(\mathbf{x}, t) \tag{2.4}$$

The displacement vector **U** is derived with respect to material coordinates and is called the material displacement vector. The material displacement vector describes the displacement undergone by the material particle that was originally located at the reference position **X**. The displacement vector **u** is derived with respect to spatial coordinates and is called the spatial displacement vector. The spatial displacement vector describes the displacement undergone by the material particle that is currently located at the spatial position **x**. The material and spatial displacement vectors have the same values, but they are functions of different arguments. As the mechanical behaviour of solid materials is often described with respect to material coordinates, the material description is generally preferred in structural analyses. Conversely, as the material coordinates of fluid particles are often of little practical interest, the spatial description is generally preferred in fluid dynamics analyses.

2.2.3 Deformation

Consider two neighbouring material particles which are located within the reference configuration of a continuum body. As shown in Figure 2.2, the infinitesimal line element that connects the material particles within the reference configuration may be described by the vector $d\mathbf{X}$. During the motion of the body, the particles are then transformed from their position within the reference configuration to corresponding positions within the current configuration. As shown in Figure 2.2, the infinitesimal line element that connects the material particles within the current configuration may

be described by the vector $d\mathbf{x}$. The relationship between these vectors is provided by the deformation gradient tensor which may be defined as follows:

$$d\mathbf{x} = \frac{\partial \mathbf{x}}{\partial \mathbf{X}} d\mathbf{X} = \boldsymbol{\nabla}_0 d\mathbf{X} = \mathbf{F} d\mathbf{X} \tag{2.5}$$

The tensor $\mathbf{F}$ describes the change in configuration of infinitesimal line elements as the body transforms from the reference to the current configuration and is called the deformation gradient tensor. The term $\boldsymbol{\nabla}_0$ denotes the gradient operator with respect to material coordinates. Noting the definition of the material displacement vector, the deformation gradient tensor may also be defined as follows:

$$\mathbf{F} = \frac{\partial \mathbf{X}}{\partial \mathbf{X}} + \frac{\partial \mathbf{U}}{\partial \mathbf{X}} = \boldsymbol{\nabla}_0 \mathbf{X} + \boldsymbol{\nabla}_0 \mathbf{U} = \mathbf{I} + \mathbf{H} \tag{2.6}$$

The tensor $\mathbf{H}$ denotes the gradient of the material displacement vector with respect to material coordinates whilst the tensor $\mathbf{I}$ denotes the identity tensor. As it has been assumed that the inverse motion $\boldsymbol{\varphi}^{-1}$ exists, the inverse of the deformation gradient tensor must also exist and may be defined as follows:

$$d\mathbf{X} = \frac{\partial \mathbf{X}}{\partial \mathbf{x}} d\mathbf{x} = \boldsymbol{\nabla} d\mathbf{x} = \mathbf{F}^{-1} d\mathbf{x} \tag{2.7}$$

The tensor $\mathbf{F}^{-1}$ describes the change in configuration of infinitesimal line elements as the body transforms from the current to the reference configuration and is called the inverse deformation gradient tensor. The term $\boldsymbol{\nabla}$ denotes the gradient operator with respect to material coordinates. Noting the definition of the spatial displacement vector, the inverse deformation gradient tensor may be defined as follows:

$$\mathbf{F}^{-1} = \frac{\partial \mathbf{x}}{\partial \mathbf{x}} - \frac{\partial \mathbf{u}}{\partial \mathbf{x}} = \boldsymbol{\nabla} \mathbf{x} + \boldsymbol{\nabla} \mathbf{u} = \mathbf{I} - \mathbf{h} \tag{2.8}$$

The tensor $\mathbf{h}$ denotes the gradient of the spatial displacement vector with respect to spatial coordinates. The deformation gradient tensor is a key measure of deformation in continuum mechanics and may be employed to describe local changes in volume and area. Consider an infinitesimal volume element whose size may be described by the scalars dV and dv in the reference and current configurations, respectively. The

relationship between these scalars is provided by the determinant of the deformation gradient tensor, which may be defined as follows:

$$J = \det(\mathbf{F}) = \frac{dv}{dV} \tag{2.9}$$

The determinant of the deformation gradient tensor is referred to as the Jacobian determinant and, as shown in Equation 2.9, it describes the local volume ratio. Next consider an infinitesimal surface element whose size may be described by the scalars dS and ds in the reference and current configurations of the body, respectively. The relationship between these scalars may be written as follows:

$$\mathbf{n}ds = J\mathbf{F}^{-1}\mathbf{N}dS \tag{2.10}$$

The vectors **N** and **n** are the unit normal vectors of the infinitesimal surface elements dS and ds, respectively, and Equation 2.10 is referred to as Nanson's relation.

2.2.4 Rotation and Stretch

Although the deformation gradient tensor describes the change in configuration of infinitesimal line elements, it does not distinguish between rigid-body motions and deformations. Through the application of the polar decomposition theorem, however, the deformation gradient tensor may be decomposed as follows:

$$\mathbf{F} = \mathbf{RU} = \mathbf{vR} \tag{2.11}$$

The orthogonal tensor **R** describes the rotation of infinitesimal line elements and is referred to as the rotation tensor whilst the symmetric tensors **U** and **v** describe the extension (or contraction) of infinitesimal line elements and are called the right and left stretch tensors, respectively. The right and left stretch tensors are derived with respect to material and spatial coordinates, respectively, and the relationship between these tensors is provided by the rotation tensor as follows:

$$\mathbf{v} = \mathbf{RUR}^{\mathrm{T}} \tag{2.12}$$

Equation 2.11 implies that the change in configuration of infinitesimal line elements may be described by a pure rotation followed by a pure deformation, or alternatively, by a pure deformation followed by a pure rotation.

2.2.5 Strain

Consider the change in the squared length of an infinitesimal line element that occurs as the body transforms from the reference to the current configuration. The change in the squared length of the line element may be defined as follows:

$$(d\mathbf{x})^2 - (d\mathbf{X})^2 = d\mathbf{X}\left(\mathbf{F}^{\mathrm{T}}\mathbf{F} - \mathbf{I}\right)d\mathbf{X} = d\mathbf{X}(\mathbf{C} - \mathbf{I})d\mathbf{X} \tag{2.13}$$

The tensor $\mathbf{C}$ describes the deformation of infinitesimal line elements with respect to material coordinates and is referred to as the right Cauchy-Green deformation tensor. The change in squared length of the line element may also be defined as follows:

$$(d\mathbf{x})^2 - (d\mathbf{X})^2 = d\mathbf{x}\left(\mathbf{I} - \mathbf{F}^{-1}\mathbf{F}^{-\mathrm{T}}\right)d\mathbf{x} = d\mathbf{x}(\mathbf{I} - \mathbf{b}^{-1})d\mathbf{x} \tag{2.14}$$

The tensor $\mathbf{b}$ describes the deformation of infinitesimal line elements with respect to spatial coordinates and is referred to as the left Cauchy-Green deformation tensor. The right and left Cauchy-Green deformation tensors are symmetric tensors and may be written in terms of the right and left stretch tensors as follows:

$$\mathbf{C} = \mathbf{F}^{\mathrm{T}}\mathbf{F} = (\mathbf{RU})^{\mathrm{T}}(\mathbf{RU}) = \mathbf{U}^{\mathrm{T}}\mathbf{R}^{\mathrm{T}}\mathbf{RU} = \mathbf{U}^2 \tag{2.15}$$

$$\mathbf{b} = \mathbf{F}\mathbf{F}^{\mathrm{T}} = (\mathbf{vR})(\mathbf{vR})^{\mathrm{T}} = \mathbf{vRR}^{\mathrm{T}}\mathbf{v}^{\mathrm{T}} = \mathbf{v}^2 \tag{2.16}$$

During a rigid-body motion, the right and left Cauchy-Green deformation tensors are reduced to the identity tensor and Equations 2.13 and 2.14 are both reduced to zero. During a deformation, however, the right and left Cauchy-Green deformation tensors are not reduced to the identity tensor and Equations 2.13 and 2.14 describe the strain incurred by infinitesimal line elements. This observation results in the derivation of the following material and spatial strain tensors:

$$\mathbf{E} = \frac{1}{2}(\mathbf{C} - \mathbf{I}) = \frac{1}{2}(\mathbf{U}^2 - \mathbf{I}) \tag{2.17}$$

$$\mathbf{e} = \frac{1}{2}(\mathbf{I} - \mathbf{b}^{-1}) = \frac{1}{2}(\mathbf{I} - \mathbf{v}^{-2}) \tag{2.18}$$

The tensors $\mathbf{E}$ and $\mathbf{e}$ describe the strain incurred by infinitesimal line elements and are referred to as the Green-Lagrange and Euler-Almansi strain tensors, respectively. The Green-Lagrange and Euler-Almansi strain tensors are symmetric by definition

and are derived with respect to material and spatial coordinates respectively. Noting the definition of the deformation gradient tensor in Equations 2.6 and 2.8, the Green-Lagrange and Euler-Almansi strain tensors may be rewritten as follows:

$$\mathbf{E} = \frac{1}{2}[(\boldsymbol{\nabla}_0\mathbf{U}) + (\boldsymbol{\nabla}_0\mathbf{U})^{\mathrm{T}} + (\boldsymbol{\nabla}_0\mathbf{U})(\boldsymbol{\nabla}_0\mathbf{U})^{\mathrm{T}}] \tag{2.19}$$

$$\mathbf{e} = \frac{1}{2}[(\boldsymbol{\nabla}\mathbf{u}) + (\boldsymbol{\nabla}\mathbf{u})^{\mathrm{T}} + (\boldsymbol{\nabla}\mathbf{u})(\boldsymbol{\nabla}\mathbf{u})^{\mathrm{T}}] \tag{2.20}$$

As shown in Equations 2.19 and 2.20, the Green-Lagrange and Euler-Almansi strain tensors are nonlinear functions of displacement. If displacements are assumed small, however, the quadratic terms in Equations 2.19 and 2.20 are negligible compared to the linear terms. Under the assumption of small displacements, the Green-Lagrange and Euler-Almansi strain tensors may then be reduced as follows:

$$\boldsymbol{\varepsilon} = \frac{1}{2}[(\boldsymbol{\nabla}_0\mathbf{U}) + (\boldsymbol{\nabla}_0\mathbf{U})^{\mathrm{T}}] = \frac{1}{2}[(\boldsymbol{\nabla}\mathbf{u}) + (\boldsymbol{\nabla}\mathbf{u})^{\mathrm{T}}] \tag{2.21}$$

If displacements are assumed to be small, the tensor $\boldsymbol{\varepsilon}$ describes the strain incurred by infinitesimal line elements and is called the infinitesimal strain tensor. Unlike the Green-Lagrange and Euler-Almansi strain tensors, which are both exact measures of strain, the infinitesimal strain tensor is an approximate measure of strain and is only accurate when displacements are small. As the infinitesimal strain tensor provides a linear measure of strain, however, it is typically preferred to the Green-Lagrange and Euler-Almansi strain tensors in small displacement analyses.

2.2.6 Principal Values and Directions

A fundamental property of symmetric tensors is that there is at least one coordinate system for which the off-diagonal components of the tensor are reduced to zero. The remaining diagonal components of the tensor are called the principal values and the corresponding directions of the coordinate axes are called the principal directions. To demonstrate this property of symmetric tensors, consider the right stretch tensor. To identify the principal values and the corresponding principal directions of the right stretch tensor, the following system of algebraic equations is solved:

$$(\mathbf{U} - \lambda\mathbf{I})\hat{\mathbf{N}} = 0 \tag{2.22}$$

The scalar λ denotes a principal value of the right stretch tensor whilst the vector $\widehat{\mathbf{N}}$ denotes the corresponding principal direction. In order to obtain non-trivial solutions for Equation 2.22, the determinant of the coefficients must equal zero:

$$\det(\mathbf{U} - \lambda\mathbf{I}) = 0 \tag{2.23}$$

The expansion of this determinant yields a cubic polynomial in λ that is referred to as the characteristic equation of the right stretch tensor:

$$\lambda^3 - I_U\lambda^2 + II_U\lambda - III_U = 0 \tag{2.24}$$

The coefficients of the characteristic equation are called the first, second and third scalar invariants of the right stretch tensor and may be defined as follows:

$$\begin{aligned} I_{\mathbf{U}} &= \mathrm{tr}(\mathbf{U}) = \lambda_1 + \lambda_2 + \lambda_3 \\ II_{\mathbf{U}} &= \frac{1}{2}[(\mathrm{tr}\mathbf{U})^2 - \mathrm{tr}(\mathbf{U})^2] = \lambda_1^2 + \lambda_2^2 + \lambda_3^2 \\ III_{\mathbf{U}} &= \det(\mathbf{U}) = \lambda_1\lambda_2\lambda_3 \end{aligned} \tag{2.25}$$

Given the values of the three scalar invariants, it is possible to calculate the roots of the characteristic equation. In general, these roots are imaginary and of little practical use. As the right stretch tensor is symmetric, however, the characteristic equation has three real roots λ_1, λ_2 and λ_3 which correspond to the principal values of the tensor. The principal values may be substituted back into Equation 2.22 in order to find the corresponding principal directions $\widehat{\mathbf{N}}_1$, $\widehat{\mathbf{N}}_2$ and $\widehat{\mathbf{N}}_3$. If the principal values are distinct, then the principal directions form the mutually-orthogonal principal axes.

2.2.7 Rate Quantities

As many processes are time-dependent, it is necessary to consider the rate of change of quantities such as displacement and strain. The velocity of a material particle is defined as the time rate of change of its displacement. As a result, the velocity of a material particle may be derived with respect to material coordinates by taking the material derivative of the material displacement vector as follows:

$$\mathbf{V} = \frac{d\mathbf{U}}{dt} = \frac{\partial\mathbf{U}}{\partial t} \tag{2.26}$$

In a similar fashion, the acceleration of a material particle is defined as the time rate of change of its velocity and may be derived with respect to material coordinates by taking the material derivative of the material velocity vector as follows:

$$\mathbf{A} = \frac{d\mathbf{V}}{dt} = \frac{\partial \mathbf{V}}{\partial t} = \frac{\partial^2 \mathbf{U}}{\partial t^2} \tag{2.27}$$

As shown in Equations 2.26 and 2.27, it is easy to find the material derivative of a material quantity. Finding the material derivative of a spatial quantity, however, is slightly more complex. The spatial acceleration vector, for example, may be derived from the material derivative of the spatial velocity vector as follows:

$$\mathbf{a} = \frac{d\mathbf{v}}{dt} = \frac{\partial \mathbf{v}}{\partial t} + \left(\frac{\partial \mathbf{v}}{\partial \mathbf{x}}\right)\frac{\partial \mathbf{x}}{\partial t} = \frac{\partial \mathbf{v}}{\partial t} + (\boldsymbol{\nabla}\mathbf{v})\mathbf{v} \tag{2.28}$$

The first term on the right-hand side of Equation 2.28 is called the local derivative whilst the second term on the right-hand side is called the convective derivative. The local derivative describes the acceleration at a spatial position as a result of a change in time whilst the convective derivative describes the acceleration due to the motion of the particle. The spatial gradient of the spatial velocity vector is referred to as the velocity gradient tensor. The velocity gradient tensor may be additively decomposed into the sum of a symmetric tensor and a skew-symmetric tensor as follows:

$$\mathbf{l} = \frac{\partial \mathbf{v}}{\partial \mathbf{x}} = \mathbf{d} + \mathbf{w} \tag{2.29}$$

The symmetric tensor **d** describes the rate of strain of infinitesimal line elements and is called the rate of deformation (or the rate of strain) tensor. The rate of deformation tensor is derived in terms of spatial coordinates and is written as follows:

$$\mathbf{d} = \frac{1}{2}\left(\mathbf{l} + \mathbf{l}^{\mathrm{T}}\right) = \frac{1}{2}\left[(\boldsymbol{\nabla}\mathbf{v}) + (\boldsymbol{\nabla}\mathbf{v})^{\mathrm{T}}\right] \tag{2.30}$$

The skew-symmetric tensor **w** describes the rate of rotation of infinitesimal line elements and is called the vorticity (or spin) tensor. As before, the vorticity tensor is derived in terms of spatial coordinates and is written as follows:

$$\mathbf{w} = \frac{1}{2}\left(\mathbf{l} - \mathbf{l}^{\mathrm{T}}\right) = \frac{1}{2}\left[(\boldsymbol{\nabla}\mathbf{v}) - (\boldsymbol{\nabla}\mathbf{v})^{\mathrm{T}}\right] \tag{2.31}$$

2.3 Stress and Conservation Laws

2.3.1 Force, Traction and Stress

The motion of a body is often produced by the action of externally applied forces. These externally applied forces may be described as body forces or surface forces. Body forces, such as gravitational and magnetic forces, act upon all of the material particles within a body and are defined per unit volume (or mass). Surface forces, such as pressure and frictional forces, act across internal and external surfaces and are defined per unit area. Consider the current configuration of a body which, as shown in Figure 2.3, may be divided into two individual regions by a plane surface. Next, consider a surface element Δs which is located at the position $\mathbf{x}$ on the dividing surface and whose orientation is described by the unit normal vector $\mathbf{n}$. The body deforms under the action of external loads so that resultant forces are transmitted across the surface. If the resultant force acting on the surface element Δs is denoted by $\Delta\mathbf{f}$, the corresponding traction vector may be defined as follows:

$$\mathbf{t}^{(\mathbf{n})} = \lim_{\Delta s \to 0} \frac{\Delta \mathbf{f}}{\Delta s} = \frac{d\mathbf{f}}{ds} \tag{2.32}$$

The vector $\mathbf{t}^{(\mathbf{n})}$ describes the force measured per unit surface area that acts upon the infinitesimal surface element ds and is referred to as the Cauchy traction vector. The Cauchy traction vector is derived with respect to spatial coordinates and is a function of the unit normal vector $\mathbf{n}$. According to Newton's third law, traction vectors that act upon opposite sides of the same surface must be equal in magnitude and opposite in direction. As such, Newton's third law may be written as follows:

$$\mathbf{t}^{(-\mathbf{n})} = -\mathbf{t}^{(\mathbf{n})} \tag{2.33}$$

To develop the idea of a stress tensor, the traction vector associated with each of the Cartesian coordinate directions $\mathbf{e}_i$ is written in component form as follows:

$$\begin{aligned}
\mathbf{t}^{(\mathbf{e}_1)} &= t_1^{(\mathbf{e}_1)}\mathbf{e}_1 + t_2^{(\mathbf{e}_1)}\mathbf{e}_1 + t_3^{(\mathbf{e}_1)}\mathbf{e}_1 = \sigma_{11}\mathbf{e}_1 + \sigma_{12}\mathbf{e}_2 + \sigma_{13}\mathbf{e}_3 \\
\mathbf{t}^{(\mathbf{e}_2)} &= t_1^{(\mathbf{e}_2)}\mathbf{e}_2 + t_2^{(\mathbf{e}_2)}\mathbf{e}_2 + t_3^{(\mathbf{e}_2)}\mathbf{e}_2 = \sigma_{21}\mathbf{e}_1 + \sigma_{22}\mathbf{e}_2 + \sigma_{23}\mathbf{e}_3 \\
\mathbf{t}^{(\mathbf{e}_3)} &= t_1^{(\mathbf{e}_3)}\mathbf{e}_3 + t_2^{(\mathbf{e}_3)}\mathbf{e}_3 + t_3^{(\mathbf{e}_3)}\mathbf{e}_3 = \sigma_{31}\mathbf{e}_1 + \sigma_{32}\mathbf{e}_2 + \sigma_{33}\mathbf{e}_3
\end{aligned} \tag{2.34}$$

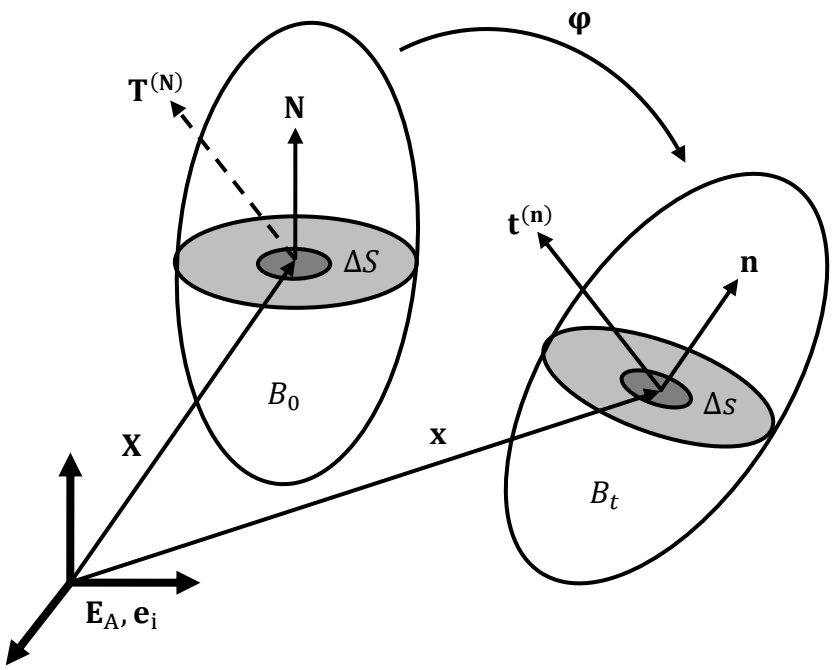

Figure 2.3: Traction vectors acting upon infinitesimal surface elements within the reference and current configurations of a continuum body.

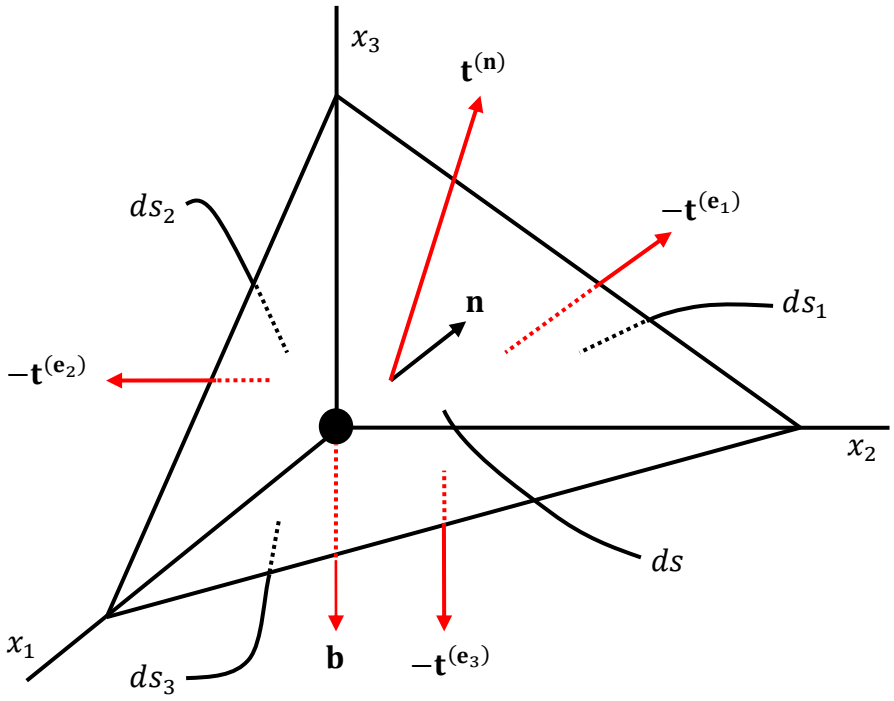

Figure 2.4: Free-body diagram of an infinitesimal tetrahedral element

To identify the relationship between the traction vector and its components, consider the general equilibrium of the infinitesimal tetrahedral element shown in Figure 2.4. If the vector **b** describes the body force that acts per unit volume, the equilibrium of the infinitesimal tetrahedral element may be written as follows:

$$\mathbf{t}^{(\mathbf{n})}ds - \mathbf{t}^{(\mathbf{e}_1)}ds_1 - \mathbf{t}^{(\mathbf{e}_2)}ds_2 - \mathbf{t}^{(\mathbf{e}_3)}ds_3 + \mathbf{b}dv = 0 \tag{2.35}$$

If the area of the orthogonal faces and the volume of the element are written in terms of the largest face ds then Equation 2.35 may be rewritten as follows:

$$\mathbf{t}^{(\mathbf{n})} = \mathbf{t}^{(\mathbf{e}_1)}n_1 + \mathbf{t}^{(\mathbf{e}_2)}n_2 + \mathbf{t}^{(\mathbf{e}_3)}n_3 - \mathbf{b}\left(\frac{h}{3}\right) \tag{2.36}$$

Finally, taking the limit as $h \to 0$ allows Equation 2.36 to be rewritten as follows:

$$\mathbf{t}^{(\mathbf{n})} = \boldsymbol{\sigma}\mathbf{n} \tag{2.37}$$

The symmetric tensor **σ** describes the current force that acts per unit current area and is called the Cauchy stress tensor. Equation 2.37 is called Cauchy's theorem and it implies that the state of stress at any point within a body may be described in terms of the traction vectors that act upon three mutually-orthogonal planes. As the Cauchy stress tensor describes the current force that acts per unit current area, it is a natural measure of stress and is commonly referred to as the true stress tensor.

2.3.2 Alternate Measures of Stress

In certain analyses, such as nonlinear structural analyses, the current configuration of the continuum body is unknown and it may be difficult (or impossible) to derive the components of the Cauchy stress tensor. In order to derive an alternative measure of stress, consider the action of the force vector $\Delta\mathbf{f}$ upon the surface element ΔS which, as shown in Figure 2.3, is located in the reference configuration of the body:

$$\mathbf{t}^{(\mathbf{N})} = \lim_{\Delta S \to 0} \frac{\Delta \mathbf{f}}{\Delta S} = \frac{d\mathbf{f}}{dS} = \mathbf{PN} \tag{2.38}$$

The tensor **P** describes the current force that acts per unit reference area and is called the first Piola-Kirchoff stress tensor. The first Piola-Kirchoff stress tensor describes the current force that acts per unit reference area and is a very convenient measure of

stress for experimental analyses. As the first Piola-Kirchoff stress tensor is a two-point tensor and is generally non-symmetric, however, it is not particularly useful for nonlinear structural analyses. To derive an alternative measure of stress, that is both symmetric and is derived with respect to material coordinates, the force vector $\Delta\mathbf{f}$ is first written with respect to material coordinates as follows:

$$\Delta\mathbf{F} = \mathbf{F}^{-1}\Delta\mathbf{f} \tag{2.39}$$

In order to derive a third measure of stress, consider the action of the transformed force vector $\Delta\mathbf{F}$ upon the surface element ΔS as follows:

$$\mathbf{T}^{(\mathbf{N})} = \lim_{\Delta S \to 0} \frac{\Delta\mathbf{F}}{\Delta S} = \frac{d\mathbf{F}}{dS} = \mathbf{S}\mathbf{N} \tag{2.40}$$

The tensor **S** describes the transformed force that acts per unit reference area and is called the second Piola-Kirchoff stress tensor. As the second Piola-Kirchoff stress tensor is symmetric and is derived with respect to material coordinates, it is a very convenient measure of stress for nonlinear structural analyses. As the second Piola-Kirchoff stress tensor is described in terms of a transformed force vector, however, it is difficult to interpret and cannot be physically measured. Finally, the various stress tensors may be related using the deformation gradient tensor as follows:

$$\boldsymbol{\sigma} = J^{-1}\mathbf{P}\mathbf{F}^{\mathrm{T}} = J^{-1}\mathbf{F}\mathbf{S}\mathbf{F}^{\mathrm{T}} \tag{2.41}$$

$$\mathbf{P} = J\boldsymbol{\sigma}\mathbf{F}^{-\mathrm{T}} = \mathbf{F}\mathbf{S} \tag{2.42}$$

$$\mathbf{S} = J\mathbf{F}^{-1}\boldsymbol{\sigma}\mathbf{F}^{-\mathrm{T}} = \mathbf{F}^{-1}\mathbf{P} \tag{2.43}$$

In summary, no single measure of stress is ideal and multiple different measures of stress may be required during an analysis. In the following section, the fundamental conservation laws of continuum mechanics are introduced. These conservation laws describe the conservation of physical quantities such as mass, linear momentum and energy. In this thesis, however, it is assumed that the procedures under investigation are adiabatic and, as such, only the conservation laws of mass and linear momentum are discussed. The conservation laws of mass and linear momentum are first derived in the context of global equations which are then employed to derive local equations which are valid at every location within a continuum body.

2.3.3 Conservation of Mass

Every continuum body, as well as every material particle within a continuum body, is endowed with a non-negative scalar quantity called mass. Physically, the mass of a body is related to its inertia, i.e. its ability to resist changes in motion. To develop the concept of mass, consider an infinitesimal volume element dv which is located in the current configuration of a continuum body. If the scalar Δm denotes the mass of the volume element, then its mass density may be defined as follows:

$$\rho = \lim_{\Delta v \to 0} \frac{\Delta m}{\Delta v} \tag{2.44}$$

The scalar ρ denotes the mass density of the infinitesimal volume element dv. The total mass of the current configuration of the body may be determined by integrating over the entire volume of the current configuration as follows:

$$m = \int_v \rho dv \tag{2.45}$$

The law of conservation of mass states that the mass of a body remains invariant. As such, the material derivative of Equation 2.45 must equal zero as follows:

$$\frac{d}{dt}\int_v \rho dv = 0 \tag{2.46}$$

Through the application of Reynold's transport theorem, the differentiation may be carried out inside the integral and Equation 2.46 may be rewritten as follows:

$$\int_V \left[\frac{\partial \rho}{\partial t} + \boldsymbol{\nabla} \cdot (\rho \mathbf{v})\right] = 0 \tag{2.47}$$

As Equation 2.47 applies to any arbitrary volume element, the discrete form of the law of conservation of mass may be written as follows.

$$\frac{\partial \rho}{\partial t} + \boldsymbol{\nabla} \cdot (\rho \mathbf{v}) = 0 \tag{2.48}$$

Equation 2.48 describes the conservation of mass with respect to spatial coordinates and is often referred to as the continuity equation. If the material under investigation

is incompressible, the time rate of change of mass density remains constant and the law of conservation of mass may be reduced as follows:

$$\boldsymbol{\nabla} \cdot \mathbf{v} = 0 \tag{2.49}$$

To derive the material description of the law of conservation of mass, consider an infinitesimal volume element dV which is located in the reference configuration of a continuum body. As before, if the scalar Δm_0 denotes the mass of the infinitesimal volume element, then its mass density may be defined as follows:

$$\rho_0 = \lim_{\Delta V \to 0} \frac{\Delta m_0}{\Delta V} \tag{2.50}$$

The scalar ρ_0 denotes the mass density of the infinitesimal volume element dV. The total mass of the reference configuration of the body may be derived by integrating over the entire volume of the reference configuration as follows:

$$m_0 = \int_V \rho_0 dV \tag{2.51}$$

As stated previously, the law of conservation of mass states that the mass of a body remains invariant. As a result, the difference between the total mass of the reference and current configurations of the body must equal zero as follows:

$$\int_V \rho_0 dV - \int_v \rho dv = 0 \tag{2.52}$$

Noting the definition of the Jacobian determinant, Equation 2.52 may be rewritten solely in terms of material coordinates as follows:

$$\int_V \rho_0 dV - \int_V \rho J dV = 0 \tag{2.53}$$

As Equation 2.53 must apply to any infinitesimal volume element, the local form of the law of conservation of mass may be written as follows:

$$\rho_0 = \rho J \tag{2.54}$$

Equation 2.54 describes the conservation of mass in terms of material coordinates.

2.3.4 Conservation of Linear Momentum

The law of conservation of linear momentum states that the time rate of change of linear momentum, i.e. mass times velocity, must balance the sum of external forces that act upon a body and is written in terms of spatial coordinates as follows:

$$\frac{d}{dt}\int_v \rho\,\mathbf{v}dv = \int_s \mathbf{t}^{(\mathbf{n})}ds + \int_v \mathbf{b}dv \tag{2.55}$$

As a consequence of the law of conservation of mass, the term on the left-hand side of Equation 2.55 may be written with respect to material coordinates. As a result, the differentiation may be performed inside the integral using the chain rule and the term may then be rewritten with respect to spatial coordinates as follows:

$$\frac{d}{dt}\int_v \rho\,\mathbf{v}dv = \frac{d}{dt}\int_V \rho\mathbf{v}JdV = \int_v \rho\mathbf{a}dv \tag{2.56}$$

Through the application of the divergence theorem, the first term on the right-hand side of Equation 2.55 may be rewritten as a volume integral as follows:

$$\int_s \mathbf{t}^{(\mathbf{n})}ds = \int_s \boldsymbol{\sigma}\mathbf{n}ds = \int_v \boldsymbol{\nabla}\cdot\boldsymbol{\sigma}dv \tag{2.57}$$

The law of conservation of linear momentum may then be rewritten as follows:

$$\int_v \rho\mathbf{a}dv = \int_v \boldsymbol{\nabla}\cdot\boldsymbol{\sigma}dv + \int_v \mathbf{b}dv \tag{2.58}$$

As Equation 2.58 must apply to any infinitesimal volume element, the local form of the law of conservation of linear momentum may be written as follows:

$$\rho\mathbf{a} = \boldsymbol{\nabla}\cdot\boldsymbol{\sigma} + \mathbf{b} \tag{2.59}$$

Equation 2.59 describes the conservation of linear momentum with respect to spatial coordinates and is generally referred to as the equation of motion (or the momentum equation). If the time rate of change of velocity, i.e. acceleration, equals zero, the law of conservation of linear momentum may be reduced as follows:

$$\boldsymbol{\nabla}\cdot\boldsymbol{\sigma} + \mathbf{b} = 0 \tag{2.60}$$

Equation 2.60 is commonly referred to as the equilibrium equation. Alternatively, the law of conservation of linear momentum may be written with respect to material coordinates using the first Piola-Kirchoff stress tensor as follows:

$$\frac{d}{dt}\int_V \rho_0 \mathbf{V} dV = \int_S \mathbf{T}^{(\mathbf{N})} dS + \int_V \mathbf{B} dV \tag{2.61}$$

The vector **B** describes the body force acting per unit volume with respect to material coordinates and is defined using the Jacobian determinant as follows:

$$\mathbf{B} = J\mathbf{b} \tag{2.62}$$

As the infinitesimal volume element dV remains constant, the differentiation of the term on the left-hand-side of Equation 2.61 may be carried out as follows:

$$\frac{d}{dt}\int_V \rho_0 \mathbf{V} dV = \int_V \rho_0 \mathbf{A} dV \tag{2.63}$$

Again, through the application of the divergence theorem, the first term on the right-hand side of Equation 2.61 may be rewritten as a volume integral as follows:

$$\int_S \mathbf{T}^{(\mathbf{N})} dS = \int_S \mathbf{P}\mathbf{N} ds = \int_V \boldsymbol{\nabla} \cdot \mathbf{P} dV \tag{2.64}$$

The law of conservation of linear momentum may then be rewritten as follows:

$$\int_V \rho_0 \mathbf{A} dV = \int_V \boldsymbol{\nabla}_0 \cdot \mathbf{P} dV + \int_V \mathbf{B} dV \tag{2.65}$$

As Equation 2.65 applies to any infinitesimal volume element, the local form of the law of conservation of linear momentum may be written as follows:

$$\rho_0 \mathbf{A} = \boldsymbol{\nabla}_0 \cdot \mathbf{P} + \mathbf{B} \tag{2.66}$$

Equation 2.66 describes the conservation of linear momentum in terms of material coordinates. As before, if the time rate of change of velocity equals zero, the law of conservation of linear momentum may be reduced as follows:

$$\boldsymbol{\nabla}_0 \cdot \mathbf{P} + \mathbf{B} = 0 \tag{2.67}$$

2.4 Constitutive Equations

2.4.1 Linear Elastic Solid

An elastic material is defined as a material that stores energy under loading and then returns to its original configuration once the loading is removed. In a mathematical sense, an elastic material is defined as a material for which a strain energy (or stored energy) function may be derived and then differentiated with respect to a suitable measure of strain to determine the stress within the material. A strain energy function is simply a scalar valued function that relates the strain energy in the material to the deformation gradient tensor. Any elastic material for which a strain energy function may be derived is referred to as a hyperelastic material and the general constitutive equation for a hyperelastic material is written in terms of the second Piola-Kirchoff stress tensor and the Green-Lagrange strain tensor as follows:

$$\mathbf{S} = \frac{\partial W}{\partial \mathbf{E}} \tag{2.68}$$

The scalar W denotes the strain energy function. A hyperelastic material is referred to as a linear elastic material if displacements are assumed to be small and stress is assumed to be a linear function of strain. As displacements are assumed to be small, the general constitutive equation for a linear elastic material may be written in terms of the Cauchy stress tensor and the infinitesimal strain tensor as follows:

$$\boldsymbol{\sigma} = \frac{\partial W}{\partial \boldsymbol{\varepsilon}} \tag{2.69}$$

In order to derive a relationship between stress and strain for a linear elastic material, consider the general quadratic expansion of the strain energy function in terms of the infinitesimal strain tensor which may be written as follows:

$$W = \boldsymbol{\mathcal{C}}_0 + \boldsymbol{\mathcal{C}\varepsilon} + \frac{1}{2}\boldsymbol{\mathcal{C}\varepsilon^2} + \cdots \tag{2.70}$$

This expansion may be differentiated with respect to the infinitesimal strain tensor in order to derive the following relationship between stress and strain:

$$\boldsymbol{\sigma} = \boldsymbol{\mathcal{C}\varepsilon} \tag{2.71}$$

The fourth-order tensor $\boldsymbol{\mathcal{C}}$ is called the elasticity tensor. The elasticity tensor has 81 unknown components that must be derived from experimental analyses. Fortunately, due to the existence of the strain energy function and to the symmetry of the Cauchy stress tensor and the infinitesimal strain tensor, the number of unknown components is reduced to 21. Additionally, if the material is assumed to be isotropic, the number of unknown components is further reduced to 2 and the general constitutive equation for an isotropic linear elastic material may be written as follows:

$$\boldsymbol{\sigma} = \lambda \mathrm{tr}(\boldsymbol{\varepsilon})\mathbf{I} + 2\mu\boldsymbol{\varepsilon} \tag{2.72}$$

The constants λ and μ are called Lamé constants and are derived from experimental analyses. For an isotropic linear elastic solid the constants are derived as follows:

$$\lambda = \frac{\nu E}{(1+\nu)(1-2\nu)} \tag{2.73}$$

$$\mu = \frac{E}{2(1+\nu)} \tag{2.74}$$

The terms E and ν are called the Young's modulus and Poisson's ratio, respectively. As shown in Equation 2.72, the mechanical behaviour of an isotropic linear elastic material is completely characterised by these two elastic constants.

2.4.2 Nonlinear Elastic Solid

Through the application of the chain rule, the general constitutive equation for a hyperelastic material may be rewritten in terms of the second Piola-Kirchoff stress tensor and the right Cauchy-Green deformation tensor as follows:

$$\mathbf{S} = \frac{\partial W}{\partial \mathbf{E}} = \frac{\partial W}{\partial \mathbf{C}}\frac{\partial \mathbf{C}}{\partial \mathbf{E}} = 2\frac{\partial W}{\partial \mathbf{C}} \tag{2.75}$$

According to the representation theorem of invariants, an isotropic scalar-valued tensor function can be written in terms of the invariants of its argument. This implies that the strain energy function may be written as a function of the scalar invariants of the right Cauchy-Green deformation tensor as follows:

$$W = W[I_{\mathrm{C}}, II_{\mathrm{C}}, III_{\mathrm{C}}] \tag{2.76}$$

Using the chain rule, the strain energy function may be differentiated with respect to the right Cauchy-Green deformation tensor as follows:

$$\frac{\partial W}{\partial \mathbf{C}} = \frac{\partial W}{\partial I_{\mathrm{C}}}\frac{\partial I_{\mathrm{C}}}{\partial \mathbf{C}} + \frac{\partial W}{\partial II_{\mathrm{C}}}\frac{\partial II_{\mathrm{C}}}{\partial \mathbf{C}} + \frac{\partial W}{\partial III_{\mathrm{C}}}\frac{\partial III_{\mathrm{C}}}{\partial \mathbf{C}} \tag{2.77}$$

By calculating the derivatives of the individual scalar invariants of the right Cauchy-Green deformation tensor and then substituting these derivatives into Equation 2.75, the general constitutive equation for a nonlinear isotropic hyperelastic material may be written with respect to material coordinates as follows:

$$\mathbf{S} = 2\left[\left(\frac{\partial W}{\partial I_{\mathrm{C}}} + I_{\mathrm{C}}\frac{\partial W}{\partial II_{\mathrm{C}}}\right)\mathbf{I} - \frac{\partial W}{\partial II_{\mathrm{C}}}\mathbf{C} + III_{\mathrm{C}}\frac{\partial W}{\partial III_{\mathrm{C}}}\mathbf{C}^{-1}\right] \tag{2.78}$$

As shown in Equation 2.41, the Cauchy stress tensor may be written in terms of the second Piola-Kirchoff stress tensor and the deformation gradient tensor as follows:

$$\boldsymbol{\sigma} = J^{-1}\mathbf{F}\mathbf{S}\mathbf{F}^{\mathrm{T}} \tag{2.79}$$

By substituting Equation 2.78 into Equation 2.79 and noting that the scalar invariants of both the right and left Cauchy-Green deformation tensors are identical, the general constitutive equation for a nonlinear isotropic hyperelastic material may be written with respect to spatial coordinates as follows:

$$\boldsymbol{\sigma} = 2J^{-1}\left[\left(II_{\mathrm{b}}\frac{\partial W}{\partial II_{\mathrm{b}}} + III_{\mathrm{b}}\frac{\partial W}{\partial III_{\mathrm{b}}}\right)\mathbf{I} + \frac{\partial W}{\partial I_{\mathrm{b}}}\mathbf{b} - III_{\mathrm{b}}\frac{\partial W}{\partial II_{\mathrm{b}}}\mathbf{b}^{-1}\right] \tag{2.80}$$

As many hyperelastic materials can sustain large strains without noticeable changes in volume, they are often characterised as incompressible materials. To describe the behaviour of these materials the following constraint is introduced:

$$J = \det(\mathbf{F}) = III_{\mathrm{C}} = 1 \tag{2.81}$$

To derive a general constitutive equation for a nonlinear incompressible hyperelastic material, the general form of the strain energy function is written as follows:

$$W = W[I_{\mathrm{C}}, II_{\mathrm{C}}] - \frac{1}{2}p(III_{\mathrm{C}} - 1) \tag{2.82}$$

The scalar p denotes a Lagrange multiplier and is most commonly interpreted as an indeterminate pressure. As a result, the general constitutive equation for a nonlinear incompressible isotropic hyperelastic material may be written as follows:

$$\mathbf{S} = -p\mathbf{C}^{-1} + 2\frac{\partial W}{\partial \mathbf{C}} \tag{2.83}$$

By differentiating the strain energy function with respect to the right Cauchy-Green deformation tensor and substituting the derivatives into Equation 2.83, the general constitutive equation for a nonlinear incompressible isotropic hyperelastic material may be written with respect to material coordinates as follows:

$$\mathbf{S} = -p\mathbf{C}^{-1} + 2\left(\frac{\partial W}{\partial I_{\mathrm{C}}} + I_{\mathrm{b}}\frac{\partial W}{\partial II_{\mathrm{C}}}\right)\mathbf{I} - 2\frac{\partial W}{\partial II_{\mathrm{C}}}\mathbf{C} \tag{2.84}$$

By substituting Equation 2.84 into Equation 2.79 and noting that the scalar invariants of both the right and left Cauchy-Green deformation tensors are identical, the general constitutive equation for a nonlinear incompressible isotropic hyperelastic material may be written with respect to spatial coordinates as follows:

$$\boldsymbol{\sigma} = -p\mathbf{I} + 2\frac{\partial W}{\partial I_{\mathrm{b}}}\mathbf{b} - 2\frac{\partial W}{\partial II_{b}}\mathbf{b}^{-2} \tag{2.85}$$

Until now, the strain energy function has been described in terms of the principal invariants of the Cauchy-Green deformation tensors but its functional form has not been discussed. One of the simplest strain energy functions, called the neo-Hookean function, was proposed by Ronald Rivlin in 1948 and is defined as follows:

$$W = C_1(I - 3) \tag{2.86}$$

The term C_1 is a material constant that is employed to fit the strain energy function to the appropriate experimental data. Another popular strain energy function, called the Mooney-Rivlin function, was proposed by Melvin Mooney in 1940 and rewritten in terms of principal invariants by Ronald Rivlin in 1948. The Mooney-Rivlin function takes the form of a general polynomial and is defined as follows:

$$W = C_1(I - 3) + C_2(II - 3) \tag{2.87}$$

As before, the scalars C_1 and C_2 denote material constants. A third well known strain energy function, called the Ogden function, was proposed by Ray Ogden in 1972 and is written in terms of the principal stretches as follows:

$$W = \sum_{i=1}^{n} \frac{2\mu_i}{\alpha_i} \left(\lambda_1^{\alpha_i} + \lambda_2^{\alpha_i} + \lambda_3^{\alpha_i} - 3 \right) \tag{2.88}$$

Again, the scalars α_i and μ_i denote material constants. The mechanical behaviour of a nonlinear isotropic hyperelastic material is completely characterised by the choice of strain energy function and the associated material constants.

2.4.3 Rate-Independent Elastic-Plastic Solid

An elastic-plastic material is defined as a material that experiences permanent plastic deformation once it is loaded beyond a critical stress value called the yield stress. To describe the mechanical behaviour of an elastic-plastic material, the deformation is divided into an elastic part and a plastic part. If the elastic deformation is assumed to be small in comparison to the plastic deformation (which is true for a wide range of metals, soils and polymers), the total strain increment may be decomposed into the sum of an elastic strain increment and a plastic strain increment as follows:

$$d\boldsymbol{\varepsilon} = d\boldsymbol{\varepsilon}^e + d\boldsymbol{\varepsilon}^p \tag{2.89}$$

The elastic strain increment $d\boldsymbol{\varepsilon}^e$ is related to the stress increment through the linear elastic constitutive equation whilst the plastic strain increment is related to the stress increment through the specification of an appropriate yield criterion, hardening law and plastic flow rule. The yield criterion is used to determine whether the mechanical response of the material is elastic or plastic and is defined as follows:

$$\Phi(\boldsymbol{\sigma}) = 0 \tag{2.90}$$

The yield criterion describes a surface, referred to as the yield surface, which divides the principal stress space into an elastic region and a plastic region. If the state of stress lies within the region bounded by the yield surface, the mechanical response of the body is elastic. Alternatively, if the state of stress lies upon the yield surface, the mechanical response of the body is plastic. As experimental studies have determined that the assumption of incompressible plastic deformations holds for a wide range of

ductile metallic materials, it is convenient to introduce a deviatoric measure of stress. To derive a deviatoric measure of stress, the Cauchy stress tensor is decomposed into the sum of a deviatoric component and a dilational component as follows:

$$\boldsymbol{\sigma} = \mathbf{s} - p_0\mathbf{I} \tag{2.91}$$

The tensor $\mathbf{s}$ describes the deviatoric component of the Cauchy stress tensor and is called the deviatoric stress tensor whereas the scalar p_0 describes the mean normal stress and is called the hydrostatic pressure. The von Mises yield criterion, which is often employed to describe the inelastic behaviour of ductile materials, assumes that yielding is initiated once the second scalar invariant of the deviatoric stress tensor exceeds the uniaxial yield stress and may be written as follows:

$$\Phi(\boldsymbol{\sigma}) = II_{\mathbf{s}} - \sigma_y = \sqrt{\frac{3}{2}\mathbf{s} : \mathbf{s}} - \sigma_y = \sigma_e - \sigma_y = 0 \tag{2.92}$$

The term σ_e denotes the second scalar invariant of the deviatoric stress tensor and is called the equivalent stress (ES) whilst the term σ_y denotes the uniaxial yield stress of the material. Experimental analyses have also shown that materials subjected to previous plastic deformation tend to exhibit an increased resistance to further plastic deformation. This phenomenon, which is referred to as hardening, may be accounted for by varying the size and/or position of the yield surface during plastic deformation using a suitable hardening law. If the yield surface remains fixed in stress space but increases uniformly in size during plastic deformation, the hardening law is termed isotropic and the von Mises yield criterion may be rewritten as follows:

$$\Phi(\boldsymbol{\sigma}, \boldsymbol{\alpha}) = \sqrt{\frac{3}{2}\mathbf{s} : \mathbf{s}} - \sigma_y(\alpha) = 0 \tag{2.93}$$

The term $\boldsymbol{\alpha}$ denotes a set of internal hardening variables and, if isotropic hardening is assumed, this set typically contains a single scalar variable α that determines the size of the yield surface during plastic loading. The isotropic hardening law is limited in that it does not predict the Bauschinger effect, where a hardening in tension causes a subsequent softening in compression. As such, the isotropic hardening law is not suitable in analyses where the body is subject to cyclic loading conditions. If the size

of the yield surface remains fixed during plastic deformation and its position is then translated through stress space, however, the hardening law is termed kinematic and the von Mises yield criterion may be rewritten as follows:

$$\Phi(\boldsymbol{\sigma}, \boldsymbol{\alpha}) = \sqrt{\frac{3}{2}(\mathbf{s} - \overline{\boldsymbol{\alpha}}) : (\mathbf{s} - \overline{\boldsymbol{\alpha}})} - \sigma_y = 0 \tag{2.94}$$

For kinematic hardening, the set of hardening variables $\boldsymbol{\alpha}$ generally contains a single tensor $\overline{\boldsymbol{\alpha}}$, called the back stress tensor, that translates the yield surface relative to the principal stress axes during plastic loading. Finally, the plastic flow rule describes the direction of the plastic strain increment and is written as follows:

$$d\boldsymbol{\varepsilon}^p = d\lambda \frac{\partial g(\boldsymbol{\sigma}, \boldsymbol{\alpha})}{\partial \boldsymbol{\sigma}} = d\lambda \frac{\partial \Phi(\boldsymbol{\sigma}, \boldsymbol{\alpha})}{\partial \boldsymbol{\sigma}} \tag{2.95}$$

The scalar-valued function $d\lambda$ describes the magnitude of the plastic strain increment and is called the plastic multiplier whilst the scalar-valued function g describes the direction of the plastic strain increment and is referred to as the plastic potential. For ductile metallic materials, the plastic potential is often set equal to the yield criterion and the flow rule is termed associative. For an associative flow rule, the direction of the plastic strain increment is normal to the yield surface. Finally, the plastic flow rule is complemented by the following loading/unloading conditions:

$$d\lambda \geq 0, \qquad \Phi \leq 0, \qquad d\lambda\Phi = 0 \tag{2.96}$$

These loading/unloading conditions are referred to as the Kuhn-Tucker conditions. The first condition states that the plastic multiplier is non-negative, i.e. during elastic loading $d\lambda = 0$ whilst during plastic loading $d\lambda > 0$. The second condition implies that the state of stress lies within or upon the yield surface, i.e. during elastic loading $\Phi < 0$ whilst during plastic loading $\Phi = 0$. Finally, the third condition implies that the state of stress remains located upon the yield surface during plastic loading. This third condition is often expressed in rate form as follows:

$$d\Phi = \frac{\partial \Phi}{\partial \boldsymbol{\sigma}} : d\boldsymbol{\sigma} + \frac{\partial \Phi}{\partial \boldsymbol{\alpha}} : d\boldsymbol{\alpha} = 0 \tag{2.97}$$

Equation 2.97 is commonly referred to as the consistency condition.

2.4.4 Linear Viscous Fluid

A fundamental characteristic of a fluid is that the action of shear stresses will cause the fluid to deform continuously, so long as the stresses act. As a result, when a fluid is at rest, the traction vector $\mathbf{t}^{(\mathbf{n})}$ is proportional to the corresponding surface normal vector $\mathbf{n}$, but independent of its direction and may be written as follows:

$$\mathbf{t}^{(\mathbf{n})} = \boldsymbol{\sigma}\mathbf{n} = -p_0\mathbf{n} \tag{2.98}$$

The scalar p_0 describes the mean normal stress in the fluid and is commonly referred to as the hydrostatic pressure. From Equation 2.98, the Cauchy stress tensor may be written in terms of the hydrostatic pressure as follows:

$$\boldsymbol{\sigma} = -p_0\mathbf{I} \tag{2.99}$$

Equations 2.98 and 2.99 imply that, when a fluid is at rest (or in a state of rigid-body motion), the stress at each individual location within the fluid is compressive and the hydrostatic pressure is equal to the mean normal stress as follows:

$$p_0 = -\frac{1}{3}\mathrm{tr}(\boldsymbol{\sigma}) \tag{2.100}$$

When a fluid is in motion, the shear stresses are not equal to zero. In order to account for the shear stresses, the Cauchy stress tensor is decomposed as follows:

$$\boldsymbol{\sigma} = -p\mathbf{I} + \boldsymbol{\tau} \tag{2.101}$$

The scalar p denotes the thermodynamic pressure whilst the tensor $\boldsymbol{\tau}$ describes the state of shear stress within the fluid and is referred to as the viscous stress tensor. For a fluid in motion, the thermodynamic pressure may be defined as follows:

$$p = -\frac{1}{3}(\boldsymbol{\sigma} - \boldsymbol{\tau}) \tag{2.102}$$

In order to derive a general constitutive equation for a fluid, the Cauchy stress tensor is first written as a function of the rate of deformation tensor as follows:

$$\boldsymbol{\sigma} = \mathbf{f}(\mathbf{d}) \tag{2.103}$$

If the Cauchy stress tensor is a nonlinear function of the rate of deformation tensor, the fluid is called a Stokesian fluid. Conversely, if the Cauchy stress tensor is a linear function of the rate of deformation tensor, the fluid is called a Newtonian fluid. The general constitutive equation for a Newtonian fluid is written as follows:

$$\boldsymbol{\sigma} = \boldsymbol{\mathcal{K}}\mathbf{d} \tag{2.104}$$

The fourth-order tensor $\boldsymbol{\mathcal{K}}$ is called the viscosity tensor. The viscosity tensor has 81 unknown components that must be derived from experimental analyses. Fortunately, due to the symmetry of the Cauchy stress tensor and the rate of deformation tensor, the number of unknown constants is reduced to 36. Additionally, if the fluid is also assumed to be isotropic (most common liquids and gases are isotropic), the number of unknown components is further reduced to 2 and the general constitutive equation for an isotropic Newtonian fluid may be written as follows:

$$\boldsymbol{\sigma} = -p\mathbf{I} + \lambda \mathrm{tr}(\mathbf{d})\mathbf{I} + 2\mu\mathbf{d} \tag{2.105}$$

The constants λ and μ are similar to the Lamé constants and are generally referred to as the first and second viscosity coefficients, respectively. Using Equation 2.105, the mean normal stress for a Newtonian fluid may be written as follows:

$$\frac{1}{3}\mathrm{tr}(\boldsymbol{\sigma}) = -p + \left(\lambda + \frac{2}{3}\mu\right)\mathrm{tr}(\mathbf{d}) = -p + \kappa \mathrm{tr}(\mathbf{d}) \tag{2.106}$$

The term κ is referred to as the coefficient of bulk viscosity. In order to ensure that the hydrostatic pressure is equal to the thermodynamic pressure when a Newtonian fluid is at rest, the coefficient of bulk viscosity must equal zero as follows:

$$\kappa = \left(\lambda + \frac{2}{3}\mu\right) = 0 \tag{2.107}$$

Equation 2.107 allows the viscosity coefficients to be related as follows:

$$\lambda = -\frac{2}{3}\mu \tag{2.108}$$

Equation 2.108 ensures that the hydrostatic and thermodynamic pressures are equal when a Newtonian fluid is at rest and is referred to as Stokes' hypothesis.

2.5 Computational Structural Analysis

2.5.1 Governing Equations

The CS analyses described in this thesis were each carried out using the commercial finite element analysis package ABAQUS (Dassault Systèmes, Simulia Corporation, Providence, RI, USA) and, as a result, the theory presented in this section is based on that described within the ABAQUS Theory Manual [48]. When attempting to solve a nonlinear boundary value problem, a coupled system of equations must be solved. This system of equations often includes the kinematic relations, the local form of the law of conservation of linear momentum, an appropriate constitutive equation and a number of boundary and initial conditions. As the analytical solution of the initial boundary value problem is only possible in a small number of cases, sophisticated numerical techniques, such as the finite element method, are typically employed to obtain an approximate numerical solution to the initial boundary value problem. The basis of displacement-based finite element formulations is the introduction of a weak form of the initial boundary value problem. The weak form is determined by taking the dot product of the law of conservation of linear momentum with an arbitrary weighting function $\boldsymbol{\eta}$ and then integrating over the body as follows:

$$\int_v (\boldsymbol{\nabla} \cdot \boldsymbol{\sigma} + \mathbf{b} - \rho \mathbf{a}) \boldsymbol{\eta} dv = \mathbf{0} \tag{2.109}$$

The weighting function $\boldsymbol{\eta}$ is completely arbitrary and is commonly interpreted as a virtual displacement $\delta\mathbf{u}$ that must obey any prescribed kinematic constraints whilst possessing sufficient continuity. Through the application of the chain rule, the first term in Equation 2.109 may be then be rewritten as follows:

$$\int_v \boldsymbol{\nabla} \cdot (\boldsymbol{\sigma} \delta \mathbf{u}) dv = \int_v (\boldsymbol{\nabla} \cdot \boldsymbol{\sigma}) \delta \mathbf{u} dv - \int_v \boldsymbol{\sigma} : \boldsymbol{\nabla} \delta \mathbf{u} dv \tag{2.110}$$

Applying the divergence theorem, the first term on the right-hand side of Equation 2.110 may then be written as a surface integral. Noting the definition of the Cauchy stress tensor, this surface integral may then be rewritten as follows:

$$\int_v (\boldsymbol{\nabla} \cdot \boldsymbol{\sigma}) \delta \mathbf{u} dv = \int_s \boldsymbol{\sigma} \mathbf{n} \delta \mathbf{u} ds = \int_s \mathbf{t} \delta \mathbf{u} ds \tag{2.111}$$

Recalling the symmetry of the Cauchy stress tensor, the second term on the right-hand side of Equation 2.110 may also be rewritten as follows:

$$\int_v \boldsymbol{\sigma} : \boldsymbol{\nabla}\delta\mathbf{u}dv = \int_v \boldsymbol{\sigma} : \frac{1}{2}[\boldsymbol{\nabla}\delta\mathbf{u} + (\boldsymbol{\nabla}\delta\mathbf{u})^T]dv - \int_v \boldsymbol{\sigma} : \delta\boldsymbol{\varepsilon}dv \tag{2.112}$$

Substituting Equations 2.110, 2.111 and 2.112 into Equation 2.109 and rearranging the terms yields the weak form of the initial boundary value problem:

$$\int_v \rho\mathbf{a}\delta\mathbf{u}dv + \int_v \boldsymbol{\sigma} : \delta\boldsymbol{\varepsilon}dv - \int_s \mathbf{t}\delta\mathbf{u}ds - \int_v \mathbf{b}\delta\mathbf{u}dv = 0 \tag{2.113}$$

Equation 2.113 is derived with respect to spatial coordinates and is referred to as the spatial principle of virtual work. The first and second terms in Equation 2.113 denote the internal virtual work and the kinetic virtual work, respectively, whilst the sum of the third and the fourth terms denotes the external virtual work.

2.5.2 Discretisation

To obtain an approximate solution for the initial boundary value problem, the body is divided into a discrete number of finite elements as shown in Figure 2.5. The finite elements are interconnected by nodes and each node possesses a number of degrees of freedom. In displacement-based finite element formulations, the displacement and acceleration within each finite element are approximated as follows:

$$\mathbf{u} = \sum_{a=1}^{n} N_a\mathbf{u}_a \qquad \delta\mathbf{u} = \sum_{a=1}^{n} N_a\delta\mathbf{u}_a \qquad \mathbf{a} = \sum_{a=1}^{n} N_a\mathbf{a}_a \tag{2.114}$$

The term N_a denotes the nodal shape function, the term n denotes the total number of nodes and the terms $\mathbf{u}_a$, $\delta\mathbf{u}_a$ and $\mathbf{a}_a$ denote the nodal displacement, nodal virtual displacement and nodal acceleration vectors, respectively. Adopting matrix-vector (or Voigt) notation allows both the Cauchy stress tensor and the virtual infinitesimal strain tensor to be recast as vectors comprised of six independent components. This also allows the virtual infinitesimal strain tensor to be interpolated as follows:

$$\delta\boldsymbol{\varepsilon} = \sum_{a=1}^{n} \frac{\partial N_a}{\partial \mathbf{x}}\delta\mathbf{u}_a = \sum_{a=1}^{n} \mathbf{B}_a\delta\mathbf{u}_a \tag{2.115}$$

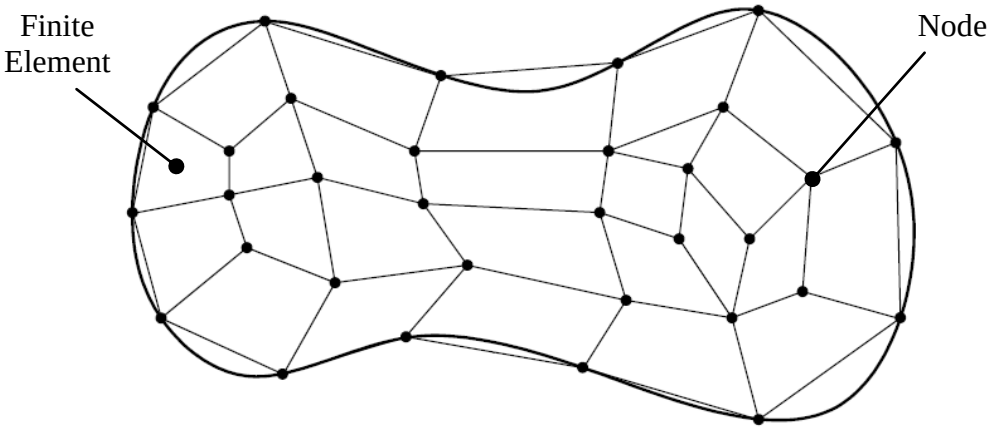

Figure 2.5: Discretisation of a continuum body into a finite element mesh.

The matrix **B** describes the spatial derivatives of the element shape functions and is referred to as the strain-displacement matrix. At this stage it is convenient to assess the contribution of a single virtual displacement $\delta\mathbf{u}_a$ at a node a located within the element e. Introducing the interpolations in Equations 2.114 and 2.115 into Equation 2.113 yields the following discretised form of the equilibrium statement:

$$\delta\mathbf{u}_a^T \left(\begin{array}{c} \int_{v^e} \rho N_a N_b \, dv \mathbf{a} + \int_{v^e} \mathbf{B}_a^T \boldsymbol{\sigma} \, dv \\ - \int_{s^e} N_a^T \mathbf{t} ds - \int_{v^e} N_a^T \mathbf{b} dv \end{array} \right) = 0 \tag{2.116}$$

Assembling the elemental equations into a global system of equations and recalling the arbitrariness of the applied virtual displacement results in a system of ordinary differential equations which may be written as follows:

$$\mathbf{Ma} + \mathbf{R}(\mathbf{u}) - \mathbf{P} = 0 \tag{2.117}$$

The individual terms in the global system of equations are as follows:

$$\mathbf{Ma} = \left(\int_v \rho \mathbf{N}\mathbf{N}^T dv \, \mathbf{I} \right) \mathbf{a} \tag{2.118}$$

$$\mathbf{R}(\mathbf{u}) = \int_v \mathbf{B}^T \boldsymbol{\sigma} \, dv \tag{2.119}$$

$$\mathbf{P} = \int_s \mathbf{N}^T \mathbf{t} ds - \int_v \mathbf{N}^T \mathbf{b} dv \tag{2.120}$$

The matrices **M** and **B** denote the assembled mass and strain-displacement matrices, respectively, whilst the vectors **a**, **u**, **R**(**u**) and **P** denote the global vectors of nodal accelerations, displacements, internal and external forces, respectively. If the inertial effects are neglected, the global system of equations is reduced to a nonlinear system of algebraic equations and may be written as follows:

$$\mathbf{R}(\mathbf{u}) - \mathbf{P} = 0 \tag{2.121}$$

In the following section, the explicit integration scheme that was employed to solve the nonlinear finite element equilibrium equations is discussed.

2.5.3 Solution

The CS analyses described as part of the proposed methodology are each carried out using the ABAQUS/Explicit solver and the discrete system of ordinary differential equations is solved using an explicit central difference integration rule:

$$\begin{aligned} \mathbf{u}^{(i+1)} &= \mathbf{u}^{(i)} + \Delta t^{(i+1)}\mathbf{v}^{\left(i+\frac{1}{2}\right)} \\ \mathbf{v}^{\left(i-\frac{1}{2}\right)} &= \mathbf{v}^{\left(i-\frac{1}{2}\right)} + \left[\frac{\Delta t^{(i+1)} + \Delta t^{(i)}}{2}\right]\mathbf{a}^{(i)} \end{aligned} \tag{2.122}$$

The superscript (i) refers to the current increment whilst the superscripts $(i - 1/2)$ and $(i + 1/2)$ refer to mid-increment values. The central difference integration rule is explicit in that the kinematic state of the body is advanced using the known values of the velocity and acceleration from the previous increment. The explicit integration rule is both simple and computationally efficient as the accelerations are computed at the start of each increment by inverting the mass matrix as follows:

$$\mathbf{a}^i = \mathbf{M}^{-1}\left[\mathbf{R}^i - \mathbf{P}^i\right] = 0 \tag{2.123}$$

As the mass matrix is diagonal, its inversion is trivial. The explicit integration rule is conditionally stable and the stability limit is determined from the maximum element eigenvalue within the system ω_{max} and may be written as follows:

$$\Delta t \leq \frac{2}{\omega_{max}} \tag{2.124}$$

2.6 Computational Fluid Dynamics Analysis

2.6.1 Governing Equations

The CFD analyses described in this thesis were carried out using the commercial CFD package ANSYS CFX (ANSYS Inc., Canonsburg, PA, USA) and, as such, the theory presented in this section is based on that described within the ANSYS CFX Theory Manual [49]. As before, the basis of CFD analyses is the introduction of an equivalent weak form of the initial boundary value problem. In the context of fluid mechanics, the finite volume method is generally adopted to obtain an approximate numerical solution to the initial boundary value problem. If the flow is assumed to be incompressible, the local form of the laws of conservation of both mass and linear momentum may be written with respect to spatial coordinates as follows:

$$\boldsymbol{\nabla} \cdot \mathbf{v} = 0 \tag{2.125}$$

$$\rho \left[\frac{\partial \mathbf{v}}{\partial t} + \mathbf{v} \cdot \boldsymbol{\nabla} \mathbf{v} \right] = \boldsymbol{\nabla} \cdot \boldsymbol{\sigma} + \rho \mathbf{b} \tag{2.126}$$

If the fluid is assumed to be Newtonian, Equation 2.105 may then be substituted into Equation 2.126 in order to obtain the following governing equations:

$$\boldsymbol{\nabla} \cdot \mathbf{v} = 0 \tag{2.127}$$

$$\rho \left[\frac{\partial \mathbf{v}}{\partial t} + \mathbf{v} \cdot \boldsymbol{\nabla} \mathbf{v} \right] = -\boldsymbol{\nabla} p + \boldsymbol{\nabla} \cdot (\mu \boldsymbol{\nabla} \mathbf{v}) + \rho \mathbf{b} \tag{2.128}$$

Equations 2.127 and 2.128 are referred to as the Navier-Stokes equations and these equations possess the following general convection-diffusion form:

$$\frac{\partial}{\partial t}(\rho \phi) + \boldsymbol{\nabla} \cdot (\rho \phi \mathbf{v}) - \boldsymbol{\nabla} \cdot \left(\Gamma_{\phi} \boldsymbol{\nabla} \phi \right) = S_{\phi} \tag{2.129}$$

The term ϕ denotes the dependent variable, Γ_{ϕ} denotes the diffusion coefficient and S_{ϕ} denotes the source term. The first three terms in Equation 2.129 are referred to as the transient, convection and diffusion terms, respectively, and are used to describe the change in the dependent variable as a result of temporal variations, convective transport and diffusion, respectively. The source term on the right hand side is then used to describe the production or destruction of the dependent variable.

2.6.2 Discretisation

In the CFD analyses described as part of the proposed methodology, the governing equations of flow, which may be represented by the general transport equation given in Equation 2.129, are discretised using a vertex-centred finite volume discretisation scheme. In order to obtain an approximate numerical solution for the boundary value problem, the fluid domain is first divided into a discrete number of finite volume cells and the governing equations are then integrated over each cell. To demonstrate the discretisation of the governing equations, consider a two-dimensional (2D) finite volume cell that is surrounded by similar cells as shown in Figure 2.6. The centre of the cell of interest is labelled P and its respective faces are labelled a, b, c and d as shown in Figure 2.6. The centres of the neighbouring cells are then labelled A, B, C and D in a similar fashion. The general transport equation given in Equation 2.129 is then integrated over the cell to derive the following integral equation:

$$\int_{\mathbf{v}} \frac{\partial}{\partial t}(\rho\phi)dv + \int_{\mathbf{v}} \boldsymbol{\nabla}\cdot(\rho\phi\mathbf{v})dv - \int_{\mathbf{v}} \boldsymbol{\nabla}\cdot\left(\Gamma_\phi \boldsymbol{\nabla}\phi\right)dv = \int_{v} S_\phi dv \qquad (2.130)$$

Applying the divergence theorem, both the convection and diffusion integrals can be written as surface integrals and Equation 2.129 may be rewritten as follows:

$$\int_{\mathbf{v}} \frac{\partial}{\partial t}(\rho\phi)dv + \int_{\mathbf{s}} \rho\phi\mathbf{v}\mathbf{n}ds - \int_{\mathbf{s}} \Gamma_\phi \boldsymbol{\nabla}\phi\mathbf{n}ds = \int_{v} S_\phi dv \qquad (2.131)$$

Equation 2.130 contains four individual terms that must be discretised. The transient term is approximated using a second-order backward Euler scheme as follows:

$$\int_{\mathbf{v}} \frac{\partial}{\partial t}(\rho\phi)dv = \frac{\Delta v}{\Delta t}\left[\frac{3}{2}(\rho\phi)^n - 2(\rho\phi)^{n-1} + \frac{1}{2}(\rho\phi)^{n-2}\right] \qquad (2.132)$$

The term Δt denotes the time step whereas the superscripts (n), $(n-1)$ and $(n-2)$ denote the variable values from the current, previous and twice previous time steps, respectively. The convection term in Equation 2.130 is then integrated as the sum of fluxes over the four faces surrounding the cell of interest as follows:

$$\int_{\mathbf{s}} \rho\phi\mathbf{v}\mathbf{n}ds = \sum_{ip=1}^{n} \dot{m}_{ip}\phi_{ip} = \sum_{ip=1}^{n} (\rho\mathbf{u}\mathbf{d}\mathbf{s})_{ip}\phi_{ip} \qquad (2.133)$$

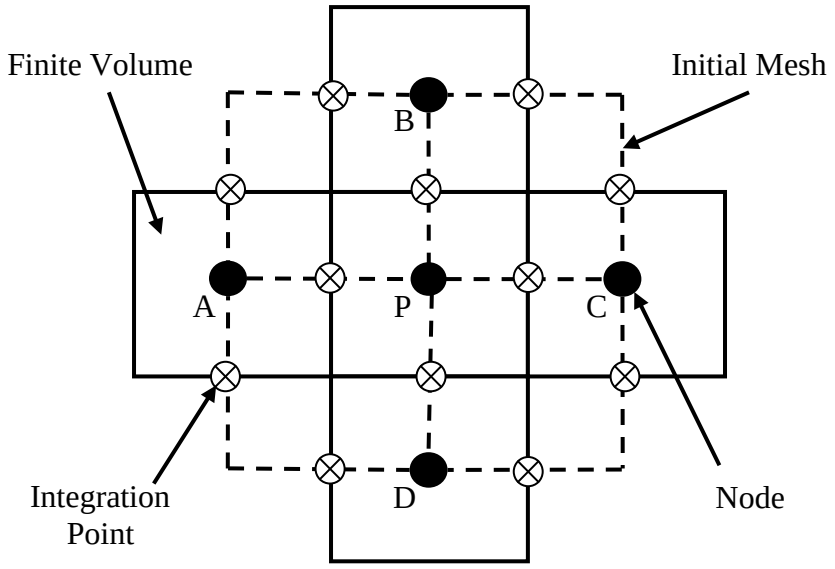

Figure 2.6: Discretisation of a continuum body into a finite volume mesh.

The terms $\dot{m}_{ip}$, $\mathbf{ds}_{ip}$ and ϕ_{ip} denote the mass flow, outward surface vector and value of the dependent variable at the respective integration points. Though the integration yields the variables at the faces, the solution variables are stored at the nodes. As a result, the face values are approximated at the integration points as follows:

$$\phi_{ip} = \phi_{up} + \beta \nabla\phi \cdot \Delta\mathbf{r} \tag{2.134}$$

The term ϕ_{ip} denotes the value of the dependent variable at an integration point, ϕ_{up} denotes the value at the upwind node, β denotes the blend factor, $\nabla\phi$ denotes the variable gradient and $\Delta\mathbf{r}$ describes a vector that extends from the integration point to the upwind node. The diffusion term is approximated as follows:

$$\int_{\mathbf{s}} \Gamma_\phi \nabla\phi \mathbf{n} ds = \sum_{ip=1}^{n} \left(\Gamma_\phi \nabla\phi \mathbf{ds}\right)_{ip} \tag{2.135}$$

Following the finite element approach, shape functions are employed to calculate the spatial derivatives in each of the diffusion terms. For example, the derivative in the x-direction at a specific integration point may be computed as follows:

$$\left(\frac{\partial\phi}{\partial x}\right)_{ip} = \sum_{a=1}^{n} \left(\frac{\partial N_a}{\partial x}\right)_{ip} \phi_n \tag{2.136}$$

The source term is approximated as follows:

$$\int_v S_\phi dv = \bar{S}_\phi \Delta v \tag{2.137}$$

The term $\bar{S}_\phi$ denotes the average value of the source term within the finite volume. When the source term is a function of the dependent variable, $\bar{S}_\phi$ is decomposed into solution-independent and solution-dependent terms as follows:

$$\bar{S}_\phi = \bar{b} + \bar{S}(\phi) \tag{2.138}$$

The final variable to be approximated is the pressure gradient term in the momentum equation which is not satisfied in the general transport equation. Pressure is obtained indirectly from the continuity equation in that, when the correct pressure is inserted into the momentum equation, the resulting velocity field must satisfy continuity. As such, the calculation of pressure and velocity is coupled. The surface integration of the pressure gradient is evaluated using shape functions as follows:

$$p_{ip} = \sum_{a=1}^{n} N_a p_a \tag{2.139}$$

Substituting the terms in Equations 2.131, 2.132, 2.134 and 2.136 back into Equation 2.130 yields the following discretised form of the general transport equation:

$$\begin{aligned} \frac{\Delta v}{\Delta t}\left[\frac{3}{2}(\rho\phi)^n - 2(\rho\phi)^{n-1} + \frac{1}{2}(\rho\phi)^{n-2}\right] + \sum_{ip=1}^{n} \dot{m}_{ip}\phi_{ip} \\ - \sum_{ip=1}^{n} \left(\Gamma_\phi \boldsymbol{\nabla}\phi \mathbf{ds}\right)_{ip} = \bar{S}_\phi \Delta v \end{aligned} \tag{2.140}$$

The application of the finite volume method to each cell results in a global system of linear equations which may be written in vector-matrix notation as follows:

$$\mathbf{A}\boldsymbol{\phi} = \mathbf{b} \tag{2.141}$$

The matrix **A** denotes the coefficient matrix, the vector $\boldsymbol{\phi}$ denotes the solution vector whilst the matrix **b** denotes the right-hand side matrix.

2.6.3 Solution

The CFD analyses described as part of the proposed methodology are each carried out using the coupled multi-grid solver in ANSYS CFX which uses an incomplete lower-upper factorisation technique to solve the discrete system of equations. For a steady-state CFD analysis, the discrete system of equations are solved only once at each consecutive time step whereas, during a transient CFD analysis, a large number of iterations are generally performed at each consecutive time step. The solution is computed in an iterative manner and begins with an approximate solution $\boldsymbol{\phi}^n$ that is adjusted by a correction $\boldsymbol{\phi}'$ to obtain an improved solution $\boldsymbol{\phi}^{n+1}$ as follows:

$$\boldsymbol{\phi}^{n+1} = \boldsymbol{\phi}^n + \boldsymbol{\phi}^{'} \tag{2.142}$$

The correction is derived in the following manner:

$$\mathbf{A}\boldsymbol{\phi}^{'} = \mathbf{r}^n \tag{2.143}$$

The term $\mathbf{r}^n$ denotes the residual vector which is obtained as follows:

$$\mathbf{r}^n = \mathbf{b} + \mathbf{A}\boldsymbol{\phi}^n \tag{2.144}$$

Solution convergence must be achieved over the course of a steady-state analysis and at each time step during a transient analysis. Solution convergence is achieved when the normalised residuals fall below some pre-specified tolerance.

2.7 Summary

In this chapter the kinematic concepts of motion, deformation and strain have been introduced and the concept of stress has been described. The conservation laws of mass and linear momentum were then presented and various constitutive equations of interest were discussed. The governing equations of structural and fluid mechanics were then derived and their discretisation and solution was discussed in terms of the finite element and finite volume formulations which are employed in ABAQUS and ANSYS CFX, respectively. In the following chapter, a comprehensive review of the literature is presented and a number of the limitations associated with the evaluation of stent performance exclusively in terms of either the mechanical or hemodynamic impact predicted within the coronary artery are then discussed.

CHAPTER 3
LITERATURE REVIEW

3.1 Introduction

In this chapter, the literature is first reviewed and the limitations associated with the evaluation of stent performance solely in terms of the mechanical or hemodynamic impact predicted within the coronary artery are noted. A number of key studies that employed CS analyses to evaluate the mechanical impact of stent deployment within a coronary artery are first discussed and a review of the literature is then presented. A number of key studies that employed CFD analyses to evaluate the hemodynamic impact of stent deployment within a coronary artery are also discussed and a review of the literature is then presented. Finally, the small number of studies that employed CS and CFD analyses to evaluate both the mechanical and hemodynamic impact of stent deployment within a coronary artery are then discussed.

3.2 Structural Analyses

One of the first studies to evaluate the deployment of a stent within a coronary artery using CS analyses was carried out by Auricchio et al. in 2001 [50]. In this study, the angioplasty balloon was neglected and the investigated stent resembled the Palmaz-Schatz stent (Johnson & Johnson, New Brunswick, NJ, USA). Initially, the coronary artery was neglected and the free-deployment of the stent was simulated through the application of a uniform pressure load upon its inner surface. In the context of stent analysis, the term free-deployment refers to the deployment of the stent without any outside impedance, i.e. neglecting the interaction between the stent and the coronary artery. Following the completion of the free-deployment analysis, a large amount of over-dilation was observed at the extremities of the investigated stent. In order to address this issue, a number of additional struts were added to the extremities of the

investigated stent. The deployment of the modified stent was then simulated within an idealised cylindrical model of a coronary artery that featured a symmetric plaque at its mid-section. The mechanical behaviour of the plaque and artery was described using hyperelastic material models that were fit to experimental data reported in the literature. Following the completion of the analysis, the performance of the modified stent was evaluated in terms of its deployed configuration and various deployment characteristics, such as the rate of radial recoil and longitudinal foreshortening, were also reported. Although the distribution of stress predicted within the coronary artery was not discussed, this study was one of the first to adopt CS analyses to investigate the deployment of a stent within an atherosclerotic coronary artery.

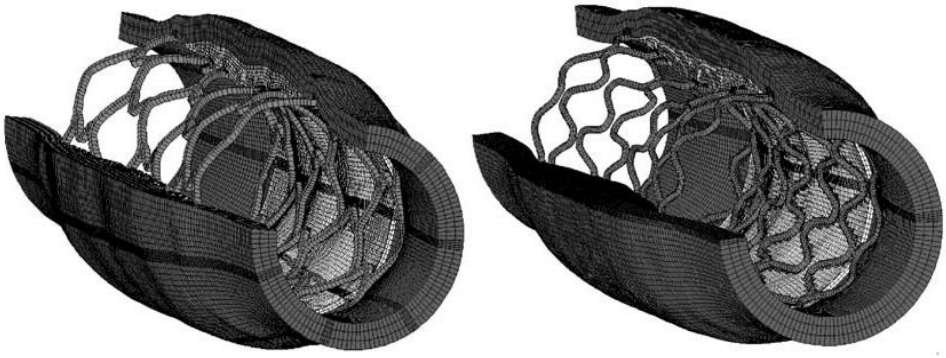

Figure 3.1: Deployment of the NIR stent (left) and the S7 AVE stent (right) within an idealised cylindrical model of an atherosclerotic coronary artery, as described by Lally et al. [51]**.**

In 2005, Lally et al. employed CS analyses to compare the mechanical impact of two different stents within an idealised model of an atherosclerotic coronary artery [51]. In this study, the angioplasty balloon was neglected and the two investigated stents resembled the S7 AVE stent (Medtronic, Minneapolis, MN, USA) and the NIR stent (Boston Scientific, Natick, MA, USA). The coronary artery was then modelled as a straight cylindrical vessel that featured a symmetric plaque at its mid-section and the mechanical behaviour of the plaque and the artery was described using hyperelastic material models that were fit to experimental data reported in the literature. Both of the stents were modelled in an expanded configuration and their deployment within the artery was simulated using a two-stage loading strategy. During the first stage of the analyses, contact between the stent and the artery was deactivated and the artery was dilated to a nominal diameter through the application of a uniform pressure load upon its inner surface. As shown in Figure 3.1, the contact between the stent and the artery was then reactivated and the uniform pressure load was gradually reduced to a

value that corresponded with mean blood pressure. Following the completion of the analyses, the mechanical impact of the investigated stents was evaluated in terms of the stress distribution predicted within the artery. Comparing the results, the volume of the artery subjected to relatively high stresses (≥ 4 MPa) was much higher for the NIR stent (21%) than for the S7 AVE stent (4%). As a much higher rate of in-stent restenosis was also observed with the NIR stent (19%) than with the S7 AVE stent (10%) in two clinical trials, the authors concluded that the proposed methodology successfully predicted certain aspects of the clinical performance of the investigated stents. This study was one of the first to employ CS analyses in order to compare the mechanical impact of two different stents within a coronary artery.

In a similar study that was carried out by Holzapfel et al. in 2005, CS analyses were employed to compare the mechanical impact of three different stents within a realistic model of an atherosclerotic iliac artery [52]. In this study, the angioplasty balloon was neglected and the investigated stents resembled the NIROYAL Elite stent (Boston Scientific), the Inflow-Gold stent (Boston Scientific) and the Multilink Tetra stent (Abbott Laboratories, Abbott Park, IL, USA). High-resolution magnetic resonance images were then used to generate a realistic model of an atherosclerotic external iliac artery and the mechanical behaviour of the various components within both the plaque and the artery was described using hyperelastic material models that were each fit to experimental data reported in the literature. During the analyses, the deployment of the stent was simulated through the application of a uniform pressure load upon its inner surface. In order to simulate the physiological loading situation, a uniform pressure load that corresponded with mean blood pressure and an axial pre-stretch of 1.05 were applied to the artery. Following the completion of the analyses, the mechanical impact of the three investigated stents was evaluated in terms of the intimal pressure distribution and, as shown in Figure 3.2, the stress distribution that was predicted in the artery. Comparing the results, the peak values of both intimal pressure and stress were observed with the Inflow Gold stent whereas the lowest values were observed with the Multilink Tetra stent. As a significantly higher rate of in-stent restenosis was also observed with the Inflow-Gold stent (50%) than with the Multilink Tetra stent (20%) in two individual clinical trials, it was concluded that the proposed methodology successfully predicted aspects of the clinical performance of the investigated stents. A parametric analysis was also carried out to evaluate the

influence of cell geometry, strut thickness and radial mismatch upon the mechanical impact of each of the investigated stents. Following the completion of the parametric analysis, it was noted that the various geometrical modifications generally lead to an improved performance with one of the stents, but little improvement with the others. For example, reducing the strut thickness at the extremities of the stents reduced the intimal pressure and stresses observed with the NIR stent but had little influence on the intimal pressure and stresses observed with the other stents. As such, no attempt was made to generalise the results of the parametric analysis. This study was one of the first to employ CS analyses to compare the mechanical impact of three different stents within a realistic model of an atherosclerotic coronary artery.

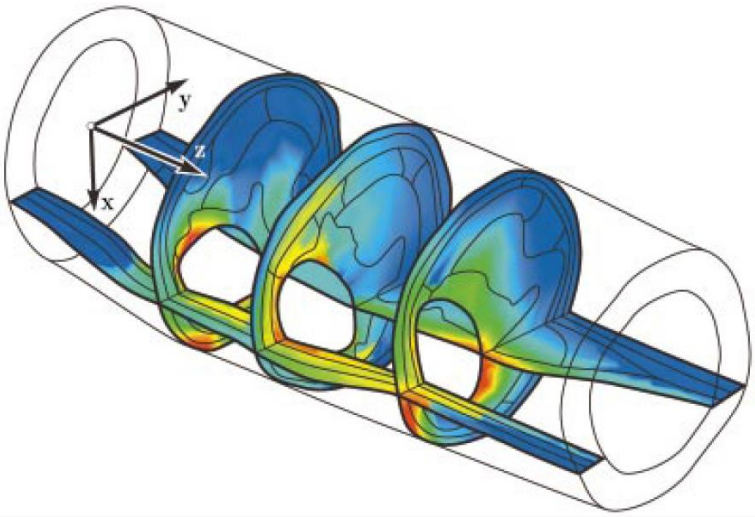

Figure 3.2: Stress distribution predicted within a realistic, patient-derived model of an atherosclerotic external iliac artery following the deployment of the Multilink Tetra stent, as described by Holzapfel et al. [52]**.**

In 2006, Bedoya et al. employed CS analyses to compare the mechanical impact of eight similar stents within an idealised model of a coronary artery [53]. In this study, the angioplasty balloon was neglected and a parametric model of a generic stent, that resembled the Multilink stent (Abbott Laboratories), was employed to generate eight similar stent models by varying the axial strut spacing, the axial ring amplitude and the radius of curvature at each of the crowns. The coronary artery was then modelled as a straight cylindrical vessel and its mechanical behaviour was described using a hyperelastic material model that was fit to experimental data derived from porcine carotid tissue. During the analyses, the deployment of each stent was simulated using a two-stage loading strategy. During the first stage of the analyses, the investigated stent was positioned outside of the artery and the artery was then dilated to a nominal

diameter through the application of a uniform pressure load upon its inner surface. During the second stage of the analyses, the stent was positioned within the artery and the uniform pressure load was reduced to a value that corresponded with mean blood pressure. Following the completion of the analyses, the mechanical impact of the investigated stents was then evaluated in terms of the stress distribution predicted within the artery. Comparing the results, the highest stresses were predicted within the artery following the deployment of stents that featured low axial strut spacing and low axial ring amplitudes. Based upon the results, the authors concluded that stents that feature both high axial strut spacing and a high axial ring amplitudes are likely to be less susceptible to in-stent restenosis within a clinical setting. Although this study provides an excellent insight into the relationship between the geometrical properties of the investigated stent and the mechanical impact within the artery, the conclusions of the study are somewhat limited as the corresponding hemodynamic influence of the various geometrical modifications was not considered.

A year later in 2007, Kiousis et al. used CS analyses to compare the mechanical impact of three similar stents within a realistic model of an atherosclerotic external iliac artery [54]. In this study, the angioplasty balloon was modelled as a membrane and a parametric model of a generic stent was employed to generate three different stent models by varying the strut width and the sinusoidal length of the stent cells. A realistic model of an atherosclerotic artery was then generated using high-resolution magnetic resonance images of a human atherosclerotic external iliac artery and the mechanical behaviour of the components of the plaque and the artery was described using hyperelastic material models that were each fit to experimental data reported in the literature. During the analyses, the deployment of the investigated stent was then simulated through the application of a uniform pressure load upon the inner surface of the angioplasty balloon. Following the deployment of each stent, the deflation of the angioplasty balloon was simulated by reducing the penalty parameter that was used to enforce the contact constraint between the stent and the angioplasty balloon. Following the completion of the analyses, the mechanical impact of the investigated stents was evaluated in terms of the contact forces predicted within the intima and, as shown in Figure 3.3, the stress distribution predicted within the artery. Comparing the results, reducing the strut width from 0.14 to 0.10 mm significantly reduced the intimal contact forces and the stress distribution predicted within the artery. As such,

the authors concluded that stents which feature narrow struts are likely to be less susceptible to in-stent restenosis within a clinical setting. Again, although this study provides an excellent insight into the relationship between the geometrical properties of the investigated stent and its mechanical impact within the artery, the conclusions of the study are somewhat limited as the corresponding hemodynamic influence of the various geometrical modifications was not considered.

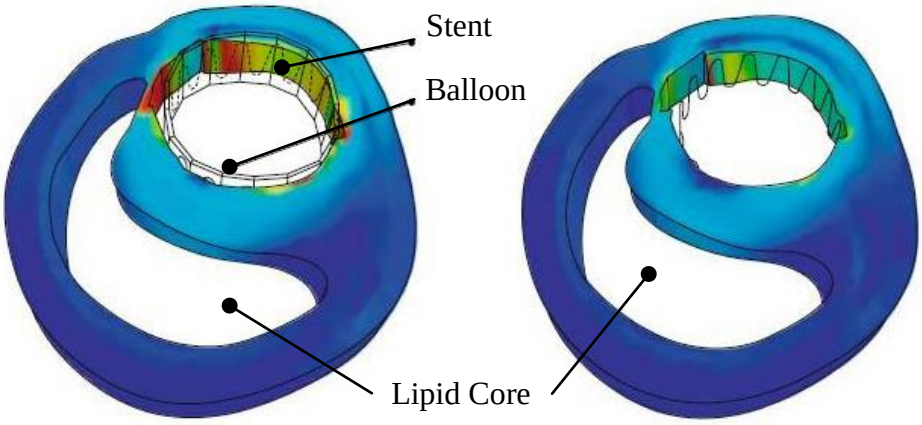

Figure 3.3: Stress distribution predicted within a realistic, patient-derived model of an atherosclerotic external iliac artery following the deployment (left) and recoil (right) of the Express stent, as described by Kiousis et al. [54]**.**

In 2008, Gervaso et al. used CS analyses to evaluate the influence of three different loading strategies on the mechanical impact of stent deployment within an idealised model of a coronary artery [55]. In this study, the investigated stent resembled the BX-Velocity stent (Johnson & Johnson) and the coronary artery was modelled as a straight cylindrical vessel. The artery was partitioned into three individual layers that represented the intima, media and adventitia and the mechanical behaviour of each layer was described using hyperelastic material models that were fit to experimental data reported in the literature. As shown in Figure 3.4, the deployment of the stent was simulated using a uniform pressure load, displacement control and a model of an angioplasty balloon during the three analyses. Adopting the first loading strategy, the deployment of the stent within the artery was simulated through the application of a uniform pressure load upon its inner surface. Adopting the second loading strategy, the angioplasty balloon was approximated using a rigid surface and the deployment of the stent within the artery was then simulated using displacement control. Finally, adopting the third loading strategy, the angioplasty balloon was modelled as a thin membrane and the deployment of the stent within the artery was simulated through

the application of a uniform pressure load upon the inner surface of the angioplasty balloon. Following the completion of the analyses, the influence of the three loading strategies upon the mechanical impact of the investigated stent was then evaluated in terms of the stress distribution predicted within the artery. Comparing the results, the radial and circumferential stress distributions predicted within the artery were found to vary significantly for the three different loading strategies. As a result, the authors concluded that a model of the angioplasty balloon should be included in CS analyses of balloon-expandable stents to ensure that the stress distribution predicted within the artery is accurately described. This study highlighted the important influence of the angioplasty balloon in CS analyses of balloon-expandable stents.

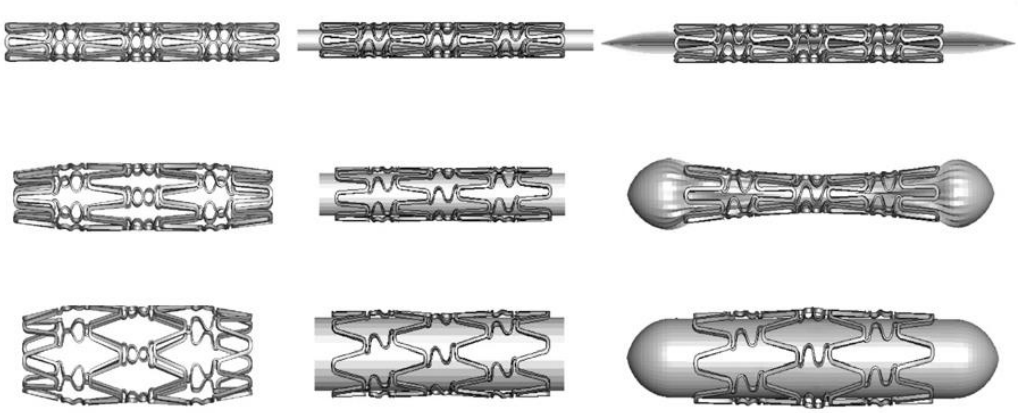

Figure 3.4: Free-deployment of the BX-Velocity stent simulated using a uniform pressure load (left), displacement control (middle) and a realistic model of an angioplasty balloon (right), as described by Gervaso et al. [55]**.**

In 2010, Gastaldi et al. employed CS analyses to compare the mechanical impact of sequential and simultaneous post-dilation after stent deployment within an idealised model of an atherosclerotic coronary bifurcation [56]. In this study, the angioplasty balloon was modelled as a thin membrane and the investigated stent resembled the BX-Velocity stent (Johnson & Johnson). The artery was then modelled as a straight cylindrical vessel that featured three symmetric plaques and a 70° bifurcation at its mid-section. The artery was partitioned into three individual layers that represented the intima, media and adventitia and the mechanical behaviour of the plaque and the components of the artery was described using hyperelastic material models that were fit to experimental data reported in the literature. A yield stress was also specified to account for plaque rupture during the analyses. In order to evaluate the mechanical impact of the sequential and simultaneous post-dilation strategies, two analyses were

carried out. During the analyses, the stent was first deployed within the main branch through the application of a uniform pressure load upon the inner surface of the angioplasty balloon. The sequential and simultaneous post-dilation strategies were then simulated through the sequential and simultaneous inflation of two additional angioplasty balloon models within both the side and main branches, respectively. Following the completion of the analyses, the mechanical impact of the post-dilation strategies was evaluated in terms of the stress distribution predicted within the artery. Comparing the results, a greater portion of the coronary bifurcation was subjected to high stresses following simultaneous post-dilation than sequential post-dilation. As a result, it was concluded that the sequential post-dilation strategy should be preferred to the simultaneous post-dilation strategy following stent deployment in a coronary bifurcation. This study was one of the first to employ CS analyses to investigate stent deployment strategies within an atherosclerotic coronary bifurcation.

In the same year, Mortier et al. adopted CS analyses to compare the mechanical impact of three different stents within a realistic, patient-derived model of a coronary bifurcation [57]. In this study, the three investigated stents resembled the Endeavor stent (Medtronic), the Cypher Select stent (Johnson & Johnson) and the Liberté stent (Boston Scientific) and a realistic model of a balloon-tipped catheter was generated that included the guide wire, the catheter shaft and the folded angioplasty balloon. A realistic model of a coronary bifurcation was also generated using data obtained from a rotational angiography procedure that was performed within a human left coronary artery. The artery was divided into three individual layers that represented the intima, media and adventitia and the mechanical behaviour of the components of the artery was described using hyperelastic material models that were fit to experimental data reported in the literature. As shown in Figure 3.5, the deployment of the stents was simulated through the application of a uniform pressure load upon the inner surface of the angioplasty balloon. Following the completion of the analyses, the mechanical impact of the investigated stents was then evaluated in terms of the stress distribution predicted in the artery. Comparing the results, the maximum circumferential stress predicted within the artery was higher for the Cypher Select stent (0.30 MPa) than for either the Endeavor stent (0.15 MPa) or the Liberté stent (0.15 MPa). To evaluate the influence of the geometrical properties of the Cypher Select stent upon the stress distribution predicted within the artery, two additional stent models were generated

by modifying the geometry of the Cypher Select stent. The first of the modified stent models was generated by reducing the overall strut thickness from 1.40 to 1.00 mm whilst the second stent model was generated by reducing the width of two individual strut segments that were located at the extremities of the stent from 1.30 to 0.90 mm. Following their deployment in the coronary bifurcation, both of the modified Cypher Select stents were found to reduce the maximum circumferential stress predicted in the artery. Based upon the results, the authors concluded that both of the modified stents are likely to be less susceptible to in-stent restenosis in a clinical setting than the original Cypher Select stent. Although the geometrical properties of the Cypher Select stent were modified to reduce its mechanical impact within the artery, the conclusions of the study are somewhat limited as the corresponding hemodynamic influence of the proposed geometrical modifications was not considered.

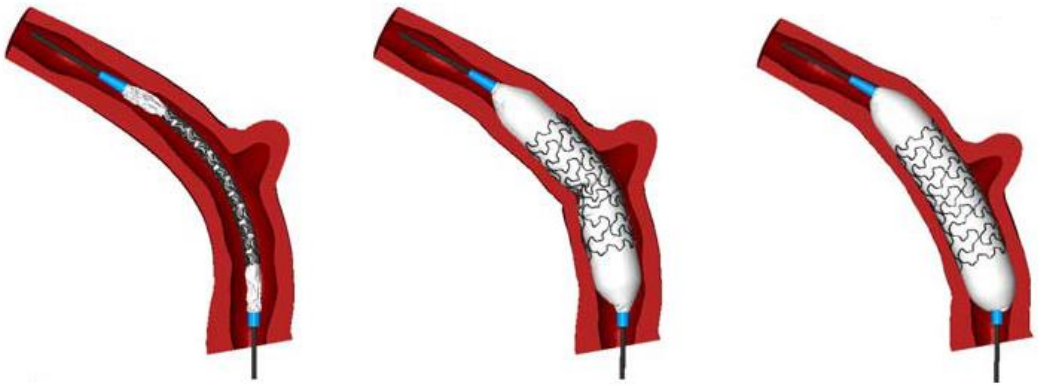

Figure 3.5: Deployment of the Cypher Select stent within a realistic, patient-derived model of a coronary bifurcation using a realistic model of a balloon-tipped catheter, as described by Mortier et al. [57]**.**

A year later in 2012, Conway et al. adopted CS analyses to compare the mechanical impact of two different stents within population-specific models of atherosclerotic coronary arteries [58]. In this study, the investigated stents resembled the Multilink stent (Abbott Laboratories) and the BX-Velocity stent (Johnson & Johnson) and a realistic model of a balloon-tipped catheter was generated that included the guide wire, the catheter shaft and the folded angioplasty balloon. The artery was modelled as a straight cylindrical vessel and three separate models were generated by varying the severity of the occlusion. The first model of the artery did not include a plaque whilst the second and third models featured asymmetric plaques at their mid-section that resulted in 50% and 60% occlusions, respectively. The arteries were divided into

three individual layers that represented the intima, media and adventitia and the mechanical behaviour of the plaque and the components of the artery was described using hyperelastic material models that were fit to experimental data reported in the literature. A yield stress was also specified to account for plaque rupture during the analyses. As shown in Figure 3.6, the deployment of the two investigated stents was simulated through the application of a uniform pressure load upon the inner surface of the angioplasty balloon. Following the completion of the analyses, the mechanical impact of the investigated stents was then evaluated in terms of the stress distribution predicted within the artery. Comparing the results, a higher portion of the intima was subjected to stresses that exceeded its ultimate tensile strength with the BX-Velocity stent than with the Multilink stent within the arteries that included no plaque and the 60% occlusion. Conversely, a higher portion of the intima was subjected to stresses that exceeded its ultimate tensile strength with the Multilink stent than with the BX-Velocity stent within the artery that included the 50% occlusion. Based upon these results, it was concluded that the severity of the occlusion is likely to have a major influence upon the performance of a stent within a clinical setting. This study was one of the first to demonstrate the critical influence of the atherosclerotic plaque in CS analyses of coronary stent deployment. This concludes the discussion of previous studies that have employed CS analyses to investigate the mechanical impact of stent deployment. An extensive review of the literature is presented in Table 3.1.

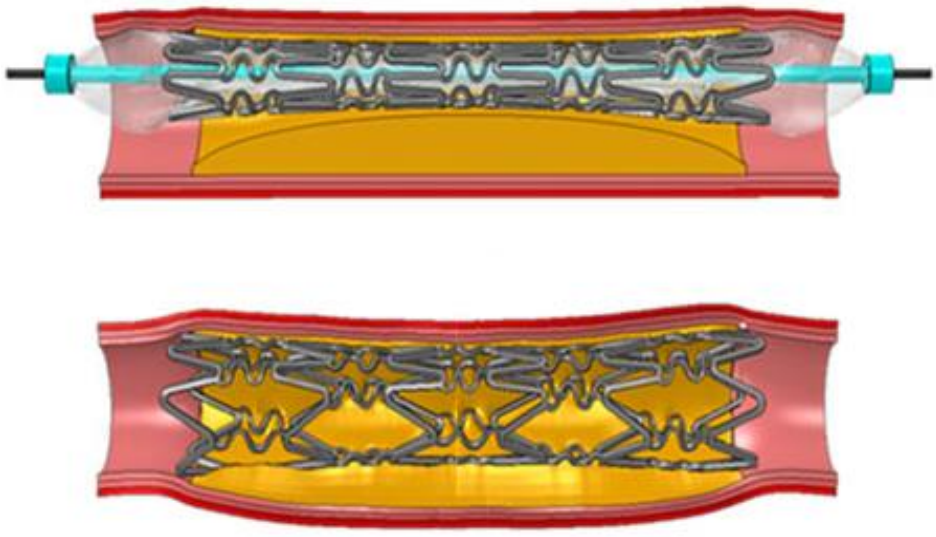

Figure 3.6: Deployment of the BX-Velocity stent within an idealised model of an atherosclerotic coronary artery using a realistic model of a balloon-tipped catheter, as described by Conway et al. [58]**.**

Year	Author	Title
1999	Rogers et al. [59]	Balloon-artery interactions during stent placement: a finite element analysis approach to pressure, compliance, and stent design as contributors to vascular injury.
2001	Auricchio et al. [50]	Finite-element analysis of a stenotic artery revascularization through a stent insertion.
2003	Prendergast et al. [60]	Analysis of prolapse in cardiovascular stents: A constitutive equation for vascular tissue and finite-element modelling.
2004	Chua et al. [61]	Finite element simulation of slotted tube (stent) with the presence of plaque and artery by balloon expansion.
2004	Migliavacca et al. [62]	Stainless and shape memory alloy coronary stents: a computational study on the interaction with the vascular wall.
2005	Holzapfel et al. [52]	Changes in the mechanical environment of stenotic arteries during interaction with stents: Computational assessment of parametric stent designs.
2005	Lally et al. [51]	Cardiovascular stent design and vessel stresses: A finite element analysis.
2005	Liang et al. [63]	Finite element analysis of the implantation of a balloon-expandable stent in a stenosed artery.
2006	Bedoya et al. [53]	Effects of stent design parameters on normal artery wall mechanics.
2007	Kiousis et al. [54]	A numerical model to study the interaction of vascular stents with human atherosclerotic lesions.
2007	Takashima et al. [64]	Simulation and experimental observation of contact conditions between stents and artery models.
2007	Timmins et al. [65]	Stented artery biomechanics and device design optimization.
2007	Wu et al. [66]	Stent expansion in curved vessel and their interactions: a finite element analysis.

2008	Gervaso et al. [55]	On the effects of different strategies in modelling balloon-expandable stenting by means of finite element method.
2008	Gijsen et al. [67]	Simulation of stent deployment in a realistic human coronary artery.
2009	Capelli et al. [68]	Assessment of tissue prolapse after balloon-expandable stenting: influence of stent cell geometry.
2009	Mortier et al. [69]	Finite element analysis of side branch access during bifurcation stenting.
2009	Pericevic et al. [70]	The influence of plaque composition on underlying arterial wall stress during stent expansion: the case for lesion-specific stents.
2009	Zahadmanesh et al. [71]	Determination of the influence of stent strut thickness using the finite element method: implications for vascular injury and in-stent restenosis.
2010	Early et al. [72]	The role of vessel geometry and material properties on the mechanics of stenting in the coronary and peripheral arteries.
2010	Gastaldi et al. [56]	Modelling of the provisional side-branch stenting approach for the treatment of atherosclerotic coronary bifurcations: Effects of stent positioning.
2010	Gu et al. [73]	The relation between the arterial stress and restenosis rate after coronary stenting.
2010	Mortier et al. [57]	A novel simulation strategy for stent insertion and deployment in curved coronary bifurcations: comparison of three drug-eluting stents.
2010	Zahadmanesh et al. [74]	Simulation of a balloon expandable stent in a realistic coronary artery: Determination of the optimum modelling strategy.
2012	Conway et al. [58]	A computational test-bed to assess coronary stent implantation mechanics using a population-specific approach.
2012	Gu et al. [75]	Arterial wall mechanics and clinical implications after coronary stenting: Comparisons of three stent designs.

Table 3.1: CS analyses carried out to evaluate the mechanical impact of stent deployment within a coronary artery.

3.3 Fluid Dynamics Analyses

One of the first studies to investigate the hemodynamic impact of stent deployment within a coronary artery using CFD analyses was carried out by LaDisa et al. in 2003 [76]. In this study, the coronary artery was modelled as a straight cylindrical vessel and the investigated stent resembled the Palmaz-Schatz stent (Johnson & Johnson). In order to evaluate the hemodynamic impact of stent deployment within the artery, a CFD model of an unstented coronary artery was also generated. Using these models, steady-state analyses were then carried out to simulate both maximum and minimum flow conditions within a canine left anterior descending coronary artery. Following the completion of the analyses, the hemodynamic impact of stent deployment within the coronary artery was evaluated by comparing the WSS distribution predicted upon the luminal surface of the stented artery to that predicted upon the luminal surface of the unstented artery. Comparing the results, stent deployment was found to have a significant influence upon the WSS distribution predicted upon the luminal surface of the artery. Specifically, the WSS distribution predicted upon the luminal surface of the unstented artery was highly uniform whereas the WSS distribution predicted upon the luminal surface of the stented artery was highly non-uniform. In the stented artery, regions of high WSS were observed upon the surface of the stent struts whilst regions of low WSS were observed both proximal and distal to the struts and were most pronounced in regions where the strut was orientated perpendicular to the main flow direction. Based upon these results, it was concluded that stent deployment is likely to have a significant influence on the hemodynamic environment in a coronary artery. This study was one of the first to employ CFD analyses in order to investigate the hemodynamic impact of stent deployment within a coronary artery.

In a similar study that was carried out by LaDisa et al. in 2004, CFD analyses were employed to compare the hemodynamic impact of five similar stents within an idealised model of a coronary artery [77]. Again, the investigated stent resembled the Palmaz-Schatz stent (Johnson & Johnson) and the coronary artery was modelled as a straight cylindrical vessel. Five similar stent models were generated by varying the number of longitudinal cells, the strut width and the strut thickness. Steady-state analyses were then carried out to simulate mean flow conditions within a canine left anterior descending coronary artery. Following the completion of the analyses, the hemodynamic impact of the investigated stents was evaluated in terms of the WSS

distribution predicted upon the luminal surface of the artery. Comparing the results, the use of both fewer longitudinal cells and thinner struts was found to reduce the percentage of the luminal surface that was subject to lower than physiological levels of WSS (< 0.5 Pa). The use of thinner struts also resulted in a marginal reduction in the percentage of the luminal surface that was subject to elevated spatial gradients of WSS (> 0.2 Pa/mm). Based upon the results, the authors concluded that stents which feature both a low number of longitudinal cells and a low strut thickness are likely to be less susceptible to in-stent restenosis within a clinical setting. Again, although the results of this study provide an excellent insight into the relationship between the geometrical properties of the investigated stent and the hemodynamic impact within the artery, the conclusions are somewhat limited as the corresponding mechanical influence of the various geometrical modifications was not considered.

In 2005, LaDisa et al. employed CFD analyses to investigate the influence of circumferential vascular deformation upon the hemodynamic environment within an idealised model of a stented coronary artery [78]. In this study, the investigated stent resembled the Palmaz-Schatz stent (Johnson & Johnson) and the coronary artery was modelled as a straight cylindrical vessel. To evaluate the influence of circumferential vascular deformation upon the hemodynamic environment within the stented artery, four different CFD models were generated by varying both the configuration of the stent and the cross-section of the artery. Specifically, two different stent models were generated by varying the number of longitudinal cells and two different arteries were also considered by specifying either a cylindrical or a polygonal longitudinal cross-section. The cylindrical cross-section was typical of that observed within idealised models of stented coronary arteries whilst the polygonal cross-section was designed to account for arterial straightening between neighbouring struts. Steady-state and transient analyses were carried out to simulate mean and pulsatile flow conditions within a canine left anterior descending coronary artery, respectively. Following the completion of the analyses, the influence of circumferential vascular deformation on the hemodynamic environment within the stented arteries was then evaluated by comparing the WSS distribution predicted upon the luminal surface of the polygonal arteries to that predicted on the luminal surface of the cylindrical arteries. As shown in Figure 3.7, the inclusion of the circumferential vascular deformation increased the percentage of the luminal surface that was subject to both lower than physiological

levels of WSS (< 0.5 Pa) and elevated spatial gradients of WSS (> 0.2 Pa/mm). This was particularly evident for the stent that featured fewer longitudinal cells. Based on the results, the authors concluded that both stent and vessel deformation are likely to exert an important influence upon the hemodynamic environment within the artery. This study was one of the first to demonstrate the important influence of both stent and vessel deformation in CFD analyses of stented vessel hemodynamics.

Figure 3.7: WSS distribution predicted upon the luminal surface of two stented coronary arteries that featured circular (top) and polygonal (bottom) cross-sections, as described by LaDisa et al. [78]**.**

In 2005, He et al. employed CFD analyses to compare the hemodynamic impact of four similar stents within an idealised model of a coronary artery [79]. In this study, a parametric model was used to generate eight similar models of a stented artery by varying the axial strut spacing, the axial ring amplitude, the radius of curvature at the individual stent crowns and the presence/absence of a longitudinal link element. For simplicity, only two neighbouring struts were considered for each of the investigated stents and the domain was assumed to be flat. In order to justify the use of the flat domain, the authors noted that the stent strut thickness was negligible compared to that of the domain. Transient analyses were carried out through the specification of a sinusoidal inlet velocity that corresponded to a heart rate of approximately 70 beats per minute. Following the completion of the analyses, the hemodynamic impact of the investigated stents was then evaluated in terms of the WSS distribution predicted upon the luminal surface of the artery. Comparing the results, the average mean WSS that was predicted between the neighbouring stent struts was increased by 42% when the axial strut spacing was increased from 1.80 to 3.60 mm. Additionally, the

percentage restoration of the axial WSS for each of the stents that neglected the longitudinal link element was as much as 11% greater than that observed with the stents that included the link element. Although flow recirculation was prominent in regions where the stent struts were aligned perpendicular to the main flow direction, varying the axial ring amplitude and the radius of curvature at the crowns did not lead to any beneficial effects. Based on the results, the authors concluded that stents which minimise the use of longitudinal link elements and maximise both the axial strut spacing and strut alignment with the main flow direction are likely to be less susceptible to in-stent restenosis in a clinical setting. Again, although the results of this study provide an excellent insight into the relationship between the geometrical properties of the investigated stent and the hemodynamic impact within the artery, the conclusions of the study are somewhat limited as the corresponding mechanical influence of the various geometrical modifications was not considered.

In 2008, Bolassino et al. employed both CS and CFD analyses to compare the hemodynamic impact of four different stents within a realistically-deformed model of an atherosclerotic coronary artery [80]. In this study, the four investigated stents resembled the BX-Velocity stent (Johnson & Johnson), the Carbostent stent (Sorin Biomedica, Saluggia, Italy), the Palmaz-Schatz stent (Johnson & Johnson) and the Jostent Flex stent (Jomed, Helsingborg, Sweden) and, to simplify the analyses, only a single unit from each stent was considered. The coronary artery was modelled as a straight cylindrical vessel that included a symmetric plaque at its mid-section and was partitioned into three individual layers that represented the intima, media and adventitia. Initially, CS analyses were carried out to simulate the deployment of the investigated stents within the coronary artery. During these analyses, the mechanical behaviour of both the plaque and the components of the artery was described using hyperelastic material models that were each fit to experimental data reported in the literature. The deployment of the investigated stents within the coronary artery was then simulated using a realistic model of an angioplasty balloon. As shown in Figure 3.8, the deformed configuration of the stent and the artery was then used to generate a realistically-deformed model of the stented coronary lumen. For each of the stents, transient CFD analyses were carried out to simulate pulsatile flow conditions within a canine left anterior descending coronary artery. Following the completion of these analyses, the hemodynamic impact of the investigated stents was evaluated in terms

of the WSS distribution predicted upon the luminal surface of the artery. Comparing the results, almost 30% of the luminal surface of the artery was subject to lower than physiological levels of WSS (< 0.5 Pa) during peak flow conditions for each of the investigated stents. An additional analysis was also carried out in which the strut thickness of the Jostent Flex stent was increased from 0.5 to 1.5 mm to evaluate the influence of strut thickness on the hemodynamic impact of the stent. Following, the completion of this analysis, the increase in strut thickness resulted in a reduction in the percentage of the luminal surface that was subjected to lower than physiological levels of WSS (< 0.5 Pa). In conclusion, the authors were unable to identify general geometrical modifications that might improve the clinical performance of the stents. It was noted, however, that the distance between the link elements and struts should be minimised to ensure that a uniform WSS distribution is achieved. Although the mechanical impact of the investigated stents was not discussed, this study was one of the first to employ CS and CFD analyses to evaluate the hemodynamic environment within realistically-deformed models of stented coronary arteries.

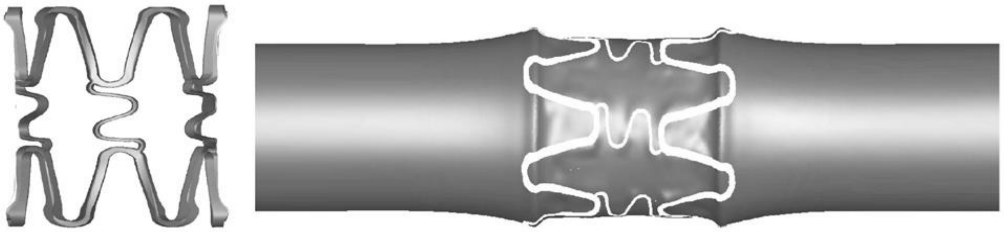

Figure 3.8: Generation of a realistically-deformed CFD model of a stented coronary lumen, as described by Bolassino et al. [80]**.**

In 2010, Pant et al. employed CFD analyses to assess the influence of strut and link configuration upon the hemodynamic impact of stent deployment within an idealised model of a coronary artery [81]. In this study, the investigated stents resembled the NIR stent (Boston Scientific), the BX-Velocity stent (Cordis, Johnson & Johnson), the BioMatrix stent (Biosensors Interventional, Kampong, Singapore), the ART stent (Arterial Remodelling Technologies, Noisy-le-Roi, France) and the Multilink Zeta stent (Abbott Laboratories) and, in order to simplify the analyses, only a symmetric section of each of the investigated stents was considered. The coronary artery was modelled as a straight cylindrical vessel and, to evaluate the hemodynamic influence of strut and link configuration, the investigated stents were each assigned a diameter

of 3 mm, a length of 8 mm, a strut width of 0.05 mm and a strut thickness of 0.10 mm. Transient analyses were carried out to simulate pulsatile flow conditions in a human left anterior descending coronary artery and, following the completion of the analyses, the hemodynamic impact of the investigated stents was then evaluated in terms of a hemodynamic low and reverse flow index (HLRFI). The HLRFI was introduced by the authors in order to evaluate the percentage of the luminal surface that was subject to either low (< 0.5 Pa) or negative WSS during the transient cycle. Comparing the results, the HLRFI was marginally higher for the BioMatrix stent (24.9%) than for the Multilink Zeta stent (24.4%), the NIR stent (22.6%), the BX-Velocity stent (21.9%) and the ART stent (18.8%). In order to further evaluate the hemodynamic impact of strut and link configuration, an additional analysis was also carried out in which the cross-flow length of the link elements of the NIR stent was varied. Following the completion of these analyses, the HLRFI decreased quite significantly as the cross-flow length of the link elements was reduced. As a result, it was concluded that stents which minimise the cross-flow length of the link elements are likely to be less susceptible to in-stent restenosis in a clinical setting. It should be noted, however, that the corresponding mechanical influence of varying the cross-flow length of the link elements of the NIR stent was not considered.

In 2010, Murphy et al. employed CFD analyses to compare the hemodynamic impact of three different stents within an idealised model of a coronary artery [82]. In this study, the three investigated stents resembled the BX-Velocity stent (Johnson & Johnson), the Palmaz-Schatz stent (Johnson & Johnson) and the Gianturco-Roubin II stent (Cook Inc., Bloomington, IN, USA) and the coronary artery was modelled as a straight cylindrical vessel. Transient analyses were carried out to simulate pulsatile flow conditions in a human left anterior descending coronary artery and, as shown in Figure 3.9, the hemodynamic impact of the stents was then evaluated in terms of the WSS distribution predicted upon the luminal surface of the artery. Both a common threshold methodology and a comprehensive statistical methodology were employed to interpret the hemodynamic impact of each stent. Comparing the results using the threshold methodology, the percentage of the luminal surface that was subject to low WSS (< 0.5 Pa) was much greater for the BX-Velocity stent (49.5%) than for either the Gianturco-Roubin II stent (32.3%) or the Palmaz-Schatz stent (22.4%) whilst the percentage of the luminal surface that was subjected to elevated spatial gradients of

WSS (> 0.2 Pa/mm) was marginally higher for the BX-Velocity stent (98.9%) than for either the Palmaz-Schatz stent (97.6%) or the Gianturco-Roubin II stent (97.4%). Comparing the results using the comprehensive statistical methodology, the area-averaged mean WSS was found to be much lower for the BX-Velocity stent (0.52 Pa) than for either the Palmaz-Schatz stent (0.76 Pa) or the Gianturco-Roubin II stent (0.76 Pa) whilst the area-averaged mean spatial gradient of WSS was much higher for the Gianturco-Roubin II stent (1.63 Pa/mm) than for either the BX-Velocity stent (1.05 Pa/mm) or the Palmaz-Schatz stent (0.94 Pa/mm). Based on the results, it was concluded that the threshold methodology may not be capable of fully-elucidating the hemodynamic impact of the investigated stents. As such, the authors identified the statistical methodology as a more effective method of analysis. This study was one of the first to employ a comprehensive statistical method of analysis to interpret the hemodynamic impact of stent deployment within a coronary artery.

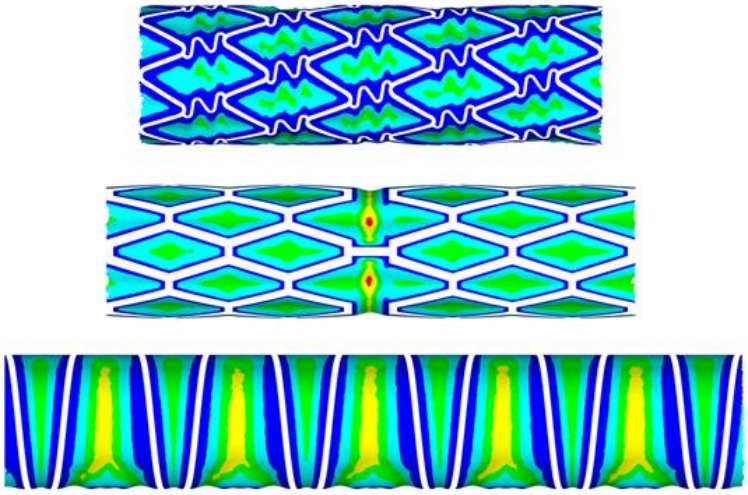

Figure 3.9: WSS distribution predicted upon the luminal surface of the artery for the BX-Velocity stent (top), the Palmaz-Schatz stent (middle) and the Gianturco-Roubin II stent (bottom), as described by Murphy et al [82]**.**

In 2012, Gundert et al. employed both CFD aalyses and an optimisation procedure to identify an optimal number of circumferentially-repeating stent cells for three similar stents [83]. In this study, the investigated stent resembled the Palmaz-Schatz stent (Johnson & Johnson) and the coronary artery was modelled as a straight cylindrical vessel. Transient analyses were carried out to simulate pulsatile flow conditions in a canine left anterior descending coronary artery and the results were then evaluated in terms of the time-averaged WSS distribution that was predicted within the centre of

the artery. Using an automated optimisation procedure, the geometry of the stent was then modified to identify the number of circumferential stent cells that minimised the difference between the WSS predicted at the centre of the artery and the theoretical WSS within the unstented region of the artery. The optimisation procedure was used to identify the optimal number of circumferential cells for a generic slotted-tube stent that featured three different intrastrut areas and were deployed in both small arteries and large arteries. For example, the identification of the optimal number of cells for a stent with intrastrut area of 1 and 2 mm^2 within 2.25 mm diameter arteries is shown in Figure 3.10. Comparing the results, the optimal number of circumferential cells was found to increase in the larger artery for all stents with a similar intrastrut area. Additionally, when the intrastrut angle was included in the optimisation process, the optimal angle was found to lie between 38.5 and 46° for each stent. This indicates that the optimal intrastrut angle is largely independent of vessel size and intrastrut area. Based on the results, it was concluded that stents which feature an intrastrut angle of 40° are likely to be less susceptible to in-stent restenosis in a clinical setting. It should be noted that the corresponding mechanical influence of the geometrical modifications was not considered. This concludes the discussion of previous studies that have employed CFD analyses to investigate the hemodynamic impact of stent deployment. An extensive review of the literature is presented in Table 3.2.

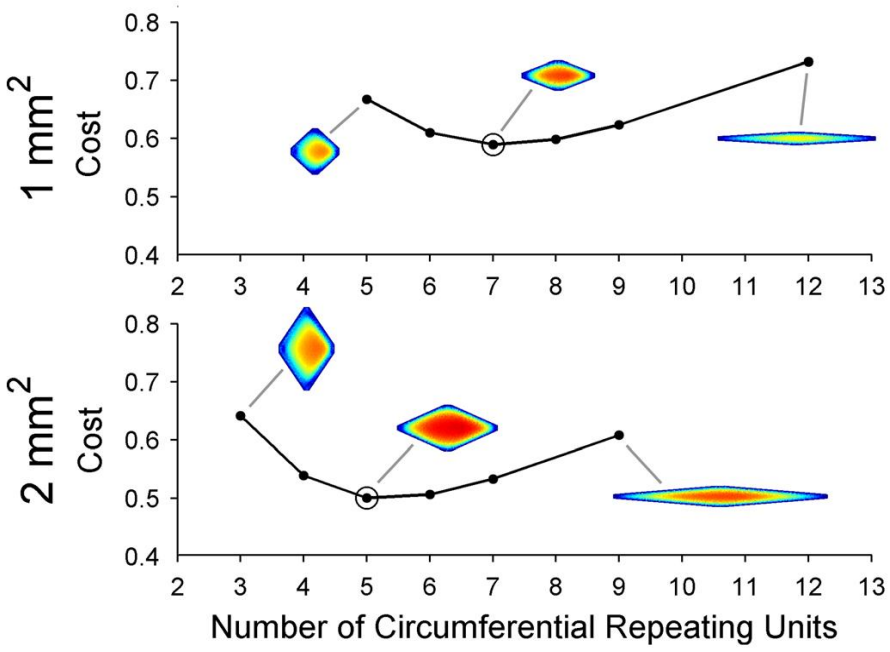

Figure 3.10: Optimisation results for stents with a 1 mm^2 (top) and 2 mm^2 (bottom) intrastrut area, as described by Gundert et al. [83]**.**

Year	Author	Title
2003	LaDisa et al. [76]	Three-dimensional computational fluid dynamics modelling of alterations in coronary wall shear stress produced by stent implantation.
2004	LaDisa et al. [77]	Stent design properties and deployment ratio influence indexes of wall shear stress: a three-dimensional computational fluid dynamics investigation within a normal artery.
2005	He et al. [79]	Blood flow in stented arteries: A parametric comparison of strut design patterns in three dimensions.
2005	LaDisa et al. [84]	Axial stent strut angle influences wall shear stress after stent implantation: Analysis using 3D computational fluid dynamics models of stent foreshortening.
2005	LaDisa et al. [85]	Alterations in wall shear stress predict sites of neointimal hyperplasia after stent implantation in rabbit iliac arteries.
2005	LaDisa et al [78]	Circumferential vascular deformation after stent implantation alters wall shear stress evaluated with time-dependent 3D computational fluid dynamics models.
2005	Seo et al. [86]	Computational study of fluid mechanical disturbance induced by endovascular stents.
2006	LaDisa et al. [87]	Alterations in regional vascular geometry produced by theoretical stent implantation influence distributions of wall shear stress: analysis of a curved coronary artery using 3D computational fluid dynamics modelling.
2006	Rajamohan et al. [88]	Developing pulsatile flow in a deployed coronary stent.
2007	Banerjee et al. [89]	Developed pulsatile flow in a deployed coronary stent.
2007	Faik et al. [90]	Time-dependent 3D simulations of the hemodynamics in a stented coronary artery.

2008	Balossino et al. [80]	Effects of different stent designs on local hemodynamics in stented arteries.
2008	Dehlaghi et al. [91]	Effect of stent geometry on phase shift between pressure and flow waveforms in stented human coronary artery.
2008	Dehlaghi et al. [92]	Analysis of wall shear stress in stented coronary artery using 3D computational fluid dynamics modelling.
2009	Chen et al. [93]	Effects of stent sizing on endothelial and vessel wall stress: potential mechanisms for in-stent restenosis.
2009	Duraiswamy et al. [94]	Comparison of near-wall hemodynamic parameters in stented artery models.
2010	Murphy et al. [95]f	A full-range, multi-variable CFD-based methodology to identify abnormal near-wall hemodynamics in a stented coronary artery.
2010	Murphy et al. [82]	A numerical methodology to fully elucidate the altered wall shear stress in a stented vessel.
2010	Pant et al. [81]	The influence of strut-connectors in stented vessels: a comparison of pulsatile flow through five coronary stents.
2010	Williams et al. [96]	Local hemodynamic changes caused by main branch stent implantation and subsequent virtual side branch balloon angioplasty in a representative coronary bifurcation.
2011	Elwein et al. [97]	Optical coherence tomography for patient-specific 3D artery reconstruction and evaluation of wall shear stress in a left circumflex coronary artery.
2012	Chen et al. [98]	Impact of main branch stenting on endothelial shear stress: role of side branch diameter, angle and lesion.
2012	Chiastra et al. [99]	Computational fluid dynamics of stented coronary bifurcations studied with a hybrid discretisation method.
2012	Gundert et al. [83]	Optimisation of cardiovascular stent design using computational fluid dynamics.

Table 3.2: CFD analyses carried out to evaluate the hemodynamic impact of stent deployment within a coronary artery.

3.4 Structural and Fluid Dynamics Analyses

In 2009, Zunino et al. employed both CS and CFD analyses to investigate the drug release from a drug-eluting stent [100]. In this study, the investigated stent resembled the BX-Velocity stent (Johnson & Johnson) and, in order to simplify the analyses, only a single repeating unit of the stent was considered. The artery was modelled as a straight cylindrical vessel that was divided into three distinct layers that represented the intima, media and adventitia. A CS analysis was first carried out to simulate the deployment of the stent within the coronary artery and, following the completion of this analysis, the deformed configuration of both the stent and the artery was used to create a realistically-deformed model of the stented coronary lumen. A steady-state CFD analysis was then carried out to simulate mean flow conditions within a human coronary artery. To evaluate the drug-release from the stent, both the continuity and momentum equations were coupled with a set of advection-diffusion equations. As drug release from the stent takes place through both advection within the lumen and diffusion within the artery, a splitting algorithm was used to separate the advection-diffusion equations into a sequence of independent problems which were then solved in a stepwise manner. Following the completion of the analysis, both the mechanical and hemodynamic impact of the stent was discussed and, as shown in Figure 3.11, the drug release from the stent within the lumen and the artery was also evaluated. Although the primary aim of this study was to investigate the drug release from the investigated stent, this study was one of the first to employ CS and CFD analyses to evaluate both the mechanical and hemodynamic impact of a coronary stent.

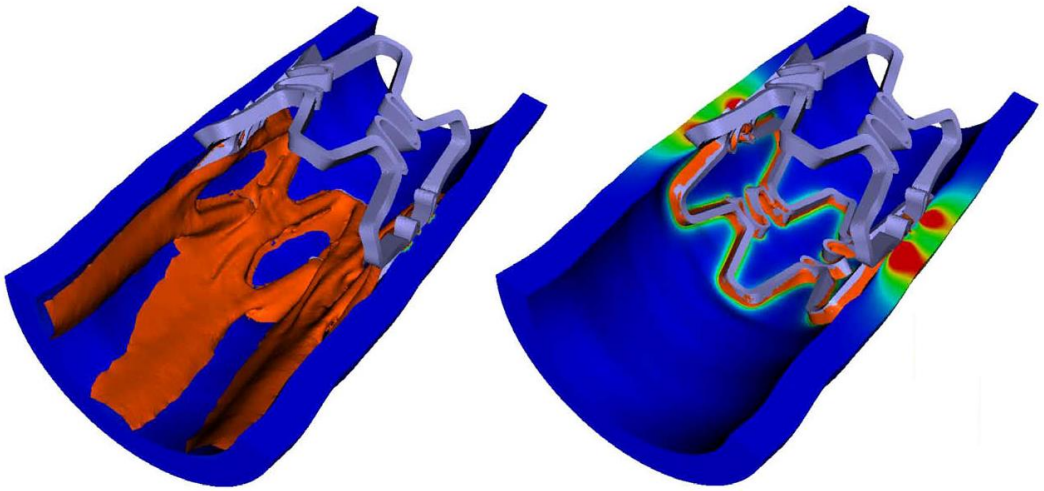

Figure 3.11: Drug-release within the lumen (left) and the artery wall (right) from a drug-eluting coronary stent, as described by Zunino et al. [100]**.**

In 2011, Pant et al. employed CS and CFD analyses to perform a multi-disciplinary multi-objective design optimisation of a balloon-expandable coronary stent [101]. A parametric model of a stent, which resembled the BX-Velocity stent (Johnson & Johnson), was employed to create 15 similar stent models by varying the axial strut spacing, the circumferential strut spacing and the cross-flow length of the individual link elements. Initially, a set of CS analyses were carried out to assess the flexibility of the crimped stents. A second set of CS analyses were then carried out to simulate the deployment of each stent within a straight cylindrical model of a coronary artery that featured a symmetric plaque at its mid-section. Following the completion of these analyses, the deformed configurations of the stent and the artery were used to generate realistically-deformed models of the stented coronary lumen. Using these models, transient CFD analyses were then carried out in order to simulate pulsatile flow conditions within a human left anterior descending coronary artery. As shown in Figure 3.12, a set of steady-state CFD analyses were also carried out to investigate the drug release from each stent within the lumen and the artery wall. During these steady-state analyses, the continuity and momentum equations were coupled with a set of advection-diffusion equations and the governing equations were then solved as a heat transfer problem due to the similarity of the two types of analyses.

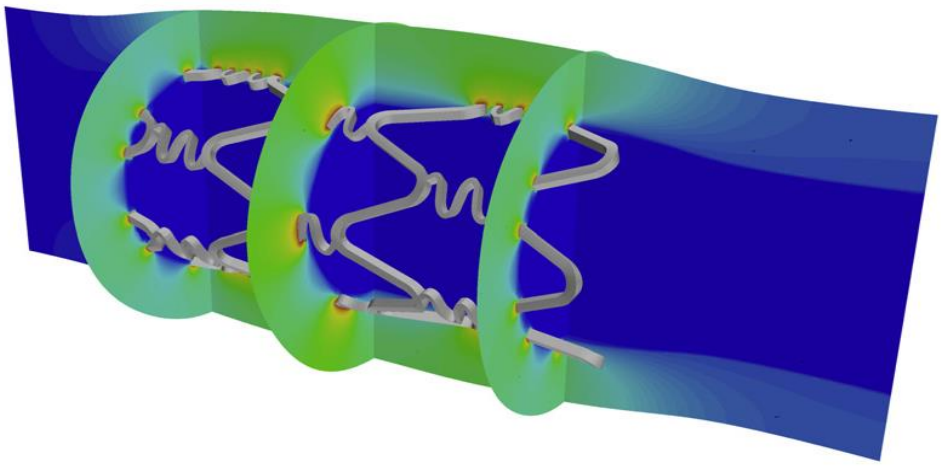

Figure 3.12: Steady-state drug concentration predicted within both the artery wall and the lumen, as described by Pant et al. [101]**.**

Following the completion of the various analyses, the performance of each stent was evaluated in terms of six objective indices which characterised the flexibility of the stent, the radial recoil of the stent, the stress distribution within the artery, the WSS

distribution upon the luminal surface of the artery, the drug concentration within the artery and drug distribution within the artery. Following the calculation of each of the indices, an initial surrogate model was generated using Kriging. The initial Krigs were searched using a non-dominated genetic sorting algorithm in order to obtain an initial Pareto front and, to improve the initial Krigs, an update process was carried out in which five update points were selected uniformly along the predicted Pareto front. Following the analysis of the five update points, the Krigs were reconstructed and the non-dominated sorting algorithm was employed to search the updated Krigs to obtain an improved Pareto front. The update process was then repeated in order to obtain a sample distribution of thirty design points. Following the completion of the optimisation procedure, various clear trade-offs were identified for the six objective indices. The clear trade-offs were each discussed and the authors proposed a number of selection paradigms for identifying the optimum stent configuration from the non-dominated designs. This study was one of the first to employ CS and CFD analyses to optimise the configuration of a balloon-expandable coronary stent.

In the same year, Morlacchi et al. employed CS and CFD analyses to investigate the mechanical and hemodynamic impact of simultaneous post-dilation following stent deployment in an atherosclerotic coronary bifurcation [102]. In this study, the investigated stent resembled the Multilink Vision stent (Abbott Laboratories) and the coronary bifurcation was modelled as a straight cylindrical vessel that included both a symmetric plaque and a 45° bifurcation at its mid-section. Initially, a CS analysis was carried out in which a realistic model of an angioplasty balloon was employed to simulate the deployment of the investigated stent within the main branch. As shown in Figure 3.13, two additional CS analyses were then carried out in order to simulate post-dilation using both a conventional cylindrical model of an angioplasty balloon and a novel tapered model of an angioplasty balloon. Following the completion of the analyses, the deformed configurations of the stent and the coronary bifurcation were used to generate realistically-deformed models of the stented coronary lumen. Transient CFD analyses were then carried out to simulate pulsatile flow conditions within a human left anterior descending coronary artery. Following the completion of both the CS and CFD analyses, both the mechanical and hemodynamic impact of simultaneous post-dilation using the cylindrical and tapered post-dilation angioplasty balloons were evaluated in terms of the stress distribution predicted within the artery

and the WSS distribution predicted on the luminal surface of the artery, respectively. Comparing the results, the maximum stress predicted within the coronary bifurcation was dramatically higher for the cylindrical angioplasty balloon (214 kPa) than for the tapered angioplasty balloon (127 kPa). Furthermore, a marginally higher percentage of the luminal surface of the artery was subject to lower than physiological levels of time-averaged WSS (< 0.5 Pa) for the cylindrical angioplasty balloon (79%) than for the tapered angioplasty balloon (71%). Based on the results, the authors concluded that the tapered angioplasty balloon is likely to promote less neointimal hyperplasia than the cylindrical angioplasty balloon following simultaneous post-dilation within a coronary bifurcation. This study was one of the first to employ both CS and CFD analyses to investigate the mechanical and hemodynamic impact of stent deployment procedures within an atherosclerotic coronary bifurcation.

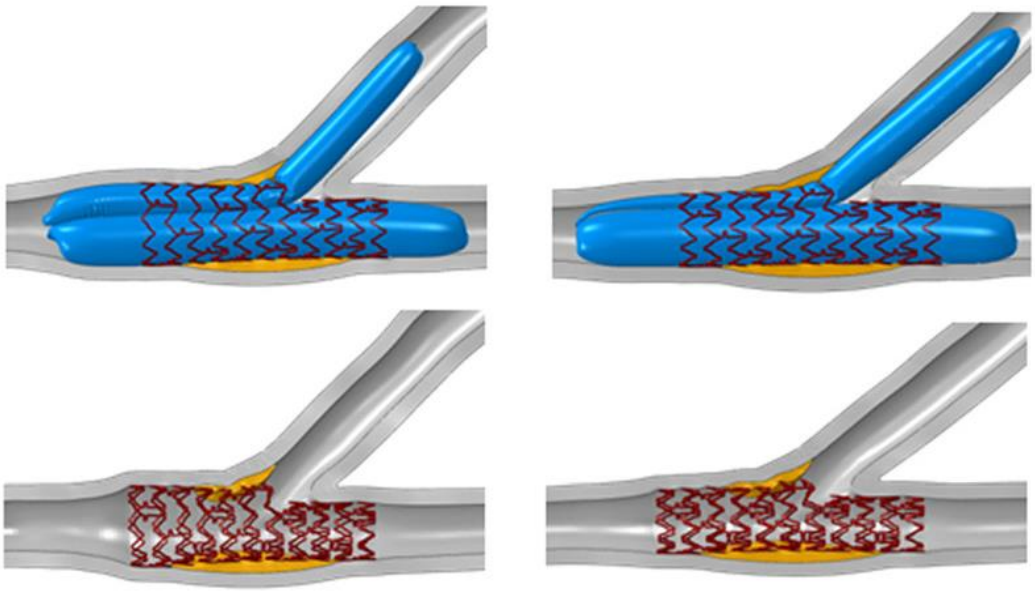

Figure 3.13: Simultaneous post-dilation using a cylindrical (left) and a tapered (right) angioplasty balloon, as described by Morlacchi et al. [102]**.**

3.5 Summary

To date, a large number of studies have employed CS and CFD analyses to evaluate either the mechanical or hemodynamic impact of stent deployment within a coronary artery. In many of these studies, the computational results are employed to identify potential geometrical modifications that may improve the clinical performance of the investigated stents. In the majority of these studies, however, the fact that in-stent restenosis has been linked to both arterial injury and altered vessel hemodynamics is neglected and, as a result, it is possible that the proposed geometrical modifications

may actually hinder the clinical performance of the investigated stents. In many CS analyses of coronary stent deployment, for example, geometrical modifications that are likely to reduce the mechanical impact of the investigated stents are suggested. As these studies focus solely upon the mechanical impact of the investigated stents, however, the corresponding hemodynamic impact of the recommended geometrical modifications is neglected. Similarly, in CFD analyses of coronary stent deployment, geometrical modifications which are likely to reduce the hemodynamic impact of the investigated stents are generally recommended. As these studies focus exclusively on the hemodynamic impact of the investigated stents, however, the corresponding mechanical impact of the recommended geometrical modifications is neglected. As in-stent restenosis has been strongly linked to both arterial injury and altered vessel hemodynamics, the sequential analysis of the mechanical and hemodynamic impact of stent deployment should provide an improved indication of stent performance. Despite this observation, however, very few numerical studies have considered both the mechanical and hemodynamic impact of stent deployment.

In the few numerical studies that have considered both the mechanical and hemodynamic impact of coronary stent deployment, only a single stent (or a single repeating unit) was considered in the analyses. Furthermore, both the mechanical and hemodynamic impact of the investigated stents were typically evaluated in terms of variables such as the maximum stress predicted within the artery and the percentage of the luminal surface subject to lower than physiological levels of WSS (< 0.5 Pa). Although these variables are useful in interpreting the mechanical and hemodynamic impact of the investigated stents, they may cloud aspects of stent performance. The maximum stress predicted within the artery, for example, is typically representative of a small region and may not adequately describe the impact of the stent upon the mechanical environment within the artery. In a similar fashion, one stent may subject a portion of the luminal surface to WSS values of 0.01 Pa whilst another stent may subject an identical portion of the luminal surface to WSS values of 0.49 Pa. Based upon these results, the first stent is likely to be more susceptible to in-stent restenosis within a clinical setting, but this cannot be determined by calculating the percentage of the luminal surface that is subject to WSS values below a threshold of 0.5 Pa. In the following chapter, a robust numerical methodology is presented for evaluating the performance of coronary stents in terms of their mechanical and hemodynamic

impact within the coronary artery. To ensure that the mechanical and hemodynamic impact of the investigated stent is fully elucidated, the methodology employs a range of different variables and a comprehensive statistical method of analysis.

CHAPTER 4
METHODOLOGY

4.1 Introduction

In this chapter, a novel numerical methodology for evaluating the performance of balloon-expandable coronary stents is presented. The proposed methodology is split into two stages. In the first stage, a CS model of the investigated stent is generated and a CS analysis is then carried out to simulate its deployment within a coronary artery. In the second stage, the results of the CS analysis are employed to generate a realistically-deformed CFD model of the stented lumen and a transient CFD analysis is carried out to simulate pulsatile flow in a left anterior descending coronary artery. Following the completion of the analyses, the mechanical impact of the investigated stent is evaluated in terms of the stress distribution predicted within the artery whilst the hemodynamic impact of the stent is evaluated in terms of the WSS distribution predicted upon the luminal surface of the artery. To ensure that both the mechanical and hemodynamic impact of the investigated stent is fully elucidated, the results of the analyses are evaluated using several mechanical and hemodynamic variables of interest and a comprehensive statistical method of analysis. In the following sections, the features of the CS and the CFD analyses are first presented and the calculation of both the variables of interest and the statistical measures is then discussed.

4.2 Structural Analysis

In the first stage of the proposed numerical methodology, a CS analysis is carried out in order to simulate the deployment of the investigated stent within a coronary artery. This CS analysis is carried out using the commercial finite element analysis package ABAQUS. In order to perform the CS analysis, a number of crucial pre-processing tasks must first be carried out. First, realistic CS models of the investigated stent, the

coronary artery and the balloon-tipped catheter are generated and the mechanical behaviour of each component is described through the specification of appropriate constitutive material models. A variety of boundary and loading conditions are then defined to simulate the deployment of the stent and a number of solver controls are specified to ensure that an accurate solution is obtained in a timely manner. Each of these pre-processing tasks is described in detail in the following sections.

4.2.1 Geometry and Discretisation

In order to generate a CS model of the investigated stent, a planar geometrical model of a single repeating unit cell is first generated in ABAQUS/CAE. The repeating unit cell is then copied in the longitudinal and transverse directions to generate a planar geometrical model of the entire stent. The planar stent model is then extruded by the appropriate strut thickness and discretised into a structured finite element mesh of reduced-integration continuum elements (C3D8R) based upon the results of a mesh convergence study that is presented in Appendix A. Following the discretisation of the planar stent model, a cylindrical finite element model of the investigated stent is generated by transforming the nodal coordinates of the planar mesh from a Cartesian to a cylindrical coordinate system. As shown in Figure 4.1, this procedure effectively wraps the planar mesh into a cylindrical mesh. The coincident nodes are then merged to generate a continuous cylindrical CS model of the investigated stent.

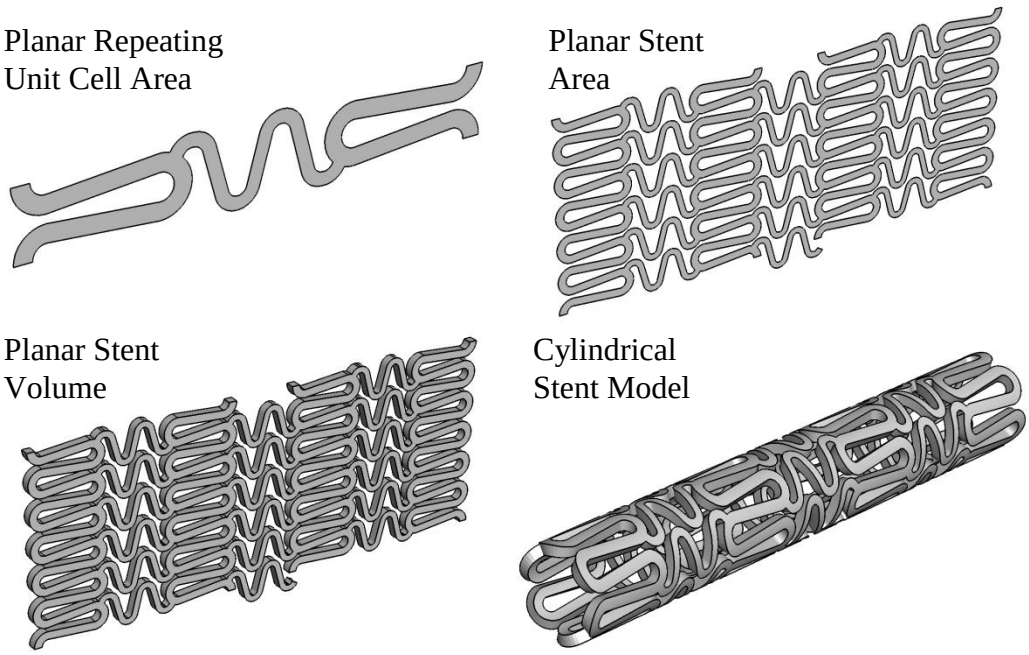

Figure 4.1: Generation of a detailed CS model of a coronary stent.

During the CS analysis, the deployment of the investigated stent is evaluated using a realistic model of a balloon-tipped catheter. The configuration of the balloon-tipped catheter resembles that of the Raptor balloon-tipped catheter (Johnson & Johnson) and includes a guide wire, a catheter shaft and a tri-folded angioplasty balloon. The guide wire is modelled as a straight cylinder and is assigned a length of 18.5 mm and a diameter of 0.2 mm. The catheter shaft is modelled as a straight cylindrical shaft and is assigned a length of 17.5 mm and internal and external diameters of 0.2 and 0.5 mm, respectively. As shown in Figure 4.2, the angioplasty balloon is modelled as a planar surface that is folded about the catheter shaft in a pleated configuration. The angioplasty balloon is assigned a length of 12 mm, a thickness of 0.2 mm and a folded diameter of 0.8 mm. The guide wire and catheter shaft are discretised using 740 and 13,104 reduced-integration continuum elements (C3D8R), respectively, and the angioplasty balloon is discretised using 12,462 reduced-integration membrane elements (M3D4R). The mesh sizing is based on the results of a mesh convergence study that is presented in Appendix A. Following the discretisation of the guide wire, the catheter shaft and the angioplasty balloon, the nodes located at the extremities of the angioplasty balloon are attached to the catheter shaft using tie constraints. The discretised CS model of the balloon-tipped catheter is shown in Figure 4.3.

To evaluate the mechanical impact of the investigated stent, an idealised model of a coronary artery is also generated. As shown in Figure 4.4, the coronary artery is modelled as a straight cylindrical vessel and assigned a length of 20 mm and internal and external diameters of 2.7 and 4.5 mm, respectively. The artery wall, which has a subsequent thickness of 0.9 mm, is divided into three individual layers that represent the intima, media and adventitia and are assigned thicknesses of 0.24, 0.32 and 0.34 mm, respectively. Both the diameter of the coronary artery and the thicknesses of its constituent layers are adopted from Holzapfel et al., who carried out experimental analyses to assess the average geometrical properties of thirteen different human left anterior descending coronary arteries [103]. The artery is discretised using 70,272 reduced-integration continuum elements (C3D8R) and 17,568, 26,352 and 26,352 continuum elements are used to discretise the intima, the media and the adventitia, respectively. As before, the mesh sizing employed in the discretisation of the artery is based on the results of a mesh convergence study that is presented in Appendix A. The discretised CS model of the coronary artery is shown in Figure 4.5.

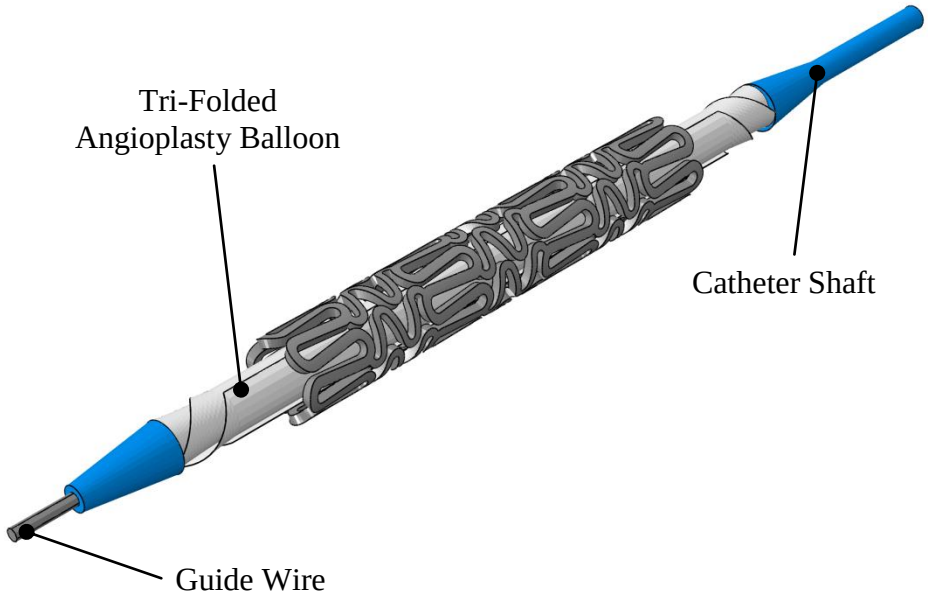

Figure 4.2: Geometry of the balloon-tipped catheter featuring the guide wire, the catheter shaft and angioplasty balloon.

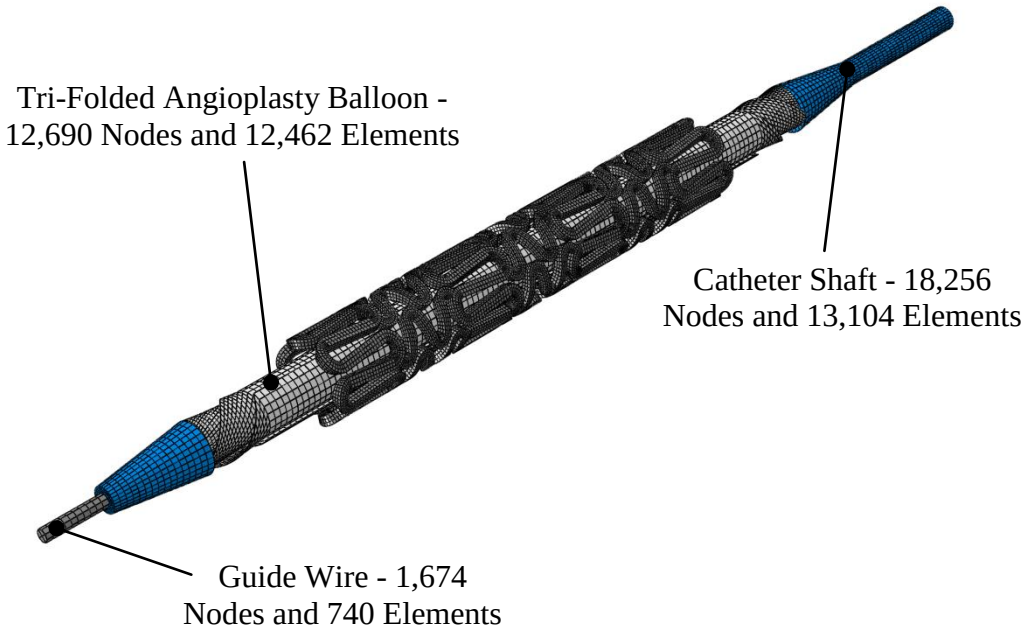

Figure 4.3: Discretised CS model of the balloon-tipped catheter featuring the guide wire, the catheter shaft and the angioplasty balloon.

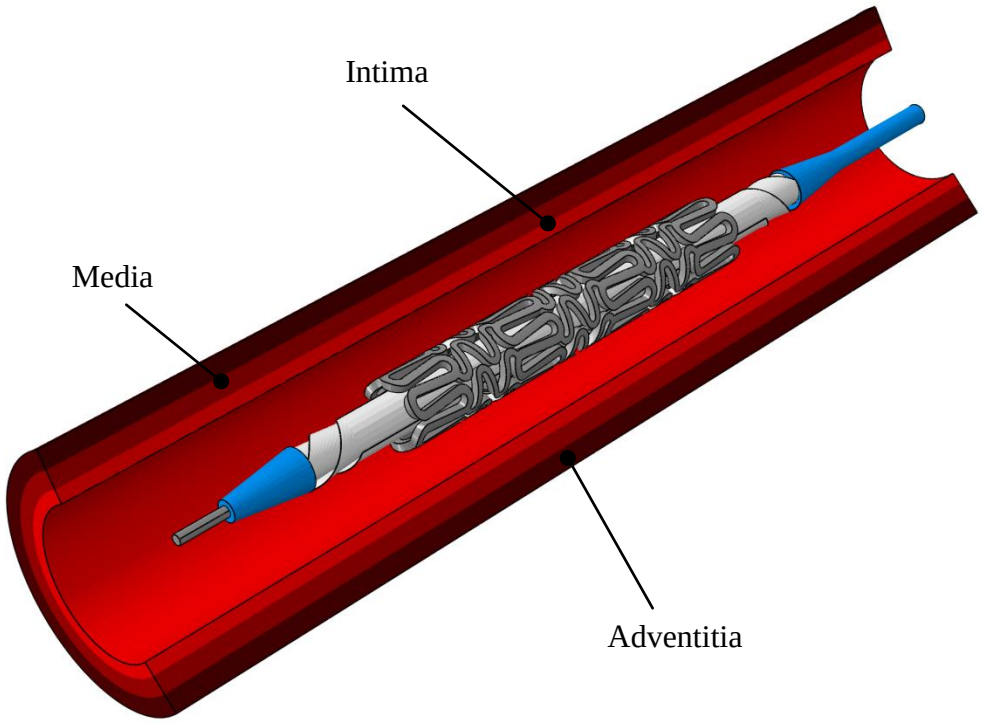

Figure 4.4: Geometrical model of the idealised coronary artery.

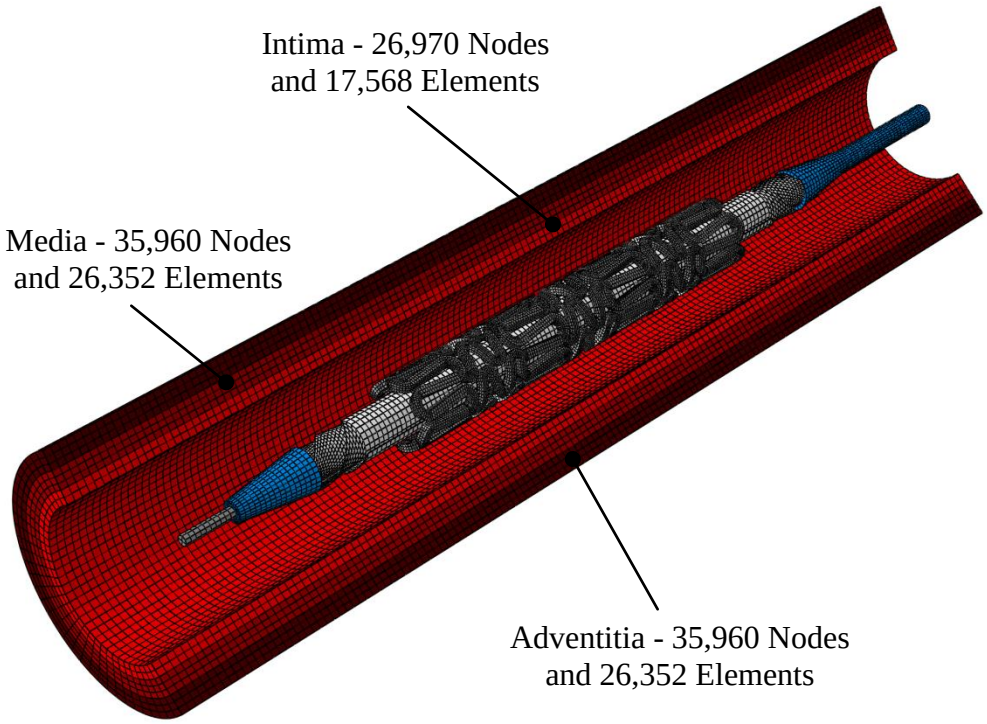

Figure 4.5: Discretised CS model of the idealised coronary artery.

4.2.2 Constitutive Material Models

During coronary stent deployment, the stent undergoes a significant degree of plastic deformation. As such, the mechanical behaviour of the investigated stent is described using a rate-independent elastic-plastic material model with isotropic hardening. In this study, the investigated stent is assumed to be manufactured from medical grade 316L stainless steel, though alternative materials, such as L605 and MP35N cobalt chromium may also be considered. The mechanical data employed to calibrate the rate-independent elastic-plastic material model is adopted from Murphy et al., who carried out uniaxial tension tests on samples of 316L stainless steel stent struts [104]. The initial elastic response of the stent is described using a Young's modulus of 196 GPa and a Poisson's ratio of 0.3. The inelastic plastic response of the stent is then described using a multi-linear function which is characterised by a yield stress of 380 MPa and an ultimate tensile strength of 750 MPa. The stress-strain response of the rate-independent elastic-plastic material model is shown in Figure 4.6.

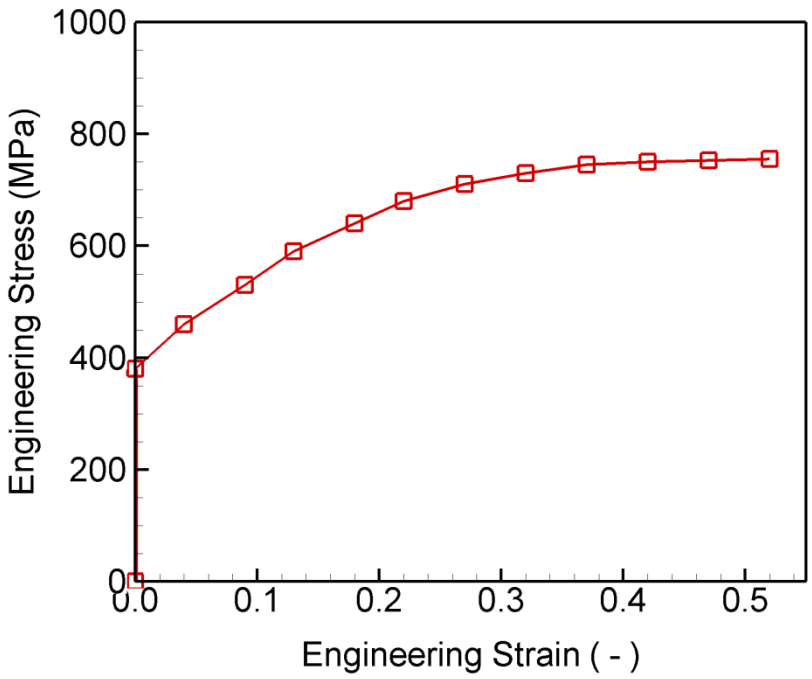

Figure 4.6: Elastic-plastic stress-strain response of the investigated stent.

The guide wire, the catheter shaft and the angioplasty balloon of the Raptor balloon-tipped catheter are manufactured from high-density nitinol, polyethylene and nylon, respectively. In order to simplify the analysis, however, the mechanical behaviour of these components is described using linear elastic material models. The mechanical data used to calibrate the linear elastic material models was adopted from Mortier et

al., who employed a realistic model of the Raptor balloon-tipped catheter to evaluate the mechanical impact of stent deployment within a bifurcated coronary artery [57]. The elastic response of the guide wire, the catheter shaft and the angioplasty balloon is described using a Young's modulus of 62 GPa, 1 GPa and 920 MPa and Poisson's ratio of 0.3, 0.4 and 0.4, respectively. To validate the use of linear elastic material models, a preliminary CS analysis was carried out to investigate the free-deployment of the angioplasty balloon. As shown in Figure 4.7, the predicted pressure-diameter response of the angioplasty balloon was in good agreement with the manufacturer's pressure-diameter compliance data for the Raptor angioplasty balloon [105].

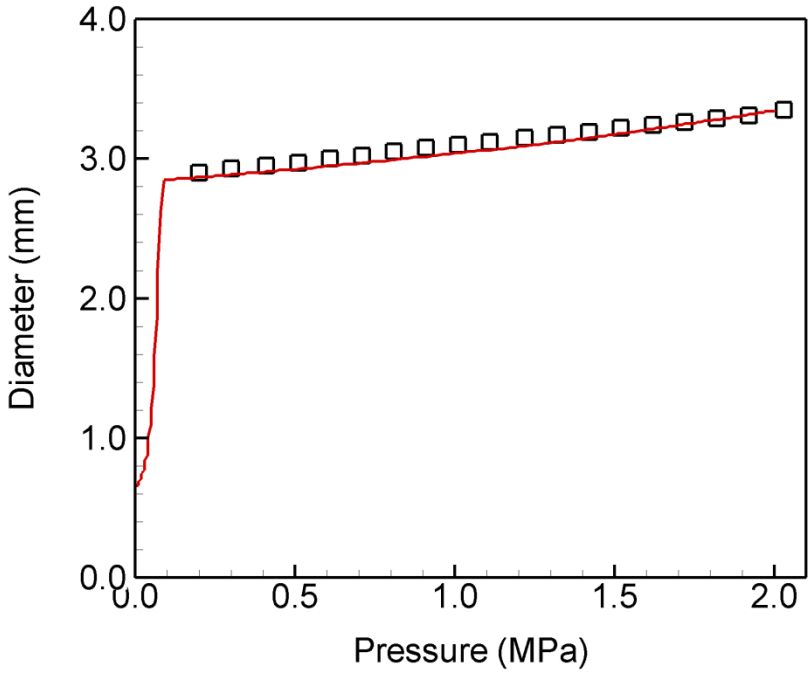

Figure 4.7: Comparison of the pressure-diameter response of the angioplasty balloon (solid line) with the manufacturer's compliance data (data points).

The mechanical behaviour of the coronary arteries is highly nonlinear and is dictated by the elongation of collagen fibres in the artery wall. At low to moderate strains, the collagen fibres assume a loose, crimped configuration and elastin fibres confer a low stiffness to the artery wall. As a result, the initial mechanical response of the artery is almost linear and large increases in strain result in relatively small increases in stress. At moderate to high strains, however, the collagen fibres begin to elongate and align with one another in the direction of loading. These collagen fibres are much stiffer than the elastin fibres and, as such, the mechanical response of the coronary artery becomes progressively stiffer such that small increases in strain result in relatively

large increases in stress. In order to account for the nonlinear response of the artery, the mechanical behaviour of the intima, the media and the adventitia was described using third-order Ogden hyperelastic material models. The third-order Ogden strain energy function is written in terms of the principal stretches as follows:

$$W = \sum_{i=1}^{n} \frac{2\mu_i}{\alpha_i}\left(\lambda_1^{\alpha_i} + \lambda_2^{\alpha_i} + \lambda_3^{\alpha_i} - 3\right) + \sum_{i=1}^{n} \frac{1}{D_i}(J-1)^{2i} \qquad (4.1)$$

The terms μ_i, α_i and D_i denote the individual hyperelastic material constants, λ_1, λ_2 and λ_3 denote the three principal stretches and J denotes the Jacobian determinant. The mechanical data used to define the three hyperelastic material models is adopted from Holzapfel et al., who carried out uniaxial tension tests upon circumferentially-orientated samples of intimal, medial and adventitial tissue [103]. The hyperelastic material models were fit to the appropriate experimental data using the curve-fitting tool in ABAQUS/CAE and the hyperelastic material constants that provided the best fit with the experimental data are presented in Table 4.1. As shown in Table 4.1, the intima, media and adventitia were each assumed to be nearly-incompressible through the specification of relatively small values for D_1 and zero for D_2 and D_3. In order to validate the accuracy of the hyperelastic material models, preliminary CS analyses were carried out to evaluate the uniaxial stress-strain response of a single continuum element. As shown in Figure 4.8, the response of the fitted hyperelastic material models was in good agreement with the respective experimental data.

Constant	Intima	Media	Adventitia
μ_1	-6.22 MPa	-1.67 MPa	-1.95 MPa
μ_2	3.84 MPa	1.04 MPa	1.18 MPa
μ_3	2.17 MPa	0.64 MPa	0.79 MPa
α_1	23.91	23.17	24.60
α_2	24.53	23.45	25.00
α_3	22.68	23.62	23.88
D_1	0.78	4.35	3.88
D_2	0	0	0
D_3	0	0	0

Table 4.1: Hyperelastic material constants used to describe the mechanical behaviour of the intima, the media and the adventitia.

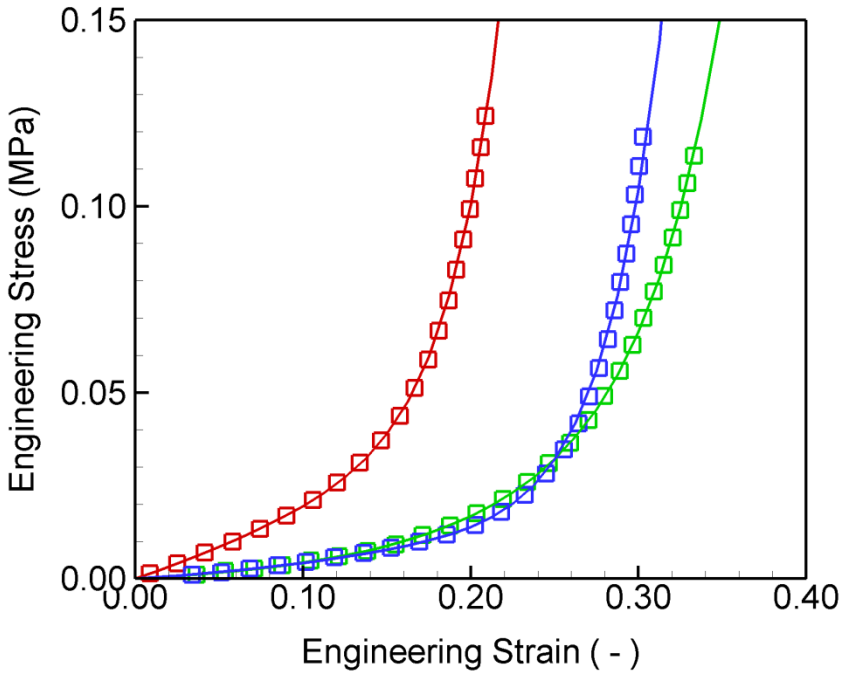

Figure 4.8: Comparison of the fitted hyperelastic material models (solid lines) with the experimental stress-strain data (data points) for the intima (red), the media (green) and the adventitia (blue).

4.2.3 Boundary and Loading Conditions

In order to simulate the deployment of the investigated stent in the coronary artery, a uniform pressure load is applied to the inner surface of the angioplasty balloon. As shown in Figure 4.9, the magnitude of the pressure load is first increased until the stent achieves a nominal diameter of 3.00 mm and then decreased to a value of -0.10 MPa to allow the stent and the artery to recoil. The nominal diameter of 3.00 mm is employed to ensure that the investigated stent achieves a stent-to-artery deployment ratio of 1.1:1, which is derived with respect to the unstented diameter of the coronary artery (2.70 mm) and is typical of current clinical procedures. Due to variations in the geometrical configuration of coronary stents, the magnitude of the pressure load required to achieve a deployment ratio of 1.1:1 varies from one stent to another. As such, a number of preliminary CS analyses are carried out to identify the magnitude of the pressure load required to achieve a deployment ratio of 1.1:1 with the specific stent. In order to prevent rigid-body motion during the CS analysis, the nodes located at the extremities of the guide wire and the coronary artery are fully-constrained and a small number of nodes located at the mid-section of the stent are constrained in the circumferential and longitudinal directions. This prevents rigid-body motion without inhibiting the deployment of the angioplasty balloon or the stent.

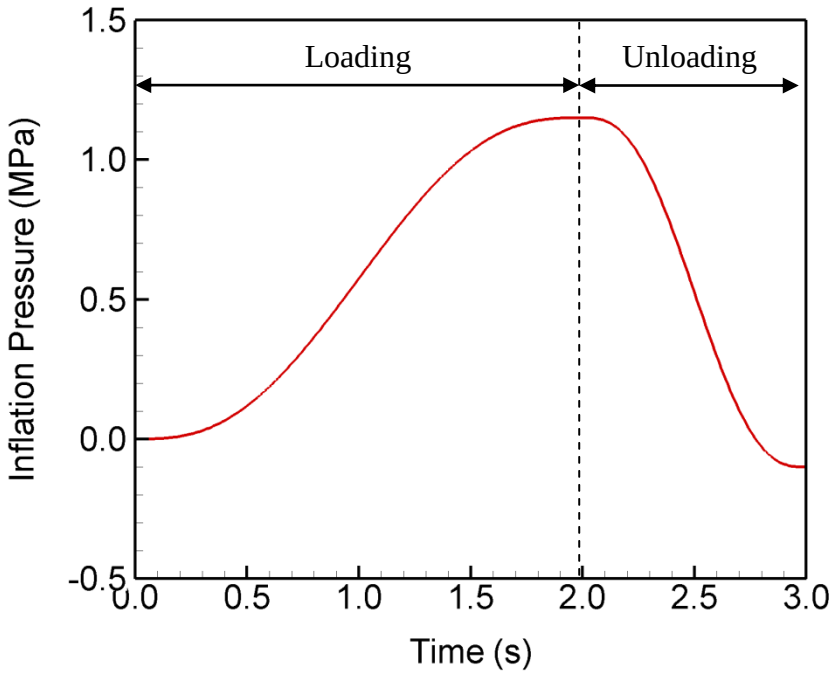

Figure 4.9: Typical loading scheme employed to simulate the inflation and subsequent deflation of the angioplasty balloon.

During the analysis, contact between the various individual components is described using the general contact algorithm that is available in ABAQUS. The robust general contact algorithm searches the current configuration of each individual component for penetration and enforces contact constraints using a penalty method. The penalty method employs a balanced master-slave routine and two sets of contact forces are calculated for each contact pair by varying the master and slave surface definitions. Specifically, an initial set of contact forces is calculated by specifying one surface as the master surface and a second set of contact forces is then calculated by specifying the same surface as the slave surface. A suitable penalty stiffness is then calculated based upon the weighted average of the two different sets of contact forces and the representative stiffness of the underlying elements. Friction is also included in the analysis through the specification of a Coulomb friction model and a static friction coefficient of 0.2 was adopted from Mortier et al. to describe the development of frictional forces between potential contact pairs [57]. A mass-proportional damping coefficient of α = 8,000 was also specified during the description of the angioplasty balloon to prevent non-physiological oscillations during its inflation. The magnitude of the mass-proportional damping coefficient was adopted from DeBeule et al. and corresponds to approximately 50% of the critical damping coefficient [105].

4.2.4 Solution

As coronary stent deployment is highly nonlinear and involves multiple contacting surfaces, the analysis is carried out using the ABAQUS/Explicit solver. Furthermore, as inertia is assumed to have a negligible role during stent deployment, the analysis is carried out using a quasi-static approach. According to ABAQUS documentation, an explicit analysis may be considered quasi-static so long as the total kinetic energy of the deforming components does not exceed 5% of the total internal energy during the majority of the solution. In order to obtain a computationally economic solution, the rate of loading is increased and a small degree of mass-scaling is introduced to artificially increase the size of the stable time increment. To ensure that the analysis remains quasi-static, a total solution time of three seconds is specified and the total kinetic and internal energy are monitored throughout the entire analysis. A typical comparison of the total kinetic and internal energy is shown in Figure 4.10.

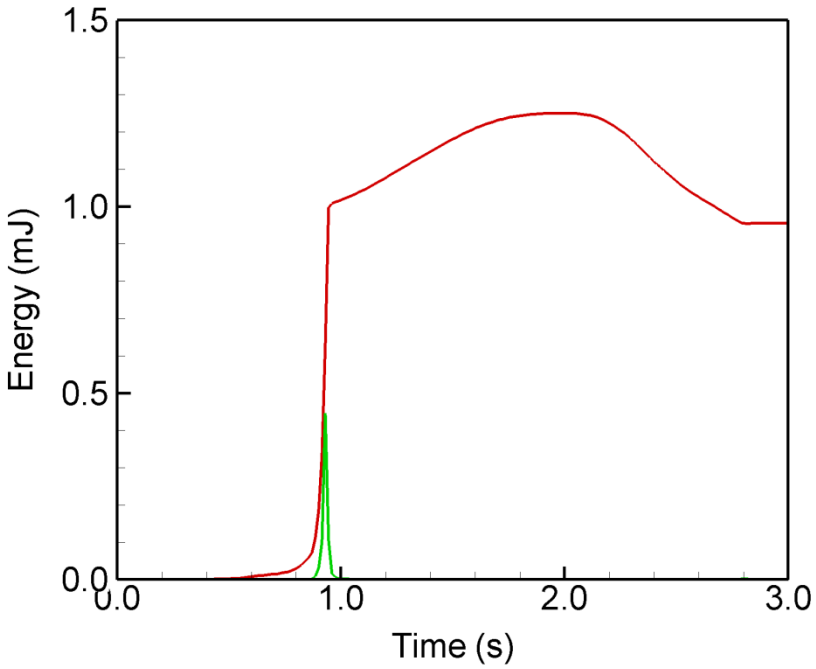

Figure 4.10: Typical comparison of 5% of the total internal energy (red) with the total kinetic energy (green) during the deployment of a stent.

4.3 Fluid Dynamics Analysis

In the second stage of the methodology, the results of the CS analysis are employed to generate a realistically-deformed CFD model of the stented lumen and a transient CFD analysis is carried out to simulate pulsatile flow conditions within a human left anterior descending coronary artery. The transient CFD analysis is carried out using

the commercial CFD package ANSYS CFX and several important pre-processing tasks are first carried out to configure the analysis. First, a CFD model of the stented coronary lumen is generated and the mechanical behaviour of whole human blood is described through the specification of an appropriate constitutive material model. A variety of boundary and loading conditions are then specified to simulate pulsatile flow conditions within a human coronary artery and a number of solver controls are specified to ensure that an accurate solution is obtained in a timely manner. Each of these pre-processing tasks is described in detail in the following sections.

4.3.1 Geometry and Discretisation

Following the completion of the CS analysis, the deformed configurations of both the investigated stent and the coronary artery are exported from ABAQUS/CAE as a triangulated surface mesh and imported into the commercially-available computer-aided design package Rhinoceros 3D (McNeel, Indianapolis, IN, USA). As shown in Figure 4.11, any elements which are not located on the luminal surface of the artery are then deleted and the geometry of the stent is extracted from that of the coronary lumen using a Boolean function. The longitudinal distance both proximal and distal to the stent at which the lumen returns to its original diameter is then measured and any elements which are located beyond these locations are removed. The subsequent triangulated surface mesh is then imported into the commercially-available meshing package ANSYS ICEM CFX (ANSYS Inc.) where it is used to generate a facetted geometrical model of the stented lumen. In order to ensure that the applied boundary conditions have no influence upon the flow within the region of interest, additional entrance and exit lengths of 32 mm are added to the facetted geometrical model. This additional length corresponds to the theoretical entrance length for laminar flow in a straight cylindrical vessel with an internal diameter of 2.7 mm that is subject to mean flow conditions (V_{in} = 0.23 m/s) in a human left anterior descending coronary artery. The resulting geometrical model of the stented coronary lumen is then discretised into a non-uniform unstructured finite volume mesh of tetrahedral elements using the robust Octree algorithm. The various mesh sizes employed during the discretisation of the stented coronary lumen are based on the results of a mesh convergence study that is presented in Appendix A. Following the discretisation of the stented coronary lumen, the resulting mesh is then exported from ANSYS ICEM CFX and imported into ANSYS CFX in order to configure the transient CFD analysis.

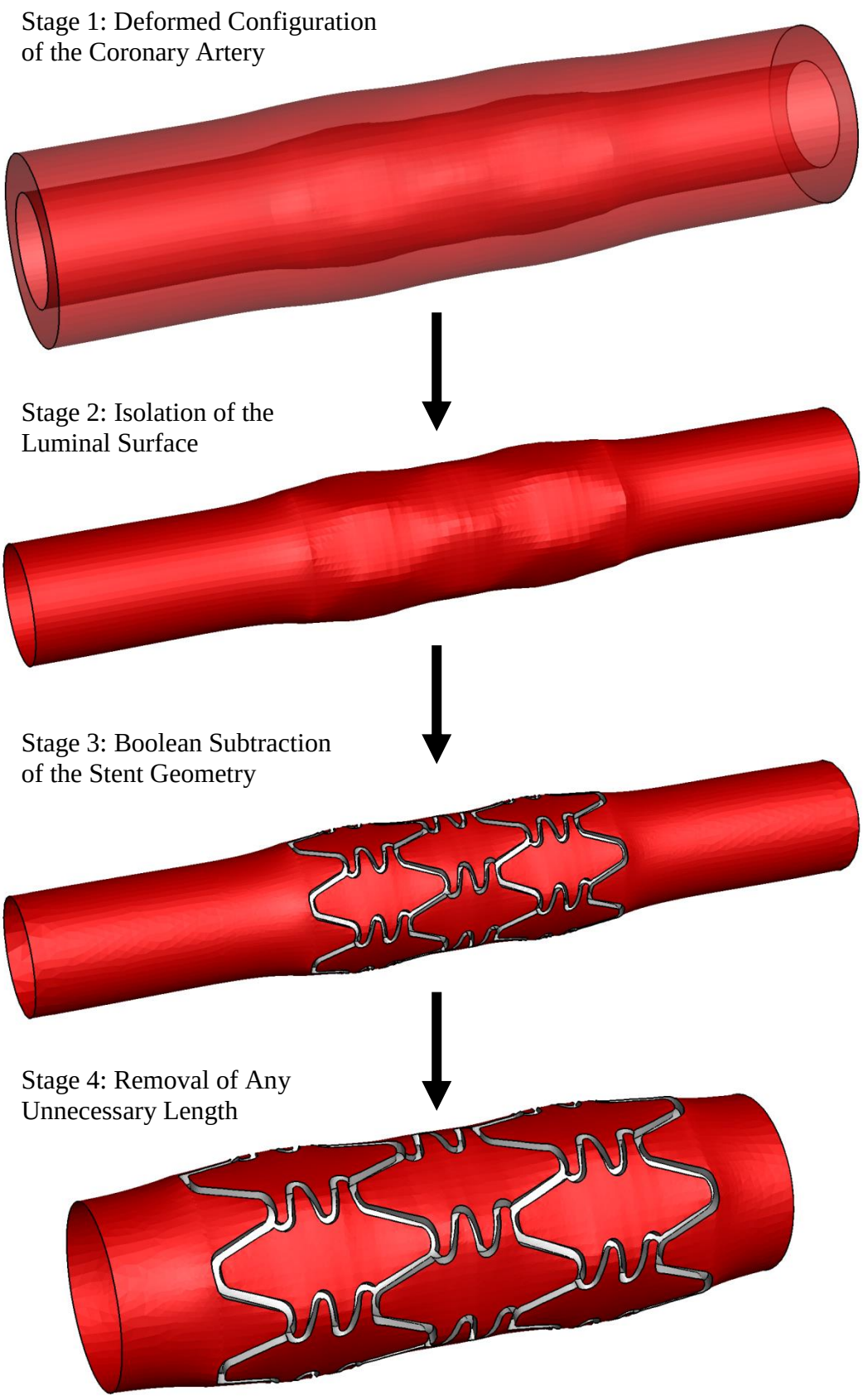

Figure 4.11: The four main stages involved in the generation of a facetted geometrical model of the stented coronary lumen.

4.3.2 Constitutive Material Models

During the CFD analysis, the mass density of blood is assigned a constant value of 1060 kg/m^3. As human blood is a non-Newtonian fluid and exhibits moderate shear thinning at shear rates greater than 100 s^{-1} and much more significant shear thinning at shear rates below 100 s^{-1}, the viscous behaviour of the blood is described using the non-Newtonian Bird-Carreau model which may be written as follows:

$$\mu = \mu_\infty + (\mu_0 - \mu_\infty)[1 + (\dot{\gamma}\lambda_t)^2]^{\left(\frac{q-1}{2}\right)} \tag{4.2}$$

The term μ denotes the dynamic viscosity, μ_0 denotes the low shear viscosity, μ_∞ denotes the high shear viscosity, λ_t denotes the time constant, $\dot{\gamma}$ denotes the scalar shear rate and n denotes the power law index. The mechanical data used to describe the viscous behaviour of the blood was adopted from Jung et al. who employed an Ubhellode capillary viscometer to measure the apparent viscosity of whole human blood at a wide range of shear rates [106]. Based upon the data reported by Jung et al., the low and high shear viscosities are assigned values of 0.056 and 0.00345 Pa·s whilst the time constant and the power law index are assigned values of 3.31 s and 0.375, respectively. As shown in Figure 4.12, the response of the fitted Bird-Carreau model was found to be in good agreement with the experimental data.

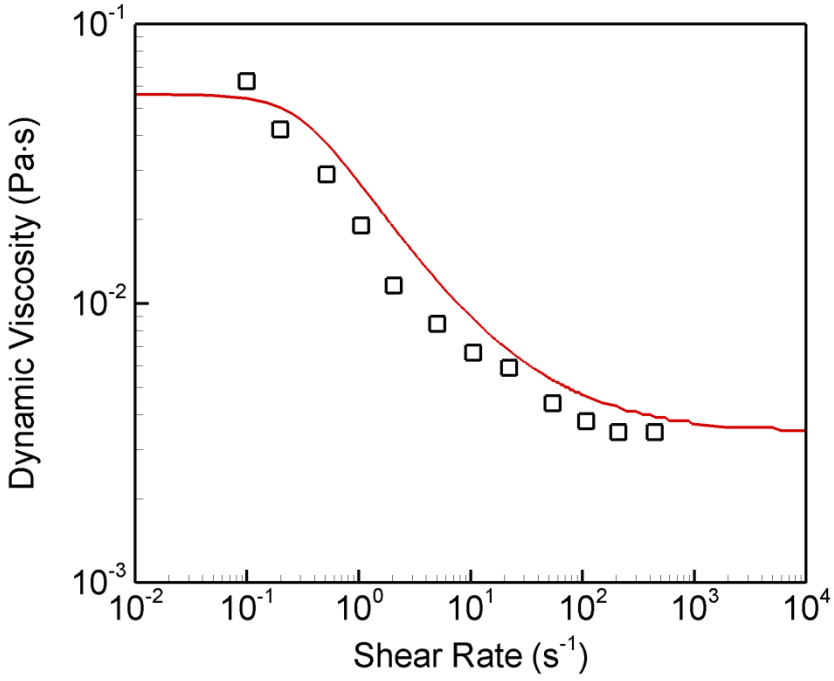

Figure 4.12: Comparison of the fitted Bird-Carreau model (solid line) with the experimental viscosity data (data points).

4.3.3 Boundary and Loading Conditions

During the transient CFD analysis, a zero relative pressure is specified at the domain outlet and a no-slip condition is specified upon both the luminal surface of the artery and the exposed stent struts. The luminal surface of the artery and the stent struts are both assumed to be rigid and a fully-developed laminar velocity profile is specified at the domain inlet using the following Hagen-Poiseuille equation:

$$v(r) = v_{cl}\left[1 - \left(\frac{r}{R}\right)^2\right] \tag{4.3}$$

The term v_{cl} denotes the centreline velocity, r denotes the radial distance from the centreline and R denotes the radius of the unstented coronary artery. To simulate the pulsatile flow conditions within a human left anterior descending coronary artery, a transient velocity profile was adopted from Murphy et al. and employed to describe the variation of the centreline velocity during the CFD analysis [82]. The transient velocity profile is described using the following Fourier series:

$$v_{cl} = a + \sum_{n=1}^{10} b_n \cos(\omega_n t - \phi_n) \tag{4.4}$$

The Fourier coefficients that are employed to describe the transient velocity profile are shown in Table 4.2. As shown in Figure 4.13, the transient velocity profile has a peak velocity of 0.43 m/s which results in a peak Reynolds number of 357.

n	b_n (m/s)	ω_n (rad/s)	ϕ_n (rad)	a (m/s)
1	-0.132311	7.853982	0.36114	0.235226
2	-0.026597	15.014100	15.014100	
3	0.049961	23.561945	1.924730	
4	-0.053343	31.415927	0.103633	
5	-0.026471	39.269908	1.217280	
6	0.003591	47.123890	2.572690	
7	-0.016947	54.977871	0.070253	
8	-0.013916	62.831853	0.714546	
9	-0.007374	70.685835	0.586379	
10	-0.007545	78.539816	0.410051	

Table 4.2: Fourier coefficients used to describe the transient velocity profile.

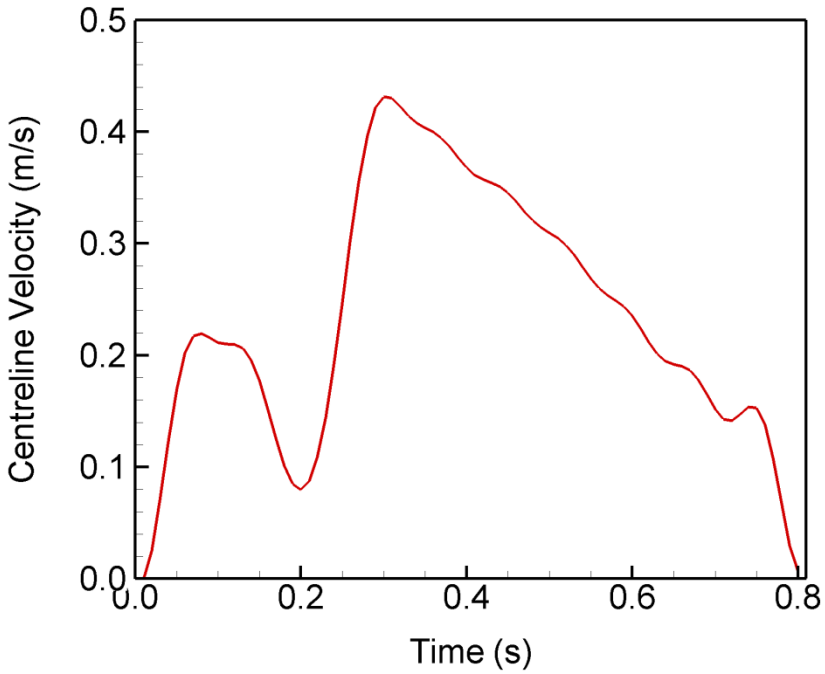

Figure 4.13: Transient velocity profile used to describe pulsatile blood flow within the stented coronary lumen.

4.3.4 Solution

Following the specification of the boundary conditions, the conservation equations of both mass and linear momentum are solved in ANSYS CFX using the multi-grid coupled solver. Unlike a traditional segregated solver, which solves the conservation equations using a guessed pressure and then calculates a suitable pressure correction equation, the coupled solver used by ANSYS CFX solves the conservation equations as a single system. As the peak Reynolds number for the transient cycle is a lot lower than the transition to turbulence value of 2,300, the flow within the stented coronary lumen is assumed to be entirely laminar. In order to ensure that cycle and time step convergence are achieved during the analysis, three consecutive transient cycles are considered and thirty two individual time steps are considered for each consecutive transient cycle. The appropriate number of transient cycles and time steps required to ensure that both cycle and time step convergence are achieved was determined from the results of cycle and time step convergence studies that are presented in Appendix A. Finally, to ensure that the results of the analysis are converged at each individual time step, a convergence criterion of 10^{-4} is specified for the root mean square value of the velocity and density residuals. Following the completion of the CFD analysis, the results obtained at each time step in the third transient cycle are then exported from ANSYS CFX as a CFD general notation system file (CGNS file).

4.4 Variables of Interest

Following the completion of the CS and CFD analyses, the general performance of the investigated stent is first evaluated in terms of its deployed configuration and its deployment characteristics. The mechanical impact of the investigated stent is then evaluated in terms of the stress distribution predicted within the artery wall. Finally, the hemodynamic impact of the investigated stent is evaluated in terms of the WSS distribution predicted on the luminal surface of the coronary artery. The deployment characteristics of the investigated stent and its mechanical impact within the artery are evaluated using the post-processing module that is available in ABAQUS/CAE. The hemodynamic impact of the investigated stent is then evaluated by importing the CGNS file that is exported from ANSYS CFX into the commercial post-processing package Tecplot 360 (Tecplot Inc., Bellevue, WA, USA). The calculation of each of the variables of interest is described in detail in the following sections.

4.4.1 Deployment Characteristics

The performance of the investigated stent is first evaluated in terms of its deployed configuration and its deployed diameter following the unloading of the angioplasty balloon. As the diameter of the stent varies along both its length and circumference, an average diameter is calculated by measuring the radial distance from each of the individual crowns to the centreline of the coronary lumen. The general performance of the investigated stent is then evaluated in terms of the radial recoil (RR) observed following the unloading of the angioplasty balloon. The RR of the stent is defined as the percentage difference between the diameter of the stent at maximum loading and at unloading of the angioplasty balloon and is calculated as follows:

$$\mathrm{RR} = \pm \frac{D_{load} - D_{unload}}{D_{load}} \times 100\% \tag{4.5}$$

The general performance of the investigated stent is also evaluated in terms of the longitudinal foreshortening (LF) observed during its deployment. The LF of the stent is defined as the percentage difference between the stent length prior to loading and at unloading of the angioplasty balloon and is calculated as follows:

$$\mathrm{LF} = \pm \frac{L_{initial} - L_{load}}{L_{initial}} \times 100\% \tag{4.6}$$

4.4.2 Equivalent Stress

The mechanical impact of the investigated stent is evaluated in terms of the stress distribution predicted within the coronary artery. Specifically, the mechanical impact of the investigated stent is evaluated in terms of the ES distribution predicted within the artery. Although other measures of stress, such as the maximum principal stress, describe the compressive or tensile nature of a state of stress, the ES allows the state of stress predicted in a material subject to multi-axial loading to be compared against its uniaxial stress-strain response. The ES was previously introduced in Chapter 2, where it was defined in terms of the deviatoric stress tensor as follows:

$$ES = II_{\mathbf{s}} = \sqrt{\frac{3}{2}\mathbf{s} : \mathbf{s}} \tag{4.7}$$

In order to assess the mechanical impact of the investigated stent, the ES distribution predicted within the artery is evaluated following the unloading of the angioplasty balloon. The ES distribution observed at recoil is preferred to that observed at peak loading when it is very difficult to distinguish stresses incurred due to balloon-artery interaction from those incurred due to stent-artery interaction. Furthermore, due to its length in comparison to that of the investigated stent, a large portion of the coronary artery is subjected to minimal stresses. As such, only the elements that are located within the longitudinal domain that extends for 5 mm both proximal and distal to the mid-section of the stent are included during the evaluation of the mechanical impact of the investigated stent. The length of the longitudinal domain of interest relative to that of the investigated stent is clearly demonstrated in Figure 4.14.

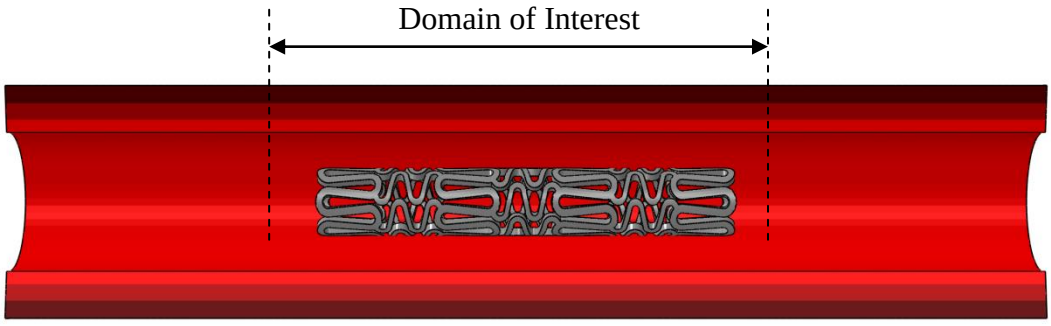

Figure 4.14: Longitudinal domain considered during the evaluation of the ES distribution within the coronary artery.

4.4.3 Time-Averaged Wall Shear Stress

The hemodynamic impact of the investigated stent is evaluated using three different hemodynamic variables of interest. The first hemodynamic variable of interest is the time-averaged WSS (TAWSS). The TAWSS is scalar-valued quantity that is adopted to evaluate the flow-induced viscous stress that is exerted upon the luminal surface during the transient cycle [82]. In order to calculate the TAWSS, the magnitude of the instantaneous WSS vector is first calculated for each time step during the third transient cycle. The TAWSS is then determined by time-averaging the magnitude of the instantaneous WSS vector over the third transient cycle as follows:

$$\text{TAWSS} = \frac{1}{T}\int_0^T |\boldsymbol{\tau}_w| dt \tag{4.8}$$

The term T denotes the period of the third transient cycle, dt denotes the time step and $|\boldsymbol{\tau}_w|$ denotes the magnitude of the instantaneous WSS vector. The integration in Equation 4.8 may be approximated using the trapezoidal rule as follows:

$$\text{TAWSS} = \frac{1}{T}\left[\frac{T}{2(n-1)}[\tau_w^1 + 2(\tau_w^2 + \cdots + \tau_w^{n-1}) + \tau_w^n]\right] \tag{4.9}$$

The term τ_w^n denotes the magnitude of the instantaneous WSS vector at the nth time step. The TAWSS is calculated for each node located upon the luminal surface of the artery through the implementation of a custom-written Python script in Tecplot 360. In order to verify both the accuracy and the implementation of the Python script that was employed to calculate the TAWSS, a number of preliminary CFD analyses were carried out to simulate laminar flow over a smooth flat plate. The various details of these preliminary CFD analyses are presented in Appendix B.

4.4.4 Oscillatory Shear Index

The second hemodynamic variable of interest is the oscillatory shear index (OSI). The OSI is a non-dimensional scalar-valued quantity that is employed to evaluate the oscillatory nature of vascular flows [82]. The OSI is defined as follows:

$$\text{OSI} = 0.5\left(1 - \frac{\left|\int_0^T \tau_w dt\right|}{\int_0^T |\tau_w| dt}\right) \tag{4.10}$$

The OSI is used to measure temporal variations in the direction of the instantaneous WSS vector during the transient cycle. An OSI of 0 indicates that the direction of the instantaneous WSS vector remains coincident with that of the time-averaged WSS vector during the transient cycle whilst an OSI of 0.5 indicates that the direction of the instantaneous WSS vector varies significantly from that of the time-averaged WSS vector during the transient cycle. The OSI is calculated at each node located on the luminal surface of the artery using a custom-written Python script in Tecplot 360. In order to verify both the accuracy and the implementation of the Python script that was used to calculate the OSI, a number of preliminary CFD analyses were carried out to simulate laminar flow over a smooth flat plate. Again, the various details of these preliminary CFD analyses are presented in Appendix B.

4.4.5 Relative Residence Time

The third hemodynamic variable of interest is the relative residence time (RRT). The RRT is a scalar-valued quantity that combines both the TAWSS and OSI to identify regions of the luminal surface at which flow stagnation and high particle residence times are likely to be observed [107]. The RRT is calculated as follows:

$$\mathrm{RRT} = \frac{1}{[1 - 2(\mathrm{OSI})]\mathrm{TAWSS}} \tag{4.11}$$

As shown in Equation 4.11, a decrease in the TAWSS causes an increase in the RRT whereas an increase in the OSI causes an increase in the RRT. Substituting Equation 4.10 into Equation 4.11 allows the RRT may be rewritten as follows:

$$\mathrm{RRT} = \frac{1}{\left|\int_0^T \tau_w dt\right|} \tag{4.12}$$

The RRT is calculated at each node located upon the luminal surface of the artery using a custom-written Python script in Tecplot 360. In order to verify the accuracy and implementation of the Python script that was employed to calculate the RRT, a number of preliminary CFD analyses were carried out to simulate laminar flow over a smooth flat plate. Again, the various details of these preliminary CFD analyses are presented in Appendix B. In the following section, the statistical analysis of each of the mechanical and hemodynamic variables of interest is discussed.

4.5 Statistical Analysis

In order to evaluate the mechanical impact of the investigated stent, the maximum ES and the volume-weighted mean ES predicted within the artery are both measured following the unloading of the angioplasty balloon. The volume weighted mean ES predicted within the coronary artery is calculated as follows:

$$\mu_{vw} = \frac{\int_v \mathrm{ES}\, dv}{\int_v dv} = \frac{\sum_{i=1}^{N}(\mathrm{ES}_i dv_i)}{\sum_{i=1}^{N} dv_i} \tag{4.13}$$

The term ES_i denotes the ES at the ith element, dv_i denotes the volume of the ith element, N denotes the total number of elements in the artery and v denotes the total volume of the artery. The volume-weighted mean ES describes the central tendency of the ES distribution and a low mean is preferable when evaluating the mechanical impact of the investigated stent. In order to fully elucidate the mechanical impact of the investigated stent, both the volume-weighted standard deviation and the volume-weighted skewness of the ES distribution are also calculated as follows:

$$\sigma_{vw} = \sqrt{\frac{\sum_{i=1}^{N}(\mathrm{ES}_i - \mu_{vw})^2 dv_i}{\sum_{i=1}^{n} dv_i}} \tag{4.14}$$

$$S_{vw} = \frac{\sum_{i=1}^{N}(\mathrm{ES}_i - \mu_{vw})^3 dv_i}{\sum_{i=1}^{N} dv_i \, {\sigma_{vw}}^3} \tag{4.15}$$

The volume-weighted standard deviation describes the variance of the distribution about the volume-weighted mean. A low deviation indicates that the mean is a good reflection of the central tendency of the distribution whilst a high deviation indicates that the mean may not be a good reflection of the central tendency of the distribution. The volume-weighted skewness describes the asymmetry of the distribution about the volume-weighted mean. A positive skewness indicates that the distribution is skewed to the right such that the majority of the values within the distribution lie to the left of the mean value whereas a negative skewness indicates that the distribution is skewed to the left such that majority of the values within the distribution lie to the right of the mean value. The magnitude of the skewness also indicates the severity to which the distribution is skewed about the mean with a high skewness indicating that the majority of the values within the distribution are much higher or lower than the

mean. In order to quantify the hemodynamic impact of the investigated stent, the area-weighted mean value of the TAWSS, OSI and RRT distribution predicted upon the luminal surface of the artery is calculated as follows:

$$\mu_{aw} = \frac{\int_s \phi \, ds}{\int_s ds} = \frac{\sum_{i=1}^{N}(\phi_i ds_i)}{\sum_{i=1}^{N} ds_i} \tag{4.16}$$

The term ϕ_i denotes the value of the specific hemodynamic variable at the ith node, ds_i denotes the surface area at the ith node, N denotes the total number of nodes on the luminal surface of the artery and s denotes the total area of the luminal surface of the artery. As before, the area-weighted mean describes the central tendency of the distribution and a high mean is preferable when evaluating the TAWSS distribution whereas a low mean is preferable when evaluating the OSI and the RRT distribution. Finally, in order to fully elucidate the hemodynamic impact of the investigated stent, both the area-weighted standard deviation and the area-weighted skewness of the TAWSS, OSI and RRT distribution are also calculated as follows:

$$\sigma_{aw} = \sqrt{\frac{\sum_{i=1}^{N}(\phi_i - \mu_{aw})^2 ds_i}{\sum_{i=1}^{N} ds_i}} \tag{4.17}$$

$$S_{aw} = \frac{\sum_{i=1}^{N}(\phi_i - \mu_{aw})^3 ds_i}{\sum_{i=1}^{N} ds_i \, {\sigma_{aw}}^3} \tag{4.18}$$

4.6 Summary

This chapter describes the proposed numerical methodology for investigating the performance of balloon-expandable coronary stents in terms of both their mechanical and hemodynamic impact in a coronary artery. The proposed methodology is divided into two stages. In the first stage, a CS model of the investigated stent is generated and a CS analysis is then carried out to simulate its deployment within a coronary artery. In the second stage, the results of the CS analysis are employed to generate a realistically-deformed CFD model of the stented lumen and a transient CFD analysis is carried out to simulate pulsatile flow in a left anterior descending coronary artery. In this chapter, the generation and discretisation of various geometrical models and the specification of material models, boundary conditions and solution controls have

each been described in detail. In the following chapter, the proposed methodology is applied to six generic stents in order to demonstrate its application. The performance of the investigated stents is then compared and contrasted to evaluate the relationship between stent design and performance. Finally, the predicted performance of three of the investigated stents is then compared to the clinical performance of three similar stents in order to determine if the proposed methodology is capable of predicting the clinical performance of balloon-expandable coronary stents.

CHAPTER 5
RESULTS

5.1 Introduction

In order to demonstrate its application, the proposed methodology was applied to six generic stents. In this chapter, the geometrical configuration of the six investigated stents is first discussed and the CS and CFD models are then presented. The general performance of the stents is then evaluated in terms of their deployed configuration and deployment characteristics. The mechanical and hemodynamic impact of each of the stents is then evaluated in terms of the ES distribution predicted within the artery and the WSS distribution predicted on the luminal surface of the artery, respectively. To investigate the relationship between stent design and performance, the predicted performance of each stent is then compared and contrasted. Finally, to determine if the proposed methodology is capable of predicting stent performance, the predicted performance of three of the stents is compared to the clinical performance of three comparable stents, as reported in two separate large-scale clinical trials.

5.2 Investigated Stents

To demonstrate its application, the proposed methodology was applied to six generic stents. The investigated stents resemble commercially-available coronary stents and are labelled from A to F as shown in Figure 5.1. Stent A resembles the BX-Velocity stent (Johnson & Johnson) and features sinusoidal strut segments that are connected by N-shaped flexible link elements in a closed-cell configuration. Stent B resembles the S7 AVE stent (Medtronic) and features sinusoidal strut segments that are welded together in an open-cell configuration. Stent C resembles the Express stent (Boston Scientific) and features both long and short sinusoidal strut segments that are each connected by inflexible straight articulations in an open-cell configuration. Stent D

resembles the NIR stent (Boston Scientific) and features sinusoidal strut segments that are connected by flexible U-shaped link elements in a closed-cell configuration. Finally, Stents E and F resemble the Multilink RX Ultra stent (Abbott Laboratories) and feature sinusoidal strut segments which are connected by straight articulations in an open-cell configuration. Stents E and F had identical geometrical configurations and only differed in terms of their respective strut thickness. Stent E was assigned a strut thickness of 0.13 mm whilst Stent F was assigned a strut thickness of 0.05 mm. The investigated stents were each assigned a length of 8 mm, an undeployed internal diameter of 1 mm and the remaining geometrical properties of the investigated stents were then adopted from the literature [3]. The various geometrical features of each of the investigated stents are presented in Table 5.1. The geometrical and CS models of the stents are shown in Figures 5.1 and 5.2, respectively. Finally, the geometrical models of the stented lumens are shown in Figures 5.3 and 5.4 whilst the discretised CFD models of the stented lumens are shown in Figures 5.5 and 5.6.

Stent	A	B	C	D	E	F
Stent Length (mm)	8.00	8.00	8.00	8.00	8.00	8.00
Undeployed Diameter (mm)	1.00	1.00	1.00	1.00	1.00	1.00
Cell Configuration	Closed	Open	Open	Closed	Open	Open
Link Configuration	Peak-to-Peak	Peak-to-Peak	Peak-to-Valley	Peak-to-Peak	Peak-to-Valley	Peak-to-Valley
Cell Number (Circumferential)	6	5	3	8	3	3
Cell Number (Longitudinal)	3	7	6	5	5	5
Strut Thickness (mm)	0.14	0.10	0.13	0.10	0.13	0.05
Strut Width (mm)	0.13	0.10	0.09	0.10	0.10	0.10
Stent-to-Artery Area (mm^2)	12.35	15.02	9.47	12.46	12.03	12.03

Table 5.1: Geometrical properties of the investigated stents.

Stent A - BX-Velocity Stent

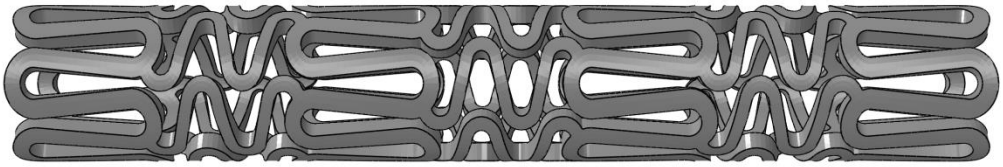

Stent B - S7 AVE Stent

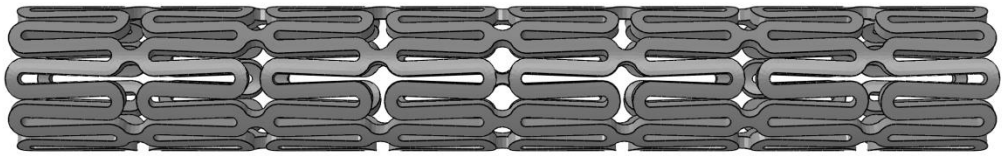

Stent C - Express Stent

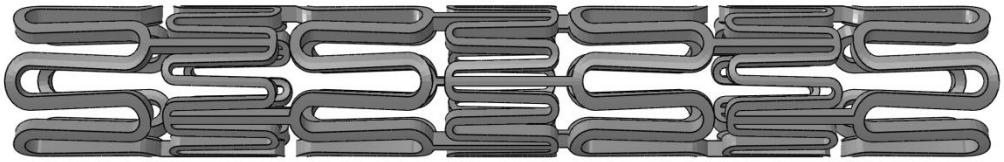

Stent D - NIR Stent

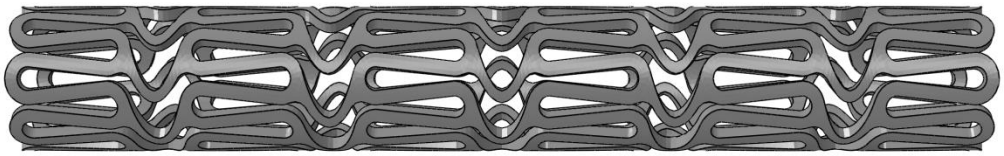

Stent E - Multilink RX Ultra Stent (thick strut)

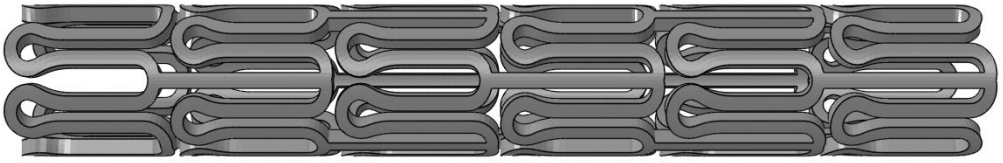

Stent F - Multilink RX Ultra Stent (thin strut)

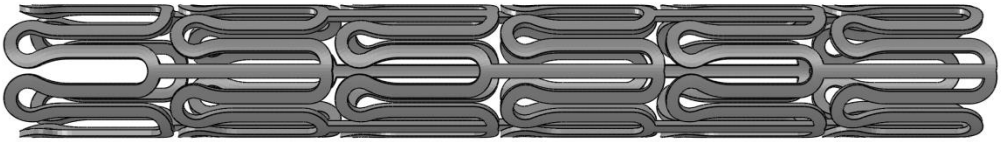

Figure 5.1: Geometrical models of the investigated stents.

Stent A - 43,472 Nodes and 24,570 Elements

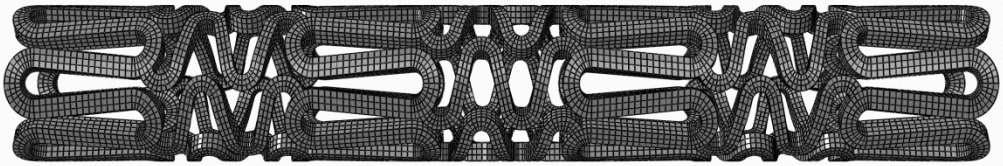

Stent B - 47,991 Nodes and 24,280 Elements

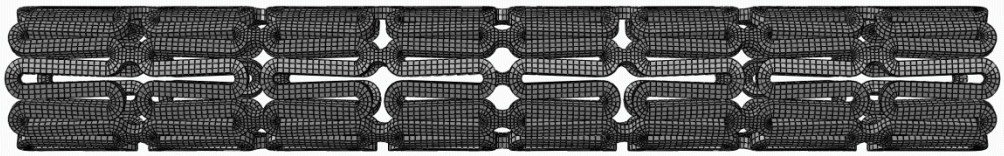

Stent C - 36,160 Nodes and 18,108 Elements

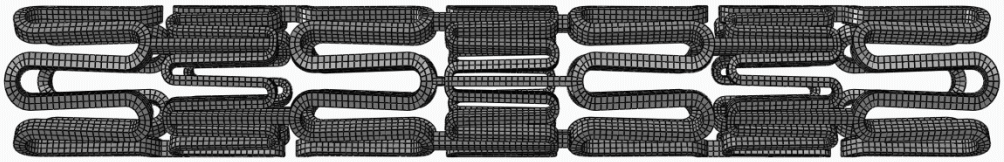

Stent D - 46,968 Nodes and 26,568 Elements

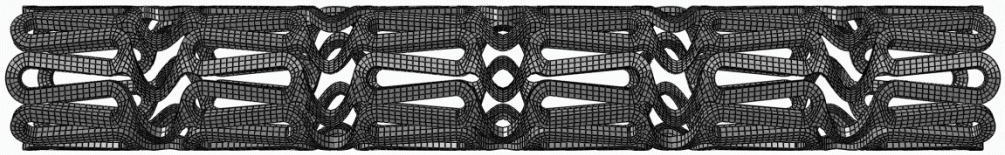

Stent E - 41,112 Nodes and 21,600 Elements

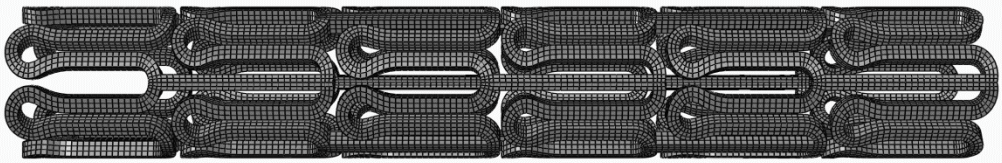

Stent F - 42,912 Nodes and 21,636 Elements

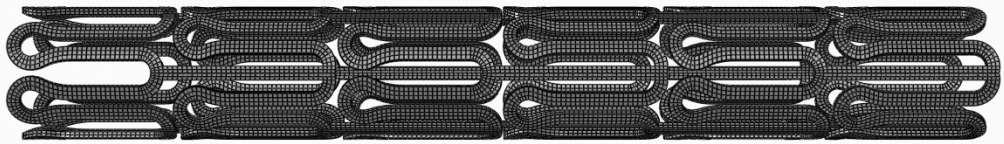

Figure 5.2: Discretised CS models of the investigated stents.

Stent A - BX-Velocity Stent

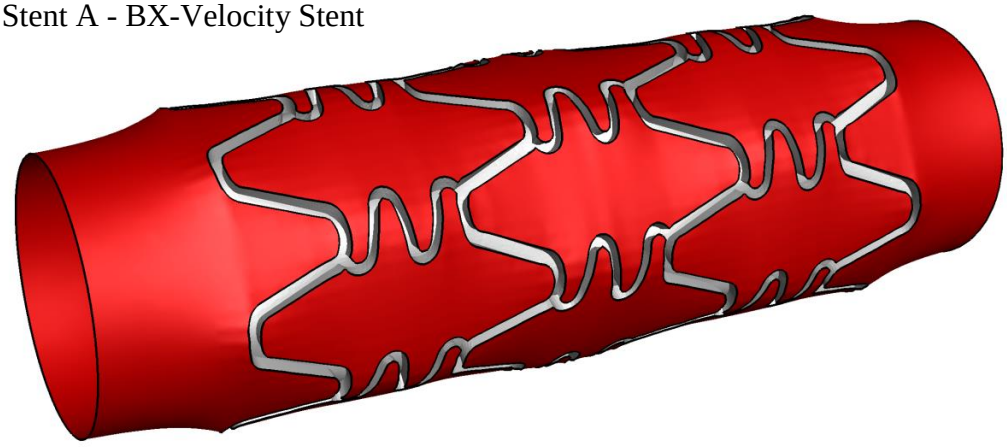

Stent B - S7 AVE Stent

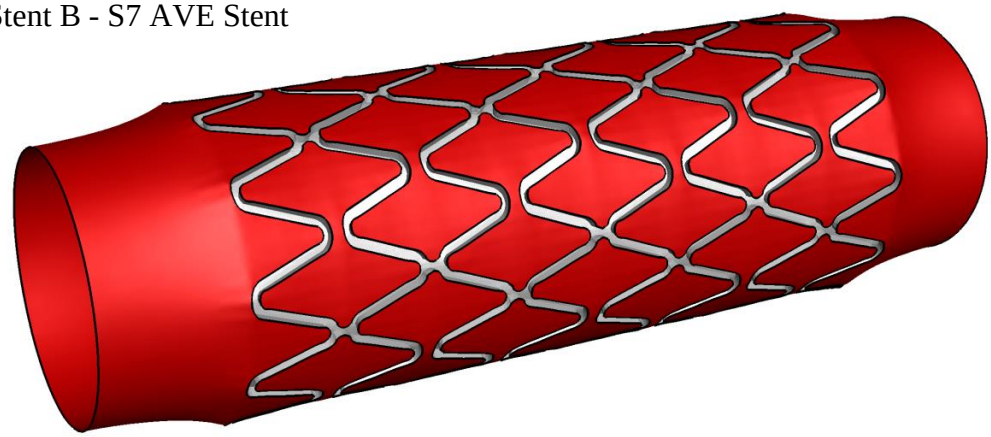

Stent C - Express Stent

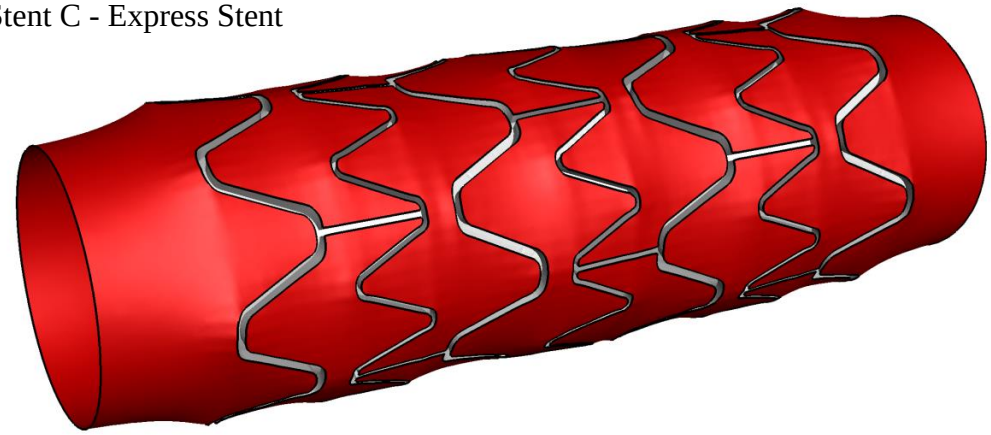

Figure 5.3: Geometrical model of the stented coronary lumen for Stent A (top), Stent B (middle) and Stent C (bottom).

Stent D - NIR Stent

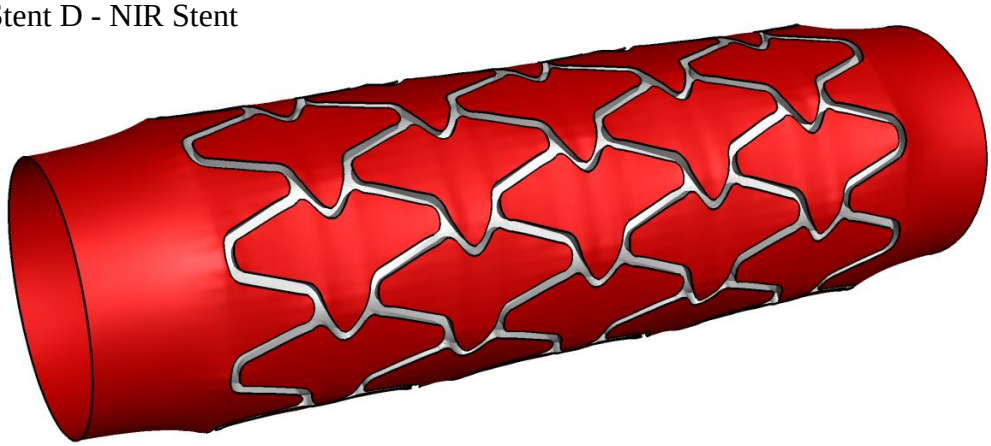

Stent E - Multilink RX Ultra Stent
(Thick Strut)

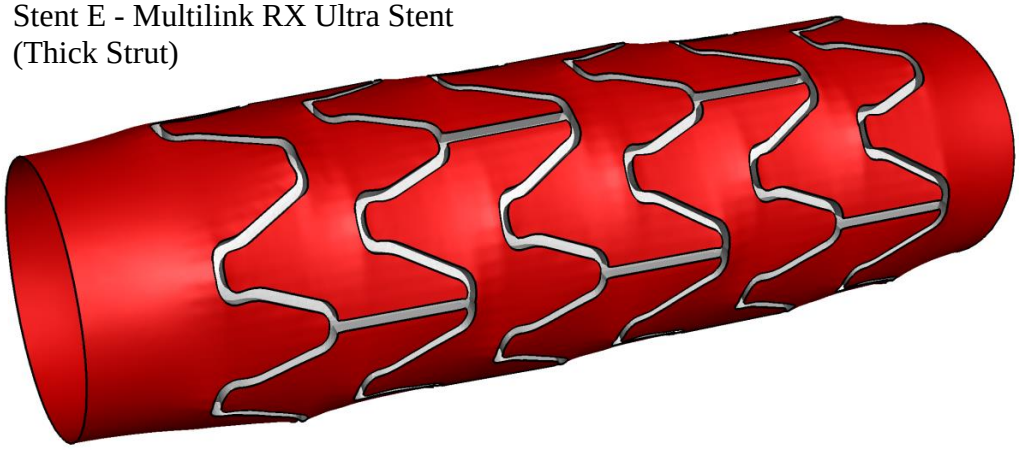

Stent F - Multilink RX Ultra Stent
(Thin Strut)

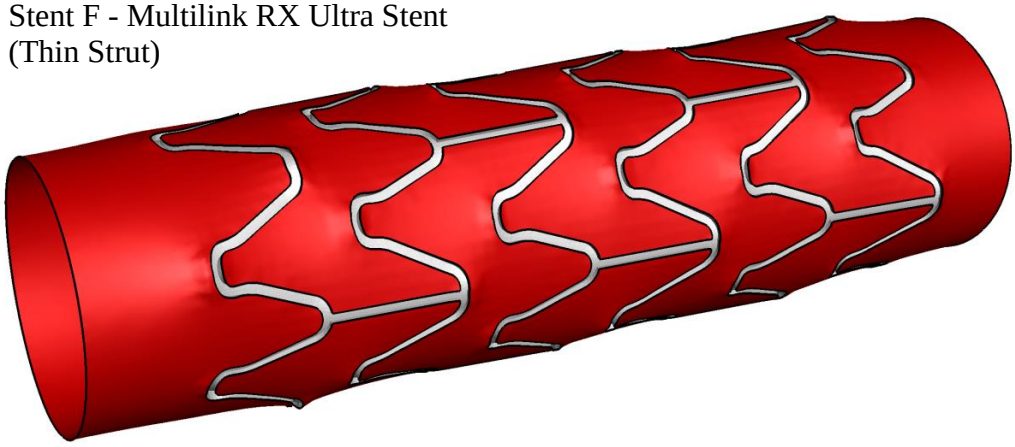

Figure 5.4: Geometrical model of the stented coronary lumen for Stent D (top), Stent E (middle) and Stent F (bottom).

Stent A - 463,984 Nodes
and 2,564,515 Elements

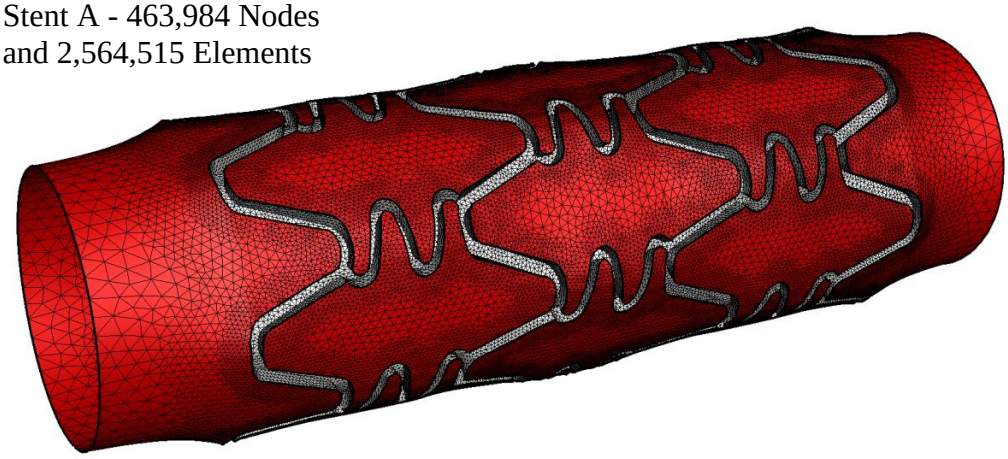

Stent B - 494,391 Nodes
and 2,734,053 Elements

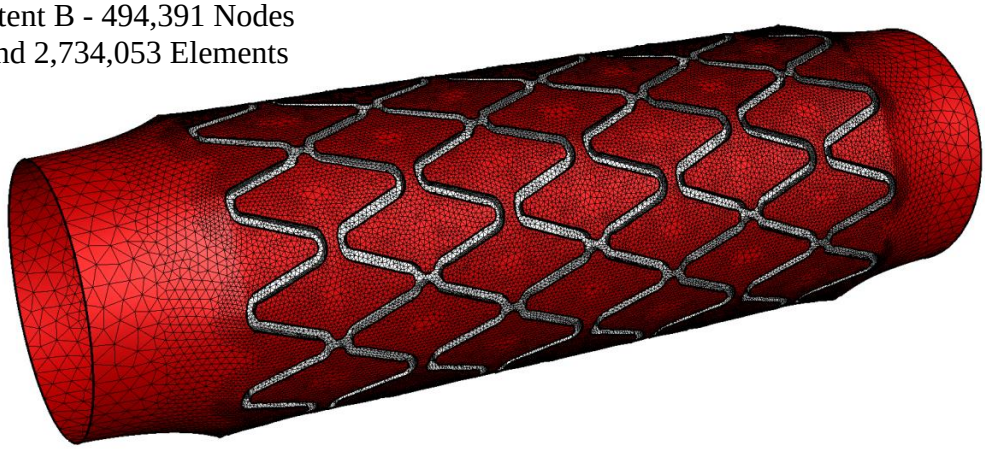

Stent C - 490,396 Nodes
and 2,710,399 Elements

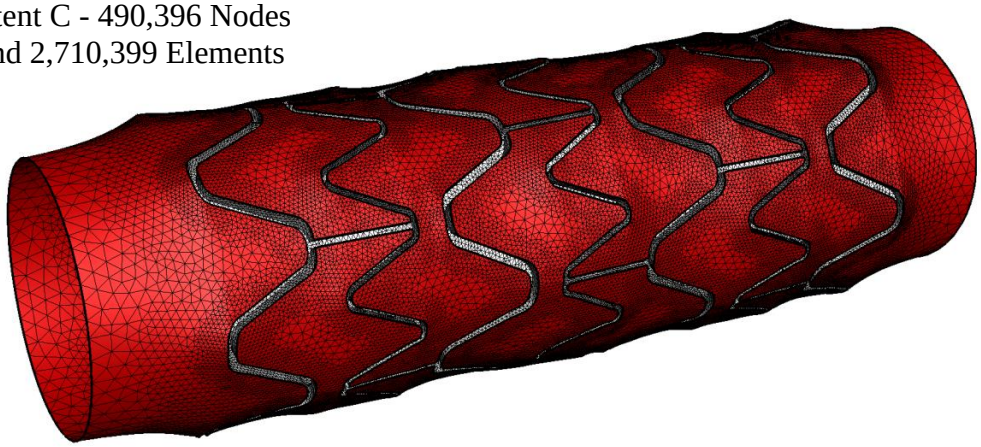

Figure 5.5: Discretised CFD model of the stented coronary lumen for Stent A (top), Stent B (middle) and Stent C (bottom).

Stent D - 472,321 Nodes
and 2,615,807 Elements

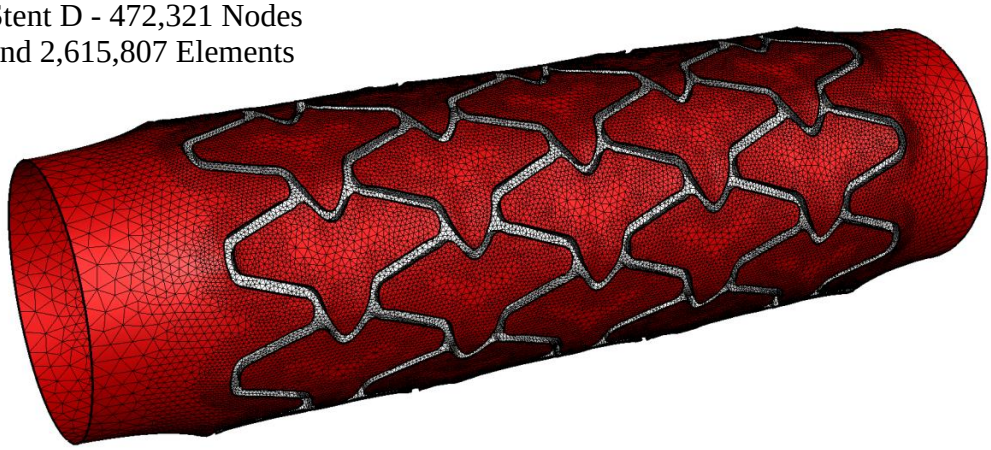

Stent E - 513,351 Nodes
and 2,844,599 Elements

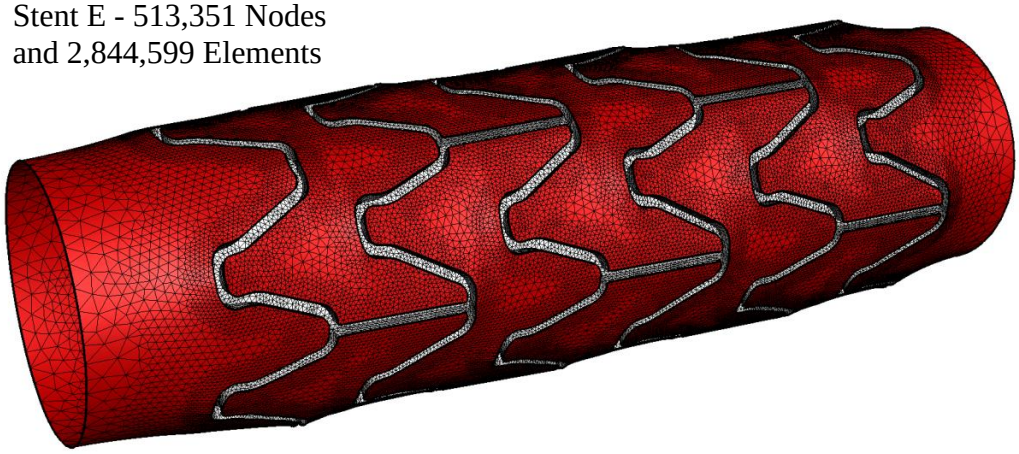

Stent F - 423,902 Nodes
and 2,345,746 Elements

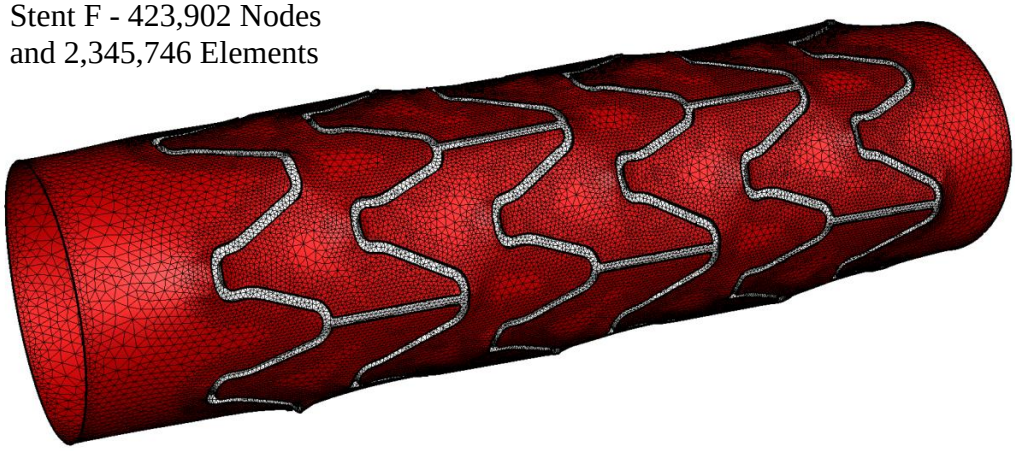

Figure 5.6: Discretised CFD model of the stented lumen for Stent D (top), Stent E (middle) and Stent F (bottom).

5.3 Results and Discussion

The results obtained from the application of the proposed methodology to each of the six investigated stents are presented in this section. The general performance of the stents is first evaluated in terms of their deployment characteristics. The mechanical impact of the stents is then evaluated in terms of the ES distribution predicted within the artery. For each of the investigated stents, the ES distribution is described using both a contour plot and a histogram. The contour plots display the distribution of ES predicted within the artery and the histograms display the total volume of the artery subject to different magnitudes of ES. Finally, the hemodynamic impact of the stents is evaluated in terms of the TAWSS, OSI and RRT distributions predicted upon the luminal surface of the artery. For each of the investigated stents, the distribution of the hemodynamic variables is described using both a contour plot and a histogram. The contour plots display the distribution of TAWSS, OSI and RRT predicted upon the luminal surface whilst the histograms display the total area of the luminal surface subjected to different magnitudes of TAWSS, OSI and RRT.

5.3.1 Deployment Characteristics

During the CS analyses of the investigated stents, a pressure load of 1.15, 1.30, 1.00, 1.00, 0.90 and 0.40 MPa was specified to ensure that a deployment ratio of 1.1:1 was achieved with Stents A, B, C, D, E and F, respectively. During the initial stages of the CS analyses, the angioplasty balloon inflated about the catheter shaft causing progressive elastic deformation of the stent. As the pressure load was increased, the stent began to yield and the subsequent deployment of the stent was first observed at its extremities. This phenomenon, which is often referred to as dog-boning, is caused by the over-dilation of the angioplasty balloon at the extremities of the stent and is well-documented in the literature [108]. In each of the CS analyses, this rapid initial deployment continued until the investigated stent made contact with the artery. From this point onward, any further increase in the pressure load resulted in only marginal increases in the diameter of the stent. This highly-compliant response is typical of that reported in experimental studies of balloon-expandable stent deployment [108]. Once the investigated stents were deployed to a nominal diameter of 3.00 mm, the uniform pressure load was reduced to a value of -0.10 MPa to simulate the deflation of the angioplasty balloon and to allow the stent and artery to recoil. The deployment of each of the investigated stents is shown in Figures 5.7 to 5.12.

Initial Configuration - Pressure Load = 0.00 MPa

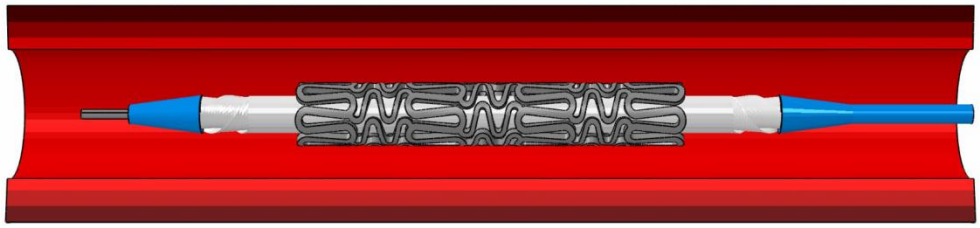

Deformed Configuration - Pressure Load = 0.50 MPa

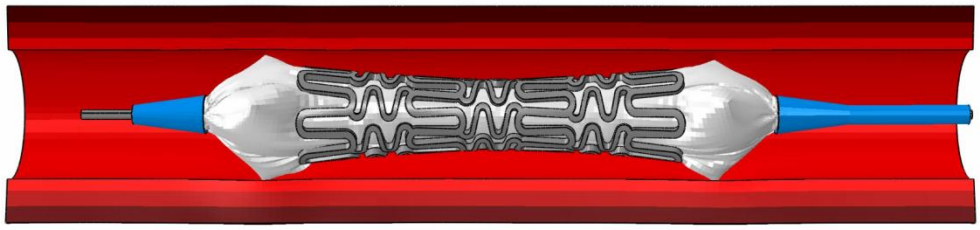

Deformed Configuration - Pressure Load = 1.15 MPa

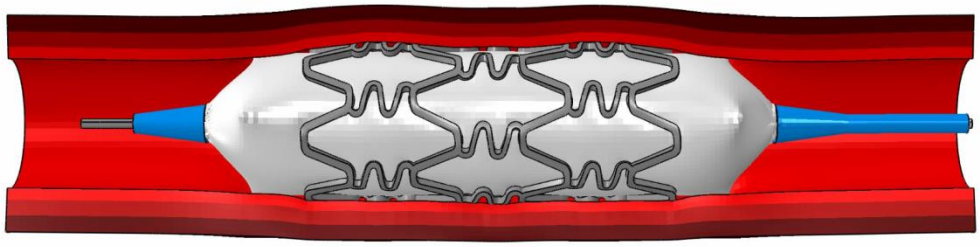

Deformed Configuration - Pressure Load = -0.10 MPa

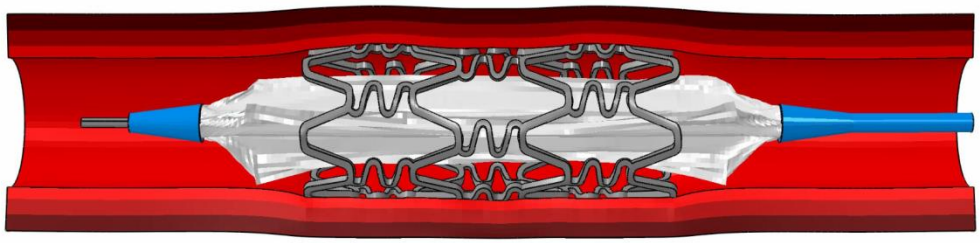

Figure 5.7: Deployment of Stent A within the coronary artery.

Initial Configuration - Pressure Load = 0.00 MPa

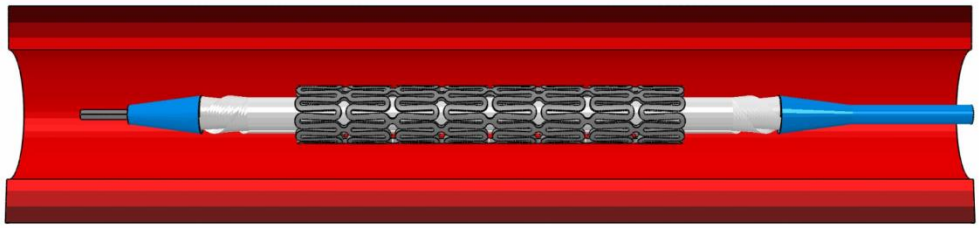

Deformed Configuration - Pressure Load = 0.40 MPa

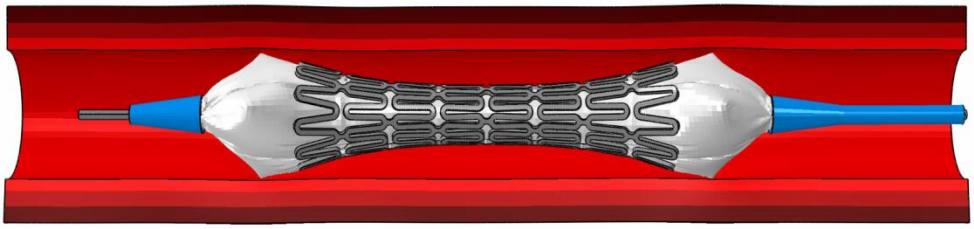

Deformed Configuration - Pressure Load = 1.30 MPa

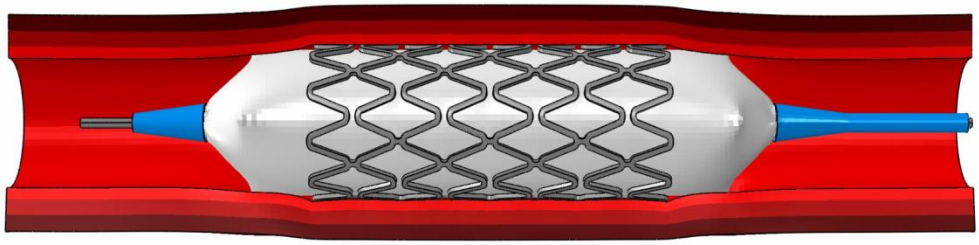

Deformed Configuration - Pressure Load = -0.10 MPa

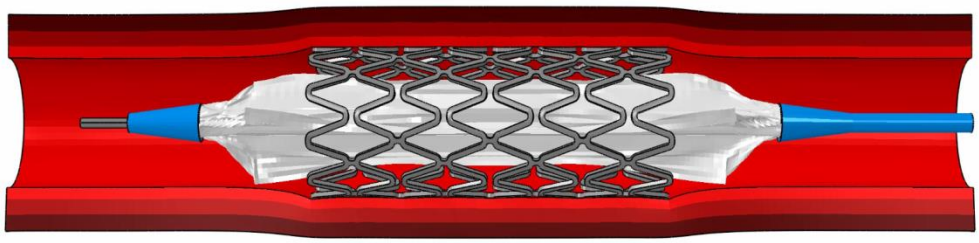

Figure 5.8: Deployment of Stent B within the coronary artery.

Initial Configuration - Pressure Load = 0.00 MPa

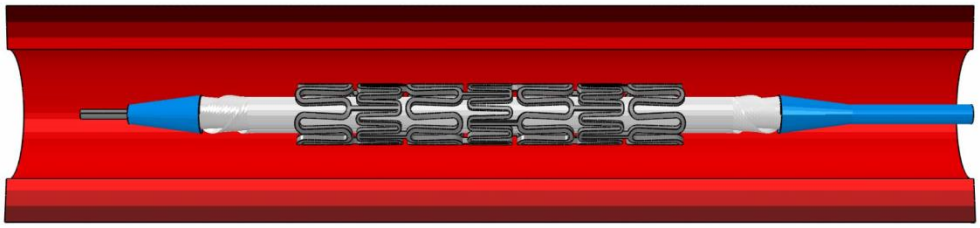

Deformed Configuration - Pressure Load = 0.30 MPa

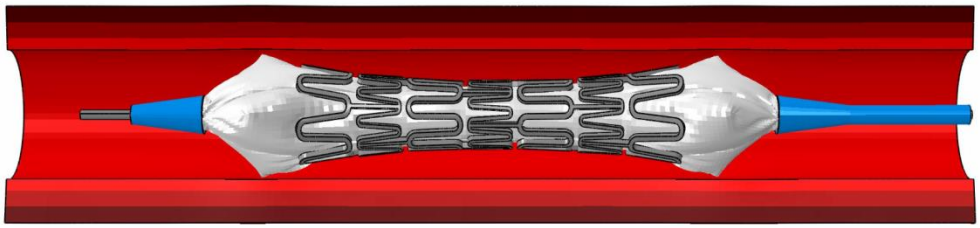

Deformed Configuration - Pressure Load = 1.00 MPa

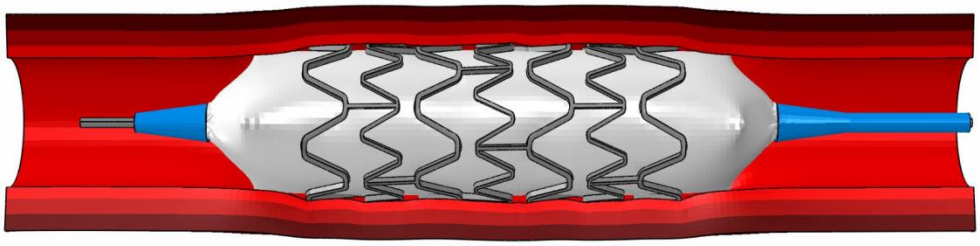

Deformed Configuration - Pressure Load = -0.10 MPa

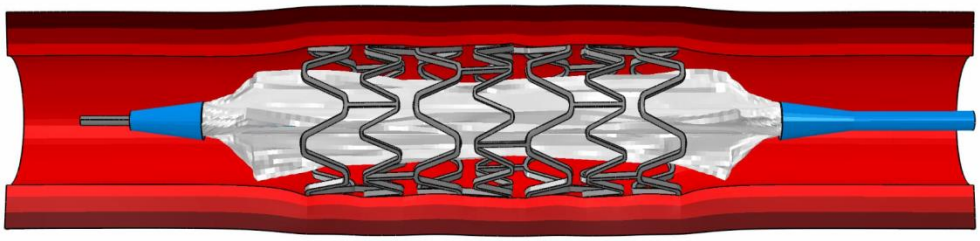

Figure 5.9: Deployment of Stent C within the coronary artery.

Initial Configuration - Pressure Load = 0.00 MPa

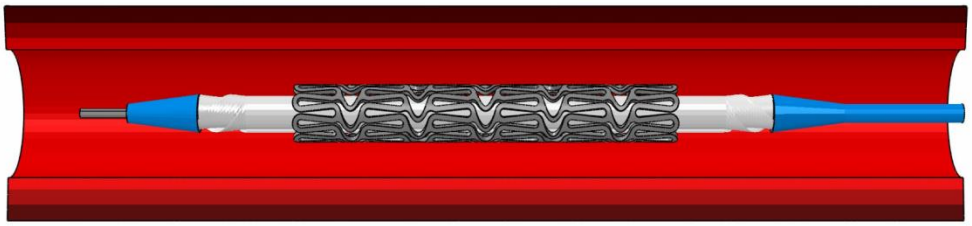

Deformed Configuration - Pressure Load = 0.35 MPa

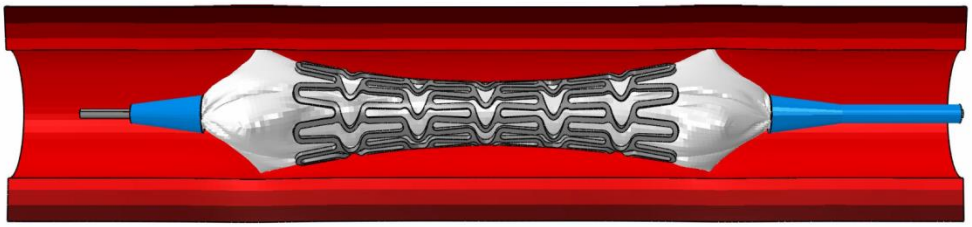

Deformed Configuration - Pressure Load = 1.00 MPa

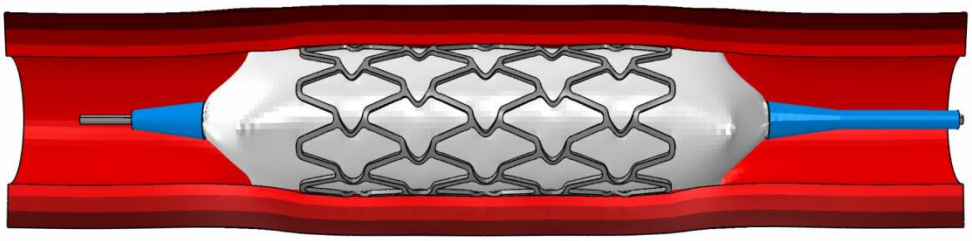

Deformed Configuration - Pressure Load = -0.10 MPa

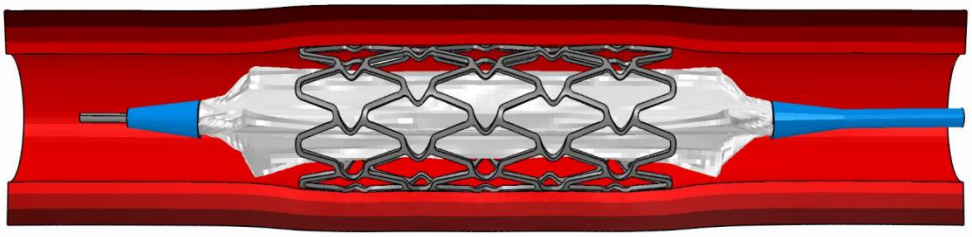

Figure 5.10: Deployment of Stent D within the coronary artery.

Initial Configuration - Pressure Load = 0.00 MPa

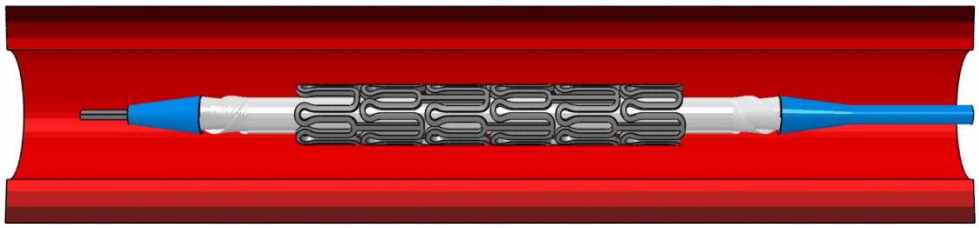

Deformed Configuration - Pressure Load = 0.30 MPa

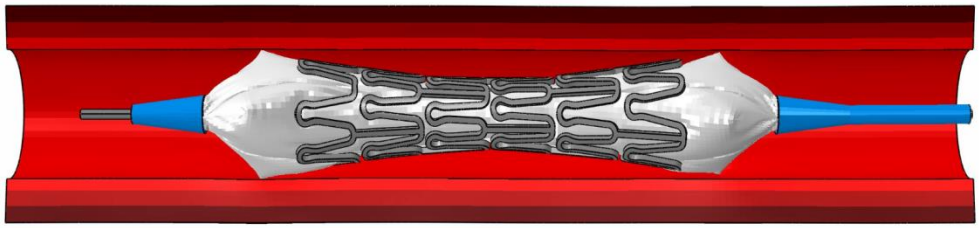

Deformed Configuration - Pressure Load = 0.90 MPa

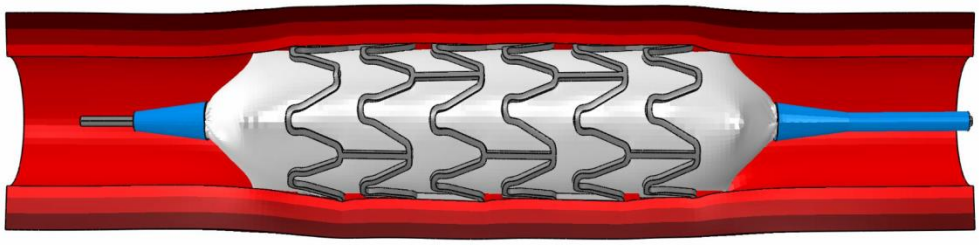

Deformed Configuration - Pressure Load = -0.10 MPa

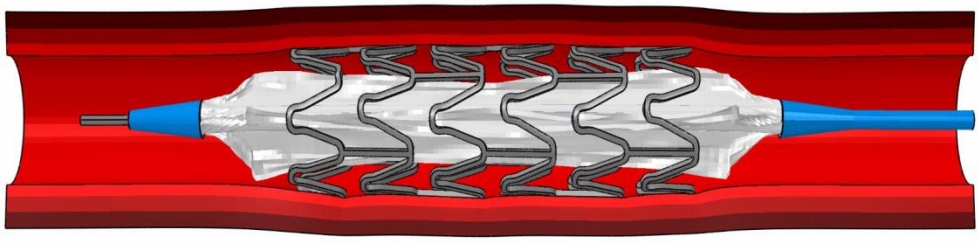

Figure 5.11: Deployment of Stent E within the coronary artery.

Initial Configuration - Pressure Load = 0.00 MPa

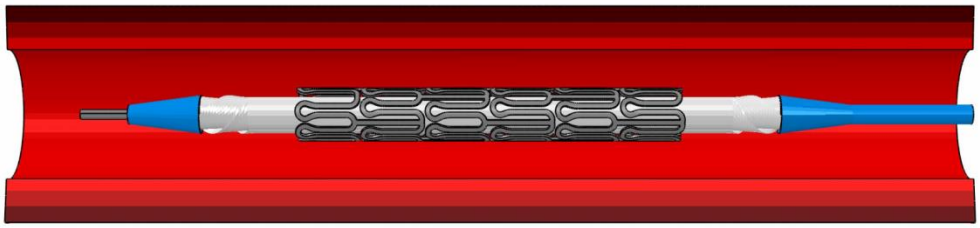

Deformed Configuration - Pressure Load = 0.15 MPa

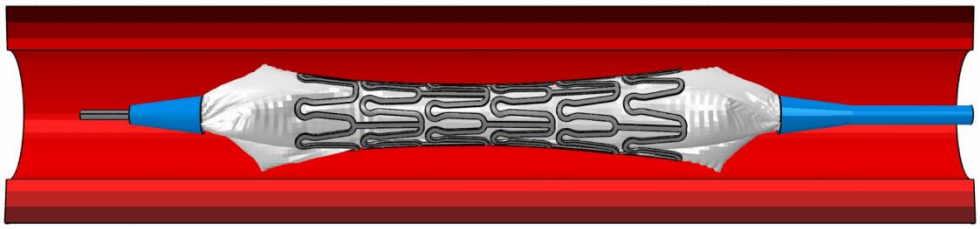

Deformed Configuration - Pressure Load = 0.40 MPa

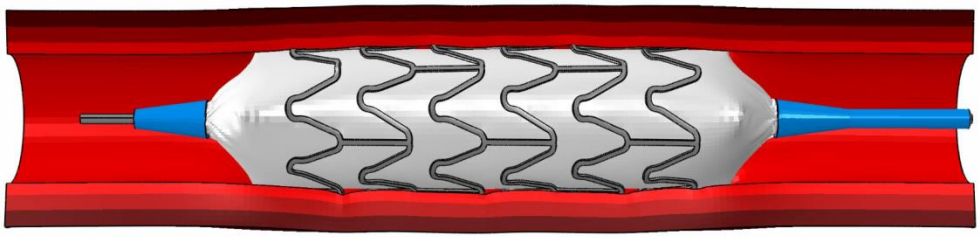

Deformed Configuration - Pressure Load = -0.10 MPa

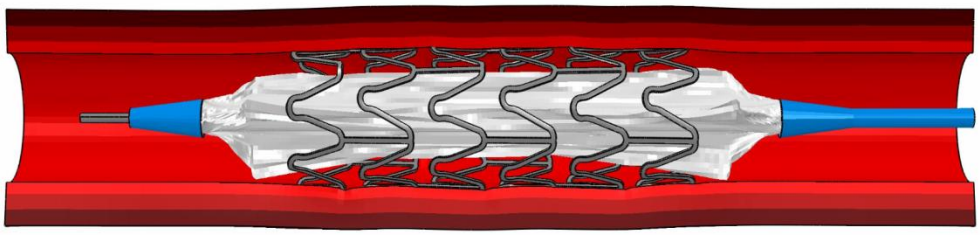

Figure 5.12: Deployment of Stent F within the coronary artery.

Following the unloading of the angioplasty balloon, RR was measured at −3.37%, −3.28%, −4.15%, −3.48%, −3.69% and -4.74% for Stents A, B, C, D, E and F, respectively. Comparing the results, the highest rate of RR of -4.74% was observed with Stent F. This was attributed to the fact that Stent F featured a non-uniform distribution of cells and a relatively low strut thickness and stent-to-artery surface area of 0.05 mm and 12.03 mm^2, respectively. Conversely, the lowest rate of RR of -3.28% was observed with Stent B. This was attributed to the fact that Stent B had a much more uniform distribution of cells and a relatively high strut thickness and stent-to-artery surface area of 0.10 mm and 15.02 mm^2, respectively. Following the unloading of the angioplasty balloon, LF was measured at −4.46%, −7.67%, −3.79%, −3.61%, +3.13% and +2.75% for Stents A, B, C, D, E and F, respectively. Comparing the results, the highest rate of LF of -7.67% was observed with Stent B. This was attributed to the fact that Stent B did not feature any link elements which tend to reduce the rate of LF during stent deployment. Conversely, the lowest rate of LF of +3.13% was observed with Stent E. As indicated by the positive value of LF, Stent E actually elongated during its deployment. Although this is not common, stent elongation has been reported in both experimental and numerical studies of balloon-expandable coronary stents [74,108]. The elongation of Stent E and F was attributed to the fact that their individual strut segments were interconnected by long, inflexible link elements that inhibited LF during their deployment. Overall, the predicted rates of both RR and LF were found to be consistent with values reported in experimental studies of balloon-expandable coronary stents [108,109]. The various deployment characteristics of each of the investigated stents are shown in Table 5.2.

Stent	Max Diameter (mm)	Final Diameter (mm)	RR (%)	LF (%)
A	3.03	2.93	-3.37	-4.66
B	3.05	2.95	-3.28	-7.67
C	3.05	2.92	-4.15	-3.79
D	3.02	2.91	-3.48	-3.61
E	3.03	2.92	-3.69	+3.13
F	3.02	2.88	-4.74	+2.75

Table 5.2: Deployment characteristics of the investigated stents.

5.3.2 Equivalent Stress

The ES distribution predicted within the coronary artery for each of the investigated stents is shown in Figure 5.13 and Figure 5.14 and the total volume of the coronary artery that was subject to different magnitudes of ES is shown in Figure 5.15. In each of the CS analyses, the peak values of ES were observed in the intimal layer of the artery. As shown in Table 5.3, the highest maximum ES of 83.84 kPa and the highest mean ES of 10.72 kPa were both observed with Stent A. This was attributed to the fact that the flexible link elements expanded to a greater diameter than the sinusoidal strut segments during the deployment of Stent A and, as shown in Figure 5.13, this imposed a circumferential stretch upon the arterial tissue located within each of the stent cells. Conversely, the lowest maximum ES of 39.60 kPa and the lowest mean ES of 3.49 kPa were both observed with Stent F. This was attributed to the fact that Stent F featured the lowest strut thickness of 0.05 mm and had the highest rate of RR following the unloading of the angioplasty balloon. For each of the investigated stents, the standard deviation of the ES distribution was relatively high. This implies a high variance about the mean ES and was attributed to the fact that the majority of the artery was subjected to either relatively high or relatively low values of ES. For each of the investigated stents, the skewness of the ES distribution was between 1.8 and 2.3. This implies that each ES distribution was skewed slightly to the right and that the majority of the artery was subjected to ES values that were lower than the mean ES. Based upon these results, it is likely that Stent A would have the greatest impact upon the mechanical environment within the artery whilst Stent F would have the least impact upon the mechanical environment within the artery.

Stent	ES_{max} (kPa)	μ_{vw} (kPa)	σ_{vw} (kPa)	S_{vw} (-)
A	83.84	10.72	16.94	2.25
B	58.98	8.83	12.52	1.85
C	67.82	8.79	12.97	2.04
D	42.10	7.34	10.18	1.80
E	74.37	9.21	13.01	1.90
F	39.60	3.49	4.61	2.08

Table 5.3: Statistical analysis of the ES distribution predicted within the coronary artery for each of the investigated stents.

Stent A - Maximum ES = 83.84 kPa

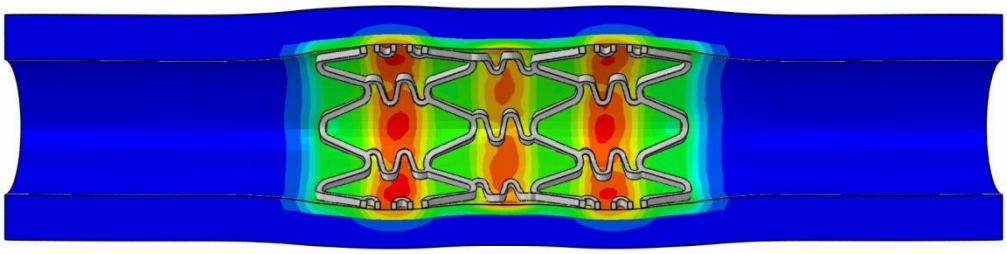

Stent B - Maximum ES = 58.98 kPa

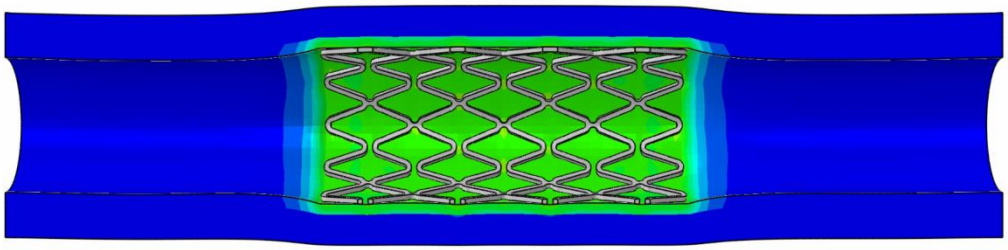

Stent C - Maximum ES = 67.82 kPa

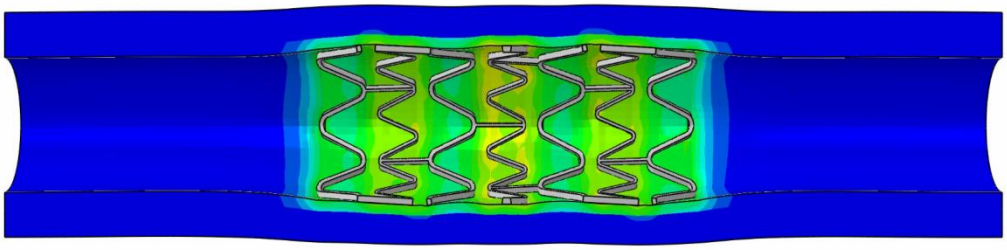

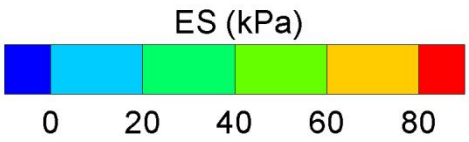

Figure 5.13: ES distribution predicted within the coronary artery following the deployment of Stent A (top), Stent B (middle) and Stent C (bottom).

Stent D - Maximum ES = 42.10 kPa

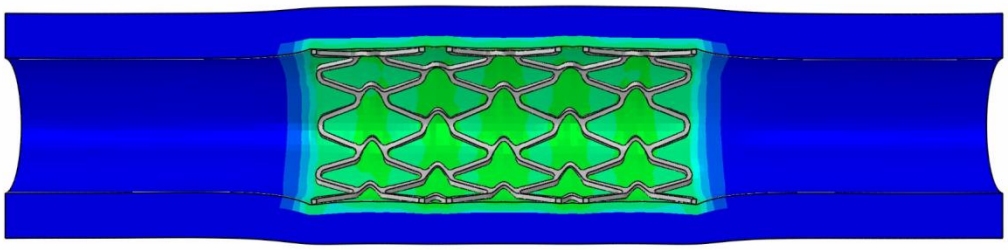

Stent E - Maximum ES = 74.37 kPa

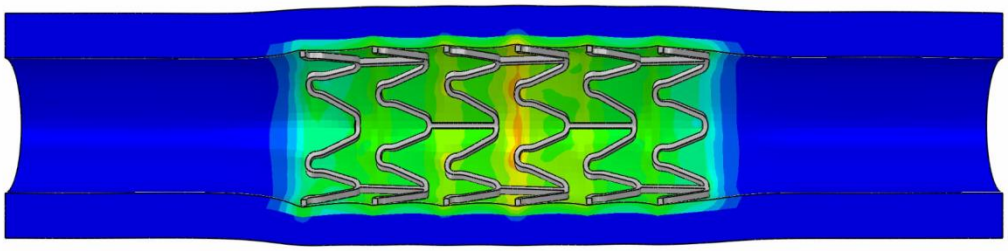

Stent F - Maximum ES = 39.60 kPa

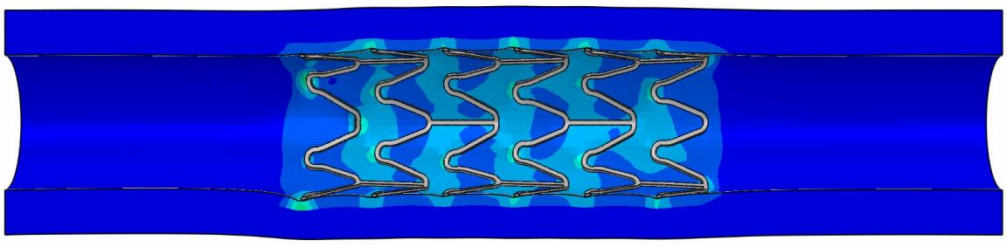

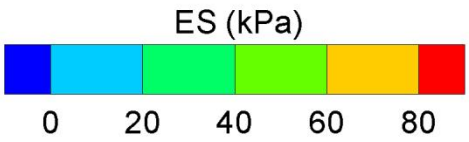

Figure 5.14: ES distribution predicted within the coronary artery following the deployment of Stent D (top), Stent E (middle) and Stent F (bottom).

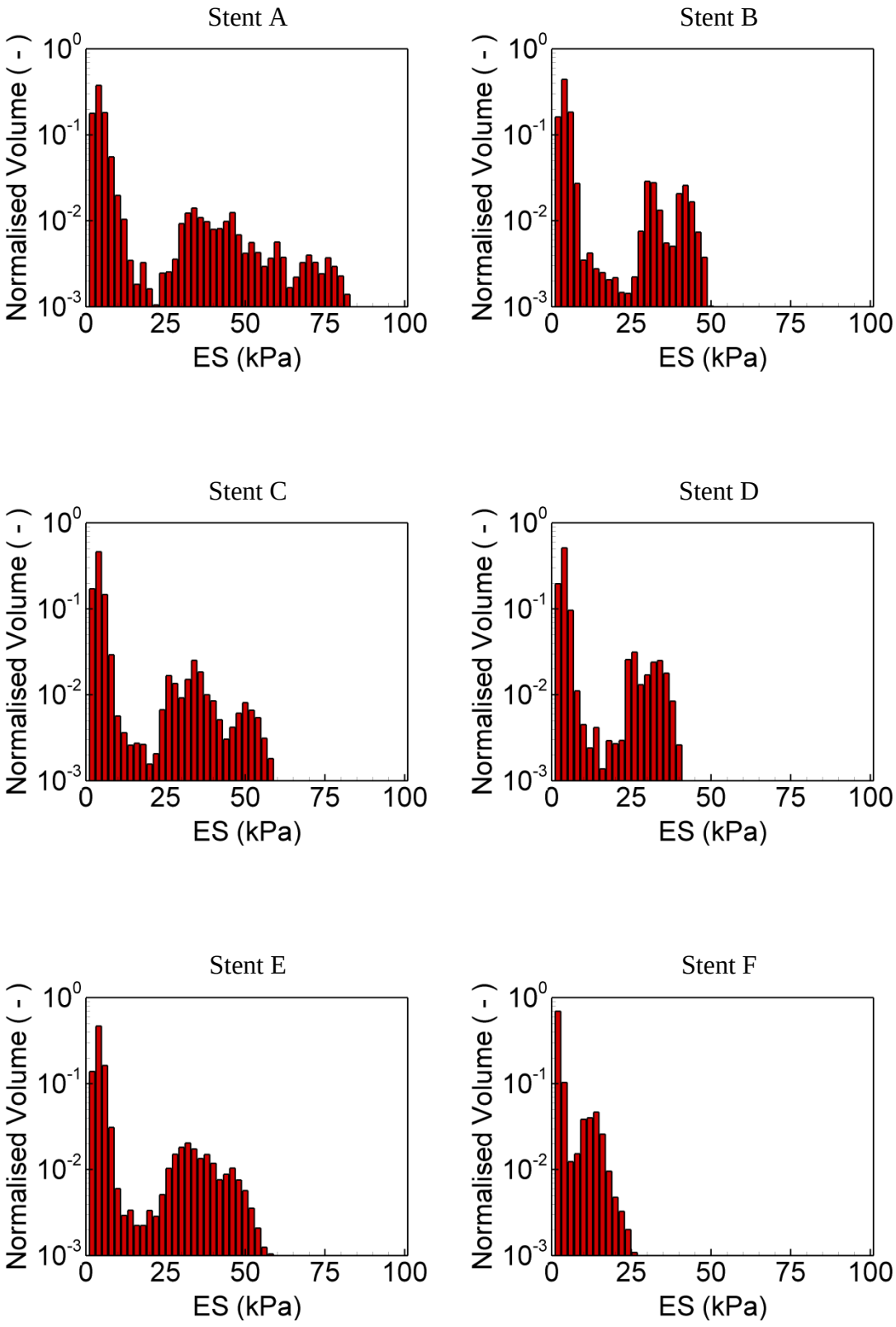

Figure 5.15: ES distribution predicted within the artery following the deployment of each of the investigated stents.

5.3.3 Time-Averaged Wall Shear Stress

The TAWSS distribution predicted upon the luminal surface of the coronary artery for each of the investigated stents is shown in Figure 5.16 and Figure 5.17 and the total area of the luminal surface that was subject to different magnitudes of TAWSS is shown in Figure 5.18. In each of the CFD analyses, the lowest values of TAWSS were predicted next to the stent struts where regions of flow separation, recirculation and reattachment were observed. As shown in Table 5.4, the lowest mean TAWSS of 0.703 Pa was observed with Stent C. This was attributed to the fact that Stent C had a relatively high strut thickness of 0.13 mm and a number of its struts were located in close proximity to one another and aligned perpendicular to the main flow direction. Conversely, the highest mean TAWSS of 1.124 Pa was observed with Stent F. This was attributed to the fact that Stent F had the lowest strut thickness of 0.05 mm and the majority of its struts were located far from each other and aligned parallel to the main flow direction. For each of the investigated stents, the standard deviation of the TAWSS distribution was relatively low. This implies a low variance about the mean TAWSS and was attributed to the fact that, for each of the investigated stents, the range of the TAWSS distribution was quite low. For most of the stents, the skewness of the TAWSS distribution was between 0.5 and 1.0. This implies that each TAWSS distribution was skewed to the right and that the majority of the luminal surface was subject to TAWSS values that were lower than the mean TAWSS. Based upon these results, it is likely that Stent C would have the greatest impact upon the magnitude of the WSS distribution within the artery whereas Stent F would have the least impact upon the magnitude of the WSS distribution within the artery.

Stent	μ_{aw} (Pa)	σ_{aw} (Pa)	S_{aw} (-)
A	0.767	0.534	0.58
B	0.750	0.540	0.95
C	0.703	0.506	0.90
D	0.797	0.509	0.66
E	0.731	0.490	0.87
F	1.124	0.432	-0.23

Table 5.4: Statistical analysis of the TAWSS distribution predicted upon the luminal surface of the artery for each of the investigated stents.

Stent A - Mean TAWSS = 0.767 Pa

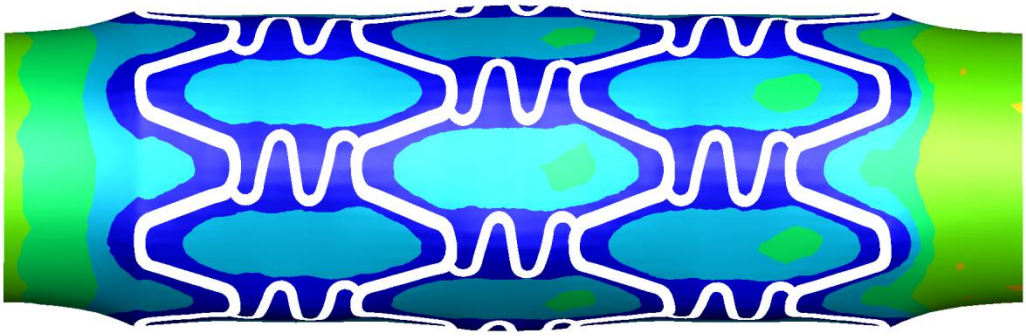

Stent B - Mean TAWSS = 0.750 Pa

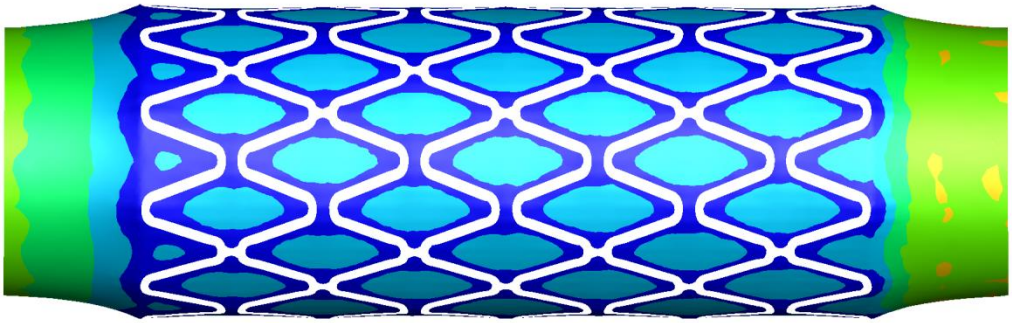

Stent C - Mean TAWSS = 0.703 Pa

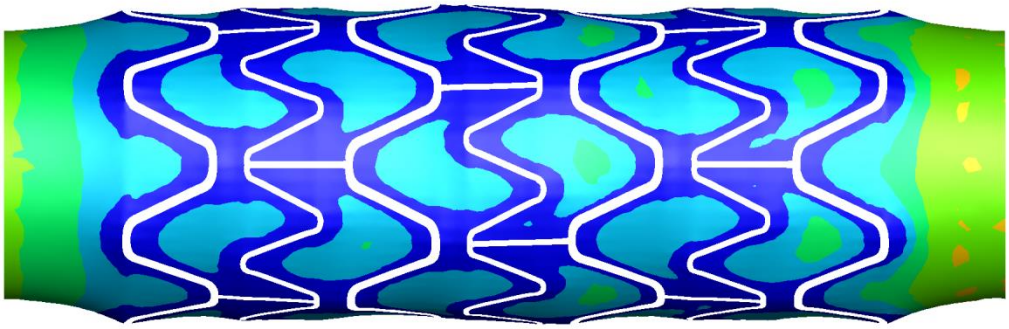

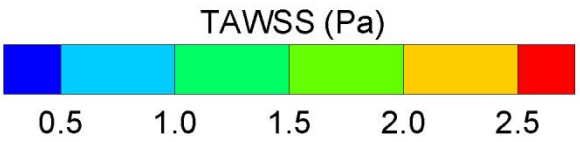

Figure 5.16: TAWSS distribution predicted upon the luminal surface of the artery for Stent A (top), Stent B (middle) and Stent C (bottom).

Stent D - Mean TAWSS = 0.797 Pa

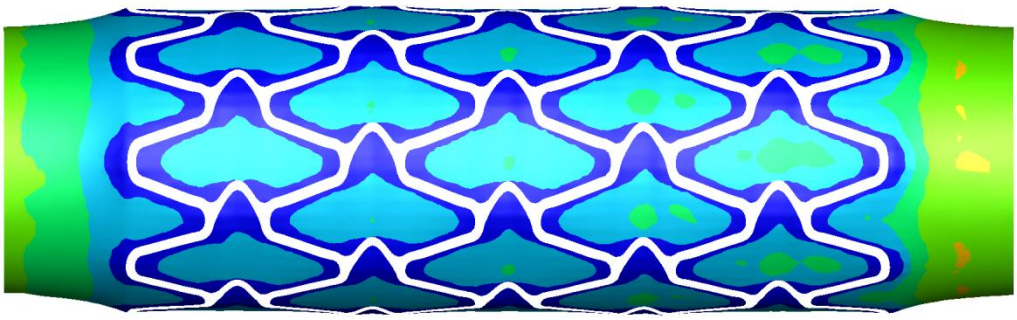

Stent E - Mean TAWSS = 0.731 Pa

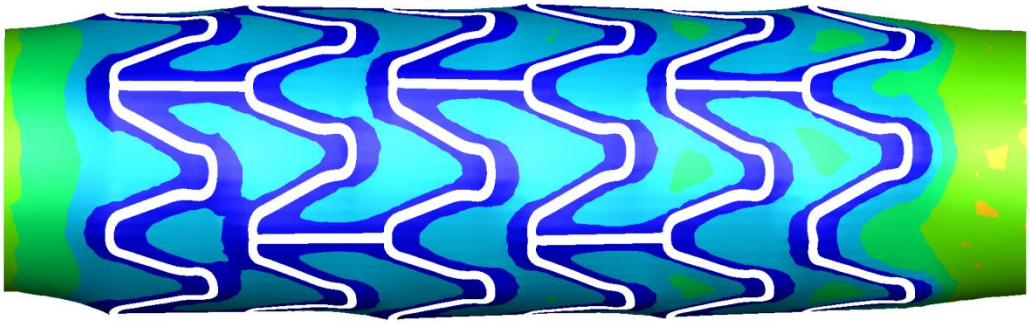

Stent F - Mean TAWSS = 1.124 Pa

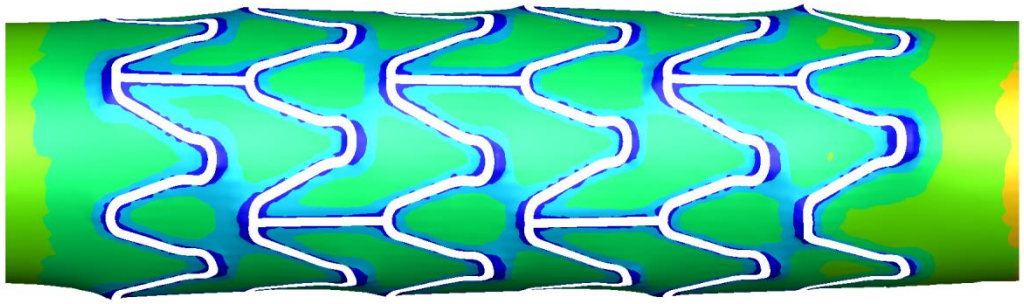

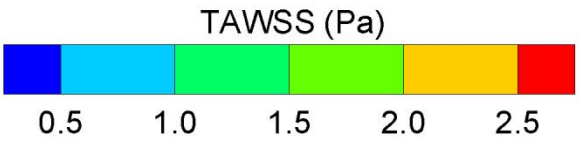

Figure 5.17: TAWSS distribution predicted upon the luminal surface of the artery for Stent D (top), Stent E (middle) and Stent F (bottom).

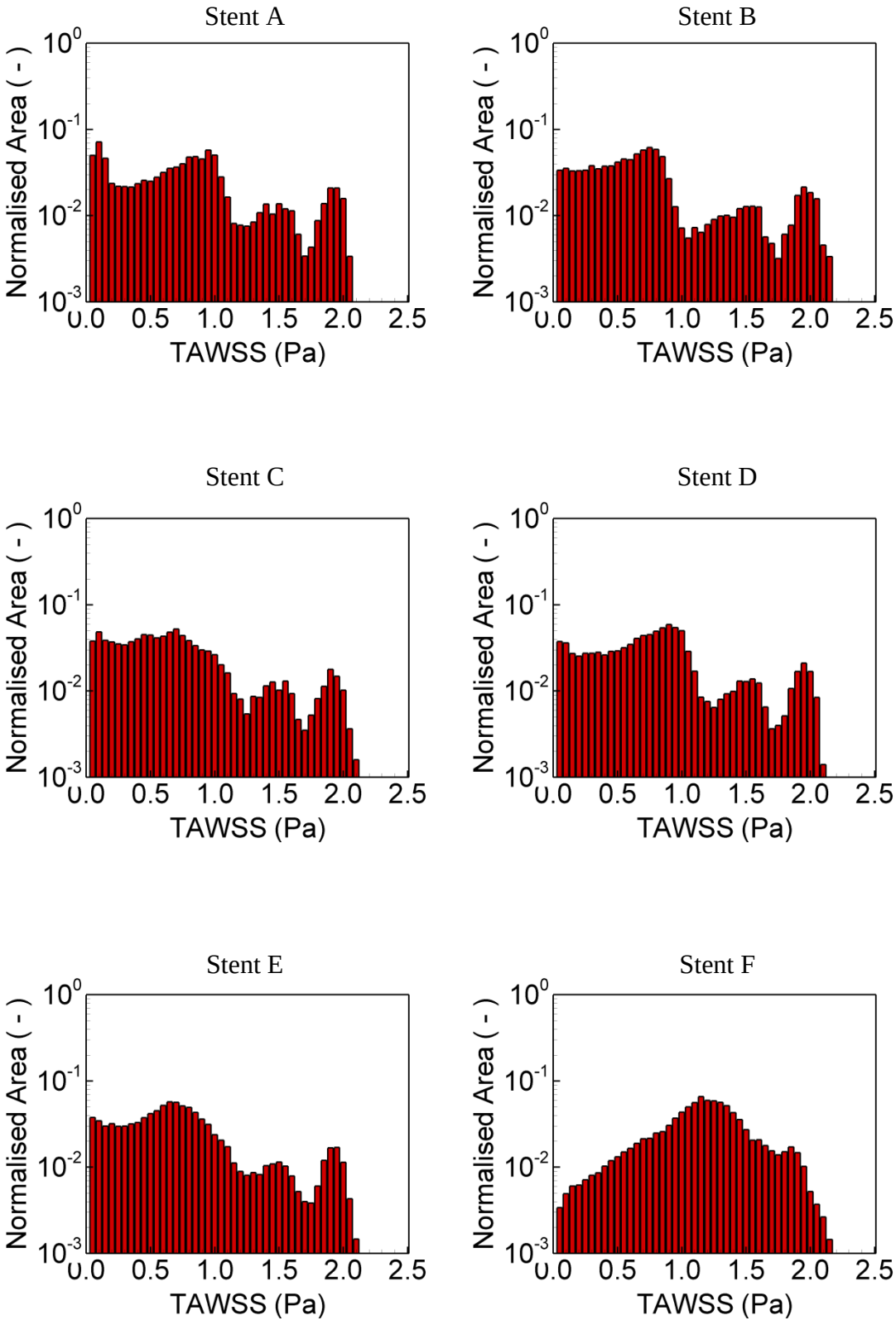

Figure 5.18: TAWSS distribution predicted upon the luminal surface of the artery for each of the investigated stents.

5.3.4 Oscillatory Shear Index

The OSI distribution predicted upon the luminal surface of the coronary artery for each of the investigated stents is shown in Figure 5.19 and Figure 5.20 and the total area of the luminal surface that was subject to different magnitudes of OSI is shown in Figure 5.21. In each of the CFD analyses, the majority of the luminal surface was subjected to low values of OSI (<0.10) and the peak values of OSI were observed in the proximal region of the artery where the stent struts were aligned perpendicular to the main flow direction. As shown in Table 5.5, the highest mean OSI of 0.018 was observed with Stent C. This was attributed to the fact that Stent C had a relatively high strut thickness of 0.13 mm and a large number of its struts were also aligned perpendicular to the main flow direction. Conversely, the lowest mean OSI of 0.009 was observed with Stent F. This was attributed to the fact that Stent F had the lowest strut thickness of 0.05 mm and the majority of its struts were aligned parallel to the main flow direction. For each of the investigated stents, the standard deviation of the OSI distribution was quite high. This implies a high variance about the mean OSI and was attributed to the fact that the majority of the luminal surface was subjected to either relatively high or low values of OSI. For each of the investigated stents, the skewness of the OSI distribution was between 7 and 35. This implies that each OSI distribution was strongly skewed to the right and the majority of the luminal surface was subjected to OSI values that were lower than the mean OSI. Based upon these results, it is likely that Stent C would have the greatest impact upon the oscillatory nature of the WSS distribution within the artery whilst Stent F would have the least impact upon the oscillatory nature of the WSS distribution within the artery.

Stent	μ_{aw} (-)	σ_{aw} (-)	S_{aw} (-)
A	0.016	0.021	7.82
B	0.016	0.018	9.12
C	0.018	0.021	8.18
D	0.015	0.017	8.90
E	0.017	0.020	9.53
F	0.009	0.006	32.43

Table 5.5: Statistical analysis of the OSI distribution predicted upon the luminal surface of the artery for each of the investigated stents.

Stent A - Mean OSI = 0.016

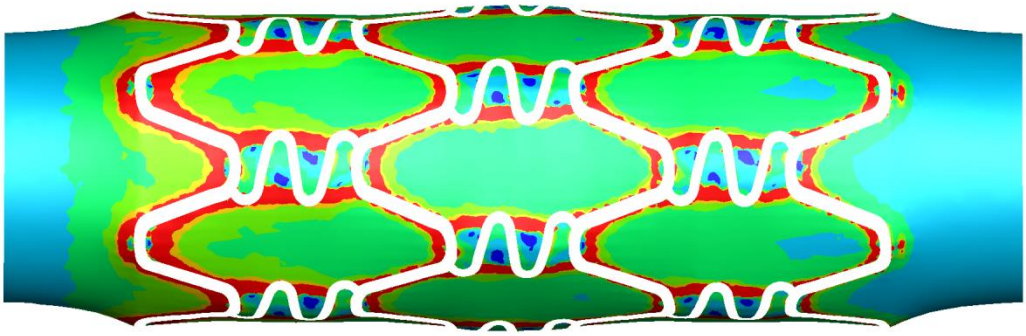

Stent B - Mean OSI = 0.016

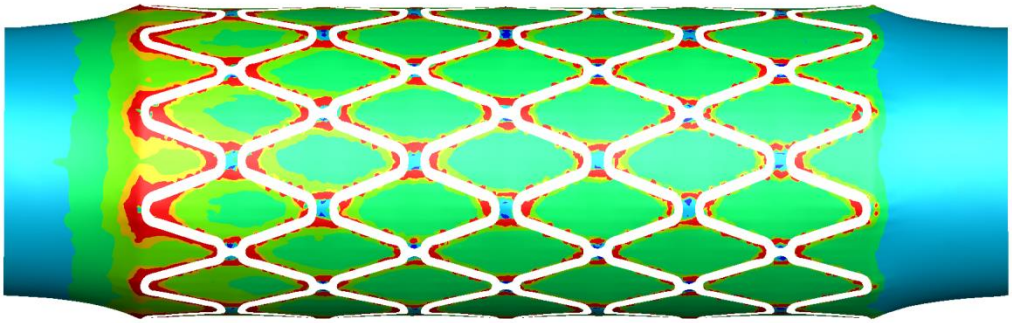

Stent C - Mean OSI = 0.018

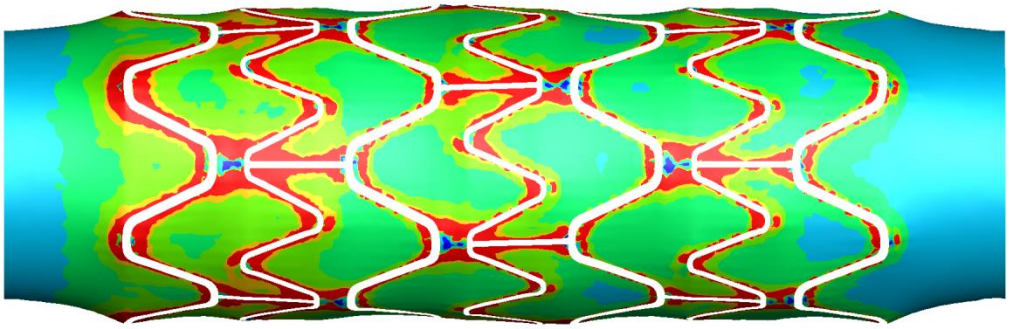

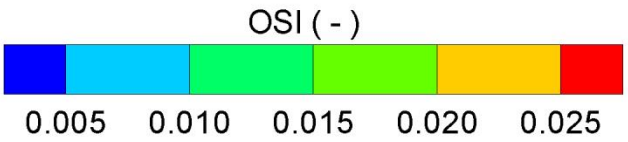

Figure 5.19: OSI distribution predicted upon the luminal surface of the artery for Stent A (top), Stent B (middle) and Stent C (bottom).

Stent D - Mean OSI = 0.015

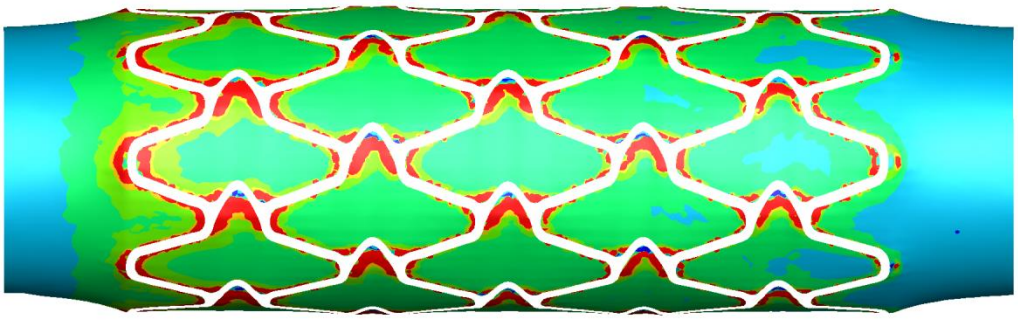

Stent E - Mean OSI = 0.017

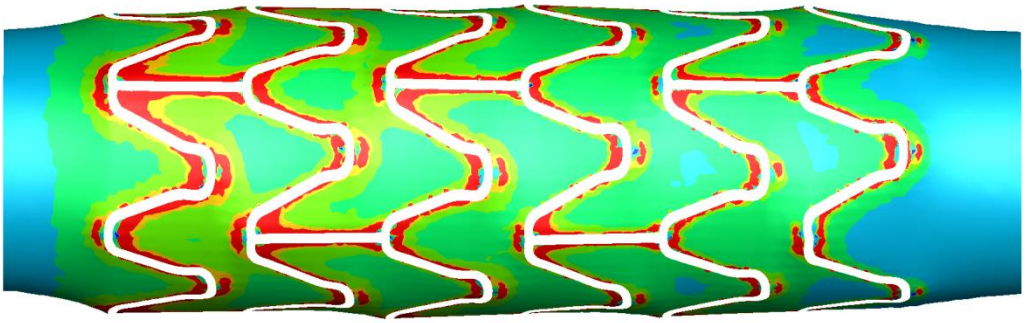

Stent F - Mean OSI = 0.009

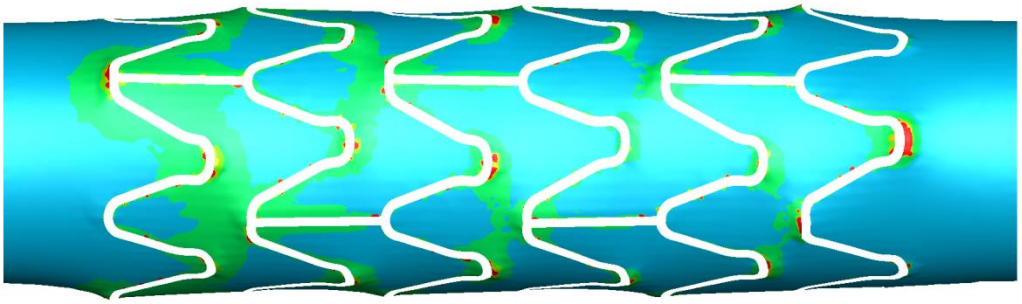

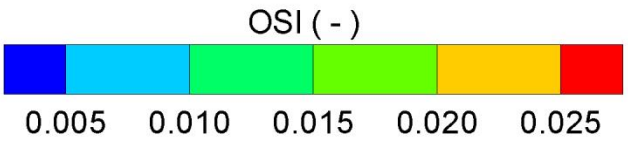

Figure 5.20: OSI distribution predicted upon the luminal surface of the artery for Stent D (top), Stent E (middle) and Stent F (bottom).

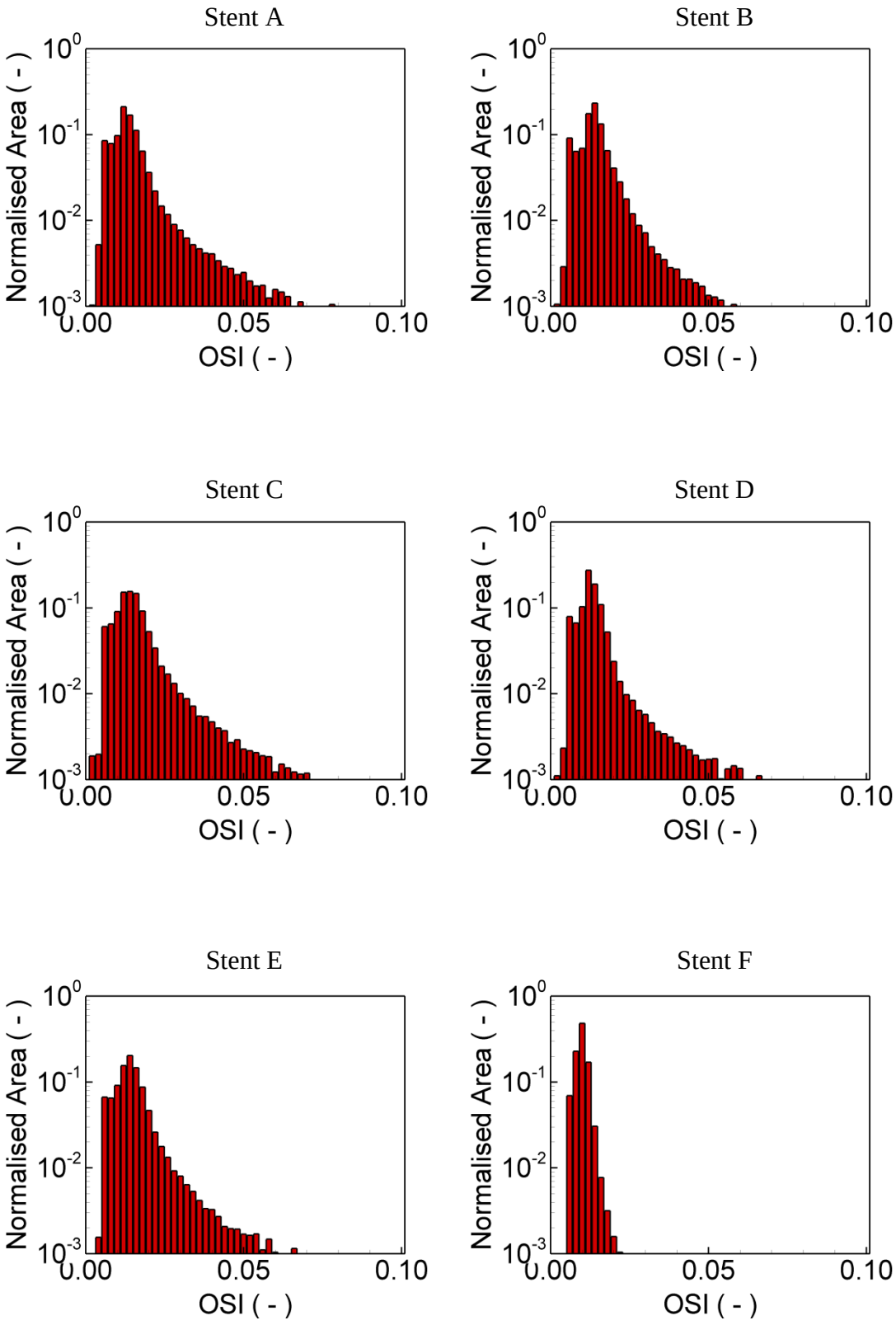

Figure 5.21: OSI distribution predicted upon the luminal surface of the artery for each of the investigated stents.

5.3.5 Relative Residence Time

The RRT distribution predicted upon the luminal surface of the coronary artery for each of the investigated stents is shown in Figure 5.22 and Figure 5.23 and the total area of the luminal surface that was subject to different magnitudes of RRT is shown in Figure 5.24. In each of the CFD analyses, the peak values of RRT were observed next to the stent struts and this was particularly apparent in regions where the struts were in close proximity to one another and aligned perpendicular to the main flow direction. As shown in Table 5.6, the highest mean RRT of 4.97 Pa^{-1} was observed with Stent A. This was attributed to the fact that Stent A exposed a relatively large portion of the luminal surface to coincident regions of low TAWSS and high OSI. Conversely, the lowest mean RRT of 1.36 Pa^{-1} was observed with Stent F. This was due to the fact that Stent F exposed a relatively small portion of the luminal surface to coincident regions of both low TAWSS and high OSI. For each of the investigated stents, the standard deviation of the RRT distribution was very high. This implies a high variance about the mean RRT and was attributed to the fact that the majority of the luminal surface was subjected to either relatively high or low values of RRT. For each of the investigated stents, the skewness of the RRT distribution was between 9 and 150. This implies that each of the RRT distributions was strongly skewed to the right and that the majority of the luminal surface was subjected to RRT values that were lower than the mean RRT. As the RRT takes the magnitude and the oscillation of the WSS distribution into account, it is likely that Stent A would have the greatest impact on the hemodynamic environment within the artery and Stent F would have the least impact on the hemodynamic environment within the artery.

Stent	μ_{aw} (Pa^{-1})	σ_{aw} (Pa^{-1})	S_{aw} (-)
A	4.97	11.80	10.07
B	4.19	12.24	15.62
C	4.82	27.38	150.95
D	3.89	9.96	9.10
E	4.26	14.05	29.28
F	1.36	4.12	38.86

Table 5.6: Statistical analysis of the RRT distribution predicted within the coronary artery for each of the investigated stents.

Stent A - Mean RRT = 4.97 Pa^{-1}

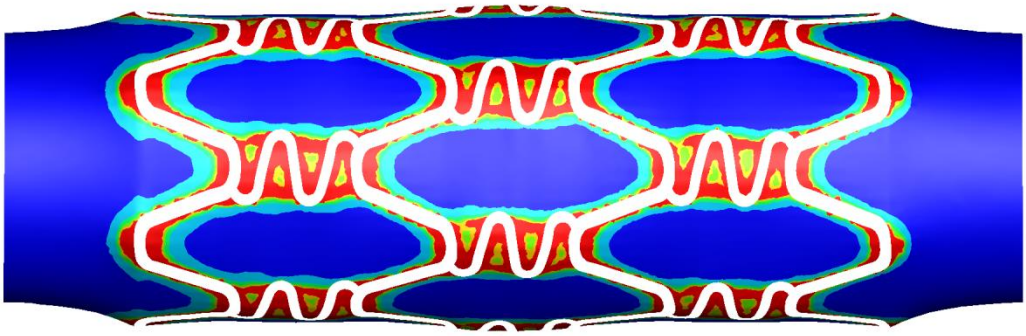

Stent B - Mean RRT = 4.19 Pa^{-1}

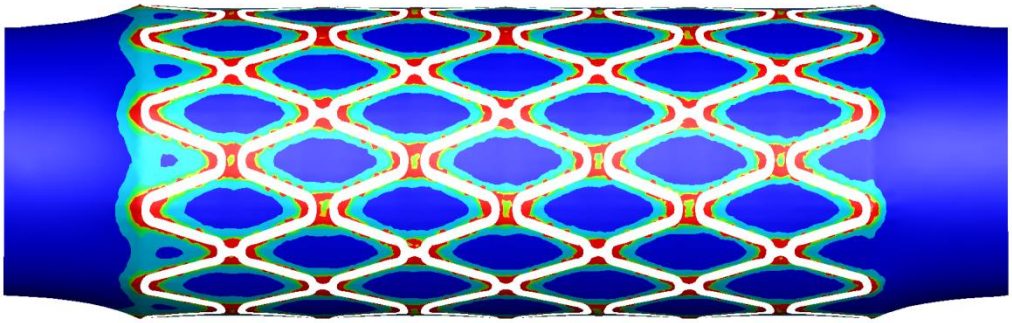

Stent C - Mean RRT = 4.82 Pa^{-1}

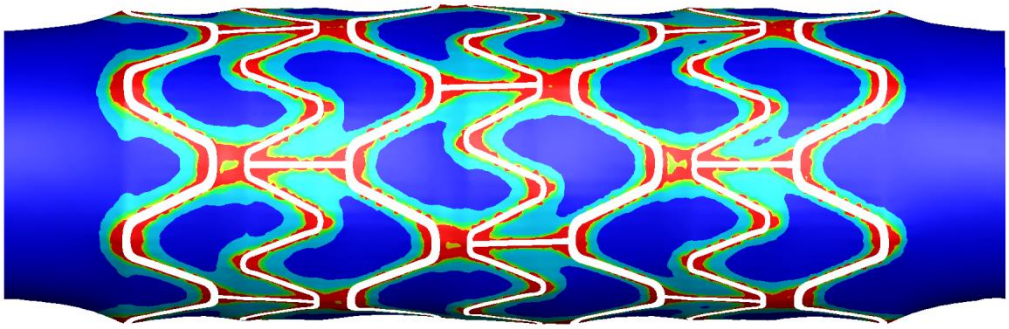

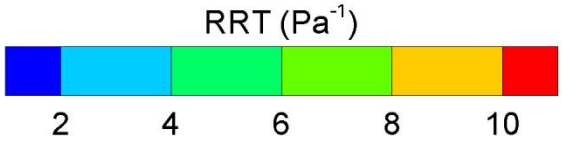

Figure 5.22: RRT distribution predicted upon the luminal surface of the artery for Stent A (top), Stent B (middle) and Stent C (bottom).

Stent D - Mean RRT = 3.89Pa^{-1}

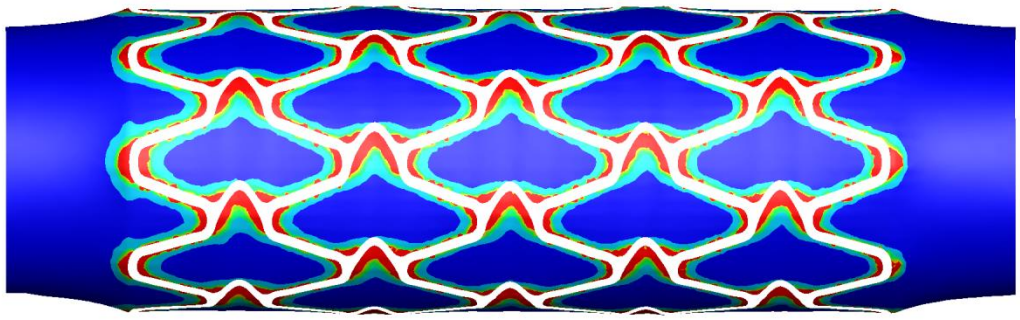

Stent E - Mean RRT = 4.26 Pa^{-1}

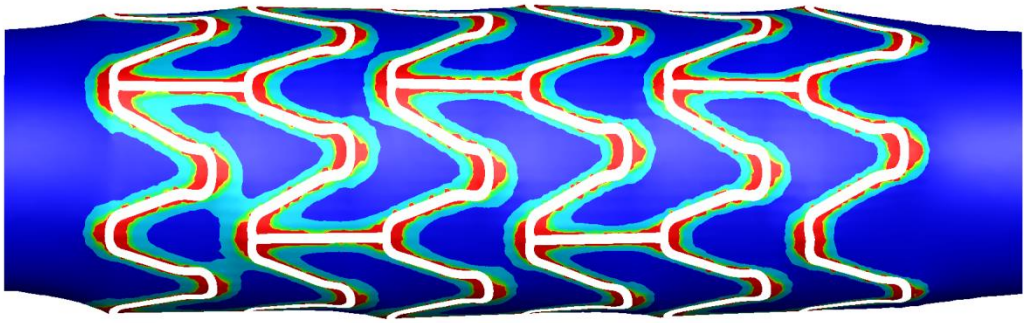

Stent F - Mean RRT = 1.36 Pa^{-1}

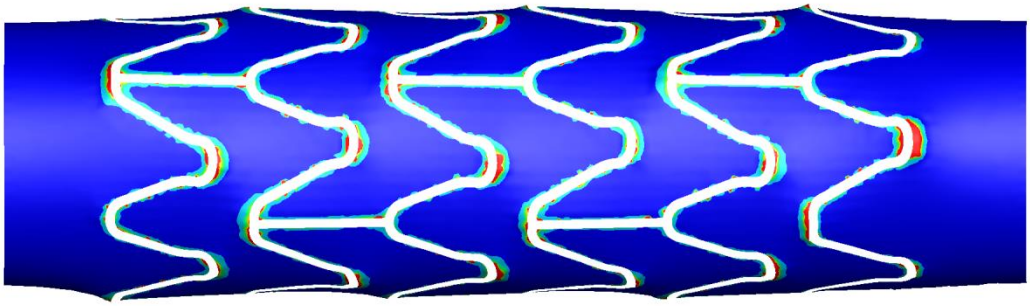

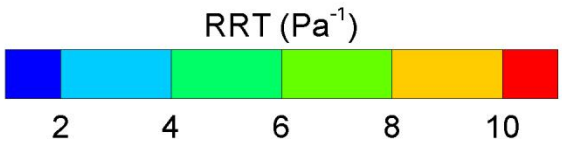

Figure 5.23: RRT distribution predicted upon the luminal surface of the artery for Stent D (top), Stent E (middle) and Stent F (bottom).

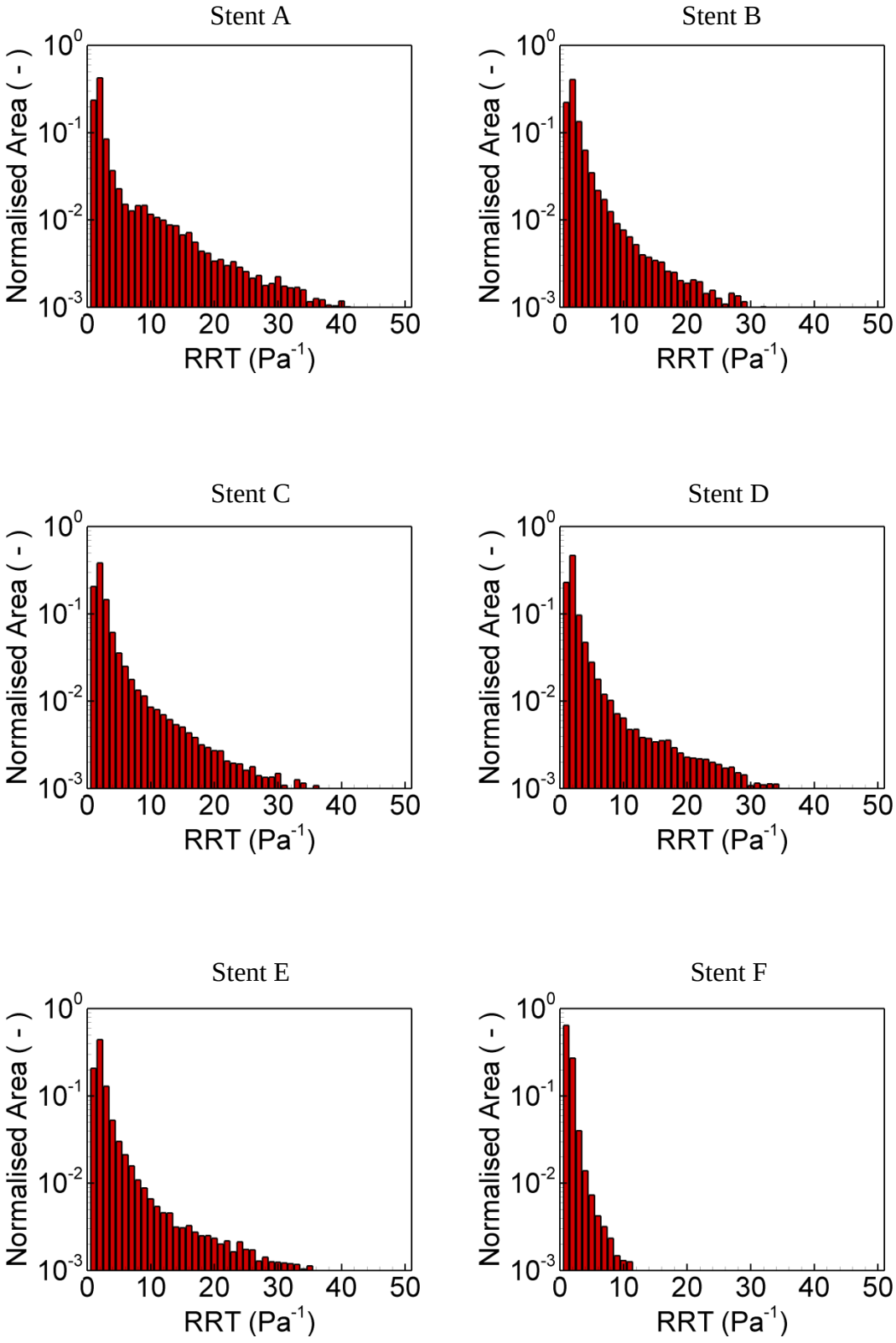

Figure 5.24: RRT distribution predicted upon the luminal surface of the artery for each of the investigated stents.

5.3.6 Discussion

As shown in Table 5.7, when the investigated stents are ranked from best to worst in terms of the mechanical and hemodynamic variables, Stents D and F are consistently ranked as the best-performing stents whilst Stents A, C and E are consistently ranked as the worst-performing stents. Based upon these results, it is likely that Stents D and F would be less susceptible to in-stent restenosis than Stents A, C and E in a clinical setting. Comparing the geometrical properties of the investigated stents, it is hard to determine why Stents D and F are consistently ranked as the best-performing stents. Stent D has a closed-cell, peak-to-peak configuration and a relatively high number of circumferential cells whilst Stent F has an open-cell, peak-to-valley configuration and a relatively low number of circumferential cells. It is also difficult to determine why Stents A, C and E are consistently ranked as the worst-performing stents. Stent A has a closed-cell, peak-to-peak configuration and features a relatively high number of circumferential cells whilst both Stents C and E have an open-cell, peak-to-valley configuration and a relatively low number of circumferential cells. Comparing the common geometrical properties of each of the investigated stents, the only property that consistently distinguishes the best-performing stents from the worst-performing stents is the strut thickness. Stents D and F feature relatively low strut thicknesses of 0.10 and 0.05 mm, respectively, whilst Stents A, C and E feature relatively high strut thicknesses of 0.14, 0.13 and 0.13 mm, respectively. The actual dependence between the common geometrical properties of the investigated stents and the mechanical and hemodynamic variables of interest is evaluated in the following section.

ES ES_{max} (kPa)	ES μ_{vw} (kPa)	TAWSS μ_{aw} (Pa)	OSI μ_{aw} (-)	RRT μ_{aw} (Pa^{-1})
F – 39.60	F - 3.49	F - 1.124	F - 0.009	F - 1.36
D – 42.10	D - 7.34	D - 0.797	D - 0.015	D - 3.89
B – 58.98	C - 8.79	A - 0.767	B - 0.016	B - 4.19
C – 67.82	B - 8.83	B - 0.750	A - 0.016	E - 4.26
E – 74.37	E - 9.21	E - 0.731	E - 0.017	C - 4.82
A – 83.84	A - 10.72	C - 0.703	C - 0.018	A - 4.97

Table 5.7: Ranking the investigated stents from best (top) to worst (bottom) in terms of both the mechanical and hemodynamic variables of interest.

5.4 Stent Design and Performance

5.4.1 Monotonic Dependence

To investigate the relationship between stent design and performance the number of longitudinal cells, number of circumferential cells, strut width, strut thickness and the stent-to-artery surface area were identified as common geometrical properties of the investigated stents. The dependence between these geometrical properties and the mechanical and hemodynamic variables was then assumed to be monotonic and the strength of this assumed monotonic dependence was measured using the Spearman rank correlation coefficient (SC). The SC is a statistical index that is used to measure the strength of the monotonic dependence between two variables. For n independent samples X_i and Y_i of two variables X and Y, the SC is calculated as follows:

$$\mathrm{SC} = \frac{\sum_{i=1}^{n}(x_i - \bar{x})(y_i - \bar{y})}{\sqrt{\sum_{i=1}^{n}(x_i - \bar{x})^2}\sqrt{\sum_{i=1}^{n}(y_i - \bar{y})^2}} \tag{5.1}$$

The terms x_i and y_i denote the ranked values of the variables X and Y whereas the terms $\bar{x}$ and $\bar{y}$ denote the mean values of the ranked values x_i and y_i, respectively. The magnitude of the SC varies from 1 to -1 with an SC of 1 indicating a perfect positive monotonic dependence, i.e. variable Y increases as variable X increases in a perfect monotonic manner, and an SC of -1 indicating a perfect negative monotonic dependence, i.e. variable Y decreases as variable X increases in a perfect monotonic manner. Finally, an SC of 0 indicates that there is no monotonic dependence between the two variables. The general guidelines shown in Table 5.8 are often employed to interpret the strength of the monotonic dependence between two variables.

Absolute Value	Interpretation
0.00 < Coefficient ≤ 0.15	Too low the be meaningful
0.15 < Coefficient ≤ 0.30	Weak dependence
0.30 < Coefficient ≤ 0.50	Low dependence
0.50 < Coefficient ≤ 0.70	Moderate dependence
0.70 < Coefficient ≤ 0.90	Strong dependence
0.90 < Coefficient ≤ 1.00	Very strong dependence

Table 5.8: Interpretation of the calculated correlation coefficient.

Following the calculation of the SC for each individual combination of the common geometrical properties and the mechanical and hemodynamic variables of interest, Student's t-distribution was employed to test the significance of the SC. For each individual SC, the corresponding t-statistic was calculated as follows:

$$t_s = \mathrm{SC}\sqrt{\frac{n-2}{1-\mathrm{SC}^2}} \tag{5.2}$$

For each individual SC, the calculated t-statistic was then employed to determine a corresponding p-value and $p < 0.05$ was considered to imply statistical significance. As shown in Table 5.9, the only common geometrical property that demonstrated a strong monotonic dependence with any of the mechanical or hemodynamic variables of interest was the strut thickness. Specifically, a statistically-significant very strong positive monotonic dependence was observed between strut thickness and both the maximum ES (SC = 0.97, $p < 0.01$) and mean RRT (SC = 0.97, $p < 0.01$) whilst a strong positive monotonic dependence was observed between the strut thickness and both the mean ES (SC = 0.85, $p = 0.03$) and mean OSI (SC = 0.79, $p < 0.06$). These results suggest that a strong positive monotonic dependence exists between the strut thickness and the maximum ES, the mean ES, the mean OSI and the mean RRT. The functional nature of this dependence is evaluated in the following section.

Variable	ES ES_{max}	ES μ_{vw}	TAWSS μ_{aw}	OSI μ_{aw}	RRT μ_{aw}
Longitudinal Cells	SC = -0.33 p = 0.52	SC = -0.27 p = 0.60	SC = -0.46 p = 0.36	SC = 0.15 p = 0.77	SC = -0.21 p = 0.69
Circumferential Cells	SC = 0.03 p = 0.95	SC = 0.15 p = 0.77	SC = 0.40 p = 0.44	SC = -0.33 p = 0.52	SC = 0.03 p = 0.95
Strut Thickness	SC = 0.97 p < 0.01	SC = 0.85 p = 0.03	SC = -0.59 p = 0.22	SC = 0.79 p = 0.06	SC = 0.97 p < 0.01
Strut Width	SC = 0.34 p = 0.51	SC = 0.51 p = 0.31	SC = 0.51 p = 0.31	SC = -0.34 p = 0.51	SC = 0.17 p = 0.75
Stent-to-Artery Surface Area	SC = -0.15 p = 0.78	SC = 0.15 p = 0.78	SC = 0.38 p = 0.46	SC = -0.49 p = 0.32	SC = -0.23 p = 0.66

Table 5.9: Calculated Spearman coefficient (SC) and corresponding p-value.

5.4.2 Functional Dependence

In order to evaluate the functional nature of the strong monotonic dependence that was observed between the strut thickness and the maximum ES, mean ES, mean OSI and mean RRT, a scatter plot was generated for each combination of these variables. As shown in Figure 5.25, the monotonic dependence between each combination of these variables was approximately linear. As such, the strength of this approximate linear dependence was then evaluated using the Pearson product-moment correlation coefficient (PC). The PC is another statistical index that is employed to measure the strength of the linear dependence between two variables. For n independent samples X_i and Y_i of two variables X and Y, the PC is calculated as follows:

$$\mathrm{PC} = \frac{\sum_{i=1}^{n}(X_i - \bar{X})(Y_i - \bar{Y})}{\sqrt{\sum_{i=1}^{n}(X_i - \bar{X})^2}\sqrt{\sum_{i=1}^{n}(Y_i - \bar{Y})^2}} \tag{5.3}$$

The terms X_i and Y_i denote the values of the variables X and Y, respectively. Like the SC, the magnitude of the PC may vary between 1 and -1 with a PC of 1 indicating a perfect positive linear dependence and a PC of -1 indicating a perfect negative linear dependence. The guidelines shown in Table 5.8 are again used to assess the strength of the linear dependence between two variables. Following the calculation of the PC between the strut thickness and the maximum ES, mean ES, mean OSI and mean RRT, Student's t-distribution was used to test for significance and the calculation of the subsequent p-value was carried out as previously described. As shown in Table 5.10, a statistically-significant very strong positive linear dependence was observed between the strut thickness and the mean ES (PC = 0.95, $p < 0.01$), the mean OSI (PC = 0.94, $p < 0.01$) and the mean RRT (PC = 0.95, $p < 0.01$) whilst a statistically-significant strong positive linear dependence was also observed between the strut thickness and the maximum ES (PC = 0.88, $p = 0.02$). The various implications of the calculated dependencies are discussed in detail in the following section.

Variable	ES ES_{max}	ES μ_{vw}	OSI μ_{aw}	RRT μ_{aw}
Strut Thickness	PC = 0.88 p = 0.02	PC = 0.95 p < 0.01	PC = 0.94 p < 0.01	PC = 0.95 p < 0.01

Table 5.10: Calculated Pearson coefficient (PC) and corresponding p-value.

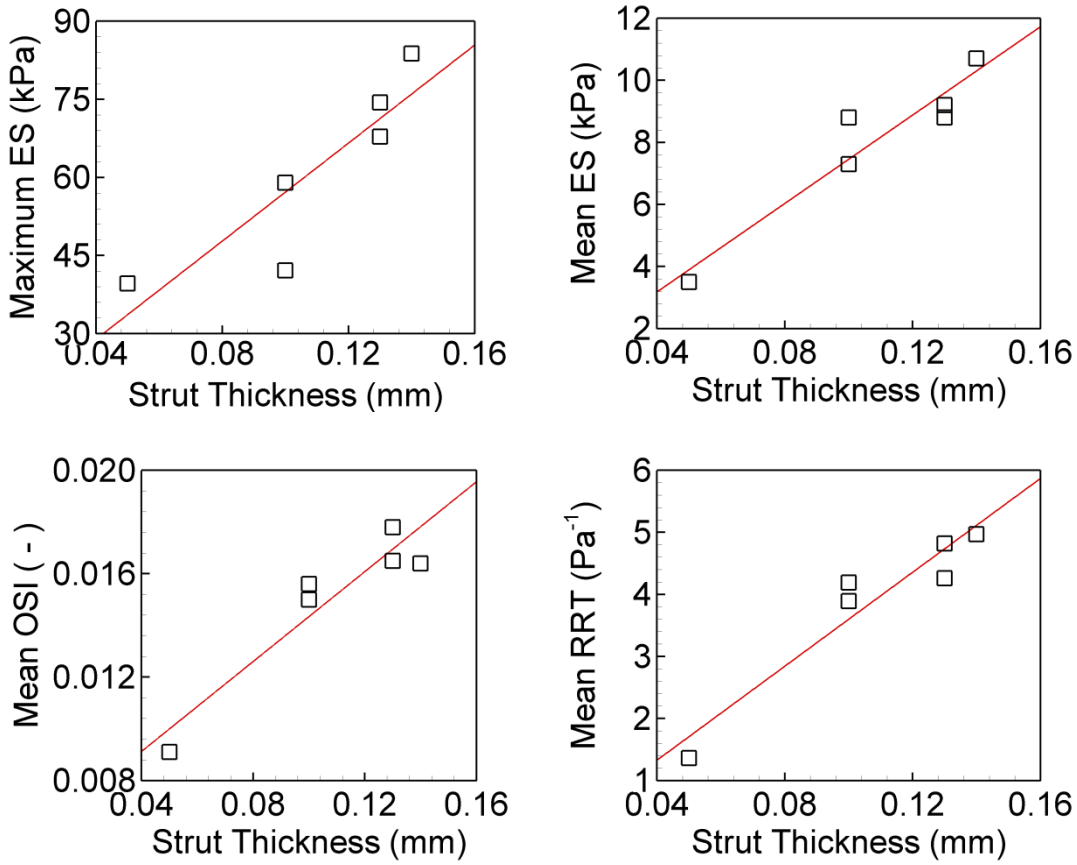

Figure 5.25: Approximate linear dependence observed between strut thickness and the maximum ES, the mean ES, the mean OSI and the mean RRT.

5.4.3 Discussion

As shown in Table 5.9, strut thickness was the only common geometrical property of the investigated stents that demonstrated a strong monotonic dependence with any of the mechanical or the hemodynamic variables of interest. Specifically, a statistically-significant strong positive monotonic dependence was observed between the strut thickness and the maximum ES, the mean ES, the mean OSI and the mean RRT. As shown in Figure 5.25, the functional nature of the strong monotonic dependence that was observed between the stent strut thickness and each variable was approximately linear. As shown in Table 5.10, a statistically-significant strong linear dependence was then identified between the strut thickness and each of these variables. These results suggest that a strong positive linear dependence exists between strut thickness and the maximum ES, the mean ES, the mean OSI and the mean RRT and that strut thickness is likely to dictate both the mechanical and hemodynamic impact of stent deployment within the artery. As such, stents that minimise strut thickness are likely to be less susceptible to in-stent restenosis within a clinical setting.

5.5 Comparison with Clinical Data

In order to determine if the proposed numerical methodology is capable of predicting the clinical performance of coronary stents, the predicted performance of three of the investigated stents was compared to the clinical performance of three similar stents, as reported in the large-scale ISAR-STEREO-I and ISAR-STEREO-II clinical trials. The ISAR-STEREO-I trial was designed to compare the performance of a thin strut and a thick strut variation of the Multilink RX Duet stent (Abbott Vascular) whereas the ISAR-STEREO-II trial was designed to compare the performance of a thin strut Multilink RX Duet stent and the thick strut BX-Velocity stent (Johnson & Johnson). As the geometrical configuration of Stents E and F closely resembles that of the thin and thick strut variations of the Multilink RX Duet stent, respectively, the predicted performance of Stents E and F was compared with the clinical performance of the thin and thick strut variations of the Multilink RX Duet stents, as reported in the ISAR-STEREO-I trial. Similarly, as the geometrical configuration of Stent A closely resembles that of the BX-Velocity stent, the predicted performance of Stents A and F was compared with the clinical performance of the BX-Velocity and the thin strut Multilink RX Duet stents, as reported in the ISAR-STEREO-II trial.

5.5.1 The ISAR-STEREO-I Trial

The ISAR-STEREO-I trial was a large-scale randomised unblinded trial that was carried out by Kastrati et al. in 2001 to evaluate whether reduced stent strut thickness results in improved angiographic and clinical results at follow-up [110]. During this trial, a total of 651 patients were randomised to receive either a thin strut Multilink RX Duet stent (n = 326) or a thick strut Multilink RX Duet stent (n = 325) for the treatment of symptomatic coronary heart disease due to lesions situated within native coronary arteries that were > 2.8 mm in diameter. The thin and thick strut Multilink RX Duet stents featured a strut thickness of 0.05 mm and 0.14 mm, respectively. The base-line demographic and clinical data was comparable between the two groups and procedural success was defined as both stent placement with a residual stenosis of < 30% and a thrombolysis in myocardial infarction flow grade of ≥ 2. Device success was defined as the achievement of procedural success with the randomly assigned stent. The primary end-point of the study was the incidence of angiographic in-stent restenosis, which was defined as a diameter stenosis of ≥ 50% in the stented segment or within the 5 mm proximal and distal segments at six month angiographic follow-

up. Secondary end-points included target-vessel revascularisation (TVR) and the rate of both death and myocardial ischemia at one year follow-up. All differences were assessed using the chi-square or Fisher's test for categorical data and the t-test for continuous data and $p < 0.05$ was considered statistically significant.

At six month follow-up, the incidence of angiographic in-stent restenosis was 15.0% for patients treated with the thin strut Multilink RX Duet stent and 25.8 % for patients treated with the thick strut Multilink RX Duet stent ($p < 0.05$). Furthermore, the incidence of TVR was 8.6% for patients treated with the thin strut Multilink RX Duet stent and 13.8% for patients treated with the thick strut Multilink RX Duet stent ($p < 0.05$). Late loss (LL), which is defined as the difference in the minimum lumen diameter measured immediately following stent deployment and that measured at six month follow-up, was 0.94 mm for patients treated with the thin strut Multilink RX Duet stent and 1.17 mm for patients treated with the thick strut Multilink RX Duet stent ($p < 0.05$). Based upon these results, the authors concluded that the use the thin strut Multilink RX Duet stent was associated with a significant reduction in the rate of angiographic in-stent restenosis, TVR and LL observed at follow-up. As shown in Table 5.11, the predicted performance of Stents E and F was in excellent agreement with the clinical performance of the thick strut Multilink RX Duet stent and the thin strut Multilink RX Duet stent, respectively. Specifically, the values of the maximum ES, the mean ES, the mean TAWSS, the mean OSI and the mean RRT all indicate that Stent E is likely to have a much greater impact upon both the mechanical and hemodynamic environment in a coronary artery. Based upon these results, Stent E is likely to be more susceptible to in-stent restenosis within a clinical setting.

5.5.2 The ISAR-STEREO-II Trial

The ISAR-STEREO-II trial was a large-scale randomised unblinded trial that was carried out by Pache et al. in 2003 in order to evaluate whether reduced stent strut thickness results in improved angiographic and clinical results at follow-up [111]. During this trial, a total of 611 patients were randomised to receive either a thin strut Multilink RX Duet stent ($n = 309$) or thick strut BX-Velocity stent ($n = 302$) for the treatment of symptomatic coronary heart disease due to lesions situated within native coronary arteries that were > 2.8 mm in diameter. The thin strut Multilink RX Duet stent and the BX-Velocity stent featured strut thicknesses of 0.05 mm and 0.14 mm,

respectively. The base-line demographic and clinical data was comparable between the two groups, although the lesions in the thin strut group were significantly more complex than those in the thick strut group ($p < 0.05$) and a higher portion of patients in the thick strut group were suffering from chronic occlusions ($p < 0.06$). Procedural success was defined as stent deployment with a residual stenosis of < 30% and a thrombolysis in myocardial infarction flow grade of ≥ 2. Device success was defined as the achievement of procedural success with the randomly assigned stent. Again, the primary end-point of the study was incidence of angiographic in-stent restenosis, which was defined as a diameter stenosis of ≥ 50% within either the stented segment or within the 5 mm proximal and distal segments at six month angiographic follow-up. Secondary end-points included TVR and the rate of both death and myocardial ischemia at one year follow-up. All differences between the groups were assessed using either the chi-square test or Fisher's test for categorical data and the t-test for continuous data and $p < 0.05$ was considered statistically-significant.

At six month follow-up, the incidence of angiographic in-stent restenosis was 17.9% for patients treated with the thin strut Multilink RX Duet stent and 31.4% for patients treated with the thick strut BX-Velocity stent ($p < 0.05$). In a similar fashion, the incidence of TVR was 12.3% for patients treated with the thin strut Multilink RX Duet stent and 21.9% for patients treated with the thick strut BX-Velocity stent ($p < 0.05$). LL, which was again defined as the difference in minimum lumen diameter measured immediately following stent deployment and that measured at six month follow-up, was 0.93 mm for patients treated with the thin strut Multilink RX Duet stent and 1.19 mm for patients treated with the thick strut BX-Velocity stent ($p < 0.05$). Based upon these results, the authors again concluded that the use the thin strut Multilink RX Duet stent was associated with a significant reduction in the rates of angiographic in-stent restenosis, TVR and LL at six month follow-up. As shown in Table 5.12, the predicted performance of Stents A and F was in good agreement with the clinical performance of the thick strut BX-Velocity stent and the thin strut Multilink RX Duet stent, respectively. Specifically, the values of the maximum ES, the mean ES, the mean TAWSS, the mean OSI and the mean RRT all indicate that Stent A would have a greater impact upon both the mechanical and hemodynamic environment within a coronary artery. Based on the results, Stent A is likely to be more susceptible to in-stent restenosis within a clinical setting.

Variable	Clinical Results	
	Multilink RX Duet (Thick Strut)	Multilink RX Duet (Thin Strut)
In-Stent Restenosis	25.8 %	15.0 %
TVR	13.8 %	8.6 %
LL	1.17 mm	0.94 mm
Variable	Predicted Results	
	Stent E	Stent F
Maximum ES	74.37 kPa	39.60 kPa
Mean ES	9.21 kPa	3.49 kPa
Mean TAWSS	0.731 Pa	1.124 Pa
Mean OSI	0.017	0.009
Mean RRT	4.26 Pa^{-1}	1.36 Pa^{-1}

Table 5.11: Comparison of the clinical results of the ISAR-STEREO-I trial with the predicted performance of Stents E and F.

Variable	Clinical Results	
	BX-Velocity	Multilink RX Duet (Thin Strut)
In-Stent Restenosis	31.4 %	17.9 %
TVR	21.9 %	12.3 %
LL	1.19 mm	0.93 mm
Variable	Predicted Results	
	Stent A	Stent F
Maximum ES	83.84 kPa	39.60 kPa
Mean ES	10.72 kPa	3.49 kPa
Mean TAWSS	0.767 Pa	1.124 Pa
Mean OSI	0.016	0.009
Mean RRT	4.97 Pa^{-1}	1.36 Pa^{-1}

Table 5.12: Comparison of the clinical results of the ISAR-STEREO-II trial with the predicted performance of Stents A and F.

5.5.3 Discussion

In order to determine if the proposed numerical methodology is capable of predicting the clinical performance of coronary stents, the predicted performance of Stents A, E and F was compared with the clinical performance of the BX-Velocity stent and the thin strut and thick strut variations of the Multilink RX Duet stent, respectively, as reported in the large-scale ISAR-STEREO-I and ISAR-STEREO-II trials. For both of the clinical trials, the predicted performance of the investigated stents was found to be in excellent agreement with the clinical performance of the investigated stents. Specifically, the proposed methodology successfully identified the stent that resulted in the higher rate of angiographic in-stent restenosis in both of the clinical trials as the stent that was likely to be more susceptible to in-stent restenosis within a clinical setting. Furthermore, the results of both the ISAR-STEREO-I and ISAR-STEREO-II trials identified stent strut thickness as a strong risk factor for in-stent restenosis and this corroborates the results presented in Section 5.4. As there are various factors which are not accounted for in the proposed methodology that may have influenced the results of the ISAR-STERO-I and ISAR-STEREO-II trials, the close agreement between the results does not validate the proposed methodology. The relatively close agreement between the results does indicate, however, that the methodology may predict certain aspects of the clinical performance of coronary stents.

5.6 Summary

In this chapter, the results obtained from the application of the proposed numerical methodology to six different generic stents are presented. The general performance of the investigated stents was first evaluated in terms of their deployed configuration and deployment characteristics. The mechanical and hemodynamic impact of the six investigated stents was then evaluated in terms of the ES distribution predicted in the artery and the TAWSS, OSI and RRT distribution predicted on the luminal surface of the artery, respectively. In order to evaluate the relationship between stent design and performance the predicted performance of each of the investigated stents was then compared and contrasted and a statistically-significant strong linear dependence was observed between the strut thickness and the maximum ES, mean ES, mean OSI and mean RRT. Finally, to determine whether the proposed methodology is capable of predicting the clinical performance of coronary stents, the predicted performance

of three of the investigated stents was compared to the clinical performance of three similar stents, as reported in the large-scale ISAR-STEREO-I and ISAR-STEREO-II clinical trials. For both clinical trials, the predicted performance of the investigated stents was in excellent agreement with the clinical performance of the similar stents. This close comparison of the predicted results and the clinical results suggests that the proposed methodology may predict certain aspects of the clinical performance of balloon-expandable coronary stents. In the following chapter, the conclusions drawn from this work, the various limitations of the proposed numerical methodology and a number of potential avenues for future research are discussed.

CHAPTER 6
CONCLUSION

6.1 Introduction

In recent years, a number of clinical studies have linked in-stent restenosis following coronary stent deployment to both arterial injury and altered vessel hemodynamics. In light of these clinical results, a significant body of research has been carried out to investigate the relationship between stent design and both arterial injury and altered vessel hemodynamics. Due to the difficulty involved in the experimental evaluation of these phenomena, however, a substantial portion of this research has been carried out using computational methods of analysis. Over the past decade, a large number of studies have employed CS and CFD analyses to investigate either the mechanical or hemodynamic impact of stent deployment in a coronary artery. In many of these studies, the results of the analyses are employed to identify potential geometrical modifications that may improve the clinical performance of the investigated stents. In the vast majority of these studies, however, the fact that in-stent restenosis has been strongly correlated with both arterial injury and altered vessel hemodynamics is overlooked. As such, it is possible that the proposed geometrical modifications may actually hinder the clinical performance of the investigated stents.

In various CS analyses of coronary stent deployment, for example, geometrical modifications which are likely to reduce the mechanical impact of the investigated stents are recommended. As these studies focus solely upon the mechanical impact of the investigated stents, however, the corresponding hemodynamic impact of the proposed geometrical modifications is neglected. Similarly, in CFD analyses of coronary stent deployment, geometrical modifications which are likely to reduce the hemodynamic impact of the investigated stents are generally recommended. As these

studies focus solely on the hemodynamic impact of the investigated stents, however, the corresponding mechanical impact of the proposed geometrical modifications is neglected. As in-stent restenosis has been linked to both arterial injury and altered vessel hemodynamics, the sequential analysis of the mechanical and hemodynamic impact of coronary stent deployment should yield an improved indication of stent performance. Despite this observation, however, few studies have considered both the mechanical and hemodynamic impact of stent deployment. Furthermore, in the few studies that have considered both the mechanical and hemodynamic impact of coronary stent deployment, only a single stent (or a single repeating unit) has been considered and the results were evaluated using variables that may not fully elucidate the mechanical and hemodynamic impact of the investigated stents.

The aim of this research was to develop a numerical methodology for evaluating the performance of balloon-expandable coronary stents in terms of their mechanical and hemodynamic impact within the coronary artery. The proposed methodology is divided into two stages. In the first stage, a CS model of the investigated stent is first generated and a nonlinear CS analysis is then carried out to simulate its deployment within a coronary artery. In the second stage, the results of the CS analysis are first used to generate a realistically-deformed CFD model of the stented coronary lumen and a transient CFD analysis is then carried out to simulate pulsatile flow conditions within a coronary artery. Following the completion of the analyses, the performance of the investigated stent is evaluated in terms of its mechanical and hemodynamic impact within the coronary artery. Following the completion of the computational analyses, the general performance of the investigated stent is evaluated in terms of its deployed configuration, deployed diameter and its deployment characteristics. Both the mechanical and hemodynamic impact of the investigated stent are then evaluated in terms of the stress distribution predicted in the artery and the WSS distribution predicted upon the luminal surface of the artery, respectively. In order to ensure that the mechanical and hemodynamic impact of the investigated stent is fully elucidated, a number of mechanical and hemodynamic variables of interest are then calculated. Finally, the distribution of the mechanical and hemodynamic variables of interest is then evaluated using a comprehensive statistical method of analysis.

In order to demonstrate its application, the proposed methodology was applied to several generic stents that each resembled commercially-available coronary stents.

The investigated stents featured a fixed length and initial undeployed diameter but varied in terms of their strut configuration. Comparing the predicted performance of the investigated stents revealed that the thinner strut stents had a lower impact on the mechanical and hemodynamic environment within the artery. In order to evaluate the relationship between stent design and performance, the number of longitudinal stent cells, number of circumferential stent cells, strut thickness, strut width and the stent-to-artery surface area were each identified as common geometrical properties of the investigated stents. A statistical analysis was then carried out to evaluate the strength of the monotonic dependence between these common geometrical properties and the mechanical and hemodynamic variables. Following the completion of the statistical analysis, a strong monotonic dependence was observed between the strut thickness and the maximum ES, mean ES, mean OSI and mean RRT. As the functional nature of the monotonic dependence that was observed between the strut thickness and each of the dependent variables was approximately linear, a second statistical analysis was carried out to measure the strength of the linear dependence between the variables. Following the completion of this analysis, a strong linear dependence was observed between the strut thickness and the maximum ES, mean ES, mean OSI and mean RRT. Finally, in order to determine whether the proposed methodology is capable of predicting the clinical performance of coronary stents, the predicted performance of three of the investigated stents was compared to the clinical performance of three similar stents, as reported in the large-scale ISAR-STERO-I and ISAR-STEREO-II trials. For both of the clinical trials, the predicted performance of the investigated stents was in good agreement with the clinical performance of the similar stents in so far as the proposed methodology identified the stents that resulted in lower rates of angiographic in-stent restenosis, TVR and LL at six month follow-up.

In a randomised clinical study carried out by Kastrati et al. in 2001 to determine whether differences in stent design resulted in different clinical outcomes following coronary stent deployment, 1,147 patients were randomly assigned to receive one of five different stainless-steel coronary stents [112]. The investigated stents were the Multilink stent (Abbott Laboratories), the NIR stent (Boston Scientific), the Inflow-Gold stent (Boston Scientific), the Palmaz-Schatz stent (Johnson & Johnson) and the PURA-A stent (Devon Medical, Hamburg, Germany). At one-year follow-up, the primary endpoint of event-free survival ranged from 69.4 to 82.4% amongst patients

treated with the five different stents ($p < 0.05$). In a similar fashion, diameter stenosis at six month follow-up varied from 38.1 to 45.6% ($p < 0.05$), LL ranged from 1.01 to 1.20 mm ($p = 0.085$) and the incidence of angiographic in-stent restenosis varied between 25.3 and 35.9% ($p = 0.145$) amongst patients treated with the five different stents. Based on these results it was concluded that stent design has a major impact on the long-term clinical outcome following coronary stent deployment. The results obtained from the present research corroborate these findings in that the severity of the mechanical and hemodynamic impact predicted within the artery varied for each of the investigated stents. These findings also demonstrate the important relationship between stent design and performance. Stent design has received less attention since the introduction of drug-eluting stents in 2003. This is attributed to the fact that drug-eluting stents have reduced rates of in-stent restenosis to less than 10% [37]. Despite the ability of anti-restenotic drugs to suppress neointimal growth, the primary aim of stent design should be the minimisation of in-stent restenosis through the reduction of both the mechanical and hemodynamic impact within the artery. With the possible introduction of biodegradable stents in the coming years, stent design may become more important than ever before. As the materials from which biodegradable stents are manufactured do not exhibit the strength of metallic materials, innovative stent designs are required to optimise their scaffolding properties against their mechanical and hemodynamic impact within the artery. To date, a small number of studies have adopted corrosion models to evaluate both the free-deployment characteristics and the scaffolding properties of bioabsorbable coronary stents [113–116].

The results obtained from the present research also corroborate the findings of the ISAR-STEREO-I and ISAR-STEREO-II trials in that stent strut thickness has been identified as a strong risk factor for in-stent restenosis from a mechanical and hemodynamic perspective. Unfortunately, improving stent performance through the reduction of strut thickness is not as straightforward as it may seem. Strut thickness is a critical feature of balloon-expandable coronary stents and has a major influence upon their mechanical properties and their deployment characteristics. Although reducing the strut thickness is likely to have a favourable influence upon both the mechanical and hemodynamic impact of the stent within the coronary artery, it may have an adverse influence upon both the radial strength and radiopacity of the stent. The conflicting requirement of reducing the strut thickness whilst maintaining the

radiopacity of coronary stents was initially addressed through the introduction of radiopaque coating materials [117,118]. Although gold-coated stainless steel stents were initially explored, clinical evaluation demonstrated increased rates of in-stent restenosis compared to uncoated stainless steel stents [117,118]. In recent years, the issues of reduced radial strength and impaired visibility associated with reduced strut thickness have been addressed through the identification and introduction of high-strength alloys, such as cobalt-chromium and platinum-chromium. These metallic alloys demonstrate increased radial strength and radiopacity compared to stainless steel and have been adopted in the development of both third-generation bare-metal and drug-eluting stents, such as the Multilink Vision stent (Abbott Laboratories) and the Promus Element stent (Boston Scientific). In light of the conflicting requirements of stent design and performance, the proposed methodology should prove useful in the pre-clinical design and optimisation of future coronary stents.

6.2 Limitations

The proposed methodology suffers from a number of limitations, mainly due to the geometrical and constitutive material models that are employed in the CS and CFD analyses. As the dimensions of commercially-available coronary stents are not made publicly available, the geometrical models of the investigated stents were generated using the limited number of dimensions that are reported in the literature [3]. As such, the investigated stents represent merely approximations of the commercially-available stents upon which they are based. Despite this limitation, however, the predicted deployment of the investigated stents was found to be in good agreement with that of the various commercially-available stents upon which they were based. The highly-compliant deployment of the investigated stents and the predicted rates of RR and LF were in good agreement with those observed in experimental studies in the literature [108,109]. Furthermore, a preliminary CS analysis was carried out to simulate the free-deployment of Stent A, whose configuration was based on that of the BX-Velocity stent (Johnson & Johnson). As shown in Figure 6.1, the deployed configuration of Stent A was found to be in good agreement with that observed in a micro-computed tomography image of the deployed BX-Velocity stent [105]. Also, the predicted pressure-diameter response of Stent A, shown in Figure 6.2, was found to be in excellent agreement with the manufacturer's pressure-diameter compliance data for the BX-Velocity stent, as reported in the literature [105].

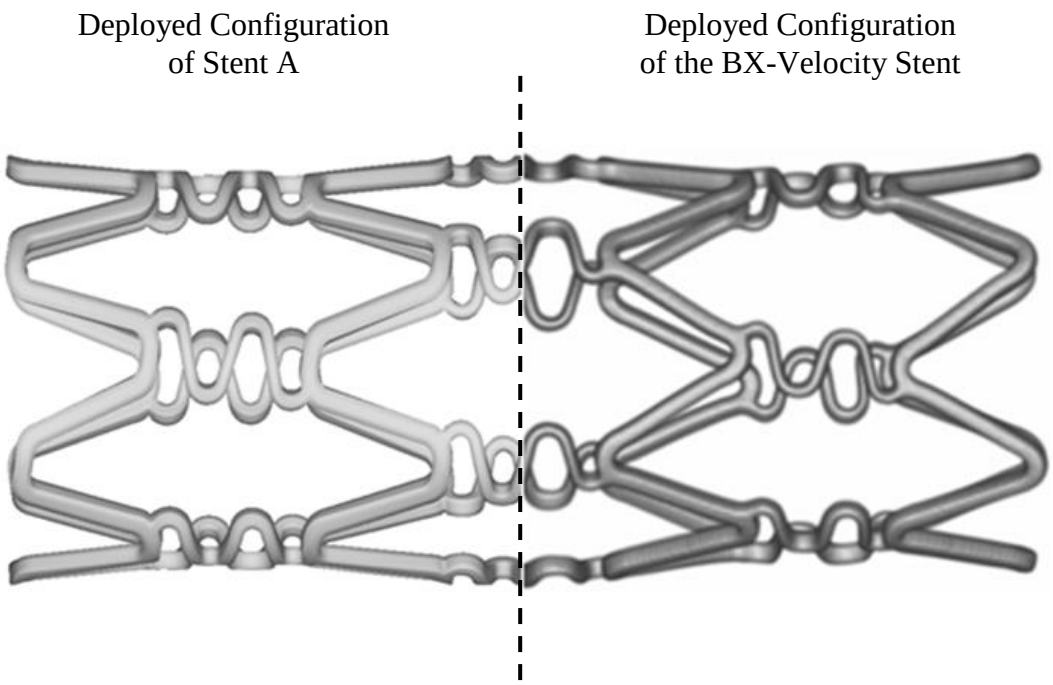

Figure 6.1: Comparison of the deployed configuration of Stent A (left), as predicted in a preliminary CS analysis, and the deployed configuration of the actual BX-Velocity stent (right), as depicted in micro-computed tomography images reported by DeBeule et al. [105]**.**

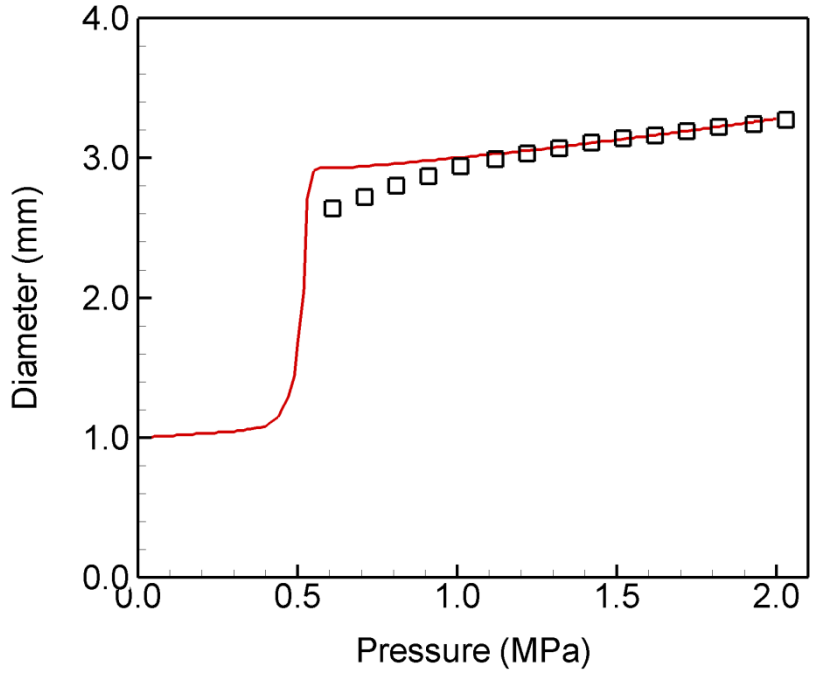

Figure 6.2: Comparison of the predicted pressure-diameter response of Stent A (solid line) with the manufacturer's pressure-diameter compliance data for the BX-Velocity stent (data points).

With regard to the coronary artery, the geometrical model adopted in the proposed methodology is heavily idealised and neglects two features which are likely to have a significant influence upon the performance of the investigated stent: the tortuosity of the artery and the presence of an atherosclerotic plaque. As the arterial tortuosity, plaque severity and plaque properties vary significantly from one person to another and are heavily-dependent upon both the artery of interest and the specific location within the artery of interest, however, it is difficult to generate an idealised model of a coronary artery that adequately accounts for these features. In order to address this issue, a small number of computational studies have adopted sophisticated imaging techniques, such as magnetic resonance imaging and optical coherence tomography, to investigate the mechanical or hemodynamic impact of stent deployment within a realistic, patient-specific model of a coronary artery [52,54,57,67]. Although patient-specific models provide an excellent description of the artery, the results from these analyses are only applicable to a single location in a single patient-specific artery. As such, it is debatable whether the conclusions in these studies should be generalised to the entire population. An alternative approach to addressing this issue was recently proposed by Conway et al. who adopted a number of idealised models of a coronary artery to investigate the mechanical impact of two generic stents in arteries featuring various degrees of arterial tortuosity, plaque severity and plaque properties [58]. Although this "population-specific" approach is likely to improve the evaluation of coronary stent performance, the computational effort required to investigate both the mechanical and hemodynamic impact of six different stents within several idealised arteries that feature varying degrees of arterial tortuosity, plaque severity and plaque properties was deemed beyond the scope of this work. As such, the tortuosity of the artery and the presence of the atherosclerotic plaque were neglected in the proposed numerical methodology and a population-specific sequential evaluation of both the mechanical and hemodynamic impact of coronary stent deployment is suggested as a possible avenue of future research and development in this area.

The material model adopted to describe the mechanical behaviour of the artery during the CS analyses is another limitation of the proposed numerical methodology. In reality, human arterial tissue exhibits an anisotropic mechanical response in both the longitudinal and circumferential directions and this anisotropic response is likely to have a significant influence upon the stresses incurred within regions of the artery

that are subject to multi-axial loading [103]. In order to account for this mechanical behaviour in CS analyses of coronary stent deployment, a number of recent studies have adopted an anisotropic hyperelastic material model to describe the mechanical response of the three individual layers of the coronary artery [52,54,57,58]. Although the inclusion of an anisotropic hyperelastic material model in the proposed numerical methodology would likely improve the evaluation of the mechanical impact of the investigated stents, anisotropic hyperelastic material models were not yet included in ABAQUS when the CS analyses were carried out. As the preparation of a custom-written material model was deemed beyond the scope of this work, the anisotropic mechanical response of the artery was neglected in the proposed methodology. As discussed in Chapter 4, the mechanical behaviour of the individual layers of the coronary artery was instead described using an isotropic hyperelastic material model that was fit to experimental stress-strain data obtained from uniaxial tension tests on circumferentially-orientated samples of human arterial tissue. Though limiting, the use of an isotropic material model to describe the mechanical response of the artery is plausible, however, as the dominant arterial response during stent deployment is in the circumferential direction. A second limitation associated with the description of the mechanical behaviour of the coronary artery is the omission of residual stresses. Residual stresses are typically caused by a combination of both cyclic loading and in-situ pre-stretch and are likely to have a major influence on the stress distribution predicted within the artery. As such, residual stresses should also be accounted for in CS analyses of procedures such as coronary stent deployment.

With regard to the CFD analyses, the limitations associated with the proposed methodology arise from the assumption of a rigid domain and the specification of a zero relative pressure as an outlet boundary condition. Though the assumption of a rigid domain is likely to influence both the flow field within the lumen and the WSS distribution predicted upon the luminal surface, very few studies have considered fluid-structure interaction in elaborate 3D models of stented coronary arteries due to the complexity of the analysis. Furthermore, the deployment of a coronary stent is likely to stiffen the stented region of the artery quite significantly. The specification of a zero relative static pressure as an outlet boundary condition is another limitation of the proposed methodology that results in the development of non-physiological pressure gradients during the transient CFD analyses. This assumption is plausible,

however, as the CFD domain is assumed to be rigid and, as a result, the velocity field is not influenced by the absolute values of pressure. In several recent studies, this issue was addressed through the specification of a Windkessel function at the domain outlet [83,97]. The three-element Windkessel function is typically defined in terms of the resistance and capacitance of the surrounding vessels and is used to account for their physiological influence. A final limitation associated with the CFD analyses arises from the fact that aggressive thrombus formation and inflammation are likely to alter the geometry of the lumen quite significantly in the hours and days following coronary stent deployment. Despite this observation, however, a number of clinical studies have linked regions subject to disturbed WSS following stent deployment to regions of increased neointimal growth at follow-up [28–31].

6.3 Future Research

With regard to future research, the structural stage of the proposed methodology could be improved through the consideration of additional geometrical models of the coronary artery and the inclusion of an atherosclerotic plaque. In order to provide an improved indication of stent performance, these additional geometrical models could include varying degrees of tortuosity and could feature atherosclerotic plaques that are varied in terms of their geometrical configuration and mechanical behaviour. The structural stage of the proposed methodology could also be expanded to include the evaluation of a number of important features such as the radial strength, longitudinal strength and the flexibility of the investigated stent. The inclusion of these analyses would provide additional information with which to interpret the mechanical and hemodynamic impact of an investigated stent. For example, the predicted mechanical and hemodynamic impact of one stent may be much lower than that of another. This information may be redundant, however, if the stent is highly inflexible and unlikely to facilitate delivery within the coronary circulation. Finally, as the majority of next-generation stents that are currently undergoing clinical evaluation are coated in anti-restenotic drugs, the proposed methodology could also be expanded such that the performance of the investigated stent is also evaluated in terms of the rate of drug transfer and the uniformity of drug transfer within the artery wall.

Another area of possible future research is in the management and interpretation of the various mechanical and hemodynamic variables that are employed to evaluate

the performance of the investigated stents. Due to the abundance of these variables within the literature, ranking stents in terms of their mechanical and hemodynamic impact within the coronary artery is quite challenging and a considerable effort was spent reducing the results so that the performance of the investigated stents could be easily evaluated. Despite this effort, it is still difficult to speculate which of the five variables of interest is of most importance with respect to neointimal hyperplasia and, as such, each of the five variables is assigned an equal significance. Whilst there is a sizable body of research related to the influence of arterial injury, altered vessel hemodynamics and subsequent in-stent restenosis, less is known about the relative significance of variables such as the maximum ES, mean ES, maximum principal stress, maximum circumferential stress, low WSS, oscillatory WSS, spatial gradients of WSS, angle gradients of WSS, temporal gradients of WSS and RRT. As a result, it is difficult to assign an appropriate significance to each variable and this problem would likely be exasperated if the drug transfer from the stent was also considered. Although the plethora of data suitably reflects the complexity of the events triggered following coronary stent deployment, the interpretation of this data is a significant challenge in the evaluation of stent performance. Experimental research is required to identify the mechanical and hemodynamic variables which are most significant with respect to in-stent restenosis. With this knowledge, the predicted performance of the investigated stent could be evaluated in a more definitive manner.

BIBLIOGRAPHY

[1] Martini F, Nath J, Bartholomew E. Fundamentals of anatomy and physiology. San Francisco: Benjamin Cummings; 2011.

[2] Nichols M, Townsend N, Scarborough P, Rayner M, Leal J, Luengo-Fernandez R, et al. European cardiovascular disease statistics 2012. Birmingham: British Heart Foundation; 2012.

[3] Serruys P, Rensing B. Handbook of coronary stents. London: Martin Dunitz; 2002.

[4] Sigwart U, Puel J, Mirkovitch V, Joffre F, Kappenberger L. Intravascular stents to prevent occlusion and re-stenosis after transluminal angioplasty. New England Journal of Medicine 1987;316:701–6.

[5] Serruys P, de Jaegere P, Kiemeneij F, Macaya C, Rutsch W, Heyndrickx G, et al. A comparison of balloon-expandable-stent implantation with balloon angioplasty in patients with coronary artery disease. New England Journal of Medicine 1994;331:489–95.

[6] Serruys P, van Hout B, Bonnier H, Legrand V, Garcia E, Macaya C, et al. Randomised comparison of implantation of heparin-coated stents with balloon angioplasty in selected patients with coronary artery disease (Benestent II). The Lancet 1998;352:673–81.

[7] Fischman D, Leon M, Baim D, Schatz R, Savage M, Penn I, et al. A randomized comparison of coronary-stent placement and balloon angioplasty in the treatment of coronary artery disease. New England Journal of Medicine 1994;331:496–501.

[8] Morice M, Serruys P, Sousa J, Fajadet J, Ban Hayashi E, Perin M, et al. A randomized comparison of a sirolimus-eluting stent with a standard stent for coronary revascularization. The New England Journal of Medicine 2002;346:1773–80.

[9] Moses J, Leon M, Popma J, Fitzgerald P, Holmes D, O'Shaughnessy C, et al. Sirolimus-eluting stents versus standard stents in patients with stenosis in a native coronary artery. The New England Journal of Medicine 2003;349:1315–23.

[10] Schofer J, Schlüter M, Gershlick A, Wijns W, Garcia E, Schampaert E, et al. Sirolimus-eluting stents for treatment of patients with long atherosclerotic lesions in small coronary arteries: double-blind, randomised controlled trial (E-SIRIUS). Lancet 2003;362:1093–9.

[11] Schampaert E, Cohen E, Schlüter M, Reeves F, Traboulsi M, Title L, et al. The Canadian study of the sirolimus-eluting stent in the treatment of patients with long de novo lesions in small native coronary arteries (C-SIRIUS). Journal of the American College of Cardiology 2004;43:1110–5.

[12] Stone G, Ellis S, Cox D, Hermiller J, O'Shaughnessy C, Mann J, et al. A polymer-based, paclitaxel-eluting stent in patients with coronary artery disease. The New England Journal of Medicine 2004;350:221–31.

[13] Fajadet J, Wijns W, Laarman G, Kuck K, Ormiston J, Münzel T, et al. Randomized, double-blind, multicenter study of the Endeavor zotarolimus-eluting phosphorylcholine-encapsulated stent for treatment of native coronary artery lesions: clinical and angiographic results of the ENDEAVOR II trial. Circulation 2006;114:798–806.

[14] Serruys P, Ong A, Piek J, Neumann F, van der Giessen W, Wiemer M, et al. A randomized comparison of a durable polymer everolimus-eluting stent with a bare metal coronary stent: The SPIRIT first trial. EuroIntervention 2005;1:58–65.

[15] Edelman E, Rogers C. Pathobiologic responses to stenting. The American Journal of Cardiology 1998;81:4E–6E.

[16] Hoffmann R, Mintz G. Coronary in-stent restenosis - predictors, treatment and prevention. European Heart Journal 2000;21:1739–49.

[17] Mudra H, Regar E, Klauss V, Werner F, Henneke K, Sbarouni E, et al. Serial follow-up after optimized ultrasound-guided deployment of Palmaz-Schatz stents. In-stent neointimal proliferation without significant reference segment response. Circulation 1997;95:363–70.

[18] Joner M, Finn A, Farb A, Mont E, Kolodgie F, Ladich E, et al. Pathology of drug-eluting stents in humans: delayed healing and late thrombotic risk. Journal of the American College of Cardiology 2006;48:193–202.

[19] Schwartz R, Huber K, Murphy J, Edwards W, Camrud A, Vlietstra R, et al. Restenosis and the proportional neointimal response to coronary artery injury: results in a porcine model. Journal of the American College of Cardiology 1992;19:267–74.

[20] Carter A, Laird J, Farb A, Kufs W, Wortham D, Virmani R. Morphologic characteristics of lesion formation and time course of smooth muscle cell proliferation in a porcine proliferative restenosis model. Journal of the American College of Cardiology 1994;24:1398–405.

[21] Rogers C, Edelman E. Endovascular stent design dictates experimental restenosis and thrombosis. Circulation 1995;91:2995–3001.

[22] Farb A, Sangiorgi G, Carter A, Walley V, Edwards W, Schwartz R, et al. Pathology of acute and chronic coronary stenting in Humans. Circulation 1999;99:44–52.

[23] Hoffmann R, Mintz G, Mehran R, Kent K, Pichard A, Satler L, et al. Tissue proliferation within and surrounding Palmaz-Schatz stents is dependent on the aggressiveness of stent implantation technique. The American Journal of Cardiology 1999;83:1170–4.

[24] Schulz C, Herrmann R, Beilharz C, Pasquantonio J, Alt E. Coronary stent symmetry and vascular injury determine experimental restenosis. Heart 2000;83:462–7.

[25] Farb A. Morphological predictors of restenosis after coronary stenting in humans. Circulation 2002;105:2974–80.

[26] Gunn J, Arnold N, Chan K, Shepherd L, Cumberland D, Crossman D. Coronary artery stretch versus deep injury in the development of in-stent neointima. Heart 2002;88:401–5.

[27] Kornowski R, Hong M, Tio F, Bramwell O, Wu H, Leon M. In-stent restenosis: contributions of inflammatory responses and arterial injury to neointimal hyperplasia. Journal of the American College of Cardiology 1998;31:224–30.

[28] Wentzel J, Krams R, Schuurbiers J, Oomen J, Kloet J, van der Giessen W, et al. Relationship between neointimal thickness and shear stress after Wallstent implantation in human coronary arteries. Circulation 2001;103:1740–5.

[29] Sanmartín M, Goicolea J, García C, García J, Crespo A, Rodríguez J. Influence of shear stress on in-stent restenosis: in vivo study using 3D reconstruction and computational fluid dynamics. Revista Española de Cardiología 2006;59:20–7.

[30] Papafaklis M, Bourantas C, Theodorakis P, Katsouras C, Naka K, Fotiadis D, et al. The effect of shear stress on neointimal response following sirolimus- and paclitaxel-eluting stent implantation compared with bare-metal stents in humans. Journal of the American College of Cardiology: Cardiovascular Interventions 2010;3:1181–9.

[31] LaDisa J, Olson L, Molthen R, Hettrick D, Pratt P, Hardel M, et al. Alterations in wall shear stress predict sites of neointimal hyperplasia after stent implantation in rabbit iliac arteries. American Journal of Physiology Heart and Circulatory Physiology 2005;288:H2465–H2475.

[32] Carlier S, van Damme L, Blommerde C, Wentzel J, van Langehove G, Verheye S, et al. Augmentation of wall shear stress inhibits neointimal

hyperplasia after stent implantation: inhibition through reduction of inflammation? Circulation 2003;107:2741–6.

[33] Martin D, Boyle F. Computational structural modelling of coronary stent deployment: a review. Computer Methods in Biomechanics and Biomedical Engineering 2011;14:331–48.

[34] Martin D, Boyle F. A coupled finite element analysis - computational fluid dynamics simulation of local hemodynamic alterations in a stented coronary artery. Proceedings of the 14th Annual Bioengineering In Ireland Conference, Sligo, Ireland: 2008.

[35] Martin D, Boyle F. A coupled finite element analysis - computational fluid dynamics simulation of blood flow in a stented coronary artery. Proceedings of the 15th Annual Bioengineering in Ireland Coference, Limerick, Ireland: 2009.

[36] Martin D, Boyle F. A numerical analysis of coronary stets. Proceedings of the 17th Annual Bioengineering in Ireland Coference, Galway, Ireland: 2011.

[37] Martin D, Boyle F. Drug-eluting stents for coronary artery disease: a review. Medical Engineering & Physics 2011;33:148–63.

[38] Martin D, Boyle F. Sequential structural and fluid dynamics analysis of balloon-expandable coronary stents. Proceedings of the 19th Annual Bioengineering in Ireland Coference, Meath, Ireland: 2013.

[39] Martin D, Boyle F. Finite element analysis of balloon-expandable coronary stent deployment: Influence of angioplasty balloon configuration. International Journal for Numerical Methods in Biomedical Engineering n.d.:Article In Press.

[40] Holzapfel G. Nonlinear solid mechanics: A continuum approach for engineering. John Wiley & Sons Ltd; 2000.

[41] Bonet J, Wood R. Nonlinear contimuum mechanics for finite element analysis. Cambridge University Press; 1997.

[42] Wriggers P. Nonlinear finite element methods. Springer Berlin Heidelberg; 2008.

[43] Anderson J. Computational fluid dynamics: The basics with applications. McGraw-Hill Book Co.; 1995.

[44] Tu J, Yeoh G, Liu C. Computational fluid dynamics: A practical approach. Elsevier Inc.; 2008.

[45] Lai W, Rubin D, Krempl E. Introduction to continuum mechanics. Butterworth Heinemann Ltd.; 1993.

[46] Mase G. Continuum mechanics for engineers. CRC Press LLC; 1999.

[47] Neto E, Peric D, Owen D. Computational methods for plasticity: Theory and applicaitons. John Wiley & Sons Ltd; 2008.

[48] ABAQUS Theory Manual. Dassault Systèmes, Simulia Corporation, Providence, RI, USA: 2013.

[49] ANSYS CFX Theory Manual. ANSYS Inc., Canonsburg, PA, USA: 2013.

[50] Auricchio F, Di Loreto M, Sacco E. Finite-element analysis of a stenotic artery revascularization through a stent insertion. Computer Methods in Biomechanics and Biomedical Engineering 2001;4:249–63.

[51] Lally C, Dolan F, Prendergast P. Cardiovascular stent design and vessel stresses: a finite element analysis. Journal of Biomechanics 2005;38:1574–81.

[52] Holzapfel G, Stadler M, Gasser T. Changes in the mechanical environment of stenotic arteries during interaction with stents: computational assessment of parametric stent designs. Journal of Biomechanical Engineering 2005;127:166–80.

[53] Bedoya J, Meyer C, Timmins L, Moreno M, Moore J. Effects of stent design parameters on normal artery wall mechanics. Journal of Biomechanical Engineering 2006;128:757–65.

[54] Kiousis D, Gasser T, Holzapfel G. A numerical model to study the interaction of vascular stents with human atherosclerotic lesions. Annals of Biomedical Engineering 2007;35:1857–69.

[55] Gervaso F, Capelli C, Petrini L, Lattanzio S, Di Virgilio L, Migliavacca F. On the effects of different strategies in modelling balloon-expandable stenting by means of finite element method. Journal of Bomechanics 2008;41:1206–12.

[56] Gastaldi D, Morlacchi S, Nichetti R, Capelli C, Dubini G, Petrini L, et al. Modelling of the provisional side-branch stenting approach for the treatment of atherosclerotic coronary bifurcations: effects of stent positioning. Biomechanics and Modeling in Mechanobiology 2010;9:551–61.

[57] Mortier P, Holzapfel G, De Beule M, Van Loo D, Taeymans Y, Segers P, et al. A novel simulation strategy for stent insertion and deployment in curved coronary bifurcations: comparison of three drug-eluting stents. Annals of Biomedical Engineering 2010;38:88–99.

[58] Conway C, Sharif F, McGarry J, McHugh P. A computational test-bed to assess coronary stent implantation mechanics using a population-specific approach. Cardiovascular Engineering and Technology 2012;3:374–87.

[59] Rogers C, Tseng D, Squire J, Edelman E. Balloon-artery interactions during stent placement: a finite element analysis approach to pressure, compliance, and stent design as contributors to vascular injury. Circulation Research 1999;84:378–83.

[60] Prendergast P, Lally C, Daly S, Reid A, Lee T, Quinn D, et al. Analysis of prolapse in cardiovascular stents: a constitutive equation for vascular tissue and finite-element modelling. Journal of Biomechanical Engineering 2003;125:692–9.

[61] Chua S, MacDonald B, Hashmi M. Finite element simulation of slotted tube (stent) with the presence of plaque and artery by balloon expansion. Journal of Materials Processing Technology 2004;155-156:1772–9.

[62] Migliavacca F, Petrini L, Massarotti P, Schievano S, Auricchio F, Dubini G. Stainless and shape memory alloy coronary stents: a computational study on the interaction with the vascular wall. Biomechanics and Modeling in Mechanobiology 2004;2:205–17.

[63] Liang D, Yang D, Qi M, Wang W. Finite element analysis of the implantation of a balloon-expandable stent in a stenosed artery. International Journal of Cardiology 2005;104:314–8.

[64] Takashima K, Kitou T, Mori K, Ikeuchi K. Simulation and experimental observation of contact conditions between stents and artery models. Medical Engineering & Physics 2007;29:326–35.

[65] Timmins L, Moreno M, Meyer C, Criscione J, Rachev A, Moore J. Stented artery biomechanics and device design optimization. Medical & Biological Engineering & Computing 2007;45:505–13.

[66] Wu W, Wang W, Yang D, Qi M. Stent expansion in curved vessel and their interactions: a finite element analysis. Journal of Biomechanics 2007;40:2580–5.

[67] Gijsen F, Migliavacca F, Schievano S, Socci L, Petrini L, Thury A, et al. Simulation of stent deployment in a realistic human coronary artery. Biomedical Engineering Online 2008;7:23.

[68] Capelli C, Gervaso F, Petrini L, Dubini G, Migliavacca F. Assessment of tissue prolapse after balloon-expandable stenting: influence of stent cell geometry. Medical Engineering & Physics 2009;31:441–7.

[69] Mortier P, De Beule M, Van Loo D, Verhegghe B, Verdonck P. Finite element analysis of side branch access during bifurcation stenting. Medical Engineering & Physics 2009;31:434–40.

[70] Pericevic I, Lally C, Toner D, Kelly D. The influence of plaque composition on underlying arterial wall stress during stent expansion: the case for lesion-specific stents. Medical Engineering & Physics 2009;31:428–33.

[71] Zahedmanesh H, Lally C. Determination of the influence of stent strut thickness using the finite element method: implications for vascular injury and in-stent restenosis. Medical & Bological Engineering & Computing 2009;47:385–93.

[72] Early M, Kelly D. The role of vessel geometry and material properties on the mechanics of stenting in the coronary and peripheral arteries. Proceedings of the Institution of Mechanical Engineers Part H, Journal of Engineering in Medicine 2010;224:465–76.

[73] Gu L, Zhao S, Muttyam A, Hammel J. The relation between the arterial stress and restenosis rate after coronary stenting. Journal of Medical Devices 2010;4:Article In Press.

[74] Zahedmanesh H, John Kelly D, Lally C. Simulation of a balloon expandable stent in a realistic coronary artery-Determination of the optimum modelling strategy. Journal of Biomechanics 2010;43:2126–32.

[75] Gu L, Zhao S, Froemming S. Arterial wall mechanics and clinical implications after coronary stenting: Comparisons of three stent designs. International Journal of Applied Mechanics 2012;4:Article In Press.

[76] LaDisa J, Guler I, Olson L, Hettrick D, Kersten J, Warltier D, et al. Three-dimensional computational fluid dynamics modeling of alterations in coronary wall shear stress produced by stent implantation. Annals of Biomedical Engineering 2003;31:972–80.

[77] LaDisa J, Olson L, Guler I, Hettrick D, Audi S, Kersten J, et al. Stent design properties and deployment ratio influence indexes of wall shear stress: a three-dimensional computational fluid dynamics investigation within a normal artery. Journal of Applied Physiology 2004;97:424–30.

[78] LaDisa J, Olson L, Guler I, Hettrick D, Kersten J, Warltier D, et al. Circumferential vascular deformation after stent implantation alters wall shear stress evaluated with time-dependent 3D computational fluid dynamics models. Journal of Applied Physiology 2005;98:947–57.

[79] He Y, Duraiswamy N, Frank A, Moore J. Blood flow in stented arteries: a parametric comparison of strut design patterns in three dimensions. Journal of Biomechanical Engineering 2005;127:637–47.

[80] Balossino R, Gervaso F, Migliavacca F, Dubini G. Effects of different stent designs on local hemodynamics in stented arteries. Journal of Biomechanics 2008;41:1053–61.

[81] Pant S, Bressloff N, Forrester A, Curzen N. The influence of strut-connectors in stented vessels: a comparison of pulsatile flow through five coronary stents. Annals of Biomedical Engineering 2010;38:1893–907.

[82] Murphy J, Boyle F. A numerical methodology to fully elucidate the altered wall shear stress in a stented coronary artery. Cardiovascular Engineering and Technology 2010;1:256–68.

[83] Gundert T, Marsden A, Yang W, LaDisa J. Optimization of cardiovascular stent design using computational fluid dynamics. Journal of Biomechanical Engineering 2012;134:Article In Press.

[84] LaDisa J, Olson L, Hettrick D, Warltier D, Kersten J, Pagel P. Axial stent strut angle influences wall shear stress after stent implantation: analysis using 3D computational fluid dynamics models of stent foreshortening. Biomedical Engineering Online 2005;4:59.

[85] LaDisa J, Olson L, Molthen R, Hettrick D, Pratt P, Hardel M, et al. Alterations in wall shear stress predict sites of neointimal hyperplasia after stent implantation in rabbit iliac arteries. American Journal of Physiology Heart and Circulatory Physiology 2005;288:H2465–2475.

[86] Seo T, Schachter L, Barakat A. Computational study of fluid mechanical disturbance induced by endovascular stents. Annals of Biomedical Engineering 2005;33:444–56.

[87] LaDisa J, Olson L, Douglas H, Warltier D, Kersten J, Pagel P. Alterations in regional vascular geometry produced by theoretical stent implantation influence distributions of wall shear stress: analysis of a curved coronary artery using 3D computational fluid dynamics modeling. Biomedical Engineering Online 2006;5:40.

[88] Rajamohan D, Banerjee R, Back L, Ibrahim A, Jog M. Developing pulsatile flow in a deployed coronary stent. Journal of Biomechanical Engineering 2006;128:347–59.

[89] Banerjee R, Devarakonda S, Rajamohan D, Back L. Developed pulsatile flow in a deployed coronary stent. Biorheology 2007;44:91–102.

[90] Faik I, Mongrain R, Leask R, Rodes-Cabau J, Larose E, Bertrand O. Time-dependent 3D simulations of the hemodynamics in a stented coronary artery. Biomedical Materials 2007;2:S28–37.

[91] Dehlaghi V, Najarian S, Shadpour M. Effect of stent geometry on phase shift between pressure and flow waveforms in stented human coronary artery. American Journal of Applied Sciences 2008;5:340–6.

[92] Dehlaghi V, Shadpoor M, Najarian S. Analysis of wall shear stress in stented coronary artery using 3D computational fluid dynamics modeling. Journal of Materials Processing Technology 2008;197:174–81.

[93] Chen H, Hermiller J, Sinha A, Sturek M, Zhu L, Kassab G. Effects of stent sizing on endothelial and vessel wall stress: potential mechanisms for in-stent restenosis. Journal of Applied Physiology 2009;106:1686–91.

[94] Duraiswamy N, Schoephoerster R, Moore J. Comparison of near-wall hemodynamic parameters in stented artery models. Journal of Biomechanical Engineering 2009;131:061006.

[95] Murphy J, Boyle F. A full-range, multi-variable, CFD-based methodology to identify abnormal near-wall hemodynamics in a stented coronary artery. Biorheology 2010;47:117–32.

[96] Williams A, Koo B, Gundert T, Fitzgerald P, LaDisa J. Local hemodynamic changes caused by main branch stent implantation and subsequent virtual side branch balloon angioplasty in a representative coronary bifurcation. Journal of Applied Physiology 2010;109:532–40.

[97] Ellwein L, Otake H, Gundert T, Koo B, Shinke T, Honda Y, et al. Optical coherence tomography for patient-specific 3D artery reconstruction and evaluation of wall shear stress in a left circumflex coronary artery. Cardiovascular Engineering and Technology 2011;2:212–27.

[98] Chen H, Moussa I, Davidson C, Kassab G. Impact of main branch stenting on endothelial shear stress: role of side branch diameter, angle and lesion. Journal of the Royal Society 2012;9:1187–93.

[99] Chiastra C, Morlacchi S, Pereira S, Dubini G, Migliavacca F. Computational fluid dynamics of stented coronary bifurcations studied with a hybrid discretization method. European Journal of Mechanics 2012;35:76–84.

[100] Zunino P, D'Angelo C, Petrini L, Vergara C, Capelli C, Migliavacca F. Numerical simulation of drug eluting coronary stents: Mechanics, fluid dynamics and drug release. Computer Methods in Applied Mechanics and Engineering 2009;198:3633–44.

[101] Pant S, Limbert G, Curzen N, Bressloff N. Multiobjective design optimisation of coronary stents. Biomaterials 2011;32:7755–73.

[102] Morlacchi S, Chiastra C, Gastaldi D, Pennati G, Dubini G, Migliavacca F. Sequential structural and fluid dynamic numerical simulations of a stented bifurcated coronary artery. Journal of Biomechanical Engineering 2011;133:Article In Press.

[103] Holzapfel G, Sommer G, Gasser C, Regitnig P. Determination of layer-specific mechanical properties of human coronary arteries with nonatherosclerotic intimal thickening and related constitutive modeling. American Journal of Physiology 2005;289:H2048–2058.

[104] Murphy B, Savage P, McHugh P, Quinn D. The stress-strain behavior of coronary stent struts is size dependent. Annals of Biomedical Engineering 2003;31:686–91.

[105] De Beule M. Finite element stent design. Ghent University, Belgium, 2008.

[106] Jung H, Choi J, Park C. Asymmetric flows of non-Newtonian fluids in symmetric stenosed artery. Korea-Australia Rheology Journal 2004;16:101–8.

[107] Himburg H, Grzybowski D, Hazel A, LaMack J, Li X, Friedman M. Spatial comparison between wall shear stress measures and porcine arterial endothelial permeability. American Journal of Physiology Heart and Circulatory Physiology 2004;286:H1916–22.

[108] Kiousis D, Wulff A, Holzapfel G. Experimental studies and numerical analysis of the inflation and interaction of vascular balloon catheter-stent systems. Annals of Biomedical Engineering 2009;37:315–30.

[109] Colombo A, Stankovic G, Moses J. Selection of coronary stents. Journal of the American College of Cardiology 2002;40:1021–33.

[110] Kastrati A, Mehilli J, Dirschinger J, Dotzer F, Schuhlen H, Neumann F, et al. Intracoronary stenting and angiographic results : strut thickness effect on restenosis outcome (ISAR-STEREO) trial. Circulation 2001;103:2816–21.

[111] Pache J, Kastrati A, Mehilli J, Schühlen H, Dotzer F, Hausleiter J, et al. Intracoronary stenting and angiographic results: strut thickness effect on restenosis outcome (ISAR-STEREO-2) trial. Journal of the American College of Cardiology 2003;41:1283–8.

[112] Kastrati A, Mehilli J, Dirschinger J, Pache J, Ulm K, Schühlen H, et al. Restenosis after coronary placement of various stent types. The American Journal of Cardiology 2001;87:34–9.

[113] Gastaldi D, Sassi V, Petrini L, Vedani M, Trasatti S, Migliavacca F. Continuum damage model for bioresorbable magnesium alloy devices: Application to coronary stents. Journal of the Mechanical Behavior of Biomedical Materials 2011;4:352–65.

[114] Grogan J, O'Brien B, Leen S, McHugh P. A corrosion model for bioabsorbable metallic stents. Acta Biomaterialia 2011;7:3523–33.

[115] Wu W, Petrini L, Gastaldi D, Villa T, Vedani M, Lesma E, et al. Finite element shape optimization for biodegradable magnesium alloy stents. Annals of Biomedical Engineering 2010;38:2829–40.

[116] Wu W, Gastaldi D, Yang K, Tan L, Petrini L, Migliavacca F. Finite element analyses for design evaluation of biodegradable magnesium alloy stents in arterial vessels. Materials Science and Engineering: B 2011;176:1733–40.

[117] Reifart N, Morice M, Silber S, Benit E, Hauptmann K, de Sousa E, et al. The NUGGET study: NIR ultra gold-gilded equivalency trial. Catheterization and Cardiovascular Interventions 2004;62:18–25.

[118] Kastrati A, Schomig A, Dirschinger J, Mehilli J, von Welser N, Pache J, et al. Increased risk of restenosis after placement of gold-coated stents : Results of a randomized trial comparing gold-coated with uncoated steel stents in patients with coronary artery disease. Circulation 2000;101:2478–83.

APPENDIX A
CONVERGENCE STUDIES

A.1 Introduction

In this appendix, the convergence studies that were carried out to identify suitable spatial discretisation, transient loading and temporal discretisation schemes for the CS and CFD analyses are discussed. The details and results of the mesh convergence studies that were carried out to identify a suitable mesh density for the angioplasty balloon, the investigated stent, the coronary artery and the stented coronary lumen are first presented. The details and results of the cycle and time step convergence studies which were carried out to identify an appropriate transient loading and spatial discretisation scheme for the transient CFD analyses are then presented.

A.2 Mesh Convergence

A.2.1 Angioplasty Balloon

In order to determine an appropriate mesh density for the angioplasty balloon, four CS analyses were carried out in which four increasingly dense meshes were adopted to evaluate the free-deployment of the angioplasty balloon. In each of the analyses, the guide wire and the catheter shaft were discretised using 740 and 13,104 reduced-integration continuum elements (C3D8R), respectively, and the angioplasty balloon was discretised using 12,462, 25,344, 33,966, 48,678 reduced-integration membrane elements (M3D4R). These meshes are referred to as Mesh 1, Mesh 2, Mesh 3 and Mesh 4, respectively, and are shown in Figures A.1, A.3, A.5 and A.7. In each of the CS analyses, the mechanical behaviour of the guide wire, the catheter shaft and the angioplasty balloon was described using the linear elastic material models discussed in Chapter 4 and the free-deployment of the angioplasty balloon was then simulated through the application of a uniform pressure load of 2.0 MPa upon its inner surface.

In order to prevent rigid-body motion during the analyses, the nodes located at the extremities of the guide wire were constrained. Contact between the components of the balloon-tipped catheter was described using the general contact algorithm and a static friction coefficient of 0.2 was adopted from Mortier et al. in order to describe the development of frictional forces between potential contact pairs [57]. In order to prevent non-physical oscillations during the analyses, a mass-proportional damping coefficient of α = 8,000 was also specified during the description of the angioplasty balloon. This value was adopted from DeBeule et al. and corresponds to almost 50% of the critical damping coefficient [105]. As the free-deployment of the angioplasty balloon is highly nonlinear and involves multiple contacting surfaces, the analyses were carried out using the ABAQUS/Explicit solver. As inertia is assumed to have a negligible role in the free-deployment of the angioplasty balloon, the analyses were also carried out using a quasi-static approach. To ensure that the analyses remained quasi-static, a total solution time of two seconds was specified and the total kinetic and internal energy was monitored during the analyses. The deployed configuration of the angioplasty balloon for each of the four different meshes is shown in Figures A.2, A.4, A.6 and A.8. Following the completion of the analyses, mesh convergence was identified when the difference between both the area-weighted mean and the area-weighted standard deviation of the ES distribution predicted in the angioplasty balloon remained below 5% for each successive mesh. As shown in Table A.1, mesh convergence was achieved with Mesh 1. Based upon these results, the mesh density adopted for Mesh 1 is employed to discretise the angioplasty balloon.

Mesh	1	2	3	4
Nodes	12,690	25,669	34,342	49,128
Elements	12,462	25,344	33,966	48,678
ES (μ_{aw})	144.3 MPa	144.3 MPa	144.4 MPa	144.1 MPa
Difference	-	0.02%	0.03%	0.18%
ES (σ_{aw})	41.9 MPa	41.3 MPa	40.9 MPa	40.9 MPa
Difference	-	1.36%	1.06%	0.06%

Table A.1: Results of the mesh convergence study carried out to identify an appropriate mesh density for the angioplasty balloon.

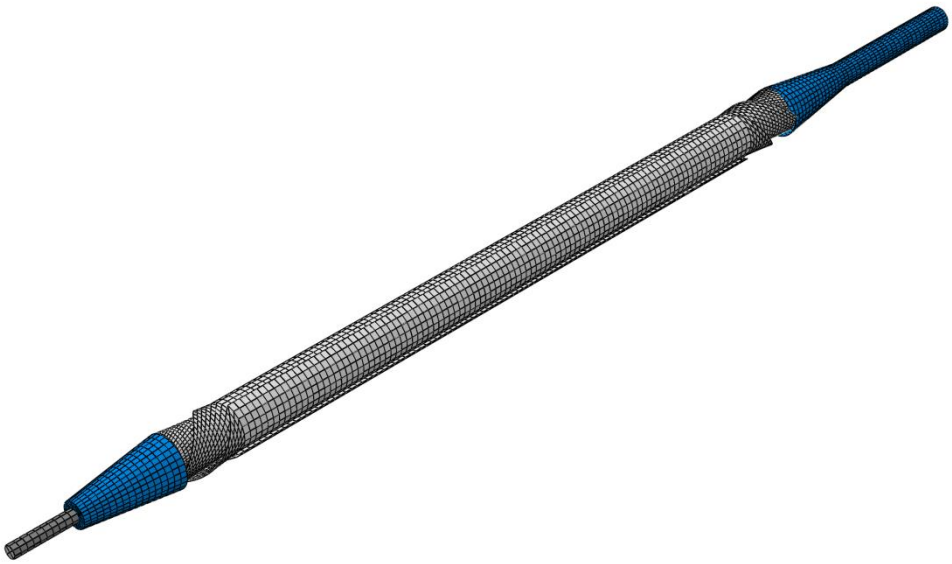

Figure A.1: Discretised CS model of the angioplasty balloon containing 12,462 reduced-integration surface elements (Mesh 1).

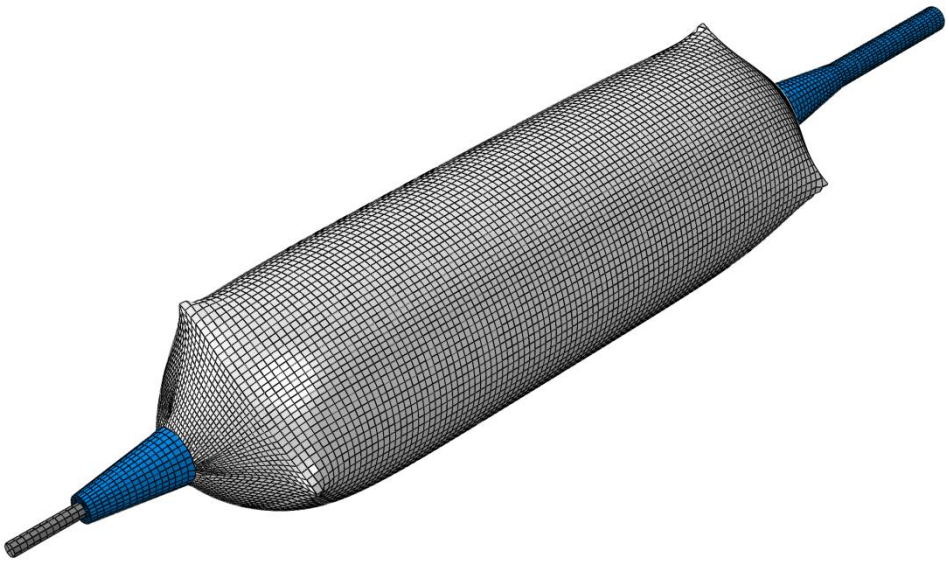

Figure A.2: Deployed configuration of the discretised angioplasty balloon containing 12,462 reduced-integration surface elements (Mesh 1).

Figure A.3: Discretised CS model of the angioplasty balloon containing 25,344 reduced-integration surface elements (Mesh 2).

Figure A.4: Deployed configuration of the discretised angioplasty balloon containing 25,344 reduced-integration surface elements (Mesh 2).

Figure A.5: Discretised CS model of the angioplasty balloon containing 33,966 reduced-integration surface elements (Mesh 3).

Figure A.6: Deployed configuration of the discretised balloon containing 33,966 reduced-integration surface elements (Mesh 3).

Figure A.7: Discretised CS model of the angioplasty balloon containing 48,678 reduced-integration surface elements (Mesh 4).

Figure A.8: Deployed configuration of the discretised angioplasty balloon containing 48,678 reduced-integration surface elements (Mesh 4).

A.2.2 Investigated Stent

In order to determine an appropriate mesh density for the investigated stents, four CS analyses were carried out in which four increasingly dense meshes were adopted to evaluate the free-deployment of Stent A. During the analyses, the guide wire and the catheter shaft were discretised using 740 and 13,104 reduced-integration continuum elements (C3D8R), respectively, and the angioplasty balloon was discretised using 12,462 reduced-integration membrane elements (M3D4R). Four increasingly dense meshes were then generated for Stent A containing 5,832, 12,348, 24,570 and 35,712 reduced-integration continuum elements (C3D8R). These meshes are referred to as Mesh 1, Mesh 2, Mesh 3 and Mesh 4, respectively, and are shown in Figures A.9, A.11, A.13 and A.15. During the CS analyses, the mechanical behaviour of the stent was described using the elastic-plastic material model discussed in Chapter 4 and the angioplasty balloon was loaded as described in Section A.2.1. To prevent rigid-body motion, a number of nodes located at the mid-section of the stent were constrained in both the circumferential and longitudinal directions. The analyses were carried out as described in Section A.2.1 and the deployed configuration of the stent for each of the meshes is shown in Figures A.10, A.12, A.14 and A.16. Following the completion of the CS analyses, mesh convergence was identified when the difference between both the volume-weighted mean and the volume-weighted standard deviation of the ES distribution predicted within the stent remained below 5% for each successive mesh. As shown in Table A.2, mesh convergence was achieved with Mesh 3. As such, the mesh density used for Mesh 3 is adopted to discretise the investigated stent.

Mesh	1	2	3	4
Nodes	13,005	24,540	43,472	59,260
Elements	5,832	12,348	24,570	35,712
ES (μ_{vw})	344.8 MPa	338.6 MPa	318.7 MPa	319.1 MPa
Difference	-	1.80%	5.85%	0.13%
ES (σ_{vw})	155.7 MPa	161.4 MPa	176.5 MPa	177.4 MPa
Difference	-	3.70%	9.35%	0.50%

Table A.2: Results of the mesh convergence study carried out to identify an appropriate mesh density for each of the investigated stents.

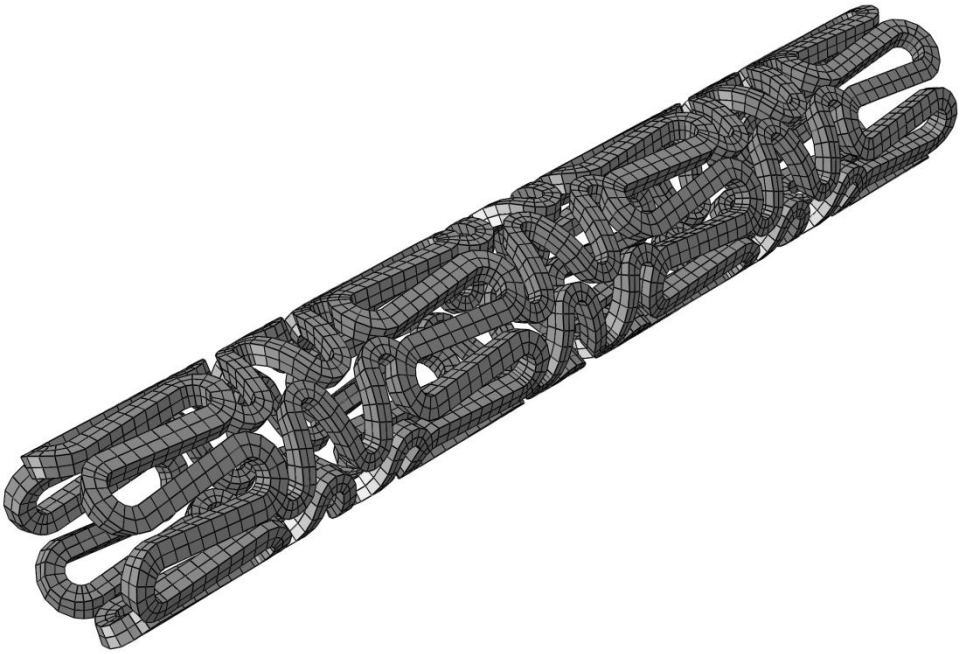

Figure A.9: Discretised CS model of Stent A containing 5,832 reduced-integration continuum elements (Mesh 1).

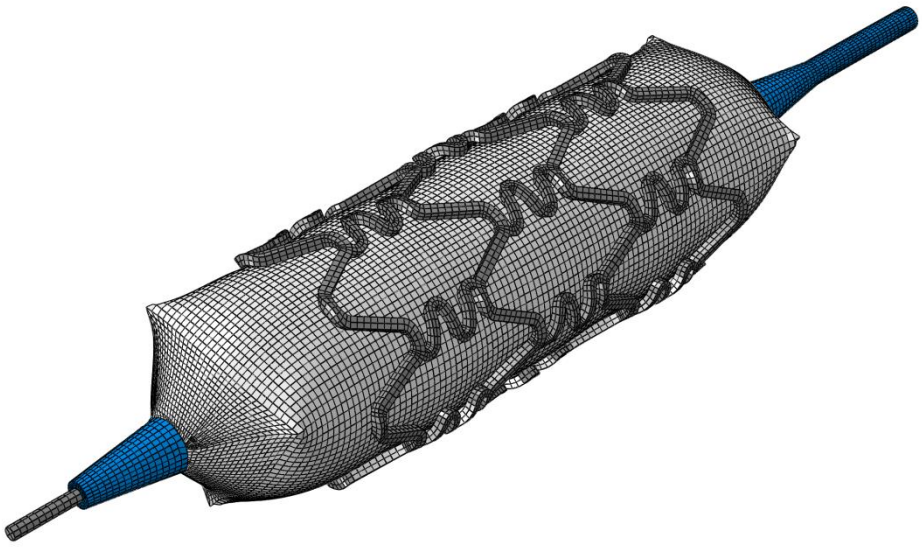

Figure A.10: Deployed configuration of the discretised stent containing 5,832 reduced-integration continuum elements (Mesh 1).

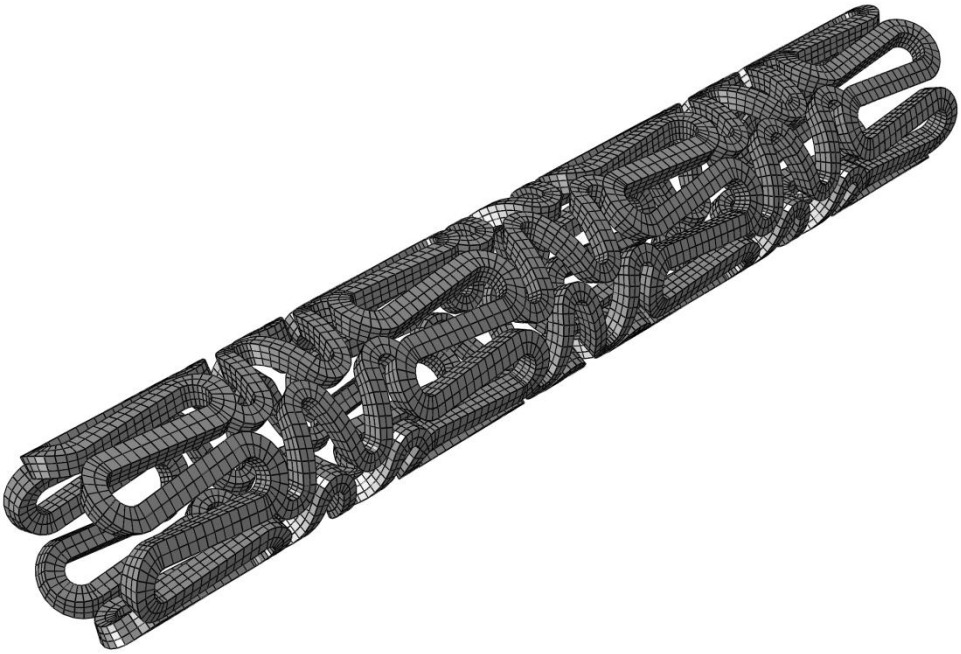

Figure A.11: Discretised CS model of Stent A containing 12,348 reduced-integration continuum elements (Mesh 2).

Figure A.12: Deployed configuration of the discretised stent containing 12,348 reduced-integration continuum elements (Mesh 2).

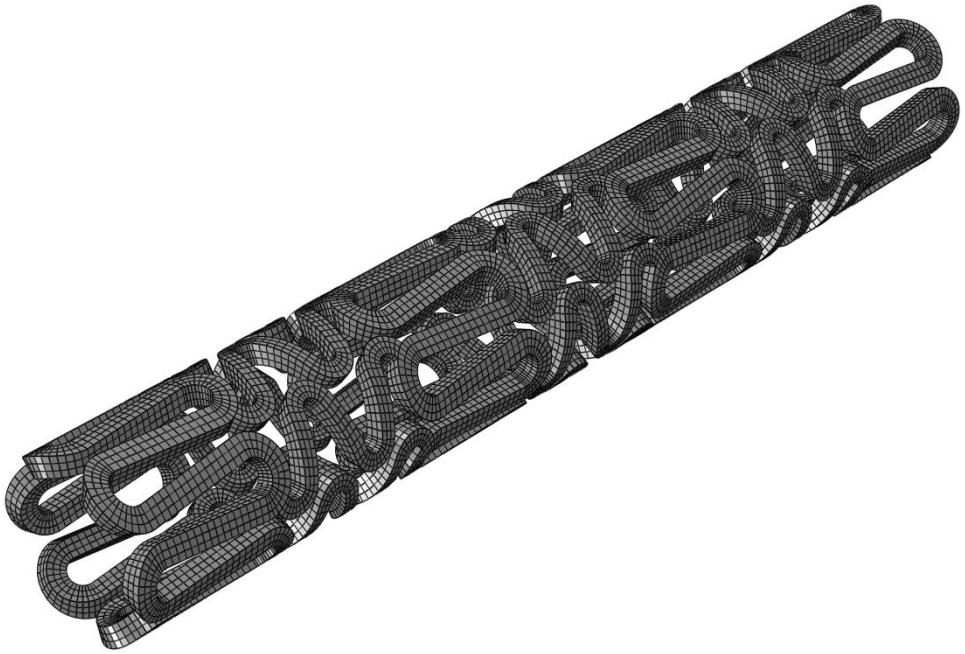

Figure A.13: Discretised CS model of Stent A containing 24,570 reduced-integration continuum elements (Mesh 3).

Figure A.14: Deployed configuration of the discretised stent containing 24,570 reduced-integration continuum elements (Mesh 3).

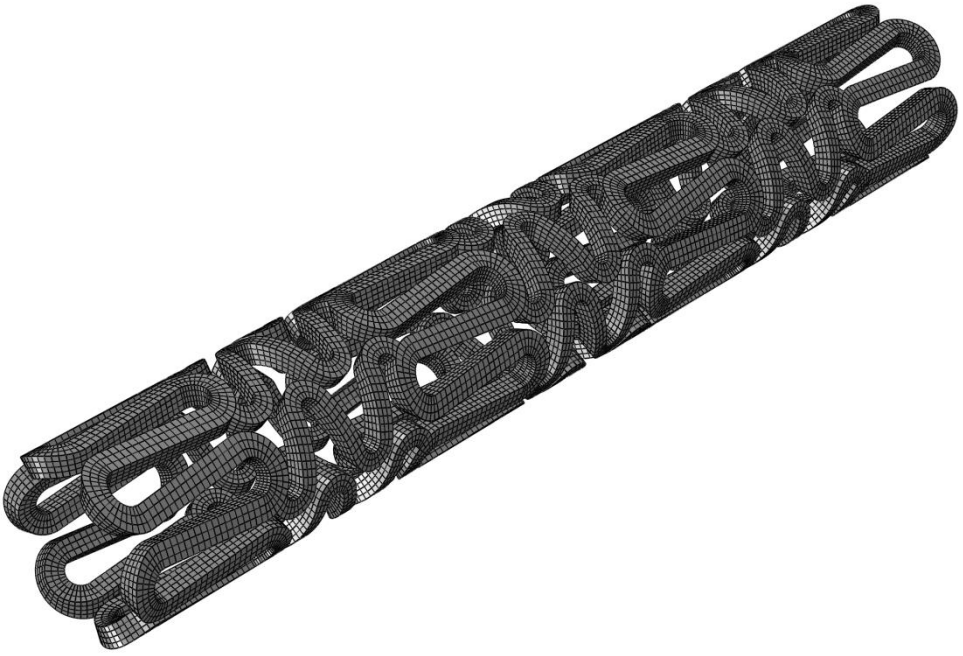

Figure A.15: Discretised CS model of Stent A containing 35,712 reduced-integration continuum elements (Mesh 4).

Figure A.16: Deployed configuration of the discretised stent containing 35,712 reduced-integration continuum elements (Mesh 4).

A.2.3 Coronary Artery

In order to determine an appropriate mesh density for the coronary artery, four CS analyses were carried out in which four increasingly dense meshes were employed to evaluate the deployment of Stent A within the artery. During the analyses, the guide wire, catheter shaft and stent were discretised using 740, 13,104 and 24,570 reduced-integration continuum elements (C3D8R), respectively, and the angioplasty balloon was discretised using 12,462 reduced-integration membrane elements (M3D4R). The artery was then discretised into four increasingly dense meshes containing 70,272, 81,840, 95,424 and 116,550 reduced-integration continuum elements (C3D8R). The four meshes are referred to as Mesh 1, Mesh 2, Mesh 3 and Mesh 4, respectively, and are shown in Figures A.17, A.19, A.21 and A.23. During the CS analyses, the mechanical behaviour of the coronary artery was described using the hyperelastic material models discussed in Chapter 4 and the angioplasty balloon was loaded as described in Section A.2.1. To prevent rigid-body motion, the nodes located at the extremities of the artery were fully-constrained. The CS analyses were carried out as described in Section A.2.1 and the deformed configuration of the artery for each of the four different meshes is shown in Figures A.18, A.20, A.22 and A.24. Following the completion of the analyses, mesh convergence was identified when the difference between the volume-weighted mean and volume-weighted standard deviation of the ES distribution predicted in the artery remained below 5% for each successive mesh. As shown in Table A.3, mesh convergence was achieved with Mesh 1. As such, the mesh density used for Mesh 1 is employed to discretise the coronary artery.

Mesh	1	2	3	4
Nodes	80,910	94,068	109,512	132,000
Elements	70,272	81,840	95,424	116,550
ES (μ_{vw})	19.3 kPa	19.5 kPa	19.1 kPa	18.7 kPa
Difference	-	1.13%	2.01%	1.99%
ES (σ_{vw})	32.8 kPa	32.9 kPa	32.2 kPa	32.3 kPa
Difference	-	0.18%	1.94%	0.33%

Table A.3: Results of the mesh convergence study carried out to identify an appropriate mesh density for the coronary artery.

Figure A.17: Discretised CS model of the coronary artery containing 70,272 reduced-integration continuum elements (Mesh 1).

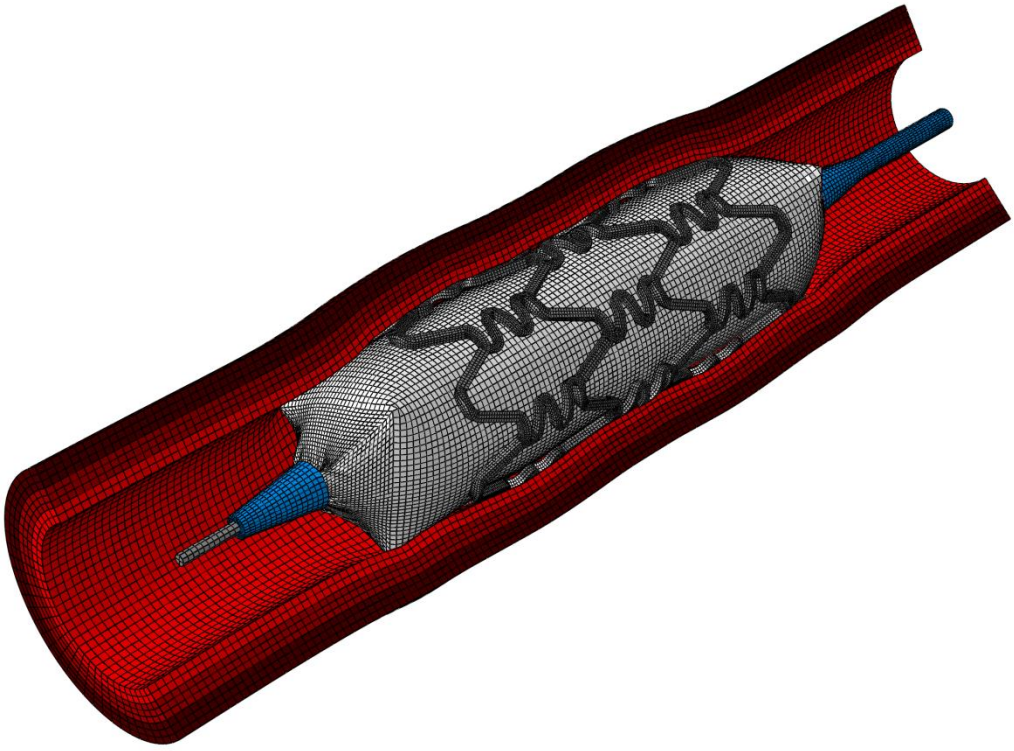

Figure A.18: Deformed configuration of the discretised coronary artery containing 70,272 reduced-integration continuum elements (Mesh 1).

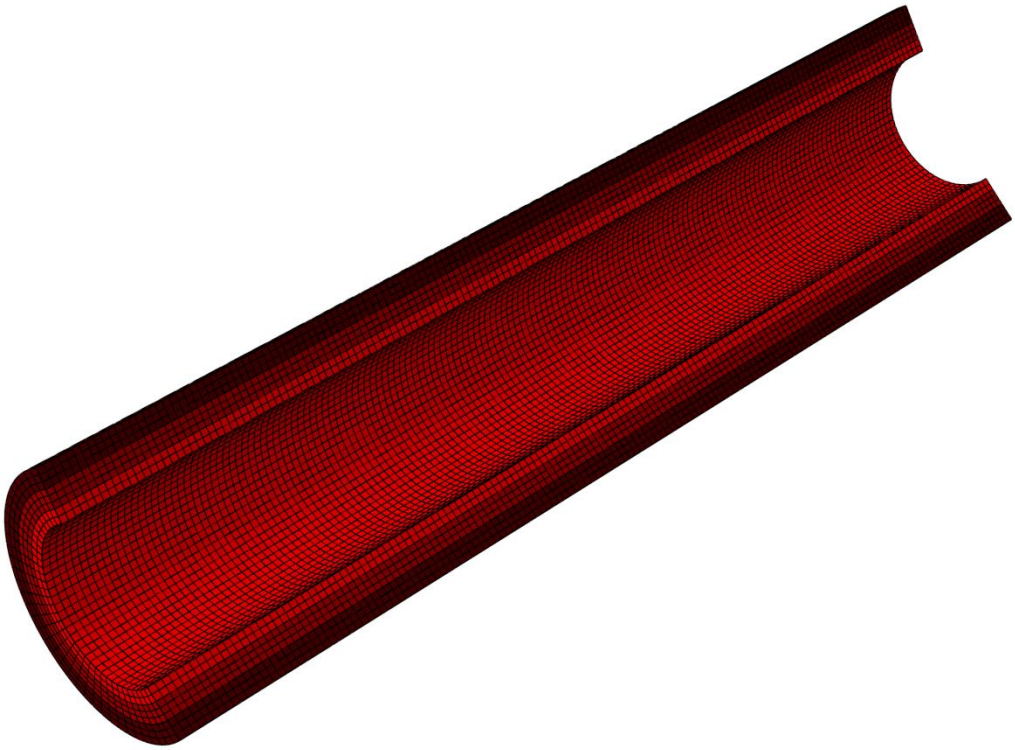

Figure A.19: Discretised CS model of the coronary artery containing 81,840 reduced-integration continuum elements (Mesh 2).

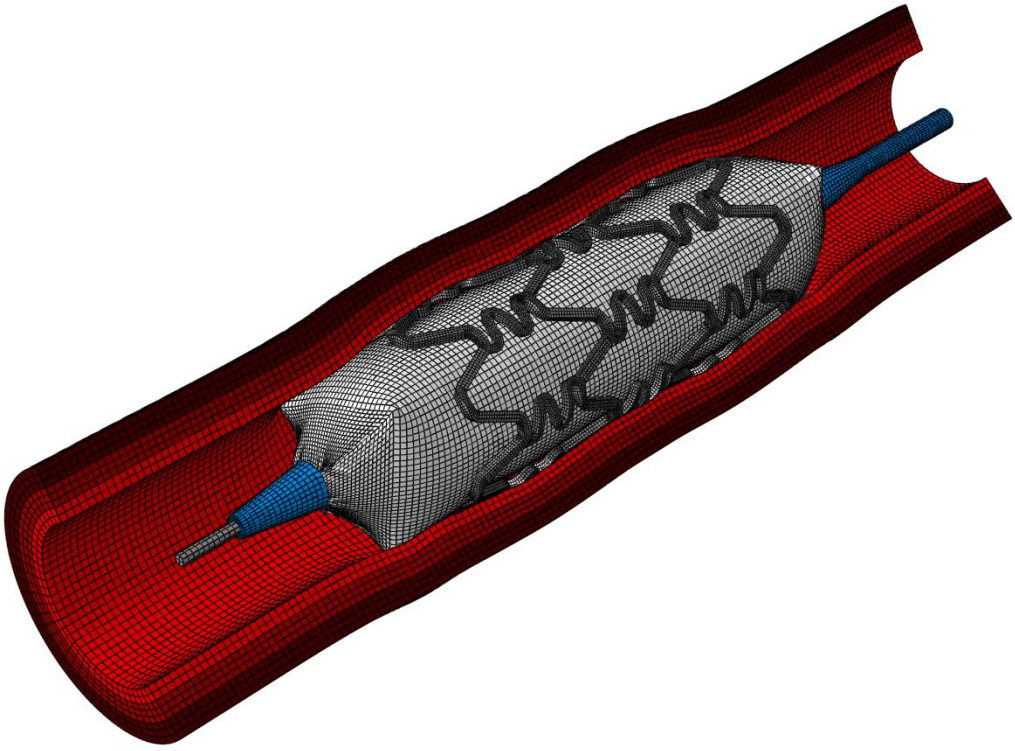

Figure A.20: Deformed configuration of the discretised coronary artery containing 81,840 reduced-integration continuum elements (Mesh 2).

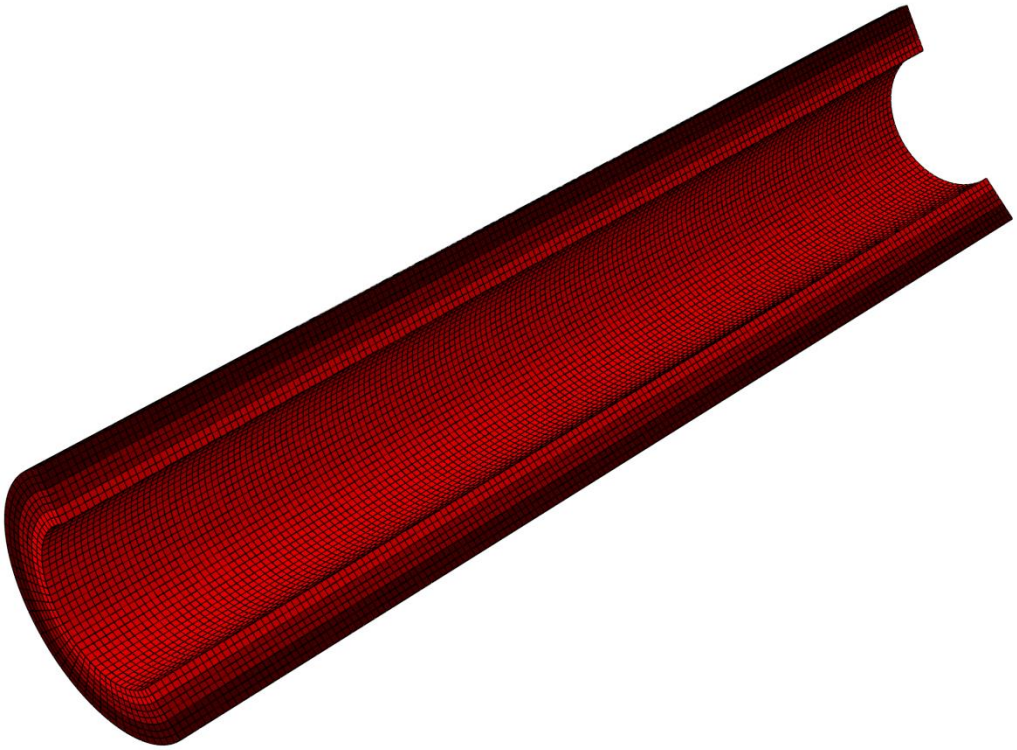

Figure A.21: Discretised CS model of the coronary artery containing 95,424 reduced-integration continuum elements (Mesh 3).

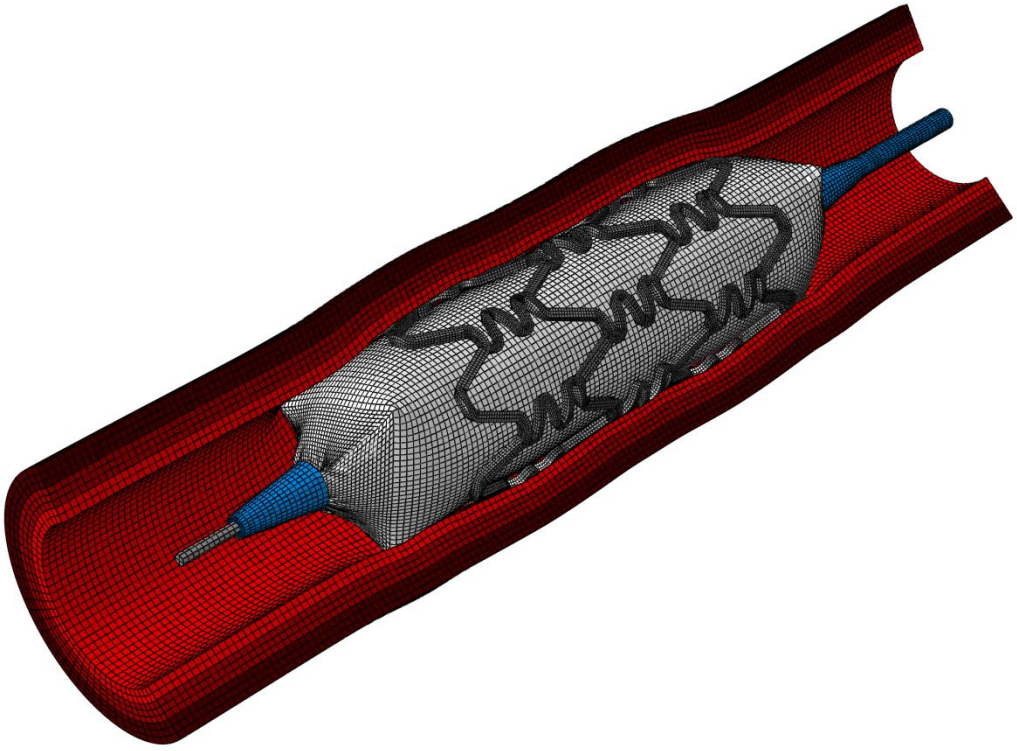

Figure A.22: Deformed configuration of the discretised coronary artery containing 95,424 reduced-integration continuum elements (Mesh 3).

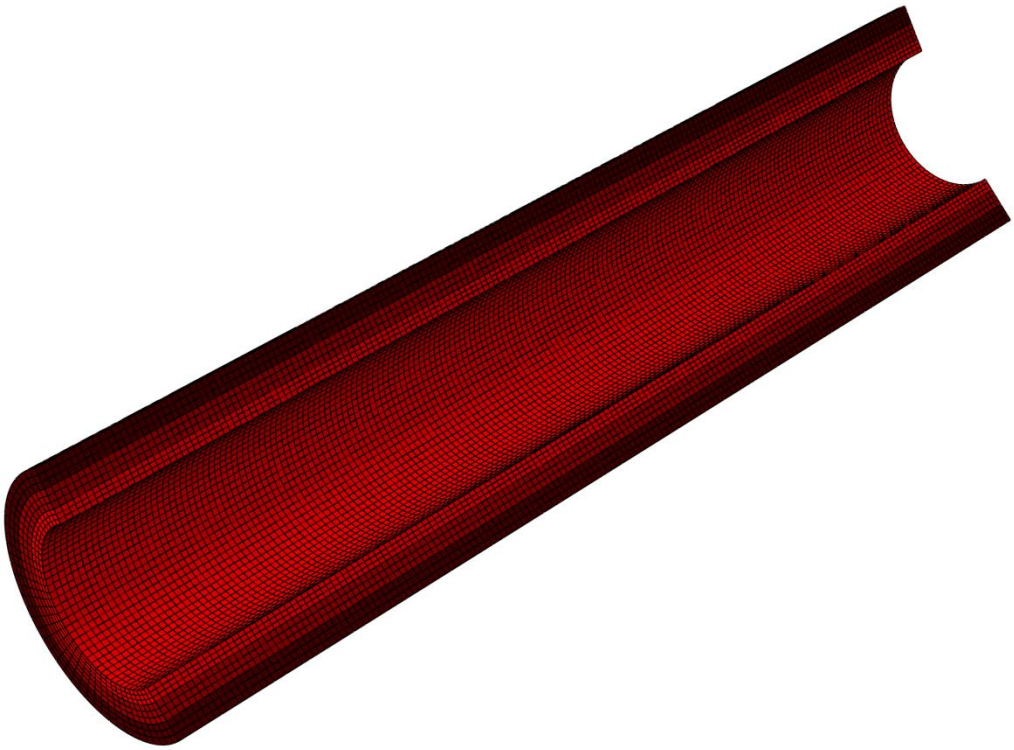

Figure A.23: Discretised CS model of the coronary artery containing 116,550 reduced-integration continuum elements (Mesh 4).

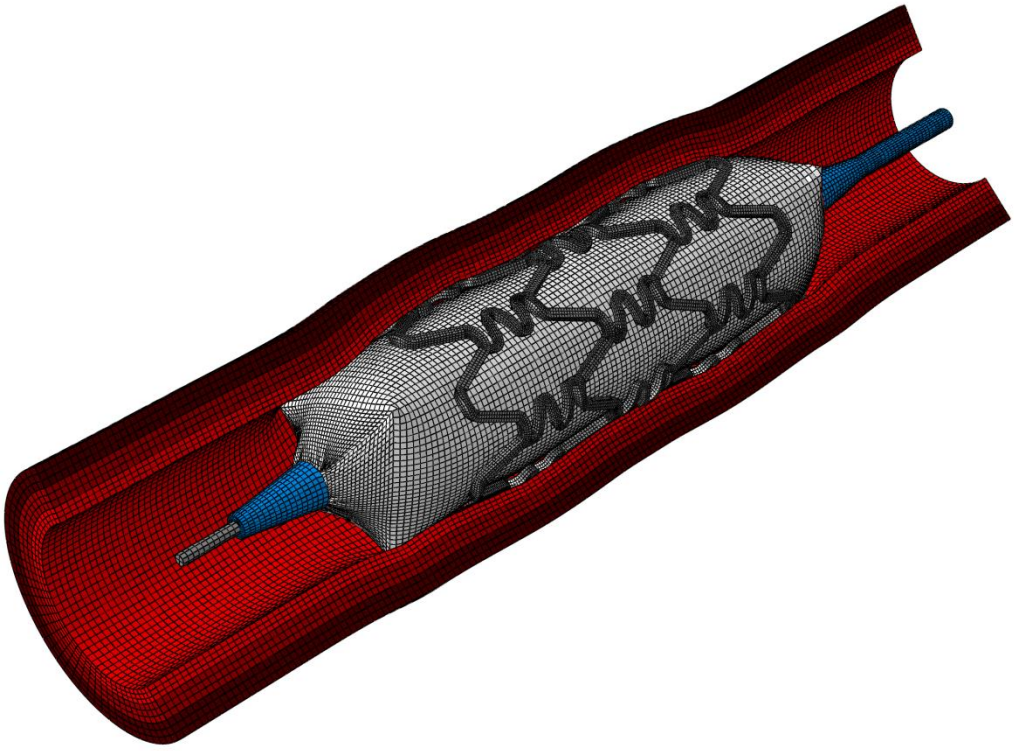

Figure A.24: Deformed configuration of the discretised coronary artery containing 116,550 reduced-integration continuum elements (Mesh 4).

A.2.4 Stented Coronary Lumen

In order to determine a suitable mesh density for the stented coronary lumen, four steady-state CFD analyses were carried out in which four increasingly dense meshes were adopted to evaluate mean flow conditions in a stented coronary artery. During the steady-state CFD analyses, the stented coronary lumen was discretised into four increasingly dense meshes using 2,709,894, 3,329,347, 4,186,199 and 5,426,405 tetrahedral elements. The meshes are referred to as Mesh 1, Mesh 2, Mesh 3 and Mesh 4, respectively, and are shown in Figures A.25 to A.32. In each of the CFD analyses, the viscous behaviour of the fluid was described using the non-Newtonian Bird-Carreau model that was discussed in Chapter 4. A zero relative pressure was then assigned at the domain outlet and a no-slip condition was specified upon both the surface of the struts and the luminal surface of the artery. To simulate mean flow conditions in a human left-anterior descending coronary artery, a fully-developed laminar velocity profile was specified at the domain inlet and the centreline velocity was assigned a value of 0.23 m/s. The analyses were carried out in ANSYS CFX and a convergence criterion of 10^{-4} was specified for the root mean square values of the velocity and density residuals. Following the completion of the CFD analyses, mesh convergence was identified when the difference between both the area-weighted mean and area-weighted standard deviation of the WSS distribution predicted on the luminal surface remained below 5% for each successive mesh. As shown in Table A.4, mesh convergence was achieved with Mesh 1. As such, the mesh density used for Mesh 1 is employed to discretise the stented coronary lumen.

Mesh	1	2	3	4
Nodes	463,984	569,739	716,423	928,562
Elements	2,709,894	3,329,347	4,186,199	5,426,405
WSS (μ_{aw})	0.762 Pa	0.755 Pa	0.762 Pa	0.758 Pa
Difference	-	0.94%	0.97%	0.51%
WSS (σ_{aw})	0.526 Pa	0.523 Pa	0.534 Pa	0.532 Pa
Difference	-	0.46%	2.00%	0.35%

Table A.4: Results of the mesh convergence study carried out to identify an appropriate mesh density for the stented coronary lumen.

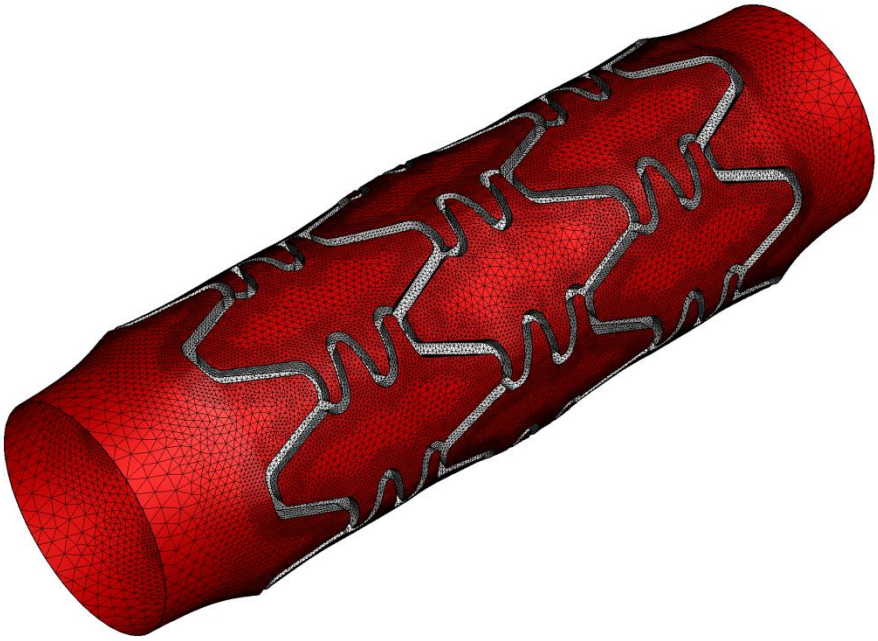

Figure A.25: Isometric view of the discretised CFD model of the stented coronary lumen containing 2,709,894 tetrahedral elements (Mesh 1).

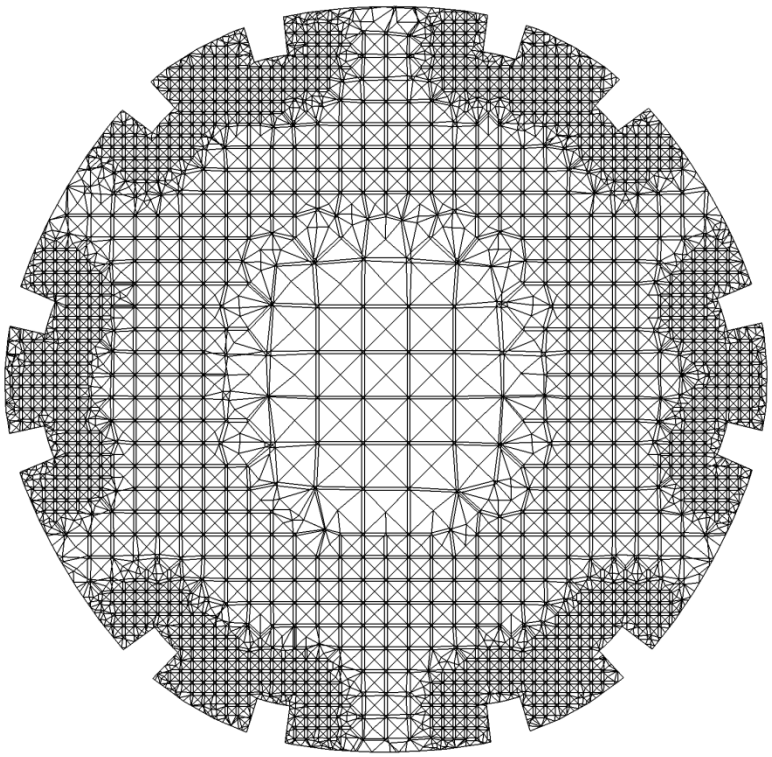

Figure A.26: Longitudinal cross-section view of the discretised stented coronary lumen containing 2,709,894 tetrahedral elements (Mesh 1).

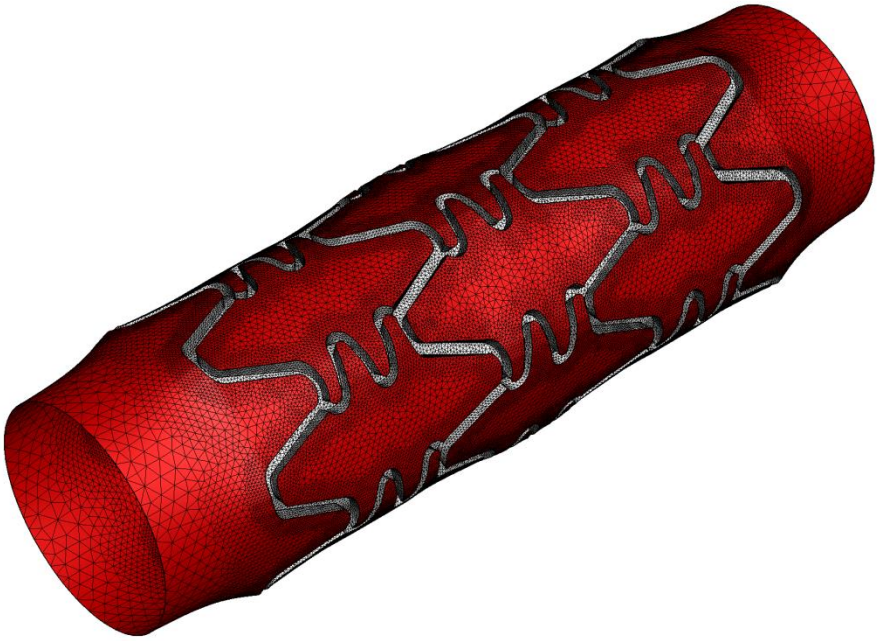

Figure A.27: Isometric view of the discretised CFD model of the stented coronary lumen containing 3,329,347 tetrahedral elements (Mesh 2).

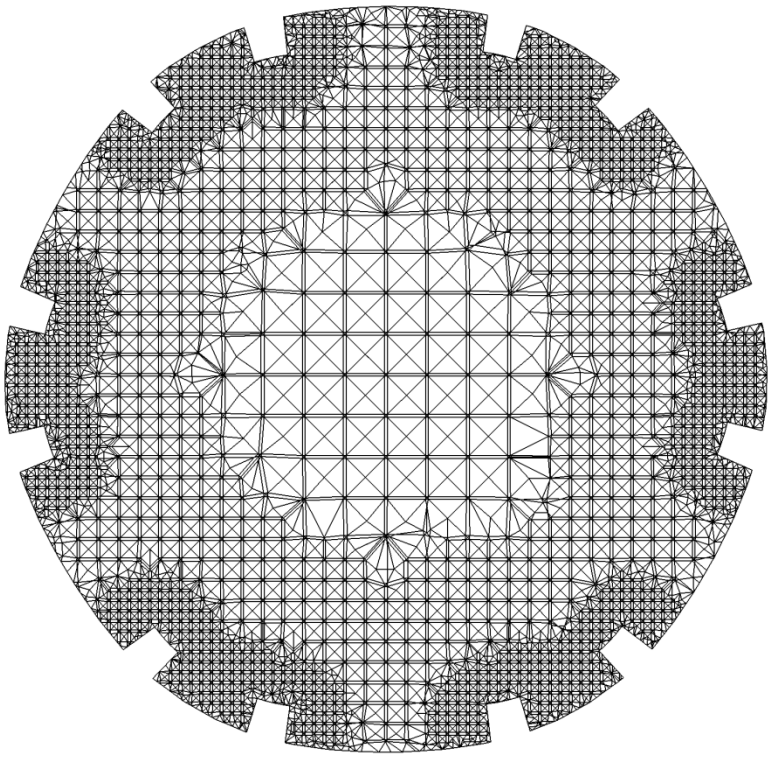

Figure A.28: Longitudinal cross-section view of the discretised stented coronary lumen containing 3,329,347 tetrahedral elements (Mesh 2).

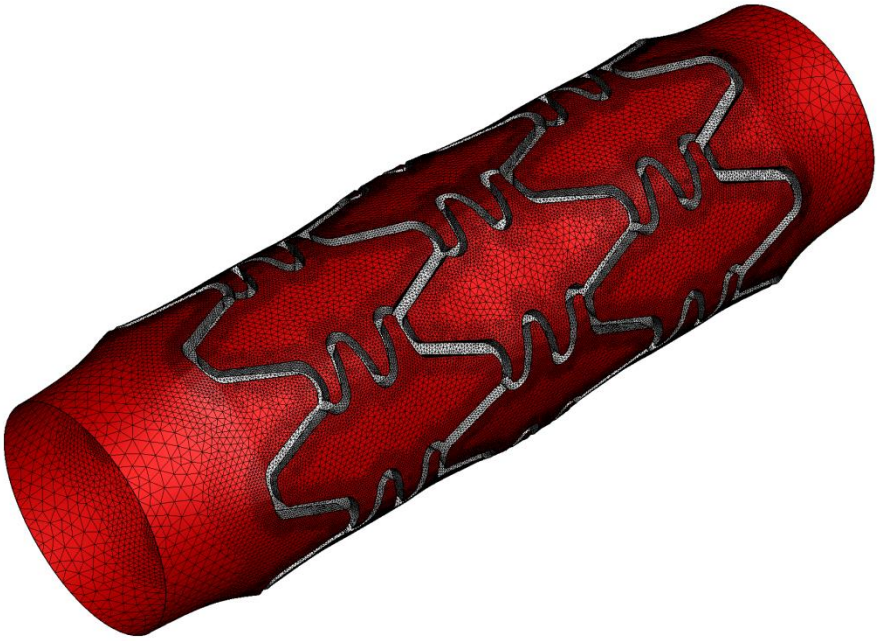

Figure A.29: Isometric view of the discretised CFD model of the stented coronary lumen containing 4,186,199 tetrahedral elements (Mesh 3).

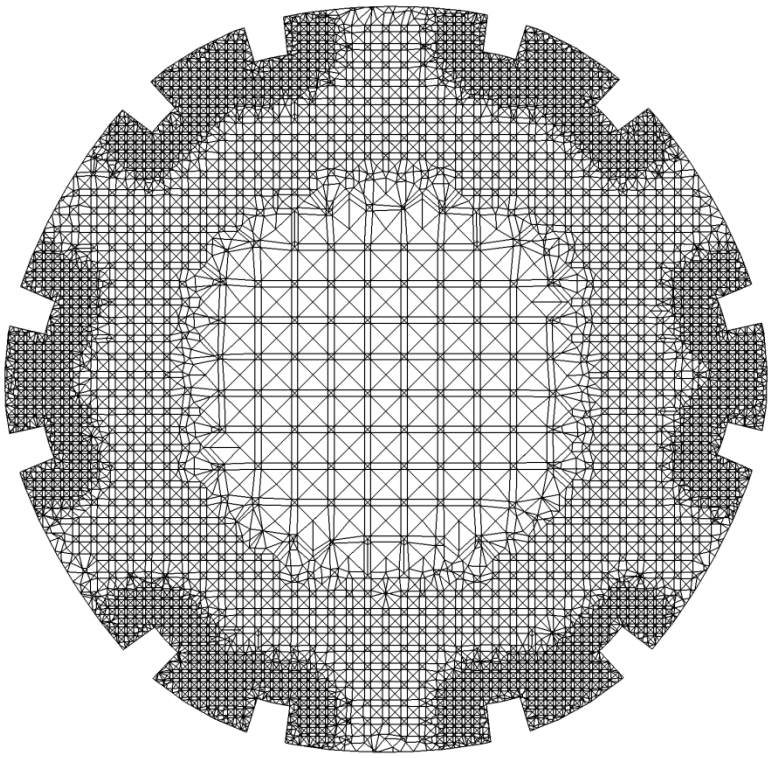

Figure A.30: Longitudinal cross-section view of the discretised stented coronary lumen containing 4,186,199 tetrahedral elements (Mesh 3).

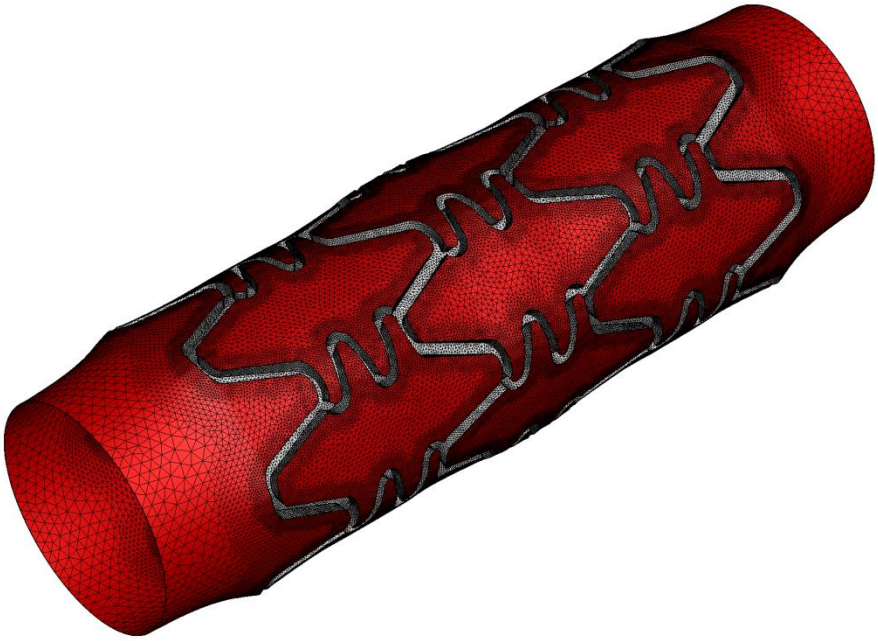

Figure A.31: Isometric view of the discretised CFD model of the stented coronary lumen containing 5,426,405 tetrahedral elements (Mesh 4).

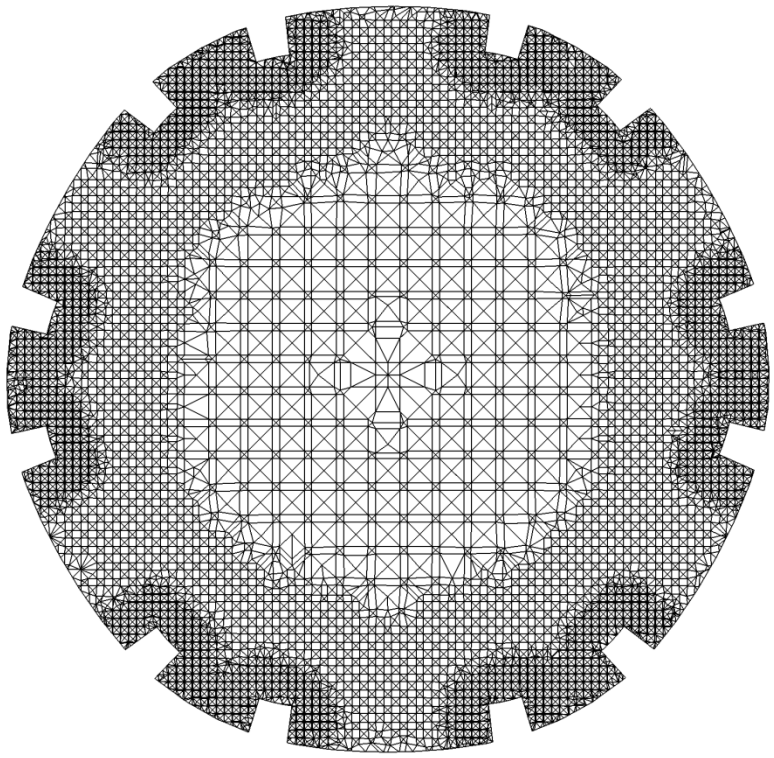

Figure A.32: Longitudinal cross-section view of the discretised stented coronary lumen containing 5,426,405 tetrahedral elements (Mesh 4).

A.3 Cycle Convergence

In order to ensure that cycle convergence is achieved in the transient CFD analyses, four preliminary CFD analyses were carried out to evaluate pulsatile flow conditions within a stented coronary artery. During each of the preliminary CFD analyses, the stented coronary lumen was discretised using 2,709,894 tetrahedral elements and the viscous behaviour of the fluid was described using the non-Newtonian Bird-Carreau model discussed in Chapter 4. A zero relative pressure was specified at the domain outlet and a no-slip condition was specified upon the stent struts and the luminal surface of the artery. To simulate pulsatile flow conditions within a human coronary artery, a fully-developed laminar velocity profile was specified at the domain inlet and the transient velocity profile discussed in Chapter 4 was employed to describe the variation of the centreline velocity during the analyses. In order to determine the number of transient cycles required to ensure that cycle convergence is achieved, four preliminary CFD analyses were carried out in which 1, 2, 3 and 4 consecutive transient cycles were specified and eight time steps were considered for each cycle. The analyses were carried out in ANSYS CFX and a convergence criterion of 10^{-4} was specified for the root mean square values of the velocity and density residuals. Following the completion of the analyses, the results were time-averaged over the final transient cycle and cycle convergence was then identified when the difference between both the area-weighted mean and the area-weighted standard deviation of the TAWSS distribution predicted upon the luminal surface remained below 1% for each successive analysis. As shown in Table A.5, cycle convergence was achieved with three consecutive cycles. As a result, three consecutive cycles are considered in the transient CFD analyses to ensure that cycle convergence is achieved.

Transient Cycles	1	2	3	4
TAWSS (μ_{aw})	0.727 Pa	0.742 Pa	0.738 Pa	0.737 Pa
Difference	-	2.18%	0.65%	0.13%
TAWSS (σ_{aw})	0.510 Pa	0.515 Pa	0.512 Pa	0.512 Pa
Difference	-	1.08%	0.59%	0.09%

Table A.5: Results of the cycle convergence study carried out to identify a suitable number of cycles for the transient CFD analyses.

A.4 Time Step Convergence

In order to ensure that time step convergence is achieved during the transient CFD analyses, four preliminary CFD analyses were carried out to evaluate pulsatile flow conditions in a stented coronary artery. During each of the CFD analyses, the stented coronary lumen was discretised using 2,709,894 tetrahedral elements and the viscous behaviour of the fluid was described using the non-Newtonian Bird-Carreau model discussed in Chapter 4. A zero relative pressure was specified at the domain outlet and a no-slip condition was specified upon the stent struts and the luminal surface of the artery. To simulate pulsatile flow conditions in a human coronary artery, a fully-developed laminar velocity profile was specified at the domain inlet and the transient velocity profile discussed in Chapter 4 was employed to describe the variation of the centreline velocity during the CFD analyses. To determine the number of time steps required to ensure that time step convergence is achieved, four preliminary analyses were carried out in which three consecutive transient cycles were specified and 8, 16. 32, 64 time steps were considered in each transient cycle. The CFD analyses were each carried out in ANSYS CFX and a convergence criterion of 10^{-4} was specified for the root mean square values of the velocity and density residuals. Following the completion of the analyses, the results were time-averaged over the final transient cycle and time step convergence was then identified when the difference between both the area-weighted mean and the area-weighted standard deviation of the TAWSS distribution predicted upon the luminal surface remained below 1% for each successive analysis. As shown in Table A.6, time step convergence was achieved with 32 individual time steps. As such, 32 time steps are considered in the transient CFD analyses in order to ensure that time step convergence is achieved.

Time Steps	8	16	32	64
TAWSS (μ_{aw})	0.738 Pa	0.781 Pa	0.767 Pa	0.763 Pa
Difference	-	5.83%	1.68%	0.54%
TAWSS (σ_{aw})	0.512 Pa	0.538 Pa	0.534 Pa	0.532 Pa
Difference	-	5.11%	0.77%	0.34%

Table A.6: Results of the time step convergence study carried out to identify a suitable number of time steps for the transient CFD analyses.

A.5 Summary

In this appendix, the details of the mesh, cycle and time step convergence studies that were carried out to identify appropriate spatial discretisation, transient loading and temporal discretisation schemes for the CS and CFD analyses are presented. The details of the mesh convergence studies that were carried out to identify a suitable mesh density for the angioplasty balloon, the investigated stent, the coronary artery and the stented coronary lumen are first presented. Based on the results of these studies, the angioplasty balloon is discretised using approximately 12,500 reduced-integration membrane elements (M3D4R) whereas the investigated stent and the coronary artery are discretised using approximately 70,000 and 20,000 reduced-integration continuum elements (C3D8R), respectively. The stented coronary lumen is then discretised using approximately 2,500,000 tetrahedral elements. The details of the cycle and time step convergence studies that were carried out to identify a suitable transient loading and temporal discretisation scheme for the transient CFD analyses are then discussed. Based on the results of these studies, three consecutive transient cycles and 32 individual time steps are specified during the transient CFD analyses to ensure that both cycle and time step convergence are achieved.

APPENDIX B
HEMODYNAMIC VARIABLES

B.1 Introduction

In order to validate both the accuracy and the implementation of the custom-written Python script that was used to calculate the TAWSS, OSI and RRT in Tecplot 360, a number of preliminary CFD analyses were carried out in ANSYS CFX. A steady-state CFD analysis was first carried out to simulate laminar flow over a flat plate and the results were validated against the exact analytical solution. Two transient CFD analyses were also carried out to simulate unidirectional and oscillatory flow over a smooth flat plate and the results were employed to verify both the accuracy and the implementation of the custom-written Python script that was used to calculate the TAWSS, OSI and RRT in Tecplot 360. In this Appendix, the fundamental concepts of boundary layer theory are first introduced and the boundary layer equations are then derived for the case of laminar flow over a smooth flat plate. The details of the preliminary CFD analyses are then presented and the results of these analyses are used to demonstrate the accuracy and implementation of the custom-written Python script that was used to calculate the TAWSS, OSI and RRT in Tecplot 360.

B.2 Boundary Layer Theory

Consider steady flow over a flat plate which is aligned parallel to the direction of the oncoming flow as shown in Figure B.1. The flat plate has an infinitesimal width and a fixed length L whilst the oncoming flow has a uniform velocity U_∞. Due to the no-slip condition, a viscous boundary layer develops at the surface of the plate. Within the boundary layer, the flow is dominated by viscous forces and the velocity of the fluid increases from a value of zero at the surface of the plate until it matches the free-stream velocity at a distance δ normal to the surface of the plate. This distance

is referred to as the boundary layer thickness and is generally defined as the distance normal to the surface of the flat plate at which the velocity reaches 99% of the free-stream velocity. Outside of the boundary layer, viscous forces are negligible and the free-stream velocity is practically unaltered. As the fluid moves along the length of the plate, however, the propagation of viscous forces between neighbouring layers of fluid particles causes the boundary layer to increase in size. Within the initial section of the boundary layer, the flow remains completely laminar. As the boundary layer thickness increases in size, however, the growth and propagation of disturbances in the boundary layer results in a gradual transition from laminar to turbulent flow. The axial distance from the leading edge of the plate at which the transition from laminar to turbulent flow occurs is dependent upon a number of factors such as the surface roughness of the plate and the pressure gradient over its surface. The predominant factor, however, is the local Reynolds number. For steady incompressible flow over a smooth flat plate, the transition form laminar to turbulent flow may not occur until the local Reynolds number reaches a value as high as Re_x = 3,000,000. For a typical commercial surface, however, the transition from laminar to turbulent flow typically occurs when the local Reynolds number reaches a value of about Re_x = 500,000. The governing equations which are employed to describe the behaviour of fluids within a viscous boundary layer were first proposed by Ludwig Prandtl in 1904 and are called the boundary layer equations. In the following section, the boundary layer equations are derived for the case of laminar flow over a smooth flat plate.

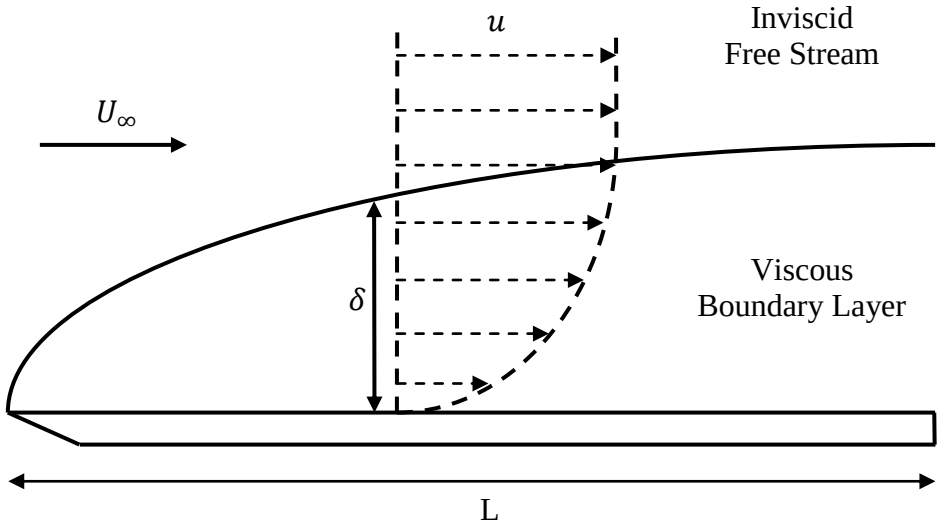

Figure B.1: Development of a viscous boundary layer over a smooth flat plate.

B.2.1 The Boundary Layer Equations

If the influence of buoyant forces is neglected and the flow over the flat plate is assumed to be steady, incompressible and laminar, the 2D continuity and momentum equations may be written in component form as follows:

$$\frac{\partial u}{\partial x} + \frac{\partial v}{\partial y} = 0 \tag{B.1}$$

$$\rho\left(u\frac{\partial u}{\partial x} + v\frac{\partial u}{\partial y}\right) = -\frac{\partial p}{\partial x} + \mu\left(\frac{\partial^2 u}{\partial x^2} + \frac{\partial^2 u}{\partial y^2}\right) \tag{B.2}$$

$$\rho\left(u\frac{\partial v}{\partial x} + v\frac{\partial v}{\partial y}\right) = -\frac{\partial p}{\partial y} + \mu\left(\frac{\partial^2 v}{\partial x^2} + \frac{\partial^2 v}{\partial y^2}\right) \tag{B.3}$$

In order to derive the boundary layer equations, both the continuity and momentum equations are written in non-dimensional form. The non-dimensional x-coordinate is defined as $x^* = (x/L)$ where L denotes the length of the plate. The non-dimensional y-coordinate is defined as $y^* = (y/\delta)$ where δ denotes boundary layer thickness and has not yet been defined. The non-dimensional x-component of the velocity vector is then defined as $u^* = (u/U_\infty)$ where U_∞ denotes the free-stream velocity. The non-dimensional y-component of the velocity vector is derived by substituting the non-dimensional variables into the continuity equation as follows:

$$\frac{\partial u^*}{\partial x^*} + \frac{L}{\delta U_\infty}\frac{\partial v}{\partial y^*} = 0 \tag{B.4}$$

As shown in Equation B.4, the non-dimensional y-component of the velocity vector may be defined as $v^* = (vL/\delta U_\infty)$. The x-momentum equation may then be divided by $(\rho U_\infty^2/L)$ and written in terms of the scaled variables as follows:

$$u^*\frac{\partial u^*}{\partial x^*} + v^*\frac{\partial u^*}{\partial y^*} = -\frac{1}{\rho U_\infty^2}\frac{\partial p}{\partial x^*} + \frac{\mu}{\rho U_\infty L}\left(\frac{L}{\delta}\right)^2\left[\left(\frac{\delta}{L}\right)^2\frac{\partial^2 u^*}{\partial x^{*2}} + \frac{\partial^2 u^*}{\partial y^{*2}}\right] \tag{B.5}$$

As shown in Equation B.5, the non-dimensional pressure may be defined in terms of the density and the free-stream velocity as $p^* = (p/\rho U_\infty^2)$. If it is assumed that the

boundary layer thickness is much smaller than the length of the plate ($\delta \ll L$) when the Reynolds number is large ($Re_x \gg 1$), the term $(\delta/L)^2$ on the right-hand side of the x-momentum equation must approach zero when the Reynolds number is large. As a result, the x-momentum equation may be reduced as follows:

$$u^* \frac{\partial u^*}{\partial x^*} + v^* \frac{\partial u^*}{\partial y^*} = -\frac{\partial p^*}{\partial x^*} + Re_x^{-1} \left(\frac{L}{\delta}\right)^2 \left(\frac{\partial^2 u^*}{\partial y^{*2}}\right) \tag{B.6}$$

Equation B.6 indicates that balance between the right- and left-hand sides of the x-momentum equation may only be achieved if $(\delta/L) = Re_x^{-1/2}$. As a result, the non-dimensional x-momentum equation may be written as follows:

$$u^* \frac{\partial u^*}{\partial x^*} + v^* \frac{\partial u^*}{\partial y^*} = -\frac{\partial p^*}{\partial x^*} + \frac{\partial^2 u^*}{\partial y^{*2}} \tag{B.7}$$

The focus is now shifted to the y-momentum equation. The y-momentum equation may be expressed in terms of the non-dimensional variables as follows:

$$\begin{aligned} &\frac{\rho U_\infty^2 \delta}{L^2}\left(u^* \frac{\partial v^*}{\partial x^*} + v^* \frac{\partial v^*}{\partial y^*}\right) \\ &= -\frac{\rho U_\infty^2}{\delta}\frac{\partial p^*}{\partial y^*} + \frac{\mu U_\infty}{\delta L}\left[\left(\frac{\delta}{L}\right)^2 \frac{\partial^2 v^*}{\partial x^{*2}} + \frac{\partial^2 v^*}{\partial y^{*2}}\right] \end{aligned} \tag{B.8}$$

Dividing Equation B.8 throughout by $\rho U_\infty^2/\delta$ and then substituting $(\delta/L) = Re_x^{-1/2}$ allows the y-momentum equation to be rewritten as follows:

$$\begin{aligned} &Re_x^{-1}\left(u^* \frac{\partial v^*}{\partial x^*} + v^* \frac{\partial v^*}{\partial y^*}\right) = \\ &-\frac{\partial p^*}{\partial y^*} + Re_x^{-1}\left(Re_x^{-1}\frac{\partial^2 v^*}{\partial x^{*2}} + \frac{\partial^2 v^*}{\partial y^{*2}}\right) \end{aligned} \tag{B.9}$$

If the Reynolds number is assumed to be large, then Re_x^{-1} must approach zero and the non-dimensional y-momentum equation may be written as follows:

$$-\frac{\partial p^*}{\partial x^*} = 0 \tag{B.10}$$

The resulting equations are generally referred to as the boundary layer equations and may be written in dimensional form as follows:

$$\frac{\partial u}{\partial x} + \frac{\partial v}{\partial y} = 0 \tag{B.11}$$

$$u\frac{\partial u}{\partial x} + v\frac{\partial u}{\partial x} = -\frac{1}{\rho}\frac{\partial p}{\partial x} + \upsilon\frac{\partial^2 u}{\partial y^2} \tag{B.12}$$

$$\frac{\partial p}{\partial y} = 0 \tag{B.13}$$

The term υ denotes the kinematic viscosity and is defined as μ/ρ. The y-momentum equation indicates that pressure is independent of the y-coordinate. As such, at any axial distance from the leading edge of the plate, the pressure within the boundary layer must equal the pressure within the free-stream. The axial pressure gradient may then be determined using Bernoulli's equation as follows:

$$\frac{\partial p}{\partial x} = -\rho U_\infty \frac{\partial U_\infty}{\partial x} \tag{B.14}$$

For the case of steady incompressible laminar flow over a flat plate, however, it is assumed that $y \to \infty$ and both the free-stream velocity and the pressure are constant. As a result, the x-momentum equation can be rewritten a final time as follows:

$$u\frac{\partial u}{\partial x} + v\frac{\partial u}{\partial x} = \upsilon\frac{\partial^2 u}{\partial y^2} \tag{B.15}$$

The resulting partial differential equations denote the boundary layer equations for steady incompressible laminar flow over a flat plate. The equations were first solved by a student of Ludwig Prandtl's named Heinrich Blasius in 1908. Blasius conducted a number of experiments to study steady incompressible laminar flow over a smooth flat plate and noted that local velocity profiles have the same non-dimensional shape. Blasius then combined the independent variables x and y into a similarity variable η which allowed the boundary layer equations to be reduced into a system of ordinary differential equations. Blasius then employed both series and asymptotic expansions in order to solve the resulting system of ordinary differential equations.

B.2.2 The Blasius Solution

From the dimensional analysis it is clear that the boundary layer thickness increases with the axial distance from the leading edge of the plate as follows:

$$\delta \approx \frac{L}{\sqrt{Re_x}} \approx \frac{x}{\sqrt{Re_x}} \tag{B.16}$$

As a result, the following similarity variable may be proposed:

$$\eta = \frac{y}{\delta(x)} = y\sqrt{\frac{U_\infty}{\nu x}} \tag{B.17}$$

It also proves convenient to work in terms of the stream function as this ensures that the continuity equation is inherently satisfied. The stream function may be written in terms of the similarity variable and a similarity function $f(\eta)$ as follows:

$$\psi(x,y) = \sqrt{\nu x U_\infty} f(\eta) \tag{B.18}$$

The x- and y-components of the velocity vector may then be written in terms of the stream function and the similarity variable as follows:

$$u = \frac{\partial \psi}{\partial y} = U_\infty \frac{df(\eta)}{d\eta} \tag{B.19}$$

$$v = -\frac{\partial \psi}{\partial x} = \frac{1}{2}\sqrt{\frac{\nu U_\infty}{x}}\left[\eta \frac{df(\eta)}{d\eta} - f(\eta)\right] \tag{B.20}$$

By substituting both Equations B.19 and B.20 into the boundary layer equations, the x-momentum equation may be rewritten, after some manipulation, as follows:

$$\frac{d^3 f(\eta)}{d\eta^3} + \frac{1}{2} f(\eta) \frac{d^2 f(\eta)}{d\eta^2} = 0 \tag{B.21}$$

Equation B.21 is referred to as the Blasius equation and, to date, it has not yielded an analytical solution. The Blasius equation can, however, be solved using a number of numerical strategies and complex expansions. The complete solution of the Blasius equation in terms of the similarity variable η is shown in Table B.1.

η	$f(n)$	$\frac{df(\eta)}{d\eta}$	$\frac{d^2f(\eta)}{d\eta^2}$
0.0	0.000000	0.000000	0.332031
0.1	0.001660	0.033203	0.332022
0.2	0.006640	0.066403	0.331958
0.3	0.014940	0.099591	0.331783
0.4	0.026558	0.132754	0.331444
0.5	0.041490	0.165872	0.330885
0.6	0.059730	0.198922	0.330053
0.7	0.081271	0.231872	0.328896
0.8	0.106100	0.264688	0.327364
0.9	0.134202	0.297331	0.325407
1.0	0.165559	0.329754	0.322982
1.5	0.370110	0.486752	0.302559
2.0	0.649974	0.629719	0.266735
2.5	0.996236	0.751206	0.217402
3.0	1.396705	0.845987	0.161356
3.5	1.837566	0.912982	0.107773
4.0	2.305586	0.955461	0.064237
4.5	2.789945	0.979459	0.033984
5.0	3.283057	0.991488	0.015909
5.5	3.780329	0.996825	0.006580
6.0	4.279351	0.998920	0.002403
6.5	4.779026	0.999646	0.000774
7.0	5.278916	0.999869	0.000220
7.5	5.778869	0.999929	0.000055
8.0	6.278838	0.999944	0.000012
8.5	6.778811	0.999947	0.000002
9.0	7.278785	0.999947	0.000000
9.5	7.778758	0.999947	0.000000
10.0	8.278732	0.999947	0.000000

Table B.1: Blasius solution in terms of the similarity variable η.

The non-dimensional components of the velocity vector may be written in terms of the similarity variable and derived from the Blasius solution as follows:

$$u^* = \frac{df(\eta)}{d\eta} \tag{B.22}$$

$$v^* = \frac{1}{2}\left(\eta \frac{df(\eta)}{d\eta} - f(\eta)\right) \tag{B.23}$$

As shown in Table B.1, $u^* = 0.99$ when $\eta \approx 5.0$. By substituting this value back into Equation B.17, the boundary layer thickness may be approximated as follows:

$$\delta \approx 5\sqrt{\frac{\nu x}{U_\infty}} = \frac{5x}{\sqrt{Re_x}} \tag{B.24}$$

In a similar fashion, the WSS that is exerted upon the surface of the flat plate may also be derived in terms of the similarity variable η as follows:

$$\tau_w = \mu \left.\frac{\partial v}{\partial y}\right|_{y=0} = \mu U_\infty \sqrt{\frac{U_\infty}{\nu x}} \left.\frac{d^2 f(\eta)}{d\eta^2}\right|_{\eta=0} \tag{B.25}$$

As shown in Table B.1, $d^2 f(\eta)/d\eta^2 \approx 0.332$ when $\eta = 0$. As such, the WSS that is exerted upon the surface of the plate may be approximated as follows:

$$\tau_w \approx \frac{0.332 \rho U_\infty^2}{\sqrt{Re_x}} \tag{B.26}$$

Alternatively, the WSS exerted upon the plate may be expressed in terms of a non-dimensional skin friction coefficient which is defined as follows:

$$C_f = \frac{2\tau_w}{\rho U_\infty^2} \tag{B.27}$$

As such, the skin friction coefficient may be approximated as follows:

$$C_f \approx \frac{0.664}{\sqrt{Re_x}} \tag{B.28}$$

B.3 Fluid Dynamics Analyses

In order to validate the accuracy of the custom-written Python script that was used to calculate the TAWSS, OSI and RRT in Tecplot 360, three preliminary CFD analyses were carried out in ANSYS CFX. A steady-state CFX analysis was first carried out to simulate steady incompressible laminar flow over a flat plate and the results were then validated by comparing the predicted non-dimensional velocity profiles at three different axial distances from the leading edge of the plate to those derived from the exact Blasius solution. The accuracy of the results was also validated by comparing the predicted magnitude of the WSS and the skin friction coefficient along the axial length of the flat plate to that derived from the exact Blasius solution. Two similar transient analyses were also carried out to simulate uni-directional and oscillatory flow over a flat plate and the results were used to validate both the implementation and accuracy of the custom-written Python script that was used to calculate the TAWSS, OSI and RRT in Tecplot 360. Specifically, the TAWSS, OSI and RRT predicted at a specific node in the transient CFD analyses were compared to values derived from a hand calculation. In the following sections, the details and results of both the steady and transient CFD analyses are described in detail.

B.3.1 Geometry and Discretisation

In order to simulate flow over a smooth flat plate, a 3D geometrical model of the fluid domain was generated in ANSYS ICEM CFX. As shown in Figure B.2, the flat plate was assigned a fixed length of 1.00 m and was preceded by a free-slip region that was assigned a length of 0.10 m. The fluid domain was assigned a height of 1.60 m and a thickness of 0.005 m and was discretised using almost 60,000 hexahedral elements. As shown in Figure B.3, the mesh was strongly biased towards both the surface and the leading edge of the flat plate. In order to carry out the preliminary CFD analyses, the resulting mesh was then imported into ANSYS CFX.

B.3.2 Constitutive Material Models

During each of the analyses, the viscous behaviour of the fluid within the flow field was assumed to be Newtonian and the fluid was assigned the properties of water. Specifically, the mass density of the fluid was assigned a value of 997 kg/m^3 whilst the dynamic viscosity of the fluid was assigned a value of 0.00089 Pa·s.

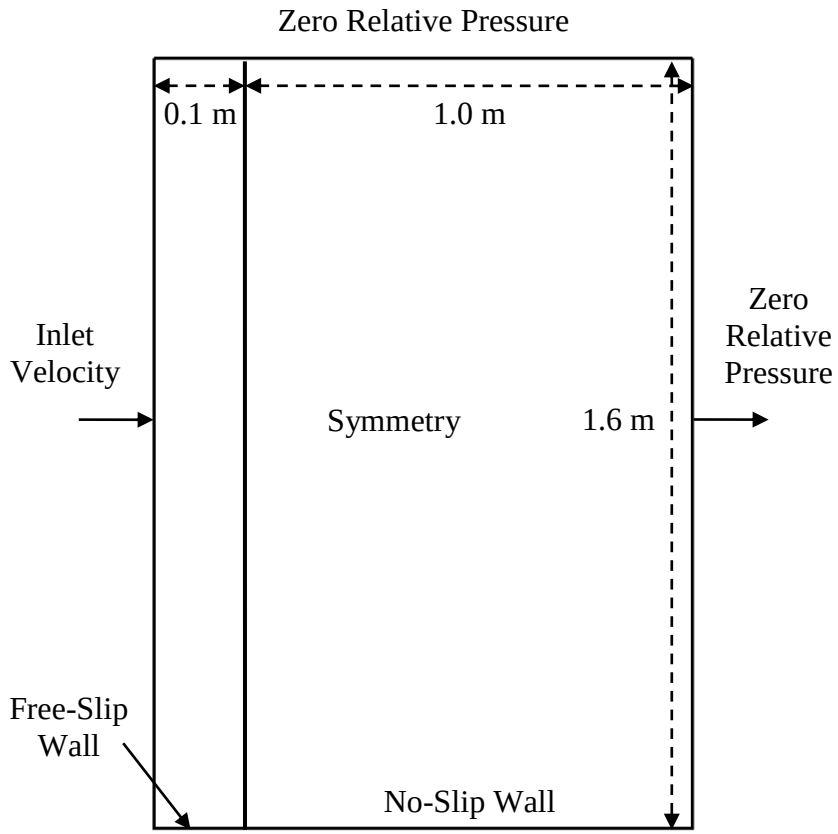

Figure B.2: Computational domain and the specified boundary conditions.

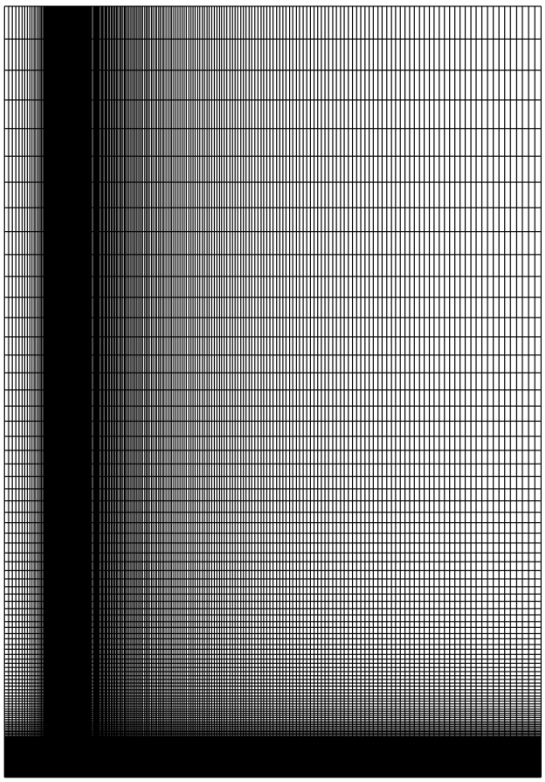

Figure B.3: CFD model generated for the flat plate analysis.

B.3.3 Boundary and Loading Conditions

As shown in Figure B.2, a number of boundary conditions were required to simulate flow over a flat plate. As the flow was assumed to be 2D, symmetry conditions were specified upon the two largest faces of the domain. The free-slip region was then described using a free-slip condition and the surface of the plate was described using a no-slip condition. A zero relative pressure was then specified at both the far field and the domain outlet. Finally, a uniform inlet velocity profile was then specified at the domain inlet. Three different analyses were carried out by varying the definition of the inlet velocity specified at the domain inlet. In the first analysis, the flow was assumed to be steady and the inlet velocity was defined as follows:

$$v = 0.5\text{m/s} \tag{B.29}$$

In the second analysis, the flow was assumed to be both transient and unidirectional and the inlet velocity profile was defined as follows:

$$v = 0.5 + 0.005[\sin(7.85398t)] \tag{B.30}$$

Equation B.30 describes a sinusoidal wave with a mean value of 0.5 m/s, a period of 0.8 s and an amplitude of 0.005 m/s. As a result, the magnitude of the inlet velocity varied by only ±1% from the mean value of 0.5 m/s throughout the transient cycle. In the third analysis, the flow was assumed to be both transient and fully-oscillatory and the magnitude of the inlet velocity profile was defined as follows:

$$v = 0.5[\sin(7.85398t)] \tag{B.31}$$

Equation B.31 describes a sine wave with a mean value of 0 m/s, a period of 0.8 s and an amplitude of 0.5 m/. As a result, the magnitude of the inlet velocity varied by ±100% from the mean value of 0 m/s throughout the transient cycle.

B.3.4 Solution

In order to ensure that both cycle and time step convergence were achieved during the transient CFD analyses, ten consecutive transient cycles were specified and eight individual time steps were considered for each cycle. During both the steady-state and transient CFD analyses, a convergence criterion of 10^{-4} was specified for the root mean square values of both the velocity and density residuals.

B.4 Results and Discussion

B.4.1 Steady Flow

The velocity distribution predicted within the fluid domain following the completion of the steady-state analysis is shown in Figure B.4 and the development and growth of a viscous boundary layer along the length of the plate is evident. Following the completion of the steady-state analysis, the non-dimensional x- and y-components of the velocity vector were calculated at three axial distances (x = 0.3 m, x = 0.6 m and x = 0.9 m) from the leading edge of the plate. These non-dimensional components were then used to plot both the non-dimensional axial and vertical velocity profiles at the three axial positions. As shown in Figure B.5 and Figure B.6, both the non-dimensional axial and vertical velocity profiles predicted at the three axial positions were found to be in good agreement with those derived from the Blasius solution. The WSS distribution predicted along the length of the plate was then evaluated and used to calculate the skin friction coefficient. As shown in Figure B.7 and Figure B.8, both the WSS distribution and the skin friction coefficient predicted along the axial length of the plate were found to be in excellent agreement with those derived from the Blasius solution. The close agreement between the predicted results and the Blasius solution demonstrates the accuracy of the flat plate analysis.

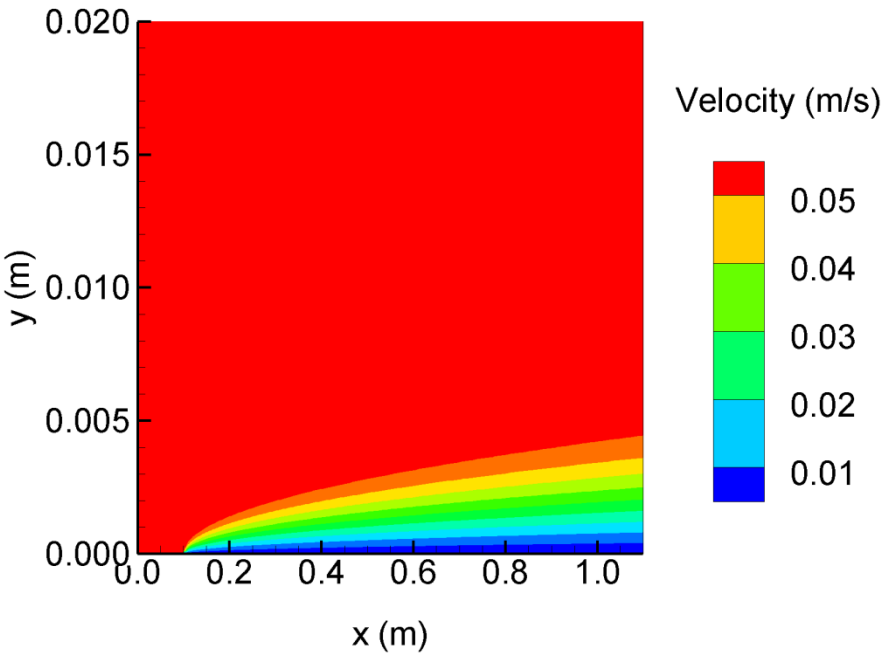

Figure B.4: Contour plot demonstrating the change in velocity and the development of the viscous boundary layer along the length of the plate.

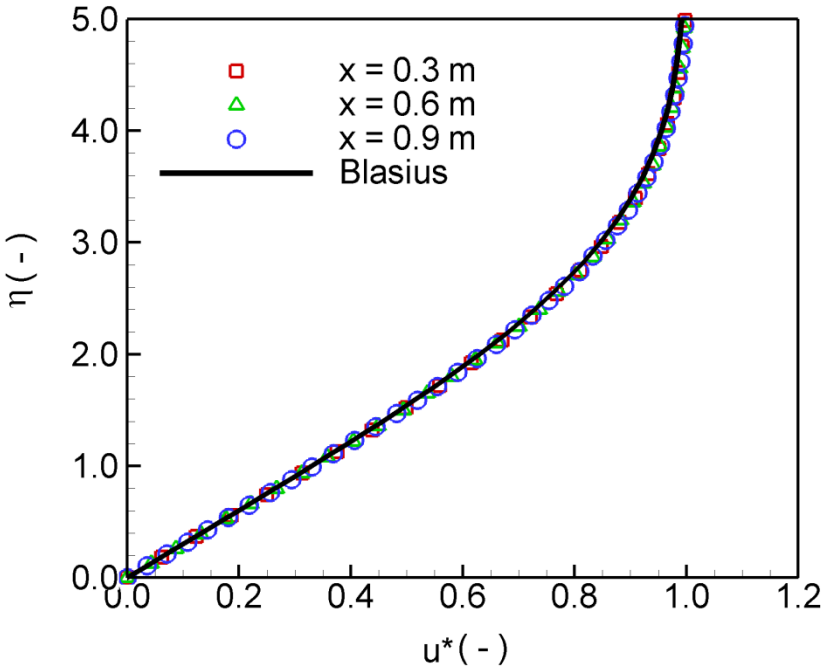

Figure B.5: Comparison of the non-dimensional axial velocity profile predicted at three axial positions along the length of the flat plate with the theoretical axial velocity profile derived from the exact Blasius solution.

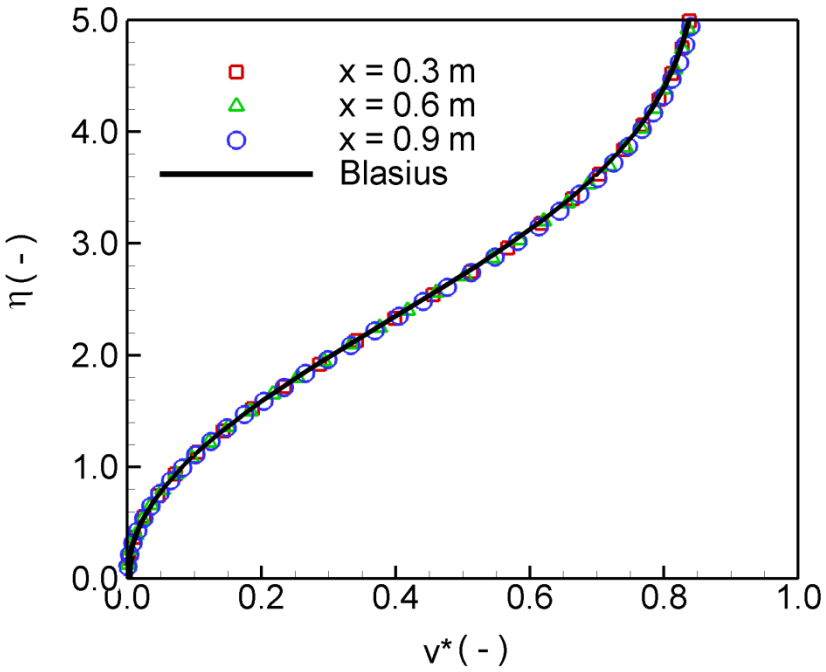

Figure B.6: Comparison of the non-dimensional vertical velocity profile predicted at three axial positions along the length of the flat plate with the theoretical vertical velocity profile derived from the exact Blasius solution.

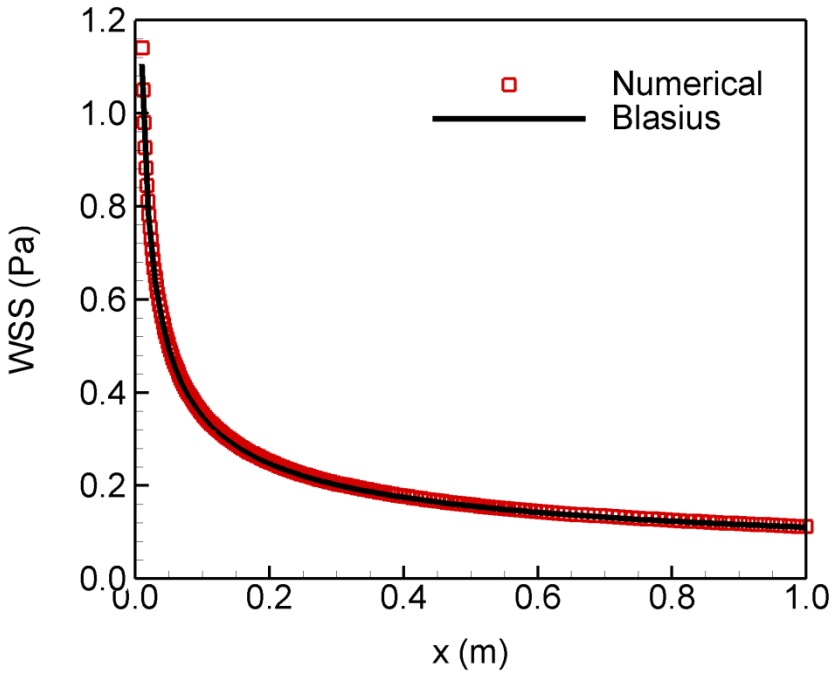

Figure B.7: Comparison of the WSS distribution predicted along the length of the flat plate with the theoretical WSS distribution derived from the exact Blasius solution.

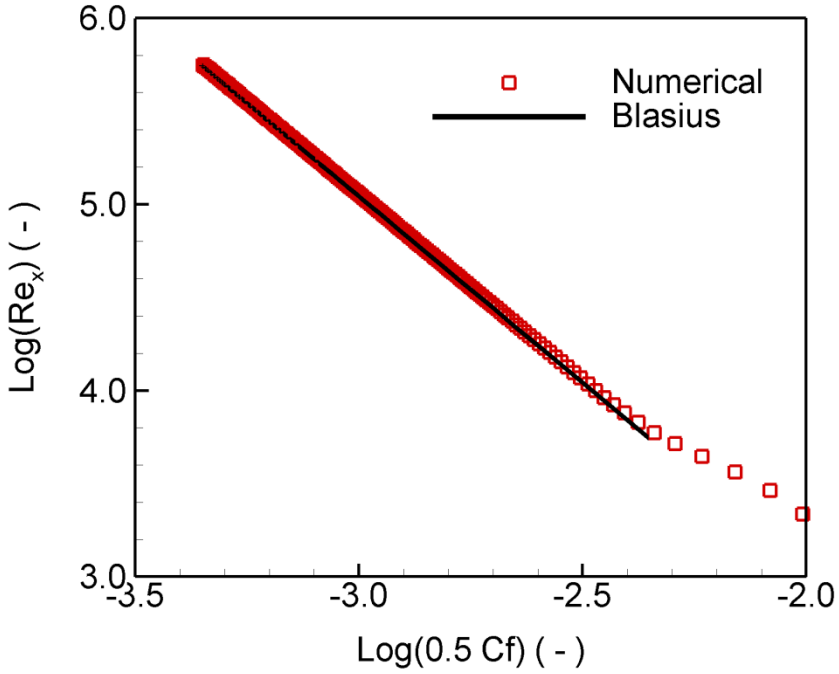

Figure B.8: Comparison of the skin friction coefficient predicted along the length of the flat plate with the skin friction coefficient derived from the exact Blasius solution.

B.4.2 Transient Unidirectional Flow

In the first transient CFD analysis, the flow was assumed to be unidirectional and the inlet velocity was specified such that its magnitude varied by ±1% from the mean value of 0.5 m/s during the transient cycle. Following the completion of the transient analysis, the TAWSS, OSI and RRT distributions predicted on the surface of the flat plate were calculated using a custom-written Python script. Attention is now focused upon a single node of interest that was located at an axial distance of 0.505 m from the leading edge of the plate. At this node, the predicted magnitude of the TAWSS, OSI and RRT was 0.158 m/s, 0 and 6.345 Pa^{-1}, respectively. In order to validate both the implementation and accuracy of the custom-written Python script, the calculation of these variables is demonstrated. To calculate the variables, the magnitude of the WSS vector and its x-, y- and z- components predicted at the node of interest at each individual time step during the transient cycle are shown in Table B.2.

Time Step	U_∞ (m/s)	$\tau_{w,x}$ (Pa)	$\tau_{w,y}$ (Pa)	$\tau_{w,z}$ (Pa)	$\boldsymbol{\tau}_\mathbf{w}$ (Pa)
1	0.500	0.166	0	0	0.166
2	0.504	0.172	0	0	0.172
3	0.505	0.169	0	0	0.169
4	0.503	0.159	0	0	0.159
5	0.500	0.149	0	0	0.149
6	0.497	0.144	0	0	0.144
7	0.495	0.147	0	0	0.147
8	0.497	0.156	0	0	0.156
9	0.500	0.166	0	0	0.166

Table B.2: Magnitude of the WSS vector and its individual components predicted at the node of interest for each time step during the transient cycle.

Using the trapezoidal rule of numerical integration, which is shown in Equation 4.9, the TAWSS is first calculated at the node of interest as follows:

$$\mathrm{TAWSS} = \frac{1}{0.8}\left[\frac{0.8}{2(9-1)}\begin{pmatrix}0.166 + 2(0.172\\ +0.169 + 0.159\\ +0.149 + 0.144\\ +0.147 + 0.156)\\ +0.166\end{pmatrix}\right] = 0.158\ \mathrm{Pa} \qquad \text{(B.32)}$$

As shown in Equation B.32, the calculated TAWSS was in exact agreement with that predicted at the node of interest. As the input velocity varied by only ±1% from the mean value of 0.5 m/s during the transient cycle, the calculated TAWSS was also in good agreement with the WSS predicted at the node of interest during the steady-state analysis and that derived from the exact Blasius solution:

$$\begin{aligned} \mathrm{WSS}_{\mathrm{Blasius}} &= 0.156 \text{ Pa} \qquad \mathrm{WSS}_{\mathrm{Steady}} = 0.158 \text{ Pa} \\ \mathrm{WSS}_{\mathrm{Transient}} &= 0.158 \text{ Pa} \qquad \mathrm{WSS}_{\mathrm{Calculated}} = 0.158 \text{ Pa} \end{aligned} \tag{B.33}$$

In order to calculate the OSI, the following integrals are first evaluated:

$$\left|\int_0^T \tau_w dt\right| = \left[\frac{0.8}{2(9-1)}\begin{pmatrix} 0.166 + 2(0.172 \\ +0.169 + 0.159 \\ +0.149 + 0.144 \\ +0.147 + 0.156) \\ +0.166 \end{pmatrix}\right] = 0.126 \text{ Pa} \tag{B.34}$$

$$\int_0^T |\tau_w| dt = \left[\frac{0.8}{2(9-1)}\begin{pmatrix} 0.166 + 2(0.172 \\ +0.169 + 0.159 \\ +0.149 + 0.144 \\ +0.147 + 0.156) \\ +0.166 \end{pmatrix}\right] = 0.126 \text{ Pa} \tag{B.35}$$

The OSI is then calculated according to Equation 4.10 as follows:

$$\mathrm{OSI} = 0.5\left(1 - \frac{0.126}{0.126}\right) = 0 \tag{B.36}$$

Again, the calculated OSI was in exact agreement with that predicted at the node of interest and its magnitude implies that the flow remained entirely unidirectional. The RRT is then calculated according to Equation 4.11 as follows:

$$\mathrm{RRT} = \frac{1}{[1 - 2(0)]0.158} = 6.345 \text{ Pa}^{-1} \tag{B.37}$$

Again, the calculated RRT was in exact agreement with that predicted at the node of interest. As the values of the TAWSS, OSI and RRT were in exact agreement with those predicted at the node of interest, it is clear that the Python script was correctly implemented in Tecplot 360 and provides accurate results.

B.4.3 Transient Oscillatory Flow

In the second transient analysis, the flow was assumed to be fully-oscillatory and the inlet velocity was specified such that its magnitude varied by ±100% from the mean value of 0 m/s during the transient cycle. Following the completion of the transient analysis, the TAWSS, OSI and RRT distribution predicted upon the surface of the plate was calculated using a custom-written Python script. Attention is again focused upon the node of interest that was located at an axial distance of 0.505 m from the leading edge of the plate. At this node, the predicted magnitude of the TAWSS, OSI and RRT was 0.888 m/s, 0.49 and 75.355 Pa^{-1}, respectively. To further validate both the implementation and accuracy of the custom-written Python script, the calculation of these variables is demonstrated. To calculate the variables, the magnitude of the WSS vector and its x-, y- and z- components predicted at the node of interest at each individual time step during the transient cycle are shown in Table B.3.

Time Step	U_∞ (m/s)	$\tau_{w,x}$ (Pa)	$\tau_{w,y}$ (Pa)	$\tau_{w,z}$ (Pa)	$\boldsymbol{\tau}_\mathrm{w}$ (Pa)
1	0.500	1.097	0	0	1.097
2	0.354	0.148	0	0	0.148
3	0.001	-0.887	0	0	0.887
4	-0.354	-1.421	0	0	1.421
5	-0.500	-1.123	0	0	1.123
6	-0.354	-0.175	0	0	0.175
7	-0.002	0.860	0	0	0.860
8	0.353	1.395	0	0	1.395
9	0.500	1.097	0	0	1.097

Table B.3: Magnitude of the WSS vector and its individual components predicted at the node of interest for each time step during the transient cycle.

Using the trapezoidal rule of numerical integration, which is shown in Equation 4.9, the TAWSS is first calculated at the node of interest as follows:

$$\mathrm{TAWSS} = \frac{1}{0.8}\left[\frac{0.8}{2(9-1)}\begin{pmatrix}1.097 + 2(0.148\\ +0.887 + 1.421\\ +1.123 + 0.175\\ +0.860 + 1.395)\\ +1.097\end{pmatrix}\right] = 0.888\ \mathrm{Pa} \qquad \text{(B.38)}$$

As shown in Equation B.38, the calculated TAWSS was in exact agreement with that predicted at the node of interest. As the input velocity varied by ±100% from the mean value of 0.5 m/s during the transient cycle, the calculated TAWSS was also found to be very different from both the WSS predicted at the node of interest during the steady-state analysis and that derived from the exact Blasius solution:

$$\begin{aligned} \mathrm{WSS}_{\mathrm{Blasius}} &= 0.156 \text{ Pa} \qquad \mathrm{WSS}_{\mathrm{Steady}} = 0.158 \text{ Pa} \\ \mathrm{WSS}_{\mathrm{Transient}} &= 0.888 \text{ Pa} \qquad \mathrm{WSS}_{\mathrm{Calculated}} = 0.888 \text{ Pa} \end{aligned} \tag{B.39}$$

In order to calculate the OSI, the following integrals are first evaluated:

$$\left|\int_0^T \tau_w dt\right| = \left[\frac{0.8}{2(9-1)}\begin{pmatrix} 1.097 + 2(0.148 \\ -0.887 - 1.421 \\ -1.123 - 0.175 \\ +0.860 + 1.395) \\ +1.097 \end{pmatrix}\right] = 0.011 \text{ Pa} \tag{B.40}$$

$$\int_0^T |\tau_w| dt = \left[\frac{0.8}{2(9-1)}\begin{pmatrix} 1.097 + 2(0.148 \\ +0.887 + 1.421 \\ +1.123 + 0.175 \\ +0.860 + 1.395) \\ +1.097 \end{pmatrix}\right] = 0.126 \text{ Pa} \tag{B.41}$$

The OSI is then calculated according to Equation 4.10 as follows:

$$\mathrm{OSI} = 0.5\left(1 - \frac{0.011}{0.126}\right) = 0.49 \tag{B.42}$$

Again, the calculated OSI was in exact agreement with that predicted at the node of interest and its magnitude indicates that the flow was almost fully-oscillatory. The RRT is then calculated according to Equation 4.11 as follows:

$$\mathrm{RRT} = \frac{1}{[1 - 2(0.49)]0.888} = 75.355 \text{ Pa}^{-1} \tag{B.43}$$

Again, the calculated RRT was in exact agreement with that predicted at the node of interest. As the values of the TAWSS, OSI and RRT were in exact agreement with those predicted at the node of interest, it is clear that the Python script was correctly implemented in Tecplot 360 and provides accurate results.

B.5 Summary

The aim of this Appendix was to validate the implementation and accuracy of the custom-written Python script that is used to calculate the magnitude of the TAWSS, OSI and RRT in Tecplot 360. To validate both the implementation and accuracy of the custom-written Python script, three preliminary CFD analyses were carried out using ANSYS CFX. A steady-state CFD analysis was first carried out to simulate steady laminar flow over a smooth flat plate and the results were validated against the exact solution. Two transient CFD analyses were also carried out to simulate uni-directional and oscillatory flow over a smooth flat plate and the results were used to demonstrate the calculation of the TAWSS, OSI and RRT. As the calculated results were in exact agreement with those predicted during the transient CFD analyses, the implementation and accuracy of the Python script were verified.